Universidad Autónoma de Madrid

Facultad de Ciencias

Volume (In)Dependence in Yang-Mills Theories

Tesis doctoral presentada por Eduardo Ibáñez Bribián
y dirigida por Margarita García Pérez
Doctorado en Física Teórica

2019

Departamento de Física Teórica

A mis padres, Mariano y Zenaida.

Contents

Agradecimientos / Acknowledgements

Agradecimientos

Nos gustaría agradecer a Antonio González-Arroyo y Alberto Ramos las valiosas discusiones acerca de los temas tratados en esta tesis y otros relacionados. Agradecemos también el apoyo económico proporcionado por las becas MINECO/FEDER FPA2015-68541-P, FPI BES-2015-071791, por los programas de Excelencia Severo Ochoa SEV-2012-0249 y SEV-2016-0597, y por el programa de investigación e innovación Horizon 2020 de la Unión Europea bajo la beca Marie Skodowska-Curie No 813942 (EuroPLEx). Las simulaciones y cálculos numéricos presentados en este trabajo se llevaron a cabo en el cluster Hydra del Instituto de Física Teórica (IFT) UAM-CSIC y en el Centro de Supercomputación de Galicia (CESGA).

Acknowledgements

We would like to thank Antonio González-Arroyo and Alberto Ramos for the useful discussions on the topics of this thesis as well as on other related ones. We also acknowledge the financial support granted by the MINECO/FEDER FPA2015-68541-P and FPI BES-2015-071791 grants, by the MINECO Centro de Excelencia Severo Ochoa SEV-2012-0249 and SEV-2016-0597 programmes, and by the Horizon 2020 research and innovation programme of the the European Union, under the Marie Skodowska-Curie grant agreement No 813942 (EuroPLEx). The simulations and numerical computations presented in this work were performed at both the Hydra cluster at the Instituto de Física Teórica UAM-CSIC (IFT) and at the Galicia Supercomputing Center (CESGA).

Resumen / Abstract

Resumen

Pese a su aparente simplicidad, las teorías de Yang-Mills dan lugar a un extraordinaria variedad de fenómenos físicamente interesantes. En particular, su estudio en volumen finito ha demostrado a lo largo de los años ser una herramienta de enorme utilidad de cara a comprender el funcionamiento de la interacción fuerte. Fenómenos como la reducción de volumen o reducción Eguchi-Kawai, conocidos desde hace décadas, demuestran que existe en dichas teorías una íntima relación entre grados de libertad espacio-temporales y grados de libertad de color, hasta tal punto que en el extremo del límite de gran número de colores los primeros se vuelven completamente redundantes, permitiendo reducir una teoría gauge definida en un toro de volumen finito a un modelo de matrices en un único punto.

Como tal, el estudio de la relación entre los grados de libertad espacio-temporales y los grados de libertad de color en teorías gauge presenta un enorme interés. El uso de las condiciones de contorno introducidas por 't Hooft en 1979, conocidas como *twisted boundary conditions*, permite además, aparte de proteger determinadas simetrías necesarias para la realización de la idea de reducción, relacionar de manera exacta y en el contexto de dualidades las teorías gauge definidas en el toro con teorías de campos no conmutativas.

En dicho contexto surge la conjetura de independencia de volumen, que propone que para teorías gauge con las condiciones de contorno anteriormente mencionadas, la dinámica de la teoría viene controlada, salvo efectos de N finito, por una longitud efectiva que emerge de manera natural y que combina la longitud física del toro con el número de colores de la teoría. Dicha longitud efectiva, además, tiene en el contexto de la dualidad una correspondencia directa con el tamaño del toro no conmutativo asociado.

El propósito de esta tesis consiste precisamente en estudiar determinados as-

pectos de dicha conjetura, en el caso particular de cuatro dimensiones. Dicho estudio se realiza a través del análisis de las propiedades de la constante de acoplamiento de 't Hooft, definida mediante técnicas de *gradient flow*, y de dos maneras distintas: mediante teoría de perturbaciones en el continuo por un lado, y empleando un esquema de cálculo no perturbativo basado en la discretización de la teoría sobre el retículo por el otro.

Para el primer caso, calculamos el comportamiento de la constante de acoplamiento fuerte de 't Hooft de una teoría $SU(N)$ en el continuo, a segundo orden en teoría de perturbaciones. Definimos la constante en un esquema de volumen finito, utilizando la técnica conocida como *gradient flow* y empleando *twisted boundary conditions* en un toro asimétrico. La constante se define en términos de la escala efectiva $\tilde{l}$ mencionada anteriormente, que combina el tamaño físico del toro con el rango N del grupo gauge, y se determina usando regularización dimensional, relacionándola con la constante de acoplamiento del esquema $\overline{\text{MS}}$. Presentamos además los resultados numéricos del cálculo de la constante en el caso particular en el que el tensor de *twist* es trivial en todos los planos menos uno, obteniendo el coeficiente que relaciona nuestro esquema con el esquema $\overline{\text{MS}}$ y determinando el cociente de parámetros Λ entre ambos. Analizamos, además, la dependencia en N de los resultados, y sus posibles implicaciones para teorías gauge no conmutativas, así como su relación con la conjetura de independencia de volumen.

Para el segundo caso, nos centramos en el caso particular de $SU(3)$. En él, calculamos el comportamiento de la constante de acoplamiento de manera no perturbativa, discretizando la teoría sobre el retículo y extrapolando al continuo. Trabajamos una vez más sobre un toro asimétrico con *twisted boundary conditions* en un solo plano, y empleamos técnicas de *gradient flow* para definir la constante de acoplamiento de 't Hooft en términos de la misma longitud efectiva que combina el tamaño de la caja con el rango del grupo. Presentamos los resultados de calcular dicha constante de acoplamiento mediante simulaciones numéricas, empleando técnicas de *step scaling*, en un amplio rango en la escala de energías, así como un estudio del comportamiento de la carga topológica en las configuraciones simuladas. Analizamos además el efecto de la elección de diversos parámetros técnicos, tales como la constante que relaciona la escala de energía con el tamaño efectivo de la caja o el observable discretizado que se usa para calcular la constante de acoplamiento, y comparamos nuestros resultados con los

obtenidos empleando teoría de perturbaciones, y con los resultados de estudios en esquemas similares.

La organización de la tesis es la siguiente: en el capítulo 1 presentamos una breve introducción al estudio de las teorías gauge en toros finitos, centrándonos en la sección 1.1 en los fenómenos de reducción de volumen, en el concepto de independencia de volumen, y en la definición e implementación de las condiciones de contorno conocidas como *twisted boundary conditions*, notablemente en relación a su conexión con teorías de campos no conmutativas. A continuación, introducimos en la sección 1.2 los conceptos de *smearing* y *gradient flow* que se emplearán, en combinación con la idea de reducción, para en la sección 1.2.5 definir la constante de acoplamiento λ_{TGF} que emplearemos a lo largo del trabajo.

En el capítulo 2 exponemos el trabajo relacionado con el cálculo de la constante de acoplamiento en teoría de perturbaciones. Introducimos al lector a la implementación de técnicas de *gradient flow* en cálculos perturbativos con las condiciones de contorno anteriormente mencionadas, y presentamos nuestro cálculo a segundo orden de la constante de acoplamiento, incluyendo detalles sobre la técnica empleada para lidiar con las divergencias ultravioletas, y sobre la relación de nuestro esquema con el esquema $\overline{\text{MS}}$ habitualmente usado en trabajos del campo. Presentamos además un estudio acerca de la dependencia de la constante de acoplamiento con el número de colores de la teoría y con una variable angular relacionada con las condiciones de contorno empleadas.

En el capítulo 3 presentamos los resultados de la obtención de la constante de acoplamiento mediante métodos no perturbativos en el retículo. Nos centramos, a modo de estudio exploratorio y para ver cuán factibles son los cálculos en esquemas similares al nuestro, en el caso particular de $SU(3)$, estudiando determinados aspectos relativos a la topología de las configuraciones generadas con nuestras condiciones de contorno. Presentamos además los resultados del estudio de la dependencia de la constante de acoplamiento con el volumen del toro, empleando técnicas de step scaling para computarla a lo largo de un amplio rango de escalas de energía.

Finalmente, presentamos en el capítulo 4 un resumen del trabajo realizado, recopilando los resultados obtenidos más relevantes y presentando las perspectivas futuras de ampliación y extensión de nuestro trabajo.

Buena parte de los detalles de los cálculos, así como las tablas con los resultados numéricos precisos de las simulaciones han sido movidos por claridad a los

apéndices A y B.

Abstract

In spite of their apparent simplicity, Yang-Mills theories give rise to an incredible variety of physically interesting phenomena. Their study in finite volume, in particular, has proven over the years to be an extremely useful tool to understand the inner workings of the strong interaction. Phenomena such as volume reduction or Eguchi-Kawai reduction, known for decades, prove that there is a deep relationship in said theories between spacetime and colour degrees of freedom, to the point that in the large N limit the former become entirely redundant, allowing one to reduce a gauge theory defined on a finite torus to a matrix model on a single point.

As such, the study of the interplay between spacetime and colour degrees of freedom in gauge theories is of great interest. Moreover, the use of the twisted boundary conditions introduced by 't Hooft in 1979, aside from protecting certain symmetries necessary for the phenomenon of reduction to hold, allows one to establish an exact correspondence, in the context of dualities, between gauge theories on the twisted torus and non-commutative field theories.

It is in such a context that the conjecture of volume independence appears. The conjecture states that, for finite volume gauge theories with twisted boundary conditions, the dynamics of the theory are controlled, barring finite N effects, by an effective length arising in a natural manner, and which combines the physical size of the torus with the number of colours of the theory. This effective length, in addition, has in the context of dualities a direct correspondence with the size of the associated non-commutative torus.

The goal of this thesis is precisely the study of certain aspects of this conjecture, in the particular case of four dimensions. The study is done through an analysis of the properties of the 't Hooft coupling, defined using gradient flow techniques and in two different manners: through the use of continuum perturbation theory on one hand, and in a non-perturbative lattice scheme in the other.

For the first case, we compute the running of the 't Hooft coupling constant of a $SU(N)$ theory in the continuum, up to second order in perturbation theory. We define the coupling in a finite volume scheme, using the technique known as the gradient flow on an asymmetrical torus with twisted boundary conditions. The

coupling constant is defined in terms of the effective scale $\tilde{l}$ that we mentioned earlier, which combines the physical size of the torus and the rank of the gauge group, and which is determined in dimensional regularisation, relating it to the coupling constant from the $\overline{\text{MS}}$ scheme. We also present the numerical results of the computation of the gauge coupling constant in the particular case in which the twist tensor is trivial in all planes but one, obtaining the coefficient relating our scheme to the $\overline{\text{MS}}$ one, and determining the ratio of Λ parameters between both schemes. We analyse, moreover, the dependence of the results on N, along with its possible implications concerning non-conmutative gauge theories, as well as its relation to the volume independence conjecture.

For the second case, we focus in the particular case of $SU(3)$. We compute the running of the coupling constant in a non-perturbative manner, discretising the theory on a lattice and extrapolating the continuum result. We once more work on top of an asymmetrical torus, with twisted boundary conditions in a single plane, and we again use the gradient flow to define the 't Hooft running coupling in terms of the same effective length combining box size and gauge rank. We present the results of computing the aforementioned coupling constant numerically, using step scaling techniques to reach a vast range of energies in the scale, along with a study of the behaviour of topological charge in the generated configurations. Moreover, we analyse the effects of the choice of several technical parameters, such as the proportionality constant relating the energy scale of the theory to the size of the box, or the discretised observable that is used to compute the coupling constant. We compare our results to those obtained using perturbation theory, and with the results from studies using similar schemes.

The thesis is organised as follows: in chapter 1 we present a brief introduction to the study of gauge theories defined on the finite torus, focusing in section 1.1 in the phenomena of volume reduction and volume independence, as well as on the definition and implementation of twisted boundary conditions. Special emphasis is made in the link between gauge theories on the twisted torus and non-commutative gauge theories. We then introduce in section 1.2 the concepts of smearing and of the gradient flow, which will be used, in combination with the idea of volume independence, to define in section 1.2.5 the coupling constant λ_{TGF} that will be used along our work.

Then, we present in chapter 2 our computation of the coupling constant in perturbation theory, introducing the reader to the implementation of perturba-

tive computations with gradient flow techniques under our choice of boundary conditions. We present our computation up to next-to-leading order of the previously defined coupling constant, including details on the way to deal with the UV divergences appearing in the computation and on the relation of our scheme to the $\overline{\text{MS}}$ one often used in the field. To conclude the chapter, we present a study on the dependence of the coupling constant with the number of colours of the theory and with an angular variable related to the choice of boundary conditions.

In chapter 3 we present our results of the computation of the coupling constant using non-perturbative methods on the lattice. We focus, in order to study the feasability of computations in schemes similar to ours, on the case of $SU(3)$, studying certain aspects of the topology of the gauge configurations generated using our boundary conditions. We moreover present the results of the study of the dependence of the coupling constant on the volume of the torus, using step scaling techniques to compute it over a wide range of energy scales.

Finally, we present in chapter 4 a summary of the work that has been performed, gathering the more relevant results and presenting the future prospects of our work.

A large share of the details of the computations have for the sake of clarity been moved, along with the tables containing the precise numerical results of our simulations, to appendices A and B.

Chapter 1

Introduction

1.1 Gauge theories on the torus

1.1.1 Introduction

The study of gauge theories in finite volume has, over the last decades, given rise to an abundance of interesting results. Aside from the fact that the use of finite volume techniques is mandatory when computing numerical results on the lattice, it has also been a key component in the study and understanding of the nature and dynamics of gauge theories, both in the continuum and on the lattice. The results obtained over the years cover a wide range of subjects, going from phenomenology and from the computation of physical quantities for experiments to a variety of purely theoretical results, including but by no means limited to the discovery of interesting properties of $SU(N)$ theory or to connections with non-commutative field theory and string theory, notably in the context of dualities[1]

In particular, from the early days and up until today, defining a gauge theory on a finite volume comes with a particular advantage: the ability to control the dynamics of the system by linking the characteristic energy scale of the theory to the size of the torus on top of which it is defined. In this way it is possible to go, modifying the volume of the torus, from a regime in which perturbation theory holds, to hadronic regions in which non-perturbative phenomena such as confinement take over. A large number of works[2] have made use of finite volume techniques and of the volume dependence of physical quantities to explore the dynamics of gauge theories.

A common example of a way to link different energy scales together is through the use of step scaling techniques, introduced in [30] and which have become extremely popular over the years (see for instance refs. [31–39], among countless others). The main idea behind them is to recursively compute a discrete version of the beta function, known as the step scaling function, which describes the behaviour of the coupling constant when the volume of the torus is modified. The size of the torus thus acts as the characteristic energy scale for the running coupling, and therefore by using tori of different volumes one is able to study

[1] We will abstain from citing the staggering amount of relevant, interesting papers produced over the last fourty years, as the list would be far too long.

[2] In the context of our work one can for instance see, among many other relevant papers, refs. [1–27] for some examples of finite volume works from the eighties and the nineties, mostly centered on the use of twisted boundary conditions that will be key to this work. Any reader interested in more can check out the reviews in refs. [28, 29] and references therein.

gauge theories over a wide range of energy scales.

The general implementation of Yang-Mills theories on the torus was originally introduced by Gerard 't Hooft, after he realised that periodic boundary conditions (PBC) are not the only option to define $SU(N)$ gauge theories on the torus. In reference [1], he introduced the more general twisted boundary conditions (TBC), as a way to define electric and magnetic fluxes in finite volume in a gauge-invariant manner.

The ground idea behind the twisted setting, given a pure gauge $SU(N)$ theory defined on a d-dimensional finite torus of periods l_μ in each μ direction, is the condition that gauge invariant observables need to be periodic. For the gauge potential $A_\mu(x)$, this translates into boundary conditions such that the field is, after winding around the torus, identical modulo an arbitrary local $SU(N)$ transformation $\Omega_\nu(x)$:

$$A_\mu(x + l_\nu \hat{\nu}) = \Omega_\nu(x) A_\mu(x) \Omega_\nu^\dagger(x) + i\Omega_\nu(x)\partial_\nu \Omega_\nu^\dagger(x). \tag{1.1}$$

The $SU(N)$ matrices $\Omega_\nu(x)$, however, are in this setting not entirely arbitrary. Indeed, if one looks at the way in which the periodicity condition for the gauge fields relates them along two different directions, trying for instance to connect the expressions of the fields $A_\mu(x)$ and $A_\mu(x + l_\nu\hat{\nu} + l_\rho\hat{\rho})$, one notices that the order in which the $l_\nu\hat{\nu}$ and $l_\rho\hat{\rho}$ translations are considered is relevant.

In order to remain consistent, one must force the result to be identical independently of the path taken, which translates into the following consistency condition, restraining which gauge transformations are valid:

$$\Omega_\mu(x + l_\nu\hat{\nu})\Omega_\nu(x) = Z_{\mu\nu}\Omega_\nu(x + l_\mu\hat{\mu})\Omega_\mu(x), \tag{1.2}$$

where $Z_{\mu\nu}$ denotes an element of the centre of the general $SU(N)$ gauge group:

$$Z_{\mu\nu} = \exp\{i2\pi n_{\mu\nu}/N\}. \tag{1.3}$$

The tensor $n_{\mu\nu}$, known as the twist tensor of the theory, is an antisymmetric tensor of integers defined modulo N. It is invariant under gauge transformations and, as such, it uniquely characterises the boundary conditions of the torus. The well-known case of periodic boundary conditions is an instance of this general setup, for the particular case of $n_{\mu\nu} = 0 \pmod N$.

The use of twisted boundary conditions (TBC) has since proven to be extremely useful, and will be crucial to our computations in what follows. A particularly relevant advantage comes in the implementation of perturbation theory, in which the use of TBC is has a massive advantage over the use of periodic ones: as we will see in section 1.1.4, zero momentum modes become incompatible with the boundary conditions, which allows one to dodge the treatment of zero momentum modes and their associated complications[3] altogether. While this has been known since the early eighties in ref. [2], the main idea came along in the context of volume reduction in large N Yang-Mills theory in refs. [4, 5]. It has, in the following three decades, been extended to many other contexts, such as those in refs. [11, 15, 16, 18–20, 26, 27, 40–72], among others, for both finite and large N.

1.1.2 Volume reduction

A particularly interesting aspect of Yang-Mills theory lies in the study of the relationship between gauge and spacetime degrees of freedom. This interest was born from an observation, nowadays known as the Eguchi-Kawai (EK) reduction, made in ref. [3] while studying the large N limit of a pure gauge $SU(N)$ theory defined on a finite lattice endowed with periodic boundary conditions.

It was shown that, under certain assumptions and in the $N \to \infty$ limit, the Schwinger-Dyson equations of Wilson loops defined on lattices of different sizes become equivalent and, as such, the number of lattice points becomes irrelevant, with finite finite volume effects disappearing in the large N limit. This equivalence can in fact be taken to its extreme, *reducing* the full $SU(\infty)$ Yang-Mills theory on the lattice to a matrix model defined on a single point lattice (hence the name of EK reduction).

This is extremely interesting from a physical point of view, as it shows that somehow, colour and spacetime degrees of freedom are linked to one another to the point that in the large N limit the latter become entirely redundant. The importance of this result is further magnified by the fact that this is an exact result, one of the few ones obtained to this day in the study of gauge theories, and as such should encode relevant information of their very nature.

Unfortunately, the proof for reduction in the original EK paper relied on the

[3] See for instance ref. [39] for an example of how to treat zero modes with PBC using the gradient flow.

assumption that the central $Z^4(N)$ symmetry in the action in four dimensions is not spontaneously broken by the dynamics of the theory, which was quickly[4] shown not to generally be the case when working in more than two dimensions. Modifications to the model, however, were swiftly proposed to salvage reduction, starting with the introduction of the Quenched Eguchi-Kawai model (QEK) in ref. [73], in which momentum quenching was used to preserve the centre symmetry. It was quickly followed by the Twisted Eguchi-Kawai (TEK) model, introduced in refs. [4, 5], in which twisted boundary conditions were used to preserve, for a particular type of twist, a $Z^4(\sqrt{N})$ subgroup of the centre symmetry that is sufficient for the proof of reduction to hold.

Aside from these two options, along the years the idea of large N reduction has grown more general, with several families of methods being developed towards its study, such as the continuum large N reduction introduced in refs. [47–51], the alterations to the Yang-Mills action in refs. [52, 53], or the many proposals introducing adjoint fermions in refs. [54–63], among others.

While these alternatives are nowadays alive and well, in the scope of this thesis we will focus on the general study of reduction in the presence of twisted boundary conditions. For reasons that will become clear further along this work, interest in this model has strongly resurged over the last decade, with many recent derived works such as the ones in refs. [64–72] studying properties of reduction on the twisted torus.

Understanding finite volume gauge theories with TBC is moreover particularly interesting from the point of view of the study of non-commutative field theories. This is due to a deep connection relating finite volume gauge theories with twisted boundary conditions and $U(N)$ non-commutative field theories: there is an exact equivalence, stemming from the Morita duality, between gauge theories defined on a finite, twisted torus and non-commutative field theories on a periodic torus defined at rational values of the adimensional non-commutativity parameter.

The first formulation of the Feynman rules of a non-commutative field theory, in fact, was achieved precisely as an offshoot of the TEK model in ref. [6], in which the Feynman vertices of the theory were shown to pick up the complex, colour-dependent phases characteristic of non-commutative theories[5]. This fact has been exploited over the years, for instance in refs. [75–77], to propose the use

[4]This could have already been expected from the results in ref. [2], but was first mentioned explicitly in ref. [73].

[5]See for instance ref. [74].

of twisted lattice gauge theories as natural regulators for non-commutative field theories.

1.1.3 Volume independence

Our work will focus on the study of reduction with twisted boundary conditions, under a more general perspective than the one of adopted in the TEK model. We will, in fact, stray away from reduction in the strict large N limit, and look at the interplay of gauge and spacetime degrees of freedom, respectively characterised by the rank N of the gauge group and the size l_μ of the sides of the twisted torus, at finite values of N.

The goal of our study lies in the exploration of a stronger version of the idea of volume reduction; a general conjecture known as *volume independence*, which states that gauge and spacetime degrees of freedom are, in pure gauge theories with twisted boundary conditions, intertwined even at finite N. While ideas regarding the interplay between both have been around for decades, in the context of our work we will focus on the version of the conjecture from ref. [42], which proposes proposing that gauge rank and torus size are combined in such a way that, under certain circumstances, the dynamics of the theory are controlled not by each parameter separately, but rather by an effective length $\tilde{l}$ whose exact expression depends on a combination of the choice of twist tensor, the physical size of the torus, and the number of dimensions of the theory[6].

Should the conjecture hold, and barring finite N corrections, the dynamics of the theory would be controlled by this effective length, relating finite volume and finite N effects to one another, and establishing a connection between different $SU(N)$ theories on differently sized tori provided their size and rank combine in such a way as to yield the same value of $\tilde{l}$. In that sense, volume reduction would simply be an example of volume independence, for the particular case of the large N limit in which finite N corrections disappear.

This version of the conjecture stems from the observations made in refs. [42, 78–82], that under certain circumstances gauge rank and torus volume always appear combined in the same manner. In refs. [42, 80, 82], in fact, volume independence was shown to hold at all orders in perturbation theory for a particular class of twist tensors, though the study of the conjecture from a non-perturbative

[6]There is an additional dependence on N through an angular variable dubbed $\hat{\theta}$ that needs to be kept fixed throughout computations, as we will see in what follows.

standpoint is a bit more complex, as some additional complications that will be relevant to our work appear. Before moving forward, however, it is interesting to present an example of the way TBC are implemented in the continuum, as well as some effects their implementation has regarding volume independence and perturbation theory.

1.1.4 Twisted boundary conditions

Let us therefore consider a pure gauge $SU(N)$ theory in the continuum, defined on a finite d-dimensional torus of physical length l_μ in each direction, and implement twisted boundary conditions as introduced in eqs. (1.1) and (1.2). We will be interested in the particular class of solutions to equation (1.2) for which the the gauge can be fixed in such a way as to make the matrices $\Omega_\mu(x)$ constant. Solutions belonging to this class are known as twist-eaters, are conventionally denoted Γ_μ and, in the appropriate gauge, significantly simplify the expression of the boundary conditions:

$$A_\mu(x + l_\nu \hat{\nu}) = \Gamma_\nu A_\mu(x) \Gamma_\nu^\dagger, \tag{1.4}$$

$$\Gamma_\mu \Gamma_\nu = Z_{\mu\nu} \Gamma_\nu \Gamma_\mu. \tag{1.5}$$

The existence of such solutions, however, is only guaranteed[7] for $d \leq 3$. In four dimensions, one can build a twist-eating solution if and only if the twist tensor satisfies:

$$\epsilon_{\mu\nu\rho\lambda} n_{\mu\nu} n_{\rho\lambda} = 0 \text{ mod } N. \tag{1.6}$$

Twist tensors satisfying this condition are known in literature as orthogonal twist tensors. Moreover, we will in what follows further restrain ourselves to the subset of twists in four dimensions that are not only orthogonal, but also irreducible.

Irreducible twists are defined as those for which the solutions to eq. (1.5) are unique modulo global gauge transformations and modulo multiplication by elements of the centre of the $SU(N)$ group or, equivalently, the subset of twist tensors such that the only matrices that commute with all twist-eaters are the ones proportional to the $SU(N)$ identity. In four dimensions[8], only N^2 inequivalent twist-eating solutions can be constructed, which are all roots of the identity in

[7] For a detailed, rigurous discussion on how to set up Yang-Mills fields on the twisted torus, and on how to construct twist-eaters in up to four dimensions, see ref. [28].

[8] See refs. [83, 84] for the details.

the sense of satisfying $\Gamma_\mu^N = \mathbb{I}$.

In the context of the study of volume independence and for the scope of this section[9], we will focus in the particular case known as symmetric twists, defined by:

$$n_{\mu\nu} = \epsilon_{\mu\nu}\frac{kN}{l_g}\,, \tag{1.7}$$

where we defined $l_g = N^{2/d_t}$ and $\epsilon_{\mu\nu} = \Theta(\nu-\mu) - \Theta(\mu-\nu)$, with Θ denoting the Heaviside function and d_t being an integer introduced for generality and set here to $d_t = d = 4$. This sort of twist is by construction orthogonal, and irreducibility is guaranteed provided k and l_g are coprime.

We then introduce, for this symmetric twist, an auxiliary set of d momentum-dependent matrices constructed through products of twist-eaters:

$$\hat{\Gamma}(q) = \frac{1}{\sqrt{2N}} e^{i\beta(q)}\Gamma_0^{s_0(q)}\ldots\Gamma_{d-1}^{s_{d-1}(q)}, \tag{1.8}$$

where $\beta(q)$ denotes an arbitrary complex phase, and $s_\mu(q)$ is the following set of integers:

$$s_\mu(q) = \tilde{\epsilon}_{\mu\nu}\bar{k}\,\frac{\tilde{l}_\nu q_\nu}{2\pi} \in \mathbb{Z}, \tag{1.9}$$

in which we introduced three auxiliary quantities:

$$k\bar{k} = 1\,(\mathrm{mod}\,l_g), \qquad \tilde{l}_\nu = l_\nu l_g, \qquad \sum_\nu \tilde{\epsilon}_{\mu\nu}\epsilon_{\nu\rho} = \delta_{\mu\rho}. \tag{1.10}$$

All $\hat{\Gamma}(q)$ matrices constructed in this manner are traceless, except for the one corresponding to $s_\mu = 0\,(\mathrm{mod}\ l_g)$, which is proportional to the identity. Excluding it, we are left with N^2-1 independendent traceless $SU(N)$ matrices that can be used as a basis for the $SU(N)$ Lie algebra. Moreover, as $\hat{\Gamma}(q)$ satisfies:

$$\Gamma_\nu\hat{\Gamma}(q)\Gamma_\nu^\dagger = e^{iq_\nu l_\nu}\hat{\Gamma}(q)\,, \tag{1.11}$$

with no summation over ν implied, the boundary conditions in (1.4) are directly

[9]The twist used in chapters 2 and 3 will be different from this one, with slightly different definitions of $\epsilon_{\mu\nu}$ and of l_g. The general formalism, however, will still apply, barring a few small changes detailed in sec. 1.1.6.

implemented through the Fourier-like expansion:

$$A_\mu(x) = V^{-\frac{1}{2}} {\sum_q}' e^{iqx} \hat{A}_\mu(q)\, \hat{\Gamma}(q)\,, \tag{1.12}$$

where $V \equiv \prod_\mu l_\mu$, and where the prime in the sum denotes the exclusion of the $\hat{\Gamma}(q) \propto \mathbb{I}$ matrix from the basis.

The group structure constants, incidentally, become in this $\hat{\Gamma}(q)$ basis momentum dependent. They are given, choosing the arbitrary phase β in eq. (1.8) adequately, by:

$$\left[\hat{\Gamma}\,(p)\,, \hat{\Gamma}\,(q)\right] = iF\,(p, q, -p-q)\,\hat{\Gamma}\,(p+q)\ , \tag{1.13}$$

where:

$$F\,(p, q, -p-q) = -\sqrt{\frac{2}{N}} \sin\left(\frac{1}{2}\theta_{\mu\nu} p_\mu q_\nu\right), \tag{1.14}$$

and:

$$\theta_{\mu\nu} = \frac{\tilde{l}_\mu \tilde{l}_\nu}{2\pi}\, \tilde{\epsilon}_{\mu\nu} \hat{\theta}, \qquad \hat{\theta} = \frac{\bar{k}}{l_g}. \tag{1.15}$$

This concludes our first look at the finite volume twisted setup for gauge theories in the continuum. There are, however, a few observations that will be extremely relevant in the study of volume independence in perturbation theory, and which must be addressed before moving on.

The first observation concerns the way momentum is quantised. As we recall, in the presence of periodic boundary conditions momentum in the torus becomes discrete, and comes in integer multiples of $2\pi/l_\mu$. Yet, in this twisted case we notice, looking at the definition of s_μ and at the implementation of the boundary conditions in eqs. (1.4), (1.9), and (1.12), that an additional l_g factor appears in the denominator. Thus, while momentum is still quantised, the quantisation is now given in terms of:

$$p_\mu = \frac{2\pi}{\tilde{l}_\mu} m_\mu, \qquad m_\mu \in \mathbb{Z}, \tag{1.16}$$

where $\tilde{l}_\mu$ is the effective length parameter, combining the physical size of the torus with the rank of the gauge group, mentioned at the beginning of this section:

$$\tilde{l}_\mu = l_g l_\mu. \tag{1.17}$$

If volume independence holds true, this length is the one driving the dynamics of the theory.

Momentum is thus quantised as if we were on a periodic torus of sides $\tilde{l}_\mu$. In the context of our work we will use this quantity, rather than the actual physical size of the torus, as the energy scale of the running coupling for both a perturbative study in the continuum in chapter 2 and a step scaling one the lattice in chapter 3.

Regarding volume independence, however, a remark has to be made concerning the statement that all dependence in N and l_μ comes through $\tilde{l}_\mu$. The affirmation is, looking at the definition of the $\hat{\theta}$ in eq. (1.15), manifestly not the case[10]. This is one of the conditions that we mentioned when introducing the concept of volume independence: for it to hold, the angular variable $\hat{\theta} = \bar{k}/l_g$ must be kept constant. This is not always possible, strictly speaking, as the irreducibility condition of having $\bar{k}$ and l_g be coprime does not allow one to keep the exact quotient constant when modifying N, but in certain cases when taking the large N limit one can find sequences of $\bar{k}, N$ whose quotient remains approximately constant and for which finite N corrections are small.

The last observation is one that we already advanced at the end on the previous section which, while not as physically relevant to our study of volume independence as the previous one, will still be quite useful, particularly regarding perturbative calculations. The observation is the fact that, as a direct consequence of the choice to use a non-trivial twist, zero momentum modes become incompatible (due to the tracelessness of the $\hat{\Gamma}$ matrices) with the boundary conditions and are excluded from the dynamics of the system, automatically introducing a mass gap in the theory. Moreover, and as we already mentioned, as zero modes lead to complications in perturbation theory, their exclusion greatly simplifies computations.

1.1.5 Large N limits

This conjecture of volume independence and the phenomena surrounding EK reduction have been studied extensively over the last few decades. Many of these studies concern the four-dimensional case, which is one of the most physically

[10]Equation (1.14) also appears to have an additional dependence on N, but in this case it cancels out when computing relevant quantities such as the Feynman rules or the gluon propagators.

relevant, though several thorough studies in $2+1$ dimensions have also been performed in refs. [42, 45, 85] and have provided a more complete understanding of the inner workings of reduction and the issues that might arise.

It is interesting to revisit the TEK reduction from the point of view of volume independence, looking at it as a particular case, discretised on a four-dimensional lattice of spacing a, of the symmetric twist introduced in the previous section. The effective length of the torus is then for the single point lattice $\tilde{l} = a\sqrt{N}$ in all directions, and volume reduction occurs in the $N \to \infty$ limit. This large N limit is an example of what is known as the *thermodynamic* limit, in which $\tilde{l}$ is taken to infinity by increasing N while keeping the lattice spacing a constant. In perturbation theory, the complex phases appearing in the Feynman vertices for this model were already shown in the initial proposal from ref. [4] to kill off non-planar diagrams in the large N limit while cancelling out in the planar ones, effectively recovering the perturbative expansion of large N gauge theories.

Yet, numerical simulations following the introduction of this model, such as the ones in refs. [86–89], showed that reduction breaks down when approaching the large N limit by increasing N at constant $k = 1$, with the centre symmetry breaking down at intermediate values of the coupling for $N > 100$. The reason for this breakdown was addressed in detail in ref. [64], in which the cause of the issue was identified to be the appearance of fluxons: classical extrema of the TEK action functional which, despite not being classical minima of the action, can become entropically favoured and dominate the partition function, breaking the remaining $Z^4(\sqrt{N})$ centre symmetry of the system and destroying reduction. A solution was proposed to avoid this issue by scaling k with N in the limit of large number of colours, keeping $k/\sqrt{N} > 1/9$ or even, to be safe, $k/\sqrt{N} > 1/4$ as N increases.

This solution of bounding $k/\sqrt{N}$ to preserve volume independence at large N seemed to work, despite the lack of a rigurous proof and the relative vagueness of the choice of bounds. As such, in the following years, the approach led to many interesting results, including the computation of the string tension in refs. [65, 66], results with $N_f = 2$ adjoint fermions in ref. [67], or the obtention the meson spectrum in refs. [90, 91], among others. Further efforts to study the breakdown of reduction have recently been performed, and have succesfully identified[11] the parameter controlling the symmetry breaking, dubbed $Z_{\min}(k, N)$,

[11] See refs. [45, 85].

with values of $|Z_{\min}(k,N)| > 0.1$ succesfully preserving reduction. More on this will be presented towards the end of this section.

We must point out, however, that the thermodynamic limit is an infinite volume limit of the gauge theory. From the point of view of finite volume schemes, it is interesting to instead consider the sort of limit called singular in ref. [92], in which the large N limit is taken while keeping the effective size $\tilde{l}$ of the lattice constant[12]. This amounts to performing a double limit by simultaneously sending N to infinity while sending the volume of the torus to zero.

These singular large N limits are in fact quite relevant in the context non-commutative field theories. The Morita duality is of particular significance here, as it implies an exact correspondence between $SU(N)$ gauge theories on a torus with twisted boundary conditions and sides l_μ and non-commutative $U(1)$ gauge theories defined on a periodic torus of sides $\tilde{l}_\mu$. This is a further argument in favour of reduction, as the effective length arising in the twisted theory is equivalent to the actual physical length of the periodic torus in the dual theory, and as such should be the scale driving its dynamics. Moreover, the other relevant variable of the twisted model, the angular quantity $\hat{\theta}$ introduced in eq. (1.15) and determined by the choice boundary conditions, also has an immediate interpretation in the dual theory as its dimensionless non-commutativity parameter.

Thus, through the use of this duality, twisted tori become a natural choice for a non-perturbative regulator of non-commutative gauge theories. Yet, for the kinds of twists that we are considering, only theories with rational values of the non-commutativity parameter $\hat{\theta} = \bar{k}/N$ can be covered. Irrational values instead need to be approached, as proposed in ref. [92], through a sequence of ordinary $SU(N_i)$ twisted Yang-Mills theories with increasing number of colours and with:

$$\hat{\theta}_i = \frac{\bar{k}_i}{N_i} \underset{i\to\infty}{\longrightarrow} \hat{\theta}, \tag{1.18}$$

Where $\hat{\theta}$ on the right hand side denotes the target irrational value of the non-commutativity parameter.

This sort of construction, however, can run into problems when taking the large N limit. Some instabilities, in fact, were already found to appear in the context of the study of non-commutative gauge theories in refs. [95, 96], related

[12]For examples of this type of limit in a similar setting to the one that we will adopt in our work, see refs. [42, 45, 85, 93]. This type of limit has also been considered in other works such as refs. [52, 78, 79], or, for more examples, in ref. [94] and references therein.

the condensation of electric fluxes and to the spontaneous breaking of centre symmetry. More recently, there have been some detailed studies in refs. [42, 45, 85] of the nature and onset of such issues in the case of the 2+1-dimensional $T_2 \times R$ twisted torus.

The problems are already visible in perturbation theory, in which the energy of the electric flux associated to a given momentum mode was in ref. [42] found to be:

$$\mathcal{E}_m^2(x,\hat{\theta})\Big|_{\rm PT} = \frac{m^2}{4x^2} - \frac{1}{x}G(\hat{\theta}m), \tag{1.19}$$

where x denotes a dimensionless quantity built from the coupling and the effective length, $m \in \mathbb{Z}^d$ is a d-dimensional integer vector associated to the momentum mode and the electric flux, and G is a particular function[13] built from Jacobi theta functions and which can become singular for certain values of m.

Looking at eq. (1.19), the issue becomes then pretty clear: at certain values of x, $\hat{\theta}$ and m, the term in $G(\hat{\theta}m)$ can become dominant, making the squared energy of the electric flux associated to a given momentum mode become negative. The problem is hence known as the appearance of *tachyonic* instabilities, whose presence is indicative of a phase transition in which the system enters a different regime. They can be avoided provided one uses a set of k and N such that:

$$\min_{x,\,m} \mathcal{E}_m^2(x,\hat{\theta}) \geq 0. \tag{1.20}$$

Going beyond perturbation theory, a numerical study in ref. [85] found that $\mathcal{E}_m^2(x,\hat{\theta})$ is well described by a more general functional form:

$$\mathcal{E}_m^2(x,\hat{\theta}) = \frac{m^2}{4x^2} - \frac{1}{x}G(\hat{\theta}m) - \frac{\pi\sigma'}{3\lambda^2}\chi_0 + \left(\frac{4\pi\sigma'}{\lambda^2}\right)^2 \phi_0^2(\hat{\theta}m)x^2, \tag{1.21}$$

where $\chi_0 \simeq 0.6$, $\sqrt{\sigma'}/\lambda$ denotes the string tension, and $\phi_0(z)$ is a positive function[14].

As the stability condition is still the given by eq. (1.20), we find that while the confining x^2 term in this expression tends to help in the suppression of tachyonic instabilities, the problematic term in G is not only still present, but is reinforced by the additional χ_0 term. In ref. [85] stability was shown to be be controlled by

[13] See ref. [45] for the exact definition and derivation of each function and parameter.
[14] See ref. [45] once again for the derivation of each function and parameter.

the behaviour of a parameter dubbed $Z_{\min}(N,k)$ and given by:

$$Z_{\min}(N,k) = \min_{m \neq 0 \,(\mathrm{mod}\, l_g)} m\,||\hat{\theta} m||\,, \tag{1.22}$$

where the symbol $||x||$ is used to denote the distance from x to the nearest integer. The condition $Z_{\min} \gtrsim 0.1$ was in particular found to be enough to guarantee that no tachyonic instabilities appear.

The challenge, however, is twofold, with two issues that need to be addressed:

- First is the question, quite relevant when considering the thermodynamic limit, of whether given a value of N, a value of k can be found such that no tachyonic instabilities appear, i.e. such that $Z_{\min} \gtrsim 0.1$. The general answer to the question was connected in ref. [85] to the Zaremba conjecture in Number Theory, which remains an open problem. Nevertheless, and while a formal, general proof remains open, it is often possible to find a particular solution for a given value of N.

- The second question is instead related to the singular limits mentioned earlier. It is a bit more complicated, as it concerns whether one can in general build a sequence of values of $\bar{k}_i/N_i$ approaching a particular irrational value $\hat{\theta}$ in the large N limit without instabilities. The answer, unfortunately, was in refs. [45, 85] found to be that such sequences cannot generically be built, except for an uncountable zero-measure set of sequences. A particular solution was found in that reference to be the sequence of values of $\bar{k}$ and N defined through $\bar{k}_i/N_i = F_{i-2}/F_i$, where F_i denotes the i-th term in the Fibonacci sequence. In that case, instabilities in the large N limit are avoided and the limiting sequence tends to $\hat{\theta} = (3-\sqrt{5})/2$.

Remarkably, and despite this condition being obtained in the 2+1-dimensional case, $Z_{\min}$ was in ref. [44] found to control the size of the contribution of non-planar diagrams to the expectation value of Wilson loops in 4-dimensional perturbation theory as well. In the context of our study, we will see later on that $Z_{\min}$ is also quite relevant.

1.1.6 Goals

Our general aim in this work is to analyse certain aspects of all that has been previously mentioned, particularly regarding the validity of volume independence

in the twisted torus and its consequences in relation to non-commutative theories. The analysis will be performed through the study of the 't Hooft running coupling $\lambda = g^2 N$, defined using gradient flow methods and following the line of constant physics imposed by taking $\lambda(\tilde{l})$ to be constant. As the effective length $\tilde{l}$ is conjectured to be the physically relevant quantity driving the dynamics of the theory, we will use it in our definition of the running coupling as the running energy scale.

The full analysis will come in two separate parts. The first one, presented in chapter 2, corresponds to a study of the running coupling in continuum perturbation theory, which will allow us to probe and study the dependence of the coupling on $\tilde{l}$ to obtain some insight on the dynamics of the system. The computation, moreover, will allow us to pry into the two sorts of limits that were previously mentioned:

- The thermodynamic limit obtained sending N and $\tilde{l}$ to infinity, allowing us to link our model to the infinite volume perturbative computation.
- The singular large N limit in which N is sent to infinity while $\tilde{l}$ is kept constant, which will allow us to peer into the connection between twisted gauge theories and non-commutative ones at irrational values of the non-commutativity parameter, notably regarding the $\bar{k}/N$ sequences that need to be taken to reach the large N limit.

As a bonus, we will also relate our perturbative computation to the one in the $\overline{\text{MS}}$ scheme, which will allow us to obtain the corresponding ratio of Λ parameters. This additional computation is quite relevant, as, despite gradient flow schemes becoming commonplace in the last years, perturbative computations are rather scarce, and the computation of the ratio of Λ parameters had not been performed before. We will moreover perform a study on the dependence of the theory on quite a few parameters related to the choice of scheme.

The second part of the analysis focuses on effects that cannot be described in perturbation theory. We will use a gradient flow scheme on the lattice, and perform a preliminary study on the feasibilty of the computation of the twisted gradient flow running coupling in the particular case of $SU(3)$, computing the running coupling through a step scaling procedure and peeking at some relevant effects derived of the topology of the configurations. The study is aimed at verifying that these sorts of lattice computations can realistically be performed

in our scheme, so that in the future we may study different values of N in order to probe both previously mentioned large N limits and their connection to ideas of volume reduction and to dualities with non-commutative gauge theories.

Before moving on, we must make a small remark regarding the choice of boundary conditions that we will use in both schemes. We will not be using the symmetric scheme that we mentioned earlier, but rather one in which only the 01 plane is twisted. The setup is quite similar to the one introduced in the previous section, but with the following boundary conditions:

$$A_\mu(x + l\hat{\nu}) = \Gamma_\nu A_\mu(x)\Gamma_\nu^\dagger, \qquad \text{for } \nu = 0, \cdots, d_t - 1, \tag{1.23}$$

$$A_\mu(x + \tilde{l}\hat{\nu}) = A_\mu(x), \qquad \text{for } \nu = d_t, \cdots, d - 1, \tag{1.24}$$

where d_t is an integer dubbed "number of twisted directions", which in four dimensions can be either four (which corresponds to the symmetric twist from earlier), or $d_t = 2$, as will be the case for our computations. The corresponding twist tensor necessary to implement these boundary conditions is given by:

$$Z_{\mu\nu} = \exp\left\{ i2\pi\epsilon_{\mu\nu}\frac{k}{l_g} \right\}, \tag{1.25}$$

where $\epsilon_{01} = -\epsilon_{10} = 1$ and $\epsilon_{\mu\nu} = 0$ in any other plane, and where we have $l_g = N$, rather than $l_g = \sqrt{N}$ as was the case with the symmetric twist.

In that situation, the expression of the $\hat{\Gamma}$ matrices from which we build our Fourier expansions become slightly different:

$$\hat{\Gamma}(q) = \frac{1}{\sqrt{2N}} e^{i\beta(q)} \Gamma_0^{s_0(q)} \dots \Gamma_{d_t-1}^{s_{d_t-1}(q)}. \tag{1.26}$$

Aside from these, all other previously shown expressions still hold, provided the appropriate values of l_g and $\epsilon_{\mu\nu}$ are used. It is however important to remark that momentum is with this sort of twist only quantised in units of the effective length $\tilde{l}_\mu$ in the $0, 1$ directions, with momenta in all other directions coming in units of $2\pi/l_\mu$. The prime in the sum from eq. (1.12), moreover, now only excludes momenta that are zero (modulo l_g) in the twisted $0, 1$ directions. More details on this will be given later on.

1.2 The gradient flow

As we mentioned in the previous section, we will use the gradient flow to define and compute the running coupling, both in the continuum and on the lattice. We will therefore provide along this section an introduction to its history and definition, as well as a brief look at step scaling techniques. We will present our specific version of the twisted gradient flow scheme as well.

1.2.1 Introduction

The idea to use flows in field space to explore the behaviour of quantum field theories has been around for a long time. In particular, the use of the gradient flow[15] in Yang-Mills theory was first introduced in the early eighties in refs. [97, 98], as a tool to study classical, continuum Yang-Mills theory.

Related smearing techniques were swifly applied to theories on the lattice, with their introduction by the APE group in ref. [99], and remained in ample use in the following two decades. Smearing, however, was along that period of time set up in a completly discrete manner, working with a finite number of smearing steps. The idea of using continuous smearing was only recovered in the early 2000s in ref. [100], where it was shown to be interpretable as a continuous, dimensionful parameter, and finally in ref. [101], in which it was shown that the divergences arising in the renormalisation of composite, unsmeared observables were absent when (continuous) smearing was used.

Leaving aside the history of smearing in general[16], we will henceforth focus on the continuous version of the gradient flow that was first introduced by Martin Lüscher in ref. [103] in an attempt to map lattice gauge theories to trivial ones. This particular version was presented for the first time in the form in which it is nowadays used in ref. [104] and has since opened a new, wide array of interesting applications, proving itself extremely useful in many contexts and becoming a staple in a variety of new settings and for plenty of computations.

In the scope of this thesis, we will focus on one of the main purposes for which it was introduced in its modern form: as a way to directly provide a precise definition of the running coupling, and to renormalise composite operators, as

[15] The gradient flow is also known as the Wilson flow in the literature, in the particular case in which the fields are smeared using the gradient of the Wilson action.

[16] Any reader interested in a more detailed account of the history and properties of smearing can find it in ref. [102], which was the basis for this short historical introduction.

seen for instance in refs. [104–109]. In that capacity, it will become one of the two pillars used to define and compute a renormalised running coupling in the two schemes that we will present along this work.

Among them, some of these applications use it in combination with finite-size scaling techniques to determine the non-perturbative scale dependence of the gauge coupling constant, with examples of this approach ranging from precise, non-perturbative determinations of the QCD coupling constant and Λ parameter in refs. [110–114] to the study of Yang-Mills theories with near conformal behaviour in refs. [115–117], or with large number of colours in ref. [93]. Several coupling renormalisation schemes based on gradient flow techniques have been proposed to that end, such as the ones in refs. [39, 104, 118–122]. Moreover, the gradient flow has been extremely useful in the context of scale setting, with the use of gradient-flow based scales such as t_0 and w_0 from refs. [104] and [119] becoming commonplace in lattice computations, displacing in some settings previously ubiquitous scales such as the Sommer scale.

Let us thus introduce, finally, the gradient flow in its full splendour, showing how it can be used for both scale setting and to define a running coupling, and present some of its more interesting characteristics along the way.

1.2.2 Definition

The fundamental idea behind the gradient flow consists in the introduction of an additional parameter t, known as flow time[17], to Yang-Mills theory[18]. The original gauge fields $A_\mu(x)$ of the theory are replaced with a new set of flow time-dependent fields $B_\mu(x,t)$ matching the original fields at $t = 0$, which are driven by the so-called flow equations:

$$\partial_t B_\mu(x,t) = D_\nu G_{\nu\mu}(x,t), \qquad B_\mu(x,t=0) = A_\mu(x), \tag{1.27}$$

[17] A somewhat unfortunate name, given that the flow time parameter t has dimensions of squared length, and is unrelated to the euclidean time x_0 of the $SU(N)$ gauge theory that will be considered.

[18] We introduce this in the case of continuum, infinite volume, pure gauge Yang-Mills theory in four dimensions, but the definition can be easily extended to other settings.

where D_μ and $G_{\mu\nu}$ respectively stand for the covariant derivative and field strength tensor of the flow fields:

$$D_\mu B_\nu(x,t) = \partial_\mu B_\nu(x,t) + i\left[B_\mu(x,t), B_\nu(x,t)\right], \tag{1.28}$$

$$G_{\mu\nu}(x,t) = \partial_\mu B_\nu(x,t) - \partial_\nu B_\mu(x,t) + i\left[B_\mu(x,t), B_\nu(x,t)\right]. \tag{1.29}$$

As the right hand side of the flow equation can simply be interpreted as the gradient of the Yang-Mills action:

$$D_\nu G_{\nu\mu} \sim -\frac{\partial S_{YM}[B]}{\partial B_\mu(x,t)}. \tag{1.30}$$

The flow fields are driven, as flow time increases, towards the classical minima of the action. Expanding in perturbation theory the fields in powers of the bare coupling, the flow equation becomes at each order i an equation of the form:

$$\partial_t B_\mu^{(i)}(x,t) - \partial^2 B_\mu^{(i)}(x,t) = R_\mu^{(i)}(x,t). \tag{1.31}$$

At leading order and if one fixes the gauge appropriately, the right hand side vanishes, $R_\mu^{(1)}(x,t) = 0$, and the flow equation becomes the heat equation in flow time:

$$\partial_t B_\mu(x,t) = \partial^2 B_\mu(x,t). \tag{1.32}$$

The solution to this is given by a gaussian heat kernel integrated over a four-sphere:

$$B_\mu(x,t) = \int d^d y K_t(x-y) A_\mu(y), \qquad K_t(z) = (4\pi t)^{-2} e^{-z^2/4t}, \tag{1.33}$$

and thus the effect of the flow is a smoothing of the gauge field $A_\mu(x)$ in a four-dimensional spherical region of radius $\sqrt{8t}$. Picking a different gauge or going to further orders in perturbation theory simply adds new gauge and nonlinear terms to this solution, but the smoothing effect persists, with the radius remaining virtually unchanged. As such, this radius becomes a natural scale of the theory, and is particularly useful in the context of scale setting or to use as the running scale when defining a renormalised coupling.

The introduction of the gradient flow comes with one extremely interesting additional property. Indeed, as shown in ref. [105], it turns out that this smooth-

ing property eliminates UV divergences, making it so that local, gauge invariant composite observables (i.e. observables constructed as the expectation value of products of flow fields) are automatically finite, renormalised quantities for $t > 0$. What is more, even in the $t \to 0$ limit in which these observables become divergent, they turn out to be decomposable into a sum of finite, renormalised operators with divergent numerical coefficients.

This makes defining a renormalised running coupling a trivial procedure, as one simply needs to find an observable that is proportional to the bare coupling at leading order in perturbation theory. One of the simplest, most commonly used observables for the definition is the the energy density $E(t)$, which was already introduced in ref. [104]:

$$\langle E(t) \rangle = \frac{1}{2} \langle \mathrm{Tr} \left(G_{\mu\nu}(x,t) G_{\mu\nu}(x,t) \right) \rangle. \tag{1.34}$$

This observable can be used to construct a dimensionless operator $t^2 \langle E(t) \rangle$, with which defining a running coupling becomes extremely easy. For example, at leading order in continuum $SU(N)$ perturbation theory, in infinite volume, this quantity was in ref. [104] found to be of the form:

$$t^2 \langle E(t) \rangle = \frac{3(N^2-1)}{128\pi^2} g_0^2 (1 + c_1 g_0^2 + \mathcal{O}(g_0^4)), \tag{1.35}$$

where g_0 is the bare coupling constant and c_1 the next-to-leading order coefficient. This expression can be related to the $\overline{\mathrm{MS}}$ coupling at a scale $\mu = 1/\sqrt{8t}$, or used to define a coupling in a brand new scheme, as we will do in the next section.

While everything mentioned so far has been in the continuum theory, many lattice implementations of the gradient flow exist, with one such example being provided already in ref. [104] in the paper introducing the gradient flow. While we will mention nothing else about lattice implementations in this chapter, we will delve into the subject in more detail in chapter 3.

We will however, and before closing this section, elaborate a bit on the two main directions that have been taken in the increasing number of works using the gradient flow that have appeared along the last decade, and which are related to the gradient flow's ease of use and convenience for both scale setting and for the implementation of precise definitions of the renormalised running coupling.

1.2.3 Scale setting

The first of the two main applications of the gradient flow, scale setting, is a direct consequence of the natural emergence of an energy scale $\mu = \sqrt{8t}$ from the smoothing radius in eq. (1.33).

All quantities in lattice computations, as is well known, are given in terms of the lattice spacing a, which depends on the bare parameters and whose value in physical units is not known a priori. In order to connect lattice quantities to physical observables, thus, a must be related to a physical scale, in a process known as scale setting[19].

This is achieved, in general terms, by setting a particular lattice observable to be equal to a given physical quantity (in physical units) at a specific value of a reference scale, through which the expression of the lattice spacing in physical units is obtained, and by extension the expression of all lattice quantities.

The process that we just described is quite general, and as such many prescriptions are possible, though three particular characteristics are universally desirable: one seeks a scale that is numerically both easy and cheap to compute, with good statistical precision, and where the effect of systematic errors is small. There are many options, each with its own advantages and disadvantages; for instance, if one is interested in using lattice computations as a tool in a phenomenological study of some sort, it is often convenient to directly set the scale in terms of a measured, physical observable, such as the mass of a given particle or some decay constant, to avoid introducing errors related to the use of a given model or theory. On the other hand, for theoretical computations, it is often more practical to simply set an arbitrary scale, which would then need to be related to phenomenological quantities in a second independent step (for instance, by extrapolating the continuum limit in lattice calculations).

Most theoretical lattice computations, in the beginning, used the string tension for scale setting in the pure gauge theory, which required a large time extent to obtain the ground state potential, as well as to take a large spatial separation limit. To improve on this, the Sommer scale r_0 was introduced in ref. [124], defining a hadronic scale in terms of the force $F(r)$ between two static quarks

[19] An interesting review on different options for scale setting on the lattice, though a little aged, can be found in ref. [123].

separated by a distance r:

$$r^2 F(r)\big|_{r=r_0} = 1.65. \tag{1.36}$$

This choice had many advantages over the use of the string tension, including good precision in the determination of r_0/a, and the fact that no large separation limit had to be taken, but as the large time extent was still required its computation can remain somewhat cumbersome.

The introduction of the gradient flow, however, comes with a natural way to define a scale through the flow time parameter. This was introduced in ref. [104], where the energy density observable was used to define a scale t_0 given by:

$$t^2 \langle E(t) \rangle \big|_{t=t_0} = 0.3. \tag{1.37}$$

Alternatively, one can use the scale w_0 introduced in [119], for which one uses the derivative of the energy density to define:

$$\left[t \frac{d}{dt} \left(t^2 \langle E(t) \rangle \right) \right]_{t=w_0^2} = 0.3. \tag{1.38}$$

Both of these definitions have by now become commonplace, as they represent a significant improvement over previous scale setting choices.

For one, they have excellent statistical precision, requiring far fewer configurations to obtain precisions comparable to the one obtained using ${r_0}^{20}$. They are also free of the systematic errors related to the presence of excited states that occur when using the Sommer scale, which are a significant source of headaches as they are difficult to quantify. And lastly, we must point out that the complications found in the scales mentioned earlier (in which large time extrapolations and fits were required) are completely absent in this computation, as the observable is a simple expectation value, obtained directly from the configurations. All of these advantages have made, over the last decade, scale setting procedures based on the gradient flow one of the preferred choices in lattice computations.

It must also be noted that, in the case of the gradient flow, the way to search for improvements to reduce cutoff effects is rather straightforward: one can simply

[20] This is due to a combination of factors, including the aforementioned finiteness of correlation functions for $t > 0$ and the fact that autocorrelations are reduced. For more details, see for instance ref. [125].

start modifying the flow equations, the Monte Carlo action driving the theory, the definition of the observable $E(t)$, or the boundary conditions. While this is not intrinsically easier than looking for improvements using the Sommer scale, it does provide for a clear, systematic angle to attack the problem.[21].

1.2.4 Running coupling

The second set of applications, on the other hand, is related to the myriad definitions for the running coupling that are possible using the gradient flow. Indeed, looking at eq. (1.35), the idea to define a renormalised coupling through the dimensionless energy density observable in different settings immediately comes to mind:

$$g^2_{GF}(\mu) = \frac{t^2}{\mathcal{N}}\langle E(t)\rangle\Big|_{t=1/8\mu^2}, \tag{1.39}$$

where $\mathcal{N}$ is an arbitrary numerical coefficient that can be chosen as part of the definition of the scheme. In the context our work, we will follow the example of ref. [121] and use it to both eliminate leading order effects in continuum perturbation theory and reduce the effect of artefacts on the lattice.

As we mentioned in the beginning of this section, a common option is to combine this with finite volume techniques[22], defining the Yang-Mills theory on a finite box of characteristic linear size[23] l which is related to the energy scale of the running coupling through:

$$\mu^{-1} = \sqrt{8t} = cl. \tag{1.40}$$

The parameter c is an arbitrary constant relating the energy scale of the theory to both flow time and to the linear size of the box. It is interpretable, looking at eq. (1.33), as the fraction of the finite box over which the gauge fields are being smoothed. The gradient flow is thus given, in these cases, in terms of the linear box size:

$$g^2_{GF}(l) = \frac{t^2}{\mathcal{N}}\langle E(t)\rangle\Big|_{t=c^2l^2/8}. \tag{1.41}$$

These sorts of finite volume schemes, naturally, are strongly dependent on the

[21] See for instance refs. [119, 126] for some examples on Symanzyk improvement.

[22] See the many references [39, 93, 104, 110–117, 119–121] mentioned earlier for actual examples.

[23] For simplicity of notation, we are considering a symmetrical torus with identical sides l in all directions, but the definition can easily be extended to an asymmetrical case.

choice of boundary conditions, and many different schemes have been proposed over time using a variety of them, ranging from the use of purely periodic ones in, for example, refs. [39, 118], of Schrödinger functional boundary conditions in ref. [120], of mixed open-SF conditions in ref. [108], or of twisted boundary conditions, either on their own in ref. [93, 121] or in combination with periodic ones in ref. [127].

Each of these choices has their own advantages in different aspects such as cutoff effects, presence of zero-momentum modes in perturbation theory, or the topological freezing in lattice simulations, among many others, though we will not go into any further detail: any reader interested in a more comprehensive summary of the perks and issues of each choice can find it in ref. [128].

In any case, no matter the boundary conditions that are used, all finite volume schemes are by construction remarkably well-suited for step scaling computations[24]. A full explanation of the technique will be provided in chapter 3, but we for now will mention that one can define what is essentially a discrete version of the beta function called the step-scaling function:

$$\sigma(u, s) = g^2_{GF}(sl)\big|_{u=g^2_{GF}(l)}\,, \tag{1.42}$$

which measures the variation in the running coupling when the scale is multiplied by a factor s. Iterating the scaling procedure n times, one can obtain the running coupling for a range of scales going from l to $s^n l$.

The use of finite volume schemes is thus particularly adequate for this, as the changes of scale directly transate to changes in the volume of the torus. In particular, on the lattice a discrete version of the step scaling function can easily be obtained by computing the running coupling in a lattice of size L and one of size sL at identical bare coupling, allowing one to obtain the running coupling in a non-perturbative setting. Any reader interested on more details on this may go directly to chapter 3.

1.2.5 Twisted gradient flow

Last but not least, there is an interesting modification to this sort of finite volume schemes, introduced in ref. [93], which links the use of the gradient flow in a finite volume scheme to ideas of volume reduction.

[24] See refs. [30, 108] for more details.

This modification consists in defining the theory on a finite torus with twisted boundary conditions, using the effective size[25] $\tilde{l} = l_g l$ introduced in section 1.1.4 as the running scale for the coupling definition in eq. 1.41, rather than the characteristic actual size l of the torus:

$$\lambda^2_{TGF}(\tilde{l}) = \frac{t^2}{\mathcal{N}}\langle E(t)\rangle\Big|_{t=c^2\tilde{l}^2/8}. \tag{1.43}$$

Here $\lambda_{TGF} = g^2_{GF}N$ denotes the 't Hooft coupling, and TGF stands for "Twisted Gradient Flow".

This sort of scheme was used in ref. [93], taking the idea of reduction to its utmost limit, to define and compute a gradient flow running coupling in a one-point lattice with twisted boundary conditions. The computation was done through a step scaling process with the peculiarity that, instead of changing the volume of the torus, the rescaling of $\tilde{l}$ was done by changing the rank N of the gauge group. This sort of definition for the coupling, in which the running energy scale used to define the coupling is given by the effective lattice size $\tilde{l}$, is in fact the one that we will be using in our work in the next two chapters, both in a continuum scheme and in a lattice one. We shall not, however, work on a one-point lattice, nor will we use the rank of the gauge group for step scaling on the lattice.

In what is left of this section, we will introduce some relevant aspects of the twisted gradient flow coupling that we will use in our computation. We will provide here a general setting, that will require some further refinement in chapters 2 and 3 to fully set up both a continuum scheme in perturbation theory, and a non-perturbative lattice scheme. The setting will be quite similar to the one introduced in ref. [121], but we will do as in ref. [93] and define the running coupling using an effective length $\tilde{l}$ as the running scale:

$$\mu^{-1} = \sqrt{8t} = c\tilde{l}. \tag{1.44}$$

Let us thus define a pure gauge $SU(N)$ theory in the continuum, in four dimensions and on top of an (in principle) asymmetrical finite torus of sides l_μ, endowed with 't Hooft twisted boundary conditions of the sort mentioned in section 1.1.6. As we will shortly explain, we will pick the torus size in such a way

[25] Assuming once more $\tilde{l}$ to be identical in all directions for simplicity of notation.

as to have the same effective length $\tilde{l} = l_\mu l_g$ in all directions.

The 't Hooft coupling is then defined, using the gradient flow, as:

$$\lambda_{TGF}(\tilde{l}) = \frac{1}{N}\mathcal{F}(c)\ \left\langle t^2 E(t)\right\rangle\big|_{t=c^2\tilde{l}^2/8}\,, \tag{1.45}$$

where $\mathcal{F}(c)$ is a normalisation constant such that:

$$\lambda_{\mathrm{TGF}}(\tilde{l}) = \lambda_0 + \mathcal{O}(\lambda_0^2), \tag{1.46}$$

in terms of the bare 't Hooft coupling λ_0, and where $E(t)$ is the energy density observable from eq. (1.34).

We will restrain ourselves, following the construction presented in section 1.1, to orthogonal, irreducible twist tensors of the form:

$$Z_{\mu\nu} = \exp\left(2\pi i \epsilon_{\mu\nu} k/N^{2/d_t}\right), \tag{1.47}$$

which as we recall allowed us to Fourier expand the gauge fields in twisted directions as in eq. (1.12), with momentum quantised in units of $2\pi/l_\mu$ in the so-called "periodic directions" corresponding to the planes in which $n_{\mu\nu} = 0$, and in units of $2\pi/l_\mu l_g$ in the planes in which $n_{\mu\nu}$ is nontrivial.

As we recall, in four dimensions two choices of d_t are available:

- One can choose the symmetric twist by taking $d_t = 4$, leading to an effective length $\tilde{l}_\mu = l_\mu\sqrt{N}$. In this situation, all momenta can be quantised in units of $2\pi/\tilde{l}_\mu$ and one can simply use a symmetric l^4 torus[26] to have them all given in terms of a single $\tilde{l}$.

- One may work with $d_t = 2$ and the twist introduced in (1.1.6), leading to $\tilde{l}_\mu = l_\mu N$. In that case, using a symmetric l^4 torus would lead to momentum being quantised in units of $2\pi/\tilde{l}_\mu$ in two directions, and in units of $2\pi/l_\mu$ in the other two. If, as we do, one wishes to quantise all momenta in terms of a single $\tilde{l}$, the simplest solution[27] is to use an asymmetrical torus of size $l^2 \times \tilde{l}^2$.

Do note that the choice to use an asymmetrical torus responds to our general goal of testing the reach of volume independendence: should the conjecture be

[26] This is the choice that was used in [93].

[27] This is the case that will be using for the numerical computations in chapters 2 and 3.

valid, the physics of the model should be fully controlled by the effective size $\tilde{l}$, and the choice of this asymmetrical scheme for $d_t = 2$ should yield similar results to the ones obtained using the symmetrical, $d_t = 4$ setting.

Chapter 2

The twisted gradient flow coupling in perturbation theory

2.1 Introduction

As we mentioned in section 1.2, the gradient flow has over the last few years received considerable attention, particularly in relation to its use to determine the scale dependence of the gauge coupling constant in finite volume schemes. Yet, and despite the importance of making contact with experiment, computations in a purely perturbative set-up remain scarce, as most schemes use perturbative calculations to at most match with known schemes such as the $\overline{\text{MS}}$ one. Nevertheless, examples of such perturbative matchings can be found, up to next-to-leading order (NLO) and next-to-next-to-leading order (NNLO) respectively, in refs. [104] and [129] for the infinite volume case, or, for the finite volume matching, up to NNLO in the Schrödinger functional scheme using numerical stochastic perturbation theory in refs. [109, 130].

Our main concern along this chapter will be the study in perturbation theory of the twisted gradient flow (TGF) coupling in the scheme introduced in section 1.2.5. As we recall, this was a renormalised 't Hooft coupling in continuum $SU(N)$ gauge theory, defined using the gradient flow on top of a four-dimensional twisted torus and, in connection to volume reduction, given in terms of an effective length $\tilde{l}$ combining the rank of the gauge theory and the size of the torus. In the context of volume independence, we will be particularly interested in the dependence of the coupling with the rank N of the gauge theory, notably regarding the thermodynamic and singular large N limits mentioned in the previous chapter. In that context, we will keep N finite but use our results to analyse the behaviour of the coupling at large values of N, computing the coupling for several values of N and for a variety of twists.

The chapter is organised as follows. In section 2.2 we will present, after a quick recapitulation of the basics of the twisted gradient flow scheme introduced in section 1.2.5, the implementation of perturbation theory, expanding the observable in powers of the bare coupling, solving the flow equations and using the Feynman rules of the theory to obtain the (analytical) expression of both the LO and NLO contributions to the renormalised coupling, given in terms of Jacobi and Siegel theta functions. Even though the many particularities to the twisted finite volume scheme will make the specifics quite different, the calculation is in broad strokes analogous to the one performed by Martin Lüscher in infinite volume in ref. [104], in which the energy density observable from eq.(1.34) was found to be,

in $d = 4 - 2\epsilon$ dimensional regularisation:

$$\langle E(t)\rangle = \frac{3(N^2-1)}{2(8\pi t)^{2-\epsilon}} g_0^2 \left[1 + (4\pi)^{\epsilon-2}(8t)^{\epsilon} N \left(\frac{11}{3\epsilon} + \frac{52}{9} - 3\log 3\right) g_0^2 + \mathcal{O}(g_0^4)\right], \quad (2.1)$$

which in terms of the $\overline{\text{MS}}$ coupling at a scale $q = 1/\sqrt{8t}$ becomes:

$$\langle E(t)\rangle = \frac{3(N^2-1)}{32\pi t^2} \alpha_{\overline{\text{MS}}}(q) \left[1 + \frac{N}{4\pi}\left(\frac{11}{3}\gamma_E + \frac{52}{9} - 3\log 3\right)\alpha_{\overline{\text{MS}}}(q) + \mathcal{O}(\alpha^2_{\overline{\text{MS}}})\right]. \quad (2.2)$$

Section 2.3 will then address the issue of how the divergences appearing in the resulting analytic expression of the renormalised coupling in terms of the bare one are handled. The main idea will be to identify from which terms these divergences are coming, and subtract them from the observable to obtain a finite quantity that can be computed numerically. The subtracted divergent terms can then be handled by relating them to a series of infinite volume integrals that can be analytically computed using dimensional regularisation. We will moreover study in that section the infinite volume limit of our expressions, correctly recovering the results from ref. [104].

Section 2.4 then contains the matching of our scheme at one-loop order to the $\overline{\text{MS}}$ one, along with the corresponding ratio of Λ parameters (which needs to be computed numerically). Numerical results for the particular case of the two-dimensional (non-trivial) twist are presented in that section as well, for a range of $SU(N)$ groups, magnetic fluxes (i.e. twists), and for several values of the scheme-defining parameter c.

We then discuss, in section 2.5, the dependence of the coupling on the number of colours (and on a twist-dependent angular variable), following similar arguments to those in refs. [44, 45] and focusing on the the singular and thermodynamic limits mentioned earlier.

Lastly, we will present a short summary of our results and some brief conclusions in section 2.6.

Many technicalities were moved for clarity to appendices A.1-A.8, including details on the algorithms used to compute the Λ parameter.

2.2 Implementation of perturbation theory

We are thus interested in using perturbation theory to compute the gradient flow running coupling up to NLO. As we already provided the definition of the coupling in section 1.2.5, we will simply recapitulate some of the more relevant aspects presented there before going into the implementation of perturbation theory itself.

2.2.1 Recapitulation: the TGF coupling

As we introduced in section 1.2, gradient flow schemes are based on the introduction of a flow time parameter t and the replacement of the gauge fields $A_\mu(x)$ in the Yang-Mills action with a set of flow fields $B_\mu(x,t)$ matching the original ones at $t = 0$, which are driven towards the classical solutions of the action by the flow equations:

$$\partial_t B_\mu(x,t) = D_\nu G_{\nu\mu}(x,t), \tag{2.3}$$

where D_μ and $G_{\mu\nu}$ are the covariant derivative and field strength tensor of the B_μ fields, defined in eqs. (1.28) and (1.29). Since, at $t > 0$, the expectation values of products of B_μ fields are renormalised quantities, we defined an energy density observable:

$$\langle E(t)\rangle = \frac{1}{2}\Big\langle \mathrm{Tr}\Big(G_{\mu\nu}(x,t)G_{\mu\nu}(x,t)\Big)\Big\rangle, \tag{2.4}$$

which is proportional to the bare coupling at leading order in perturbation theory and can as such be used to define a renormalised coupling through:

$$\lambda_{\mathrm{TGF}}(c\tilde{l}) = \frac{1}{N}\mathcal{F}(c)\ \big\langle t^2 E(t)\big\rangle\big|_{t=c^2\tilde{l}^2/8}\,, \tag{2.5}$$

where $\mathcal{F}(c)$ is a constant defined in such a way as to have $\lambda_{\mathrm{TGF}}(\tilde{l}) = \lambda_0 + \mathcal{O}(\lambda_0^2)$, in terms of the bare 't Hooft coupling λ_0.

The idea of volume reduction is implicit in the construction and evidenced by the choice of scale for the running coupling: the scale is given by $\mu = \sqrt{8t} = 1/(c\tilde{l})$, where $\tilde{l}$ is the effective length from (1.17). The parameter c denotes an arbitrary constant, chosen as an intrinsic part of the definition of the scheme.

The gauge theory is defined on top of a four-dimensional torus whose boundary conditions are given by the orthogonal irreducible twist presented in eq. (1.47), which was non-trivial in a number d_t of dimensions (known as "twisted direc-

tions") and trivial in the remaining $4-d_t$ "periodic directions". As we mentioned in section 1.2.5, the torus periods were chosen in such a way that momentum is quantised in all directions in units of the same effective length $\tilde{l}$, which amounts to using a symmetrical l^4 torus for the $d_t = 4$ symmetric twist, and an asymmetrical $l^2 \times \tilde{l}^2$ one for $d_t = 2$. All momenta are then quantised in units of $2\pi/\tilde{l}$, with $\tilde{l} = lN^{2/d_t}$, with the parameter l_g in eq. (1.7) becoming either $\sqrt{N}$ or N for $d_t = 4$ and $d_t = 2$ respectively. The theoretical development presented in what follows will be valid for either case, but numerical results will only be provided for the $d_t = 2$ case, as it is computationally much cheaper.

To conclude this short recapitulation, we will mention that the Fourier expansions with TBC will be done in the momentum-dependent basis constructed in chapter 1:

$$A_\mu(x) = V^{-\frac{1}{2}} {\sum_q}' e^{iqx} \hat{A}_\mu(q)\, \hat{\Gamma}(q), \tag{2.6}$$

where V denotes the volume of the torus and the prime in the sum denotes the exclusion of momenta such that $\tilde{l}_\mu q_\mu = 0 \,(\mathrm{mod}\, 2\pi l_g)$ in all twisted directions.

2.2.2 Expansion of the energy density observable

We may now begin the expansion of the coupling in perturbation theory, which we will carry out up to next-to-leading order in the bare 't Hooft coupling. The general plan will follow in broad strokes the one developed by Lüscher in infinite volume in ref. [104] at first, but significant differences will arise as the computation advances due to the quantisation of momentum on the torus: momentum integrals will become sums over an infinite set of discrete momenta, and the different choice of $SU(N)$ Lie algebra basis will lead to a different set of group structure constants. Nevertheless, and while the specifics of the computation diverge from the ones in infinite volume, in general lines the process remains broadly the same, to the point where even the divergent momentum sums can still be treated in dimensional regularisation[1].

In particular, in this section we will perform the expansion of the gauge fields and the observable in powers of the coupling, solving the flow equations up to third order in perturbation theory. We will moreover use the Feynman rules to rewrite the running coupling as the sum of several terms containing sums

[1] See for instance ref. [131].

over momenta and integrals over Schwinger parameters, which will allow us to rewrite the running coupling in powers of the bare coupling constant, both at leading order (LO) and at next-to leading order (NLO), in terms of Jacobi and Siegel theta functions respectively. The way to deal with the divergences in these terms, however, will be left for the next section.

The first step towards obtaining the perturbative expansion of the observable will be to fix the gauge in such a way as to have the periodicity conditions for the gauge fields mentioned in section 1.1.6:

$$A_\mu(x + l\hat{\nu}) = \Gamma_\nu A_\mu(x)\Gamma_\nu^\dagger, \qquad \text{for } \nu = 0, \cdots, d_t - 1, \tag{2.7}$$

$$A_\mu(x + \tilde{l}\hat{\nu}) = A_\mu(x), \qquad \text{for } \nu = d_t, \cdots, d - 1, \tag{2.8}$$

where Γ_μ satisfies eq. (1.5), and the twist tensor is as shown in eq. (1.25). This restricts the set of allowed gauge transformations $\Omega(x)$ down to those preserving the form of the twist matrices, i.e. those satisfying:

$$\Omega(x + l\hat{\nu}) = \Gamma_\nu \Omega(x)\Gamma_\nu^\dagger, \qquad \text{for } \nu = 0, \cdots, d_t - 1, \tag{2.9}$$

$$\Omega(x + \tilde{l}\hat{\nu}) = \Omega(x), \qquad \text{for } \nu = d_t, \cdots, d - 1. \tag{2.10}$$

These boundary conditions will be implemented through the Fourier expansion of the gauge field given in eq. (2.6), with the torus volume being given by $V = l^{d_t}\tilde{l}^{\,d-d_t}$ in the case of our (possibly) asymmetric torus, and, as we mentioned in the previous section, with momentum quantised in terms of the effective size $\tilde{l}$.

The perturbative expansion is then performed around the $A_\mu = 0$ zero-action solution. The procedure is rather straightforward: we begin by rescaling the original gauge potential with the bare coupling, $A_\mu(x) \to g_0 A_\mu(x)$, and then expand the flow fields $B_\mu(x,t)$ in powers of the bare coupling g_0:

$$B_\mu(x,t) = \sum_k g_0^k B_\mu^{(k)}(x,t), \quad B_\mu^{(k)}(x,0) = \delta_{k1} A_\mu(x)\,. \tag{2.11}$$

As this flow field satisfies the same boundary conditions as the original gauge potential, we can Fourier expand it, at any given order, in the same way:

$$B_\mu^{(k)}(x,t) = V^{-\frac{1}{2}} {\sum_q}' e^{iqx} \hat{B}_\mu^{(k)}(q,t)\,\hat{\Gamma}(q)\,. \tag{2.12}$$

Recalling the definition of the energy density observable $E(t)$ from eq. (2.4), we may then simply replace the $G_{\mu\nu}(x,t)$ field strength tensors and covariant derivatives by their expression in terms of the flow fields, and expand the $B_\mu(x,t)$ fields in powers of the coupling, discarding all terms beyond $\mathcal{O}(g_0^4)$.

The detailed computation can be found in appendix A.1, but, dropping for clarity the arguments of the fields in position space, $B_\mu^{(n)} \equiv B_\mu^{(n)}(x,t)$, the observable up to NLO in position space becomes the sum of seven different terms, exactly as in the infinite volume case:

$$\begin{aligned} E(t) = {} & g_0^2 \,\mathrm{Tr}\left(\partial_\mu B_\nu^{(1)} \partial_\mu B_\nu^{(1)} - \partial_\mu B_\nu^{(1)} \partial_\nu B_\mu^{(1)}\right) \\ & + 2ig_0^3 \,\mathrm{Tr}\left(\partial_\mu B_\nu^{(1)} \left[B_\mu^{(1)}, B_\nu^{(1)}\right]\right) \\ & + 2g_0^3 \,\mathrm{Tr}\left(\partial_\mu B_\nu^{(1)} \partial_\mu B_\nu^{(2)} - \partial_\nu B_\mu^{(1)} \partial_\mu B_\nu^{(2)}\right) \\ & + g_0^4 \,\mathrm{Tr}\left(\partial_\mu B_\nu^{(2)} \partial_\mu B_\nu^{(2)} - \partial_\mu B_\nu^{(2)} \partial_\nu B_\mu^{(2)}\right) \\ & - \frac{1}{2} g_0^4 \,\mathrm{Tr}\left(\left[B_\mu^{(1)}, B_\nu^{(1)}\right]^2\right) \\ & + 2ig_0^4 \,\mathrm{Tr}\left(\partial_\mu B_\nu^{(2)} \left[B_\mu^{(1)}, B_\nu^{(1)}\right] + \partial_\mu B_\nu^{(1)} \left[B_\mu^{(1)}, B_\nu^{(2)}\right] + \partial_\mu B_\nu^{(1)} \left[B_\mu^{(2)}, B_\nu^{(1)}\right]\right) \\ & + 2g_0^4 \,\mathrm{Tr}\left(\partial_\mu B_\nu^{(3)} \partial_\mu B_\nu^{(1)} - \partial_\mu B_\nu^{(3)} \partial_\nu B_\mu^{(1)}\right) + \mathcal{O}(g_0^5). \end{aligned} \tag{2.13}$$

The corresponding expression in momentum space, however, is specific to the TGF setup. In particular, the $SU(N)$ structure constants f^{abc} appearing in infinite volume are replaced by the momentum dependent functions $F(p,q,r)$ appearing in the commutation relations of the $\hat{\Gamma}(q)$ matrices, which were shown in eqs. (1.13) and (1.14).

At order g_0^4, seven contributions to the expectation value of $\langle E(t)\rangle$ arise, which can be identified with each of the lines in eq. (2.13). Including an additional $1/N$ factor for later convenience, and after a bit of algebra[2], one ends up with:

$$\mathcal{E}_0(t) = \frac{g_0^2}{2NV} {\sum_q}' \left(q^2\delta_{\mu\nu} - q_\mu q_\nu\right) \left\langle \hat{B}_\mu^{(1)}(-q,t)\, \hat{B}_\nu^{(1)}(q,t)\right\rangle, \tag{2.14}$$

$$\mathcal{E}_1(t) = \frac{-g_0^3}{NV^{3/2}} {\sum_{p_1,p_2,p_3}}' \delta\left(\sum p_i\right) F(p_1,p_2,p_3)\, ip_{1\mu} \left\langle \hat{B}_\nu^{(1)}(p_1,t)\, \hat{B}_\mu^{(1)}(p_2,t)\, \hat{B}_\nu^{(1)}(p_3,t)\right\rangle, \tag{2.15}$$

$$\mathcal{E}_2(t) = \frac{g_0^3}{NV} {\sum_q}' \left(q^2\delta_{\mu\nu} - q_\mu q_\nu\right) \left\langle \hat{B}_\mu^{(1)}(-q,t)\, \hat{B}_\nu^{(2)}(q,t)\right\rangle, \tag{2.16}$$

[2]See appendix A.1 for the details.

$$\mathcal{E}_3(t) = \frac{g_0^4}{2NV} \sum_q{}' \left(q^2\delta_{\mu\nu} - q_\mu q_\nu\right) \left\langle \hat{B}_\mu^{(2)}(-q,t)\, \hat{B}_\nu^{(2)}(q,t) \right\rangle, \tag{2.17}$$

$$\mathcal{E}_4(t) = \frac{g_0^4}{4NV^2} \sum_{p_1,p_2,p_3,p_4}{}' \delta\left(\sum p_i\right) F(p_1,p_2,-p_1-p_2)\, F(p_3,p_4,-p_3-p_4) \times \left\langle \hat{B}_\mu^{(1)}(p_1,t)\, \hat{B}_\nu^{(1)}(p_2,t)\, \hat{B}_\mu^{(1)}(p_3,t) \hat{B}_\nu^{(1)}(p_4,t) \right\rangle, \tag{2.18}$$

$$\mathcal{E}_5(t) = \frac{-ig_0^4}{NV^{3/2}} \sum_{p_1,p_2,p_3}{}' \delta\left(\sum p_i\right) p_{1\mu}\, F(p_1,p_2,p_3) \Big\{ \left\langle \hat{B}_\nu^{(2)}(p_1,t)\, \hat{B}_\mu^{(1)}(p_2,t)\, \hat{B}_\nu^{(1)}(p_3,t) \right\rangle + \left\langle \hat{B}_\nu^{(1)}(p_1,t) \hat{B}_\mu^{(2)}(p_2,t) \hat{B}_\nu^{(1)}(p_3,t) \right\rangle + \left\langle \hat{B}_\nu^{(1)}(p_1,t)\, \hat{B}_\mu^{(1)}(p_2,t)\, \hat{B}_\nu^{(2)}(p_3,t) \right\rangle \Big\}, \tag{2.19}$$

$$\mathcal{E}_6(t) = \frac{g_0^4}{NV} \sum_q{}' \left(q^2\delta_{\mu\nu} - q_\mu q_\nu\right) \left\langle \hat{B}_\mu^{(1)}(-q,t)\, \hat{B}_\nu^{(3)}(q,t) \right\rangle, \tag{2.20}$$

where the shorthand notation $\sum p_i$ in the δ functions was used to denote the sum over all momenta present in each term. The $\mathcal{E}_0$ term will turn out to be a combination of a leading $\mathcal{O}\left(g_0^2\right)$ term and an $\mathcal{O}\left(g_0^4\right)$ correction, whereas all other terms will turn out to be of order $\mathcal{O}\left(g_0^4\right)$.

2.2.3 Perturbative solution to the flow equations

Having performed the expansion of the observable, the next step in the computation is to obtain the expectation values in each of the $\mathcal{E}_i$ terms, to which end we will have to relate the $\hat{B}_\mu^{(i)}(p,t)$ fields to the original gauge fields in momentum space, $\hat{A}_\mu(p)$. To that end, we ought to solve the flow equations order by order in perturbation theory, though the first three orders will be enough to obtain the observable at order $\mathcal{O}\left(g_0^4\right)$. Things become much easier if one uses a set of modified flow equations:

$$\partial_t B_\mu(x,t) = D_\nu G_{\nu\mu}(x,t) + \chi D_\mu \partial_\nu B_\nu(x,t), \quad B_\mu(x,0) = g_0 A_\mu(x), \tag{2.21}$$

where χ denotes a gauge parameter that will henceforth be set to unity. At fixed t, the fields derived from this modified flow equation can be related to the solutions of the original one by a gauge transformation[3], and hence the modification will not affect gauge invariant observables such as the one we are considering. The

[3]See ref.[104] for the details.

corresponding flow-time dependent gauge transformation was shown in ref. [121] to preserve the boundary conditions from eq. (2.7) at any given flow time. This equation was already solved by M. Lüscher for the infinite volume case in ref. [104], but the results in finite volume turn out slightly different.

For the sake of readability, we will only show in this section the general outline and main results of the solution, leaving the full, detailed computation to be found in appendix A.3.

We are tasked, after expanding the fields as in eq. (2.11), with solving order by order equations of the general form:

$$\partial_t B_\mu^{(i)} = \partial_\nu^2 B_\mu^{(i)} + R_\mu^{(i)}, \qquad i \in \mathbb{Z}. \tag{2.22}$$

Where we once more dropped for clarity of notation the arguments of the fields in position space, and where, for the first three orders:

$$R_\mu^{(1)} = 0, \tag{2.23}$$

$$R_\mu^{(2)} = 2i\left[B_\nu^{(1)}, \partial_\nu B_\mu^{(1)}\right] - i\left[B_\nu^{(1)}, \partial_\mu B_\nu^{(1)}\right], \tag{2.24}$$

$$\begin{aligned} R_\mu^{(3)} = &- \left[B_\nu^{(1)}, \left[B_\nu^{(1)}, B_\mu^{(1)}\right]\right] + 2i\left[B_\nu^{(1)}, \partial_\nu B_\mu^{(2)}\right] - i\left[B_\nu^{(1)}, \partial_\mu B_\nu^{(2)}\right] \\ &+ 2i\left[B_\nu^{(2)}, \partial_\nu B_\mu^{(1)}\right] - i\left[B_\nu^{(2)}, \partial_\mu B_\nu^{(1)}\right]. \end{aligned} \tag{2.25}$$

We can then define a momentum space version of $R_\mu^{(i)}$ in the same way we did the Fourier expansion of the fields:

$$R_\mu^{(i)}(x,s) = V^{-\frac{1}{2}} {\sum_p}' e^{ipx} R_\mu^{(i)}(p,s)\,\hat{\Gamma}(p), \tag{2.26}$$

which allows us to rewrite the flow equation in momentum space in terms of the $\hat{B}_\mu(q,t)$ fields:

$$\partial_t \hat{B}_\mu^{(i)}(p,t) = -p^2 \hat{B}_\mu^{(i)}(p,t) + R_\mu^{(i)}(p,t), \tag{2.27}$$

with each $R_\mu^{(i)}(p,t)$ term being, up to third order:

$$R_\mu^{(1)}(p,t) = 0, \tag{2.28}$$

$$R_\mu^{(2)}(p,t) = \frac{i}{\sqrt{V}} {\sum_q}' F(q,p,-q-p)\,\hat{B}_\nu^{(1)}(p-q,t)\Big(2q_\nu \hat{B}_\mu^{(1)}(q,t) - q_\mu \hat{B}_\nu^{(1)}(q,t)\Big), \tag{2.29}$$

$$R_\mu^{(3)}(p,t) = V^{-1} {\sum_{q_1,q_2,q_3}}' \delta\left(p - \sum_i q_i\right) F(q_1,p,-q_1-p)F(q_2,q_3,-q_2-q_3) \tag{2.30}$$
$$\times \hat{B}_\rho^{(1)}(q_1,t)\hat{B}_\rho^{(1)}(q_2,t)\hat{B}_\mu^{(1)}(q_3,t)$$
$$- 2iV^{-\frac{1}{2}} {\sum_{q_1,q_2}}' \delta\left(p - \sum_i q_i\right) F(q_1,q_2,-q_1-q_2)\, \hat{B}_\rho^{(1)}(q_1,t)\hat{B}_\sigma^{(2)}(q_2,t)$$
$$\times \Big(q_{2\rho}\delta_{\sigma\mu} - q_{1\sigma}\delta_{\rho\mu} - \frac{1}{2}(q_2-q_1)_\mu \delta_{\rho\sigma}\Big).$$

At first order, the solution to eq. (2.27) is immediate:

$$\hat{B}_\mu^{(1)}(p,t) = e^{-p^2 t}\hat{B}_\mu^{(1)}(p,0) = e^{-p^2 t}\hat{A}_\mu(p), \tag{2.31}$$

whereas the next two orders are obtained by directly integrating $R_\mu^{(i)}(p,s)$:

$$\hat{B}_\mu^{(i)}(p,t) = \int_0^t ds e^{-(t-s)p^2} R_\mu^{(i)}(p,s), \quad i>1. \tag{2.32}$$

Higher order terms, while increasingly tedious, can be obtained through the same iterative procedure.

Using the Feynman rules in momentum space, which can be found in appendix A.2, and which were derived using the boundary condition-preserving Fourier representation mentioned in the previous section, the solutions to the flow equations can then be used to derive the expressions, in terms of sums over momenta, of the contributions to the energy density from eqs. (2.14)- (2.20).

In particular, introducing for the sake of readability the symbol:

$$\widehat{\sum_{q,r}} \equiv \tilde{l}^{-2d} \sum_{q,r} N F^2(q,r,-q-r), \tag{2.33}$$

and after some computations[4], one can rewrite all six contributions as:

$$\mathcal{E}_0(t) = \frac{1}{2}\lambda_0 \tilde{l}^{-d} {\sum_q}' e^{-2tq^2}(d-1) \tag{2.34}$$
$$+\frac{1}{4}\lambda_0^2 \widehat{\sum_{q,r}} e^{-2tq^2} \frac{1}{q^2 r^2 (q+r)^2}\left((3d-2)q^2 - 2(d-2)^2 r^2\right), \tag{2.35}$$

[4]The full details can be found in appendix A.3.

$$\mathcal{E}_1(t) = \frac{3}{2}\lambda_0^2 \widehat{\sum_{q,r}} e^{-t(q^2+r^2+p^2)} \frac{1}{q^2 r^2}(1-d), \tag{2.36}$$

$$\begin{aligned}\mathcal{E}_2(t) =& \lambda_0^2 \int_0^t ds \widehat{\sum_{q,r}} e^{-2tp^2+2s(qr)} \frac{1}{p^2 q^2 r^2} \\ &\times \left\{(d-1)p^2\left(p^2+q^2+r^2\right)+2(d-2)\left(q^2r^2-(qr)^2\right)\right\},\end{aligned} \tag{2.37}$$

$$\begin{aligned}\mathcal{E}_3(t) =& \lambda_0^2 \int_0^t ds s \widehat{\sum_{q,r}} e^{-2tp^2}\left(e^{2s(qr)}+e^{2(2t-s)(qr)}\right)\frac{1}{q^2r^2} \\ &\times \left\{2(d-1)p^2r^2+(d-2)\left(q^2r^2-(qr)^2\right)\right\},\end{aligned} \tag{2.38}$$

$$\mathcal{E}_4(t) = \frac{1}{4}\lambda_0^2 \widehat{\sum_{q,r}} e^{-2t(q^2+r^2)} \frac{1}{q^2r^2} d(d-1), \tag{2.39}$$

$$\mathcal{E}_5(t) = \lambda_0^2 \int_0^t ds \widehat{\sum_{q,r}} e^{-(t+s)(q^2+r^2)-(t-s)p^2} \frac{1}{q^2r^2}(1-d)\left(5r^2+(qr)\right), \tag{2.40}$$

$$\begin{aligned}\mathcal{E}_6(t) =& -\lambda_0^2 \int_0^t ds \widehat{\sum_{q,r}} e^{-2tq^2-2sr^2}\frac{1}{r^2}(d-1)^2 \\ &+ 2\lambda_0^2 \int_0^t ds_1 \int_0^{s_1} ds_2 \widehat{\sum_{q,r}} e^{-2tp^2+2s_1(qr)-2s_2(pq)}\frac{1}{p^2q^2} \\ &\times \left\{2(d-2)\left(p^2q^2-(pq)^2\right)+(d-1)p^2\left(2p^2-(qr)\right)\right\},\end{aligned} \tag{2.41}$$

where the bare coupling g_0 and the volume V have been replaced by the bare 't Hooft coupling λ_0 and the effective torus size $\tilde{l}$, and where we defined an auxiliary momentum $p = q + r$. The primes from the sums in the $\mathcal{O}(\lambda_0^2)$ terms have been discarded, as the corresponding $F^2(q, r, -q-r)$ factors automatically vanish for such momenta.

2.2.4 The energy density at LO

Our main goal in this chapter was, as we recall, to obtain the perturbative expansion of the observable $\langle E(t)/N \rangle$ up to NLO, which in powers of the bare 't Hooft coupling can be parametrised as:

$$\left\langle \frac{E(t)}{N} \right\rangle \equiv \lambda_0 \, \mathcal{E}^{(0)}(t) + \lambda_0^2 \, \mathcal{E}^{(1)}(t) + \mathcal{O}\left(\lambda_0^3\right) . \tag{2.42}$$

While the computation of the NLO contribution $\mathcal{E}^{(1)}(t)$ still requires some additional work that will be presented in the next section, we are already in a position

to obtain the energy density's leading order coefficient $\mathcal{E}^{(0)}(t)$.

This leading order contribution comes from the first line of $\mathcal{E}_0(t)$ in eq. (2.34), whose contribution, using the quantisation of momentum in the twisted box to rewrite $q_\mu = 2\pi m_\mu/\tilde{l}$ with $m_\mu \in \mathbb{Z}$, can be written as:

$$\mathcal{E}^{(0)}(t) = \frac{1}{2}(d-1)\,\tilde{l}^{-d} \sum_{m\in\mathbb{Z}^d}{}' e^{-8t\pi^2 m^2/\tilde{l}^2}\,. \tag{2.43}$$

We will introduce a handful of auxiliary variables and functions:

$$t' \equiv 8t/(c\tilde{l})^2, \qquad \hat{c} = \pi c^2/2, \tag{2.44}$$

$$\mathcal{A}(x) \equiv x^{d/2} \sum_{m\in\mathbb{Z}^d}{}' e^{-\pi x m^2}\,, \tag{2.45}$$

in terms of which we can rewrite:

$$\mathcal{E}^{(0)}(t) = \frac{(d-1)}{2\,(8\pi t)^{d/2}}\;\mathcal{A}(2\hat{c}t'). \tag{2.46}$$

Introducing the Jacobi theta functions θ_3, and using Poisson resummation to write it in two equivalent ways:

$$\theta_3(z,ix) = \sum_{m\in\mathbb{Z}} \exp\left\{-\pi x m^2 + 2\pi i m z\right\} = \frac{1}{\sqrt{x}} \sum_{m\in\mathbb{Z}} \exp\left\{-\pi\frac{(m-z)^2}{x}\right\}, \tag{2.47}$$

this $\mathcal{A}$ function can be expressed in two different manners:

$$\mathcal{A}(x) = x^{d/2}\;\theta_3^{(d-d_t)}(0,ix)\left\{\theta_3^{d_t}(0,ix) - \theta_3^{d_t}(0,ixl_g^2)\right\}\,, \tag{2.48}$$

$$\mathcal{A}(x) = \theta_3^{(d-d_t)}\left(0,\frac{i}{x}\right)\left\{\theta_3^{d_t}\left(0,\frac{i}{x}\right) - \frac{1}{N^2}\theta_3^{d_t}\left(0,\frac{i}{xl_g^2}\right)\right\}. \tag{2.49}$$

We have thus obtained, in terms of Jacobi theta functions, the leading order contribution to the observable used to define the renormalised 't Hooft running coupling. Additionally, as a check, we can make sure that the infinite volume expression is correctly retrieved from our result. This is achieved by sending $c \to 0$ and $\tilde{l} \to \infty$ while keeping $c\tilde{l}$ fixed, a limit in which the $\mathcal{A}$ function becomes:

$$\mathcal{A}(2\hat{c}t') \to \frac{N^2-1}{N^2}, \tag{2.50}$$

which allows us to recover the infinite volume result from ref. [104]:

$$\mathcal{E}_{\infty}^{(0)}(t) = \frac{(d-1)(N^2-1)}{2\,(8\pi t)^{d/2}N^2}\,. \tag{2.51}$$

2.2.5 The energy density at NLO

The subleading $\mathcal{O}(\lambda_0^2)$ term coming from eqs. (2.35)-(2.41), however, turns out to be far more complicated. We will in this section show that it can be rewritten, after a fair bit of algebra, in terms of twelve integrals that are obtained after eliminating the momentum quotients in the aforementioned equations, using Schwinger's parametrisation to write the denominators as integrals, and rewriting the numerators as derivatives with respect to the flow time variables. In the end, we were able to write:

$$\begin{aligned}\mathcal{E}^{(1)}(t) &= 2(d-2)\,(I_1+I_2) - 4(d-1)I_3 + 4(3d-5)I_4 + 6(d-1)\,(I_5-I_6) \\ &- 2(d-2)(d-1)I_7 + \frac{1}{2}(d-2)^2(I_8+2I_9) - 2(d-1)\,(I_{10}+I_{11}) - 4(d-1)I_{12},\end{aligned} \tag{2.52}$$

where the I_i denote twelve relatively simple integrals to be derived in what follows.

The computations are once more rather long and tedious and therefore, for the sake of simplicity, we will in this section merely show one of the easier cases, that of $\mathcal{E}_4$ in eq. (2.39), and leave the full detail of the derivation of all other contributions for appendix A.5.

As we recall, the $\mathcal{E}_4$ contribution was given by:

$$\mathcal{E}_4 = \frac{1}{4}\lambda_0^2 d\,(d-1)\,\widehat{\sum_{q,r}} e^{-2t\left(q^2+r^2\right)}\frac{1}{q^2r^2}. \tag{2.53}$$

Schwinger parametrisation allows us to lift the momenta from the denominator at the cost of introducing two new integrals, leaving us with, after a change of variable in the double integral:

$$\mathcal{E}_4 = \frac{1}{2}\,\lambda_0^2\,d(d-1)\,I, \tag{2.54}$$

where we defined:

$$I = \frac{1}{2}\widehat{\sum_{q,r}} \int_0^\infty dz z \int_0^1 dx\, e^{-(2t+xz)\,q^2-(2t+(1-x)z)\,r^2}. \tag{2.55}$$

Note that the group structure constants enter this expression through the definition of the symbol $\widehat{\sum_{q,r}}$ given in eq. (2.33). Their presence in each $\mathcal{E}_i$ will be quite useful, as it will allow us to reformulate the integrands in terms of Siegel theta functions. We may indeed rewrite NF^2 as:

$$NF^2(q,r,-q-r) = 1 - \frac{1}{2}\left(e^{i\theta_{\mu\nu}q_\mu r_\nu} + e^{-i\theta_{\mu\nu}q_\mu r_\nu}\right), \tag{2.56}$$

a substitution under which a generic integrand of the form:

$$\mathcal{I} = \widehat{\sum_{q,r}} e^{-\tilde{s}q^2-\tilde{u}r^2-2\tilde{v}qr} \tag{2.57}$$

becomes:

$$\mathcal{I} = \tilde{l}^{-2d} \sum_{m,n\in\mathbb{Z}^d} \mathrm{Re}\left\{e^{-\pi\left(sm^2+un^2+2vmn\right)}\left(1 - e^{i2\pi\hat{\theta}n\tilde{\epsilon}m}\right)\right\}, \tag{2.58}$$

where we rescaled the variables $s \equiv 4\pi\tilde{l}^{-2}\tilde{s}$, $u \equiv 4\pi\tilde{l}^{-2}\tilde{u}$, $v \equiv 4\pi\tilde{l}^{-2}\tilde{v}$, and used the quantisation of momenta in the twisted finite box to rewrite q and r in terms of integers dubbed m and n.

The connection to Siegel theta functions becomes clear once we introduce the function:

$$G(s,u,v,\hat{\theta}) \equiv \sum_{M\in\mathbb{Z}^{2d}} \mathrm{Re}\left(e^{-\pi M^t A(s,u,v,0)M} - e^{-\pi M^t A(s,u,v,\hat{\theta})M}\right), \tag{2.59}$$

with :

$$M = \begin{pmatrix} m \\ n \end{pmatrix}, \qquad A\left(s,u,v,\hat{\theta}\right) = \begin{pmatrix} s\mathbb{I}_d & v\mathbb{I}_d + i\hat{\theta}\tilde{\epsilon} \\ v\mathbb{I}_d - i\hat{\theta}\tilde{\epsilon} & u\mathbb{I}_d \end{pmatrix}, \tag{2.60}$$

and where $\mathbb{I}_d$ denotes the $d \times d$ identity matrix and the sum over M denotes the sum over the corresponding integers m_μ, n_ν, regrouped into a $2d$-dimensional

column vector M. Recalling the definition of the Siegel theta functions:

$$\Theta\left(z|A\right) \equiv \sum_{M\in\mathbb{Z}^{2d}} e^{i\pi\left(M^t A M + 2z\cdot M\right)}, \tag{2.61}$$

the relation to the matricial expression becomes clear:

$$G(s,u,v,\hat{\theta}) = \mathrm{Re}\,\left\{\Theta(0|iA(s,u,v,0)) - \Theta(0|iA(s,u,v,\hat{\theta}))\right\}. \tag{2.62}$$

Using this notation, the integral entering $\mathcal{E}_4$ reads:

$$I = \frac{1}{2}\,\tilde{l}^{-2d}\int_0^\infty dz z \int_0^1 dx\, G\left(4\pi\tilde{l}^{-2}\left(2t+xz\right), 4\pi\tilde{l}^{-2}\left(2t+(1-x)z\right), 0, \hat{\theta}\right), \tag{2.63}$$

or, in terms of the variables t' and $\hat{c}$ defined in eq. (2.44) and rescaling z appropriately:

$$I = \frac{\hat{c}^2}{32\pi^2\tilde{l}^{2d-4}}\int_0^\infty dz z \int_0^1 dx\, G\left(\hat{c}\left(2t'+xz\right), \hat{c}\left(2t'+(1-x)z\right), 0, \hat{\theta}\right). \tag{2.64}$$

Introducing an auxiliary function $\Phi(s,u,v,\hat{\theta})$, we can reabsorb the factor in front of the integral:

$$\begin{aligned}\Phi(s,u,v,\hat{\theta}) &= \mathcal{N}G(\hat{c}s,\hat{c}u,\hat{c}v,\hat{\theta}), \\ &= \mathcal{N}\ \mathrm{Re}\left\{\Theta(0|iA(\hat{c}s,\hat{c}u,\hat{c}v,0)) - \Theta(0|iA(\hat{c}s,\hat{c}u,\hat{c}v,\hat{\theta}))\right\},\end{aligned} \tag{2.65}$$

where:

$$\mathcal{N} = \frac{\hat{c}^2}{32\pi^2\tilde{l}^{2d-4}}, \tag{2.66}$$

and so we are able to rewrite the integral in $\mathcal{E}_4$ in a fairly simple manner:

$$I = \int_0^\infty z dz \int_0^1 dx\, \Phi(2t'+xz, 2t'+(1-x)\,z, 0, \hat{\theta}), \tag{2.67}$$

leading to:

$$\mathcal{E}_4 = \frac{1}{2}\lambda_0^2 d(d-1)\int_0^\infty z dz \int_0^1 dx\, \Phi(2t'+xz, 2t'+(1-x)\,z, 0, \hat{\theta}). \tag{2.68}$$

A similar procedure, shown in detail in app. A.5, can be followed for every term contributing to the energy density at NLO, leading to the result in eq. (2.52)

for $\mathcal{E}^{(1)}(t)$, with the twelve intervening integrals being given by:

$$I_1(\Phi,t') = \int_0^{t'} dx x\, \Phi(2t', 2x, x, \hat{\theta})\,, \tag{2.69}$$

$$I_2(\Phi,t') = \int_0^{t'} dx x\, \Phi(2t', 2t', x, \hat{\theta})\,, \tag{2.70}$$

$$I_3(\Phi,t') = \int_0^{\infty} dz t' \Phi(2t'+z, 2t', t', \hat{\theta}), \tag{2.71}$$

$$I_4(\Phi,t') = \int_0^{t'} dx x \int_0^1 dy\, \Phi(2t', 2x, xy, \hat{\theta})\,, \tag{2.72}$$

$$I_5(\Phi,t') = \int_0^{\infty} dz \int_0^{t'} dx x\, \Phi(2t', (z+2)x, x, \hat{\theta})\,, \tag{2.73}$$

$$I_6(\Phi,t') = \int_0^{\infty} dz \int_0^{t'} dx\, \Phi(2t'+z, 2t', x, \hat{\theta})\,, \tag{2.74}$$

$$I_7(\Phi,t') = \int_0^{\infty} dz \int_0^{t'} dx x\, \Phi(2t', (z+2)x, 0, \hat{\theta})\,, \tag{2.75}$$

$$I_8(\Phi,t') = \int_0^{\infty} dz \int_0^{\infty} dy\, \Phi(2t'+z, 2t'+y, 0, \hat{\theta})\,, \tag{2.76}$$

$$I_9(\Phi,t') = \int_0^{\infty} z dz \int_0^{\infty} dy \int_0^1 dx\, \partial_{z'} \Phi(2t'+xz+y, z', xz, \hat{\theta})\Big|_{z'=z}\,, \tag{2.77}$$

$$I_{10}(\Phi,t') = \int_0^{\infty} dz \int_0^{t'} dx x\, \partial_{t'} \Phi(2t'+z, 2t', x, \hat{\theta})\,, \tag{2.78}$$

$$I_{11}(\Phi,t') = \int_0^{\infty} dz \int_0^{t'} dx x^2\, \partial_{t'} \Phi(2t', (z+2)x, x, \hat{\theta})\,, \tag{2.79}$$

$$I_{12}(\Phi,t') = \int_0^{\infty} dz \int_0^1 dy \int_0^{t'} dx x^2\, \partial_{t'} \Phi(2t', (z+2)x, xy, \hat{\theta})\,. \tag{2.80}$$

Our objective will thus be, from here onwards, to numerically compute these twelve integrals.

It must be noted that, as these integrals are part of the defining expression of the renormalised coupling in terms of the bare one, a few of them are divergent. Thus, we will in the next section need to analytically determine the divergent terms, in order to isolate them and be able to compute the finite part of the integrals.

2.3 Structure and regularisation of the UV divergences

As the integrals from the previous section make up the expression of the renormalised coupling in terms of the bare one, several of them will be UV divergent in four dimensions. In this section, we will discuss how to parametrise and regularise their asymptotic behaviour, showing that the divergent contributions can in every case be given in terms of an infinite volume integral that can be regularised through analytic continuation in d. In section 2.3.3, we will additionally relate our results to the existing infinite volume calculation from ref. [104].

2.3.1 Origin of the UV divergences

The UV singularities are tied to the structure of the Siegel theta functions entering the definition of the Φ functions:

$$\Theta\left(0|iA(\hat{c}s,\hat{c}u,\hat{c}v,\hat{\theta})\right)=\sum_{m,n\in\mathbb{Z}^d}\exp\left(-\pi\hat{c}\left(sm^2+un^2+2vmn\right)-2\pi i\hat{\theta}m\tilde{\epsilon}n\right)\,. \tag{2.81}$$

The real part of the matrix $A(\hat{c}s,\hat{c}u,\hat{c}v,\hat{\theta})$, obtained by setting $\hat{\theta}=0$ in eq. (2.60), is a positive definite symmetric matrix whenever $\det A(\hat{c}s,\hat{c}u,\hat{c}v,\hat{\theta}=0)>0$, i.e. when $(su-v^2)>0$. This ensures that the series defining the theta function converges uniformly, and so we may introduce a new, useful parameter:

$$\alpha=s-\frac{v^2}{u}, \tag{2.82}$$

which is always positive definite in our integration ranges, and as such ensures that the determinant is positive definite everywhere[5].

The asymptotic behaviour of the integrals becomes much clearer once one applies Poisson resummation from eq. (2.47) to each component of n in the

[5]In some cases divergences occur in the points where $(s,u,v)=(2t',2t',2t')$, but they can be moved to $(s,u,v)=(2t',0,0)$ through a momentum shift, as shown in appendix A.5 but at the points in which $u=0$. This shift had already been applied in the definition of the integrals in the previous section.

definition of Θ:

$$\Theta\left(0|iA\left(\hat{c}s,\hat{c}u,\hat{c}v,\hat{\theta}\right)\right) = \qquad (2.83)$$
$$(\hat{c}u)^{-\frac{d}{2}}\sum_{m,n\in\mathbb{Z}^d}\exp\left(-\pi\hat{c}sm^2-\frac{\pi}{\hat{c}u}\left(n-\hat{\theta}\tilde{\epsilon}m-i\hat{c}vm\right)^2\right),$$

where we used the fact that $m\tilde{\epsilon}m = 0$ and that $\tilde{\epsilon}^2$ is the identity. Whenever $\hat{\theta}\tilde{\epsilon}m \notin \mathbb{Z}^d$, the corresponding term will be asymptotically finite at $u = 0$. In the case in which we have a vector of integers, however, the $\hat{\theta}$ dependence can be removed by shifting $n \to n = n + \hat{\theta}\tilde{\epsilon}m$, thus leaving the asymptotic behaviour to be driven by the shifted $n = 0$ terms which go, as we approach $u \to 0$, as:

$$(\hat{c}u)^{-\frac{d}{2}}\sum_{m\in\mathbb{Z}^d}\exp\left(-\pi\hat{c}\alpha m^2\right). \qquad (2.84)$$

This observation allows us to isolate the asymptotic divergence by identifying the cases for which $\hat{\theta}\tilde{\epsilon}m \in \mathbb{Z}^d$, which occurs in two situations: first, whenever $\hat{\theta} \equiv \bar{k}/l_g = 0$, for any value of m, in which case the $n = 0$ terms are automatically divergent, no shift required. Second, for nonzero $\hat{\theta}$, divergences will occur whenever $\tilde{\epsilon}m = 0 \pmod{l_g}$, which, as the vector $\tilde{\epsilon}m$ has nonvanishing components only along the twisted directions, will be the case when $m_\mu = 0 \pmod{l_g}$ simultaneously for all twisted directions.

Thus, the terms responsible for the UV divergences at $u = 0$ come in two categories:

- For $\hat{\theta} = 0$, terms with $n = 0$, for any value of m.
- For $\hat{\theta} \neq 0$, terms with $m_\mu = 0 \pmod{l_g}$ in all twisted directions at once and, after shifting away the $\hat{\theta}$ dependence, $n = 0$.

2.3.2 Regularisation of the UV divergences

As the part of the observable from which the UV divergences arise has been identified, we may now focus on the way to handle them. In broad strokes, the regularisation strategy will be based on splitting each integral into the sum of a finite piece that can be directly evaluated in $d = 4$ and integrated numerically, and an asymptotic term to be handled analytically through dimensional regularisation.

We will do so by first introducing an auxiliary function $H(s,u,v,\hat{\theta})$:

$$H(s,u,v,\hat{\theta}) = \mathcal{N}\sum_{n\in\mathbb{Z}^d}{\sum_{m\in\mathbb{Z}^d}}' \mathrm{Re}\,\left\{\exp\left(-\pi\hat{c}\left(sm^2+un^2+2vmn\right)-2\pi i\hat{\theta}m\tilde{\epsilon}n\right)\right\}, \tag{2.85}$$

with the usual meaning for the prime in the sum over m. This function can be used to rewrite the Φ functions entering the integrals as:

$$\Phi(s,u,v,\hat{\theta}) = H(s,u,v,0) - H(s,u,v,\hat{\theta}), \tag{2.86}$$

which is quite advantageous, as the explicit exclusion from the sum of the momenta m proportional to l_g automatically makes the term in $\hat{\theta}\neq 0$ finite for $u=0$.

All UV divergences for $d=4$ thus come, in this parametrisation, from the $H(s,u,v,0)$ term, and are of the form:

$$\Phi^{(0)}(s,u,v) = \mathcal{N}\left(\hat{c}u\right)^{-\frac{d}{2}}{\sum_{m\in\mathbb{Z}^d}}'\exp\left(-\pi\hat{c}\alpha m^2\right), \tag{2.87}$$

with α defined as in eq. (2.82), and, as we recall, positive definite everywhere in the integrals, and with $\mathcal{N}$ being the factor defined in eq. (2.66).

Hence, the sum over m is convergent, and the leading asymptotic behaviour at $u=0$ is controlled by the $u^{-d/2}$ factor (times the additional powers of u that may appear in prefactor of the integrand). It will be useful to write the function $\Phi^{(0)}$ in terms of the function $\mathcal{A}(x)$ from eq. (2.45):

$$\Phi^{(0)}(s,u,v) = \mathcal{N}\hat{c}^{-d}\left(u\alpha\right)^{-d/2}\,\mathcal{A}\left(\hat{c}\alpha\right), \tag{2.88}$$

and we will also define, for reasons that will become clear in what follows:

$$\Phi^{\infty}(s,u,v) = \mathcal{N}\hat{c}^{-d}\left(u\alpha\right)^{-d/2}, \tag{2.89}$$

in terms of which we may rewrite:

$$\Phi^{(0)}(s,u,v) = \mathcal{A}\left(\hat{c}\alpha\right)\Phi^{\infty}(s,u,v). \tag{2.90}$$

This formulation will be useful to analyse the asymptotic UV behaviour of the integrals resulting from replacing the original function Φ in the integrand

with $\Phi^{(0)}$. We will first, and before discussing the general treatment, use I_1 as a representative example of how we will deal with the divergences. In this particular case, the integral diverges when $u = 2x = 0$, i.e. at $x = 0$. The piece containing the divergence thus reads:

$$I_1(\Phi^{(0)}, t') = \int_0^{t'} dx x\, \Phi^{(0)}\left(2t', 2x, x\right) = \int_0^{t'} dx x\, \Phi^{\infty}\left(2t', 2x, x\right) \mathcal{A}\left(2\hat{c}t' - \hat{c}x/2\right), \tag{2.91}$$

which, using the definition of Φ^{∞}, becomes:

$$I_1(\Phi^{(0)}, t') = \mathcal{N}\hat{c}^{-d} \int_0^{t'} dx\, x^{1-d/2}(4t' - x)^{-d/2} \mathcal{A}\left(2\hat{c}t' - \hat{c}x/2\right) . \tag{2.92}$$

The asymptotic behaviour at small x can then be obtained by simply expanding $\mathcal{A}(2\hat{c}t' - \hat{c}x/2)$ around $x = 0$. The expansion will be of the form:

$$\mathcal{A}(2\hat{c}t' - \hat{c}x/2) = \mathcal{A}(2\hat{c}t') + \frac{\partial \mathcal{A}(2\hat{c}t' - \hat{c}x/2)}{\partial x}\Big|_{x=0} x + \mathcal{O}(x^2), \tag{2.93}$$

so in $d = 4$ the integrand of the leading term will go as $x^{1-d/2}$ and be divergent, whereas the next to leading term will go as $x^{2-d/2}$ and be convergent. Thus, the integral will behave asymptotically as:

$$I_1^{\text{div}}(t') = \mathcal{A}(2\hat{c}t') \int_0^{t'} dx x\, \Phi^{\infty}\left(2t', 2x, x\right) \equiv \mathcal{A}(2\hat{c}t')\, I_1(\Phi^{\infty}, t') . \tag{2.94}$$

Notice that in this expression the entire momentum dependence has been factorised into the normalisation constant $\mathcal{A}(2\hat{c}t')$, which happens to be the same factor that appeared at leading order in eq. (2.46).

The integral $I_1(\Phi^{\infty}, t')$ is then given by:

$$I_1(\Phi^{\infty}, t') = \mathcal{N}\hat{c}^{-d} \int_0^{t'} dx x^{1-d/2}(4t' - x)^{-d/2}, \tag{2.95}$$

which can, taking $d = 4 - 2\epsilon$, be evaluated in dimensional regularisation (see app. A.6), leading to:

$$I_1(\Phi^{\infty}, t') = \frac{\mathcal{N}\hat{c}^{-d}}{4} (2t')^{2-d} \left(\frac{1}{\epsilon} + \frac{1}{3} + \log\frac{4}{3}\right) . \tag{2.96}$$

The asymptotic expansion of all other integrals (except for I_9, which we will

address separately) can be found in detail in app. A.6, but it is obtained in the same way: we expand the function $\mathcal{A}(\hat{c}\alpha)$ appearing in the definition of $\Phi^{(0)}$ around $u = 0$, retain the leading term, and then use it to define:

$$I_i^{\text{div}}(t') = \mathcal{A}(2\hat{c}t')\, I_i(\Phi^\infty, t'). \tag{2.97}$$

Remarkably, the integrals $I_i(\Phi^\infty, t')$ match, up to a factor depending on N, the ones appearing in the infinite volume calculation, which we will present shortly in sec. 2.3.3, along with their relation to our finite volume integrals.

Let us thus summarise, still keeping I_9 aside, the regularisation strategy. The idea is to decompose the finite volume integrals into two pieces, one that is finite in four dimensions:

$$I_i^{\text{fin}}(t') = I_i(\Phi - \Phi^{(0)}, t') + I_i(\Phi^{(0)}, t') - I_i^{\text{div}}(t'), \tag{2.98}$$

and another one, shown in eq. (2.97) above, that requires analytic continuation to four dimensions and is proportional to each corresponding infinite volume integral. The UV divergences of the original integral are contained in this last piece, and will appear as poles in $1/\epsilon$ with $d = 4 - 2\epsilon$, though only I_1, I_4, I_5 and I_7 will turn out to have such poles, the rest being finite.

As for the strategy to regularise I_9, some modifications are required. We will leave the details for appendix A.6.2, and show only the main points and results. The initial integral is decomposed into:

$$I_9(t') = I_9(\Phi - \theta(1-z)\Phi^{(0)}, t') - I_9(\theta(z-1)\Phi^{(0)}, t') + I_9(\Phi^{(0)}, t')\,, \tag{2.99}$$

with the Heaviside step function θ restricting the interval of integration over z. The first term on the right hand side is finite in four dimensions, while the other two have to be analytically continued to $d = 4$. Denoting I_9^{reg} these analytic continuations, after some algebra we end up with:

$$I_9^{\text{reg}}(\Phi^{(0)}, t') = 0\,, \tag{2.100}$$

$$I_9^{\text{reg}}(\theta(z-1)\Phi^{(0)}, t') = -\mathcal{N}\hat{c}^{-4} \int_0^\infty dz \left\{ (2t'+z)^{-2} \mathcal{A}\left(\hat{c}(2t'+z)\right) \right. \tag{2.101}$$
$$\left. + \int_0^1 dx\ (2t' + x(1-x) + z)^{-2}\, \mathcal{A}\left(\hat{c}(2t' + x(1-x) + z)\right) \right\},$$

and therefore:

$$I_9^{\text{fin}}(t') = I_9(\Phi - \theta(1-z)\Phi^{(0)}, t') - I_9^{\text{reg}}(\theta(z-1)\Phi^{(0)}, t')\,, \tag{2.102}$$

$$I_9^{\text{div}}(t') = 0. \tag{2.103}$$

The integral is thus finite, and we have determined an expression for the regularised term to be computed numerically.

2.3.3 The infinite volume limit

We are now interested in retrieving the expression of the energy density in infinite volume, which is achieved by making the following substitutions in eqs. (2.34)-(2.41):

$$\tilde{l}^{-d} \sum_{q}{}' \longrightarrow \frac{N^2-1}{N^2} \int \frac{d^d q}{(2\pi)^d}, \tag{2.104}$$

$$\widehat{\sum_{q,r}} \equiv \tilde{l}^{-2d} \sum_{q,r} NF^2(q,r) \longrightarrow \frac{N^2-1}{N^2} \int \frac{d^d q}{(2\pi)^d} \int \frac{d^d r}{(2\pi)^d}. \tag{2.105}$$

The resulting expressions for the contributions to the energy density can, much like in the finite volume case and after integrating over the d-dimensional momenta, be expressed in terms of twelve basic integrals, which are in fact closely related to the $I_i(\Phi^\infty, t')$ integrals that appeared in the finite volume regularisation from the previous section. We will, to show this relation, connect the finite and infinite volume cases in the case of $\mathcal{E}_4$ as an illustrative example, and then present the results for the general case.

The infinite volume expression for $\mathcal{E}_4$ is obtained using the substitutions from eqs. (2.104) and (2.105) above in eq. (2.39). After integrating over momenta, one obtains:

$$\mathcal{E}_4^\infty(t) = \frac{\lambda_0^2\, d\,(d-1)\,(N^2-1)}{4N^2(4\pi)^d} \left(\int_0^\infty dz (2t+z)^{-d/2} \right)^2, \tag{2.106}$$

which, setting $t = \hat{c}\tilde{l}^2 t'/(4\pi)$, can be trivially rewritten in terms of Φ^∞ from (2.89):

$$\mathcal{E}_4^\infty(t) = \frac{\lambda_0^2}{2}\, d\,(d-1)\, \frac{N^2-1}{N^2}\, I_8(\Phi^\infty, t'). \tag{2.107}$$

Then, if we recall the expression of the full finite volume contribution of $\mathcal{E}_4$:

$$\mathcal{E}_4 = \frac{\lambda_0^2}{2}\, d\,(d-1)\, I_8(\Phi, t') \equiv \frac{\lambda_0^2}{2}\, d\,(d-1)\left(I_8^{\text{fin}}(t') + \mathcal{A}(2\hat{c}t')\, I_8(\Phi^\infty, t')\right)\,, \quad (2.108)$$

we can immediately see the relation between the finite and infinite volume expressions.

In fact, and as we will see in more detail in section 2.5, the infinite volume term can be obtained from the finite volume one by taking the $\hat{c} \to 0$, $\tilde{l} \to \infty$ limit at fixed t', as in that limit $I_8^{\text{fin}}(t')$ vanishes and $\mathcal{A}(2\hat{c}t')$ becomes $(N^2-1)/N^2$.

The results are identical for every other $\mathcal{E}_i$ contribution, i.e. for every integral. The infinite volume energy density can thus be reproduced by simply performing a change in the finite volume formula from eq. (2.52):

$$I_i(\Phi, t') \longrightarrow \frac{N^2-1}{N^2}\, I_i^\infty(t')\,, \quad (2.109)$$

where, as shown in appendix A.6, $I_9^\infty(t') = 0$ and $I_i^\infty(t') = I_i(\Phi^\infty, t')$ for the rest.

In fact, retrieving the values of the $I_i(\Phi^\infty, t')$ from eqs. (A.335)-(A.345) and summing them with the appropriate coefficients from eq. (2.52), we can easily derive the infinite volume energy density in $d = 4-2\epsilon$ dimensional regularisation:

$$\left\langle \frac{E(t)}{N} \right\rangle = \frac{\lambda_0 (N^2-1)(d-1)}{2N^2 (8\pi t)^{d/2}} \left\{ 1 + \lambda_0 \frac{(8t)^\epsilon (4\pi)^\epsilon}{16\pi^2} \left(\frac{11}{3\epsilon} + \frac{52}{9} - 3\log 3 \right) \right\}, \quad (2.110)$$

which agrees with the result obtained by Lüscher in ref. [104], and acts as a nice check of our computations so far.

2.4 The 't Hooft coupling at one-loop

We are finally, now that a regularised expression for the expectation value of the energy density has been provided, in a position to obtain numerical results for the 't Hooft coupling in perturbation theory. In this section, we will first derive the running coupling in terms of the bare one, relate it to the $\overline{\text{MS}}$ coupling, obtain the Λ parameter, and finally present our computation and results of said parameter in the case of the two-dimensional $d_t = 2$ twist for several values of the parameters c, $\hat{\theta}$ and for several $SU(N)$ gauge groups.

2.4.1 Perturbative matching to the $\overline{\text{MS}}$ coupling

We will begin with a quick recapitulation of what has been achieved so far. We have expanded the observable $\langle E(t)/N \rangle$ up to $\mathcal{O}(\lambda_0^2)$, where λ_0 denotes the bare 't Hooft coupling:

$$\left\langle \frac{E(t)}{N} \right\rangle \equiv \lambda_0 \, \mathcal{E}^{(0)}(t) + \lambda_0^2 \, \mathcal{E}^{(1)}(t) + \mathcal{O}\left(\lambda_0^3\right), \tag{2.111}$$

and found the leading $\mathcal{O}(\lambda_0)$ term to be:

$$\mathcal{E}^{(0)}(t) = \frac{(d-1)\mathcal{A}(2\hat{c}t')}{2(8\pi t)^{d/2}}, \tag{2.112}$$

where $\mathcal{A}(x)$ is a function defined in eq. (2.48), and the variables $\hat{c} = \pi c^2/2$ and $t' = 8t/(c\tilde{l})^2$ have been introduced for clarity.

The $\mathcal{O}(\lambda_0^2)$ next-to-leading order term was obtained in terms of the twelve integrals given in eqs. (2.69)- (2.80), and was regulated through analytic continuation in $d = 4 - 2\epsilon$ in the previous section. After isolating the leading asymptotic behaviour of each integral, we devised a subtraction procedure allowing us to write the NLO contribution to the energy density as:

$$\mathcal{E}^{(1)}(t) = \mathcal{E}^{(1)}_{\text{fin}}(t) + \mathcal{E}^{(1)}_{\text{div}}(t)\,. \tag{2.113}$$

The second term contains all of the divergences, given by $1/\epsilon$ poles arising in dimensional regularisation, and is trivially related to the infinite volume result $\mathcal{E}^{(1)}_{\infty}(t)$ through:

$$\mathcal{E}^{(1)}_{\text{div}}(t) = \frac{N^2\mathcal{A}(2\hat{c}t')}{N^2-1}\mathcal{E}^{(1)}_{\infty}(t). \tag{2.114}$$

Thus, bringing in the infinite volume result, the full expectation value of the energy density at NLO is given by:

$$\left\langle \frac{E(t)}{N} \right\rangle = \lambda_0 \, \mathcal{E}^{(0)}(t) \left\{ 1 + \lambda_0 \frac{(8t)^\epsilon (4\pi)^\epsilon}{16\pi^2} \left(\frac{11}{3\epsilon} + \frac{52}{9} - 3\log 3 + C_1(t) \right) + \mathcal{O}(\lambda_0^2) \right\}, \tag{2.115}$$

where $C_1(t)$ corresponds to contribution of the first term in eq. (2.113), and is given by:

$$C_1(t) = \frac{16\pi^2}{\mathcal{E}^{(0)}(t)} \, \mathcal{E}^{(1)}_{\text{fin}}(t). \tag{2.116}$$

This can then be related to the $\overline{\text{MS}}$ coupling at one-loop order by simply replacing the bare coupling with its expression in terms of the $\overline{\text{MS}}$ one:

$$\lambda_0 = \lambda_{\overline{\text{MS}}}\,\mu^{2\epsilon}\left(4\pi e^{-\gamma_E}\right)^{-\epsilon}\left\{1 - \frac{\lambda_{\overline{\text{MS}}}}{16\pi^2}\,\frac{11}{3\epsilon}\right\}, \tag{2.117}$$

leading to:

$$\left\langle \frac{E(t)}{N} \right\rangle = \mathcal{E}^{(0)}(t)\lambda_{\overline{\text{MS}}}\left\{1 + \frac{\lambda_{\overline{\text{MS}}}}{16\pi^2}\left(\frac{11}{3}\log(8t\mu^2 e^{\gamma_E}) + \frac{52}{9} - 3\log 3 + C_1(t)\right)\right\}. \tag{2.118}$$

Setting the $\overline{\text{MS}}$ energy scale to the corresponding TGF one, $\mu = 1/\sqrt{8t} = 1/c\tilde{l}$, both couplings can be related at one-loop order:

$$\lambda_{\text{TGF}}(\tilde{l}) = \lambda_{\overline{\text{MS}}}(\mu)\left\{1 + c_1\lambda_{\overline{\text{MS}}}(\mu)\right\}, \tag{2.119}$$

where the one-loop matching coefficient is given by:

$$c_1 = \frac{1}{16\pi^2}\left(\frac{11}{3}\gamma_E + \frac{52}{9} - 3\log 3 + \mathcal{C}_1\right), \quad \text{with } \mathcal{C}_1 = C_1(t = c^2\tilde{l}^2/8). \tag{2.120}$$

Lastly, we can determine the ratio between Λ parameters in both schemes in terms of the finite one-loop constant c_1:

$$\log\left(\frac{\Lambda_{\text{TGF}}}{\Lambda_{\overline{\text{MS}}}}\right) = \frac{c_1}{2b_0} = \frac{3}{22}\left(\frac{11}{3}\gamma_E + \frac{52}{9} - 3\log 3 + \mathcal{C}_1\right). \tag{2.121}$$

2.4.2 The matching coefficient for a two-dimensional twist

In the remainder of this section, we will focus on obtaining the finite constant $\mathcal{C}_1$ entering the ratio $\Lambda_{\text{TGF}}/\Lambda_{\overline{\text{MS}}}$ numerically, using what was provided in sec. 2.3.1. We will focus on the case of a single non-trivially twisted plane, $d_t = 2$, as the computational cost of working with the 4×4 matrices (at most) entering the expression for Φ is considerably smaller than that of the 8×8 matrices required for $d_t = 4$. In particular, we have:

$$\begin{aligned} H(s,u,v,\hat{\theta}) &= \mathcal{N}\Theta^{d-2}\left(0|iA_0\left(\hat{c}s,\hat{c}u,\hat{c}v\right)\right) \\ &\quad\times \text{Re}\left\{\Theta\left(0|iB\left(\hat{c}s,\hat{c}u,\hat{c}v,\hat{\theta}\right)\right) - \Theta^2\left(0|iA_0\left(\hat{c}sl_g^2,\hat{c}u,\hat{c}vl_g\right)\right)\right\}, \end{aligned} \tag{2.122}$$

$$\Phi^{(0)}(s,u,v) = \mathcal{N}(\hat{c}u)^{-d/2}\;\theta_3^{d-2}(0,i\hat{c}\alpha)\left\{\theta_3^2(0,i\hat{c}\alpha) - \theta_3^2(0,i\hat{c}\alpha l_g^2)\right\}, \tag{2.123}$$

where ϵ denotes the two-dimensional Levi-Civita symbol, and where we defined a 2×2 matrix A_0 and a 4×4 matrix B containing the $\hat{\theta}$ dependence:

$$A_0\,(s,u,v) = \begin{pmatrix} s & v \\ v & u \end{pmatrix}\,, \tag{2.124}$$

$$B\left(s,u,v,\hat{\theta}\right) = \begin{pmatrix} A_0(s,u,v) & -i\hat{\theta}\epsilon \\ i\hat{\theta}\epsilon & A_0(s,u,v) \end{pmatrix}\,. \tag{2.125}$$

With this, we can begin the numerical calculation of $\mathcal{C}_1$, starting from the equations defining I_i^{fin}, eqs. (2.98) and (2.102). As all of the integrals involved are finite by construction, d and l_g can be freely set to four and N respectively in all intervening expressions. The calculation will come in two steps, the first of which will involve using a short Mathematica program to evaluate the twelve terms:

$$I_i(\Phi^{(0)}, t'=1) - \mathcal{A}(2\hat{c})\, I_i(\Phi^{\infty}, t'=1), \qquad i \neq 9, \tag{2.126}$$

$$I_9^{\text{reg}}(\theta(z-1)\Phi^{(0)}, t'=1). \tag{2.127}$$

The default Mathematica packages were used to both obtain the required Jacobi theta functions and perform the numerical integration, while the derivatives appearing in some of the integrals were computed using finite differences.

The second step is far more complex from a numerical viewpoint, as it encompasses the calculation of:

$$I_i(\Phi - \Phi^{(0)}, t'=1), \qquad i \neq 9, \tag{2.128}$$

$$I_9(\Phi - \theta(1-z)\Phi^{(0)}, t'=1). \tag{2.129}$$

Two independent codes were prepared for this second step, one of them written in Mathematica[6], and the other in C++. The former, much like in the first step, made use of the standard Mathematica packages, numerical integrators, and finite differences to compute the integrals, whereas the full details of the inner workings of the latter can be found in appendix A.7.

We will simply mention here that different errors were used for each of the integrals, depending on computation time, with the relative errors ranging from

[6]In this case it turned out to be convenient to evaluate the two steps of the calculation jointly.

c	$\mathcal{C}_1$	c	$\mathcal{C}_1$	c	$\mathcal{C}_1$	c	$\mathcal{C}_1$
0.18	0.224(8)	0.34	0.301(5)	0.50	-1.831(3)	0.66	-4.577(12)
0.19	0.289(7)	0.35	0.228(6)	0.51	-2.014(6)	0.67	-4.727(20)
0.20	0.353(7)	0.36	0.142(2)	0.52	-2.198(3)	0.68	-4.862(17)
0.21	0.404(6)	0.37	0.0530(16)	0.53	-2.383(3)	0.69	-4.998(17)
0.22	0.451(2)	0.38	-0.0464(5)	0.54	-2.569(3)	0.70	-5.119(15)
0.23	0.493(2)	0.39	-0.152(3)	0.55	-2.755(4)	0.71	-5.239(10)
0.24	0.536(3)	0.40	-0.268(2)	0.56	-2.947(8)	0.72	-5.359(10)
0.25	0.557(3)	0.41	-0.385(2)	0.57	-3.125(9)	0.73	-5.460(17)
0.26	0.570(2)	0.42	-0.525(4)	0.58	-3.303(10)	0.74	-5.581(14)
0.27	0.567(4)	0.43	-0.664(3)	0.59	-3.482(10)	0.75	-5.705(10)
0.28	0.558(3)	0.44	-0.813(2)	0.60	-3.646(14)	0.76	-5.806(18)
0.29	0.532(5)	0.45	-0.971(5)	0.61	-3.808(10)	0.77	-5.877(60)
0.30	0.508(4)	0.46	-1.134(5)	0.62	-3.968(12)	0.78	-6.011(40)
0.31	0.473(4)	0.47	-1.302(4)	0.63	-4.125(16)	0.79	-6.141(40)
0.32	0.426(6)	0.48	-1.474(3)	0.64	-4.280(12)	0.80	-6.248(40)
0.33	0.361(3)	0.49	-1.650(3)	0.65	-4.435(16)		

Table 2.1: Results for $\mathcal{C}_1$ for the $SU(3)$ gauge group and a range of values of c.

10^{-8} in the best cases (the single integrals), to 10^{-3} at worst for I_9, which was by far the bottleneck. The value of c also had significant effects, with lower values taking longer times to compute.

Two key aspects are particularly interesting in the analysis of the results: the dependence on c of the coupling at constant $\hat{\theta}$, and the general dependence in $\hat{\theta}$. For an example of the former, we analysed in detail the case of $SU(3)$ with $\bar{k} = 1$ and with c ranging from 0.18 to 0.8. The resulting values of $\mathcal{C}_1$ for that case are shown in table 2.1, along with a curve of the corresponding $\log(\Lambda_{\mathrm{TGF}}/\Lambda_{\overline{\mathrm{MS}}})$ values, displayed as a function of c in figure 2.1.

In a few points of the figure, we plotted the results obtained with both the Mathematica and the C++ codes, which are perfectly compatible (errors in the data points are smaller than the size of the symbol), along with a yellow horizontal line showing the result obtained when the gradient flow coupling is evaluated at infinite volume.

A detailed analysis of the approach to the infinite volume and the dependence on the number of colours will be presented in sec. 2.5, but for now we will simply mention that at constant energy scale $\mu = (c\tilde{l})^{-1}$ and fixed N, taking $c \to 0$ is equivalent to taking the large volume limit, in which $\log(\Lambda_{\mathrm{TGF}}/\Lambda_{\overline{\mathrm{MS}}})$ should

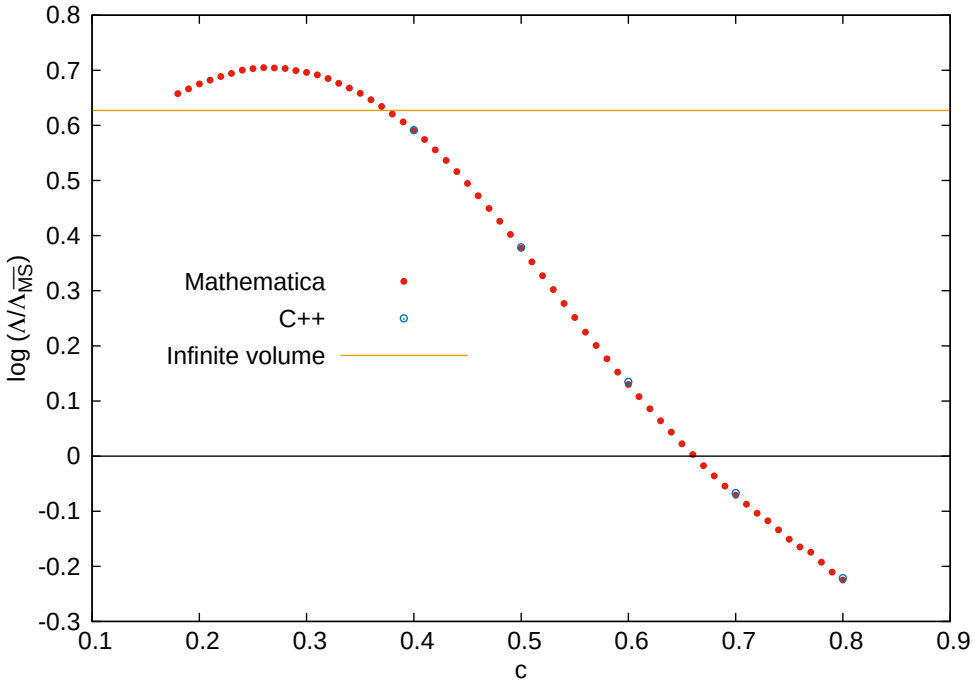

Figure 2.1: We display $\log(\Lambda/\Lambda_{\overline{\text{MS}}})$ as a function of c for the $SU(3)$ gauge group and $\bar{k} = 1$.

approach the yellow line in the plot.

As for the study of the general dependence on $\hat{\theta}$, we considered a series of coprime values of $\bar{k}$ and (small) N such that $\hat{\theta}$ ranged from 0.14 to 0.5. The full results for $\mathcal{C}_1$ are shown in table 2.2 and fig. 2.2, in which they are plotted as a function of $\hat{\theta}$ for several values of c, and where we observe that the dependence on $\hat{\theta}$ is rather smooth for the considered values of $\bar{k}$ and N. A deeper discussion about the $\hat{\theta}$-dependence for larger values of N will be presented in sec. 2.5.

$\bar{k}$	N	$\hat{\theta} = \bar{k}/N$	c=0.4	c=0.5	c=0.6	c=0.7	c=0.8
1	7	0.1429	-4.672(15)	-5.814(20)	-6.813(26)	-7.799(39)	-8.693(62)
1	6	0.1667	-4.274(14)	-5.729(19)	-6.979(24)	-8.097(35)	-9.080(47)
1	5	0.2000	-3.417(12)	-5.098(17)	-6.573(23)	-7.811(33)	-8.843(43)
1	4	0.2500	-2.049(12)	-3.808(16)	-5.475(22)	-6.833(30)	-7.912(40)
2	7	0.2857	-1.187(13)	-2.891(15)	-4.634(20)	-6.050(29)	-7.156(39)
1	3	0.3333	-0.261(14)	-1.818(14)	-3.614(19)	-5.087(29)	-6.220(38)
3	8	0.3750	0.327(14)	-1.073(16)	-2.888(19)	-4.395(26)	-5.545(37)
2	5	0.4000	0.583(14)	-0.724(16)	-2.542(19)	-4.064(26)	-5.222(37)
3	7	0.4286	0.791(12)	-0.418(16)	-2.236(19)	-3.771(26)	-4.937(36)
5	11	0.4545	0.911(09)	-0.228(15)	-2.045(19)	-3.587(26)	-4.757(36)
1	2	0.5000	1.077(13)	-0.092(16)	-1.914(19)	-3.461(26)	-4.634(36)

Table 2.2: Results for $\mathcal{C}_1$ for several $SU(N)$ gauge groups and values of $\bar{k}$.

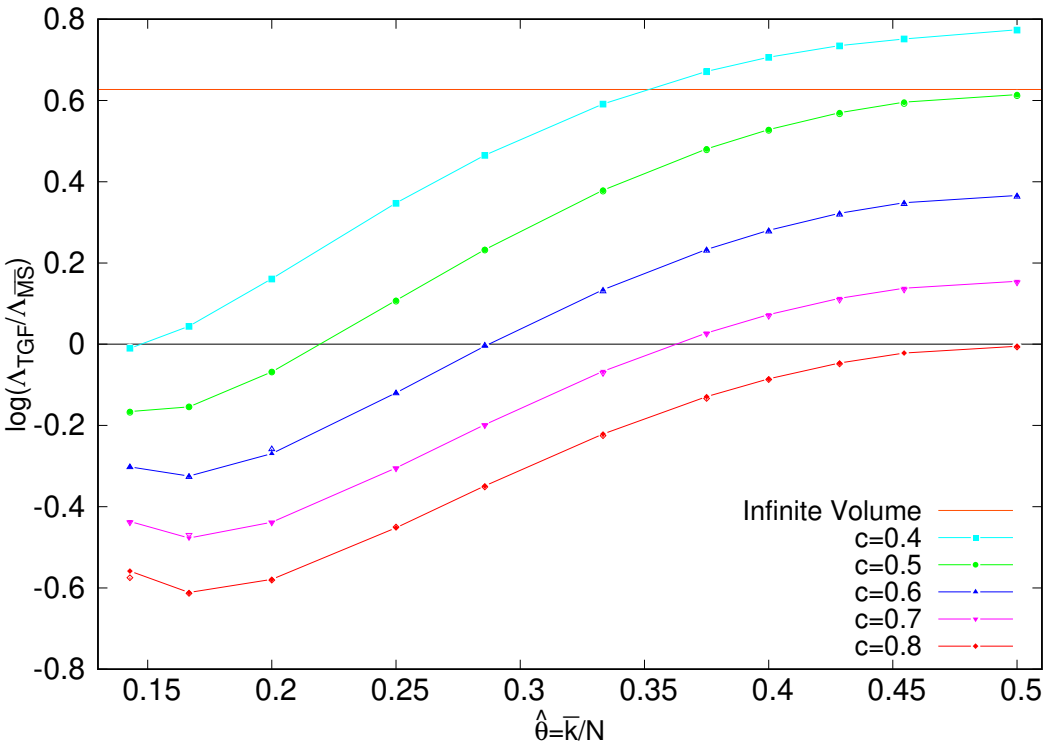

Figure 2.2: We display $\log(\Lambda_{\rm TGF}/\Lambda_{\overline{\rm MS}})$ as a function of $\hat{\theta} = \bar{k}/N$ for different choices of gauge group and magnetic flux. The hollow and full symbols correspond to the results of the Mathematica and C++ codes respectively, though the overlap makes them indistinguishable in almost every case. The error bars of the results are smaller than the symbols used, but can easily be worked out from table 2.2.

2.5 Dependence on the number of colours and the magnetic flux

In this section, we will analyse the dependence of the renormalised coupling $\lambda_{TGF}(c\tilde{l})$ on the number of colours N and the angular variable $\hat{\theta} = \bar{k}/l_g$. We will consider two different limits, both of them taken at fixed value of the renormalised 't Hooft coupling: a first, singular large N limit in the spirit of those introduced in ref. [92], in which N is sent to infinity while the torus size is sent to zero in such a way as to keep $\tilde{l}$ fixed, and the thermodynamic limit, achieved by simultaneously sending c to zero and $\tilde{l}$ to infinity while keeping $c\tilde{l}$ fixed. The idea that the infinite volume limit can be attained at $\tilde{l} \to \infty$ by sending either the torus size or the number of colours to infinity is implicit in our construction.

2.5.1 Singular large N limit and $\hat{\theta}$-dependence

As we recall from section 1.1, singular large N limits such as the ones described above have been employed in many contexts. Before going into the determination of the N and $\hat{\theta}$ dependence of the coupling in our scheme, it is convenient to do a quick recapitulation of some of the relevant ideas introduced in the aforementioned section. An example of a singular large N limit related to of our computation is the one introduced ref. [93], in which the non-perturbative running of the $SU(\infty)$ 't Hooft coupling was computed through a step scaling procedure implemented by changing the rank of the gauge group, in the extreme case of TEK reduction on a one-site lattice with an effective size given by $\tilde{l} = a\sqrt{N}$, where a denotes the lattice spacing. The continuum limit at fixed $\tilde{l}$ was achieved by sending N to infinity, allowing the authors to compute the evolution of the coupling constant through a wide range of scales, and matching the two-loop perturbative formula at small coupling rather well.

These type of limits have also been considered in the framework of non-commutative field theory, as the gauge theory we are considering is equivalent, through the Morita duality, to a non-commutative gauge theory. The corresponding rational adimensional non-commutativity parameter is given precisely by the angular variable $\hat{\theta}$, a mapping through which the effective torus size $\tilde{l}$ corresponds directly to the size of the non-commutative torus in the dual theory.

One of the proposals raised in ref. [92] was to define non-commutative gauge theories at irrational values of $\hat{\theta}$ through a sequence of ordinary $SU(N_i)$ twisted

Yang-Mills theories with increasing number of colours and $\hat{\theta}_i = \bar{k}_i/N_i \to \hat{\theta}$. In 2+1 dimensions, ref. [45] has shown that such sequential definitions can only be realised, in order to avoid tachyonic instabilities, for an uncountable zero-measure set of values of $\hat{\theta}$, such as for instance a sequence of values of $\bar{k}$ and N defined through $\bar{k}_i/N_i = F_{i-2}/F_i$, where F_i denotes the ith term in the Fibonacci sequence. In that case, instabilities in the large N limit are avoided and the limiting sequence tends to $\hat{\theta} = (3-\sqrt{5})/2$. In 2+1 dimensions, the condition required to avoid instabilities was shown to be controlled by a quantity dubbed $Z_{\min}$:

$$Z_{\min}(N,k) = \min_{m \neq 0 \,(\mathrm{mod}\, l_g)} m\, ||\hat{\theta} m||\,, \tag{2.130}$$

where the symbol $||x||$ is used to denote the distance from x to the nearest integer (see refs. [45, 85]). Tachyonic instabilities and symmetry breaking transitions can be avoided as long as $Z_{\min} > 0.1$. Remarkably, as shown in ref. [44], in 4-dimensional perturbation theory this parameter also controls the size of the contribution of non-planar diagrams to the expectation value of Wilson loops.

The limiting procedure to define non-commutative gauge theories at irrational values of the non-commutativity parameter relies on the assumption of continuity in $\hat{\theta}$. The one-loop matching constant $\mathcal{C}_1$ depends on the choice of the parameter c defining the renormalisation scheme, the rank of the group, and the magnetic flux k, and, in particular, given a fixed value of c, one should analyse under which conditions the k and N dependence is fully encoded in the dimensionless ratio $\bar{k}/N$ defining $\hat{\theta}$.

While we will not get into a detailed and exhaustive analysis of the $\hat{\theta}$ dependence, we will look at the integrals I_1 and I_2 entering the definition of $\mathcal{C}_1$ as representative examples of integrals that are respectively UV divergent and finite after dimensional regularisation.

Figures 2.3 and 2.4 show how the I_1 and I_2 contributions to $\mathcal{C}_1$ depend on $\hat{\theta}$ for $c = 0.15$ and $c = 0.30$ respectively, for which we explored many values of N ranging from $N = 2$ to $N = 75025$, the latter as part of the aforementioned Fibonacci sequence. For $c = 0.3$, we noticed that the dependence on $\hat{\theta}$ of both integrals is continuous, with the exception of the point $N = 2$ in the case of I_1. As c decreases, however, several other points corresponding to small values of N deviate from the general curve, and, in the case of I_1, we observe a steep dependence on $\hat{\theta}$ for sequences approaching rational values of $\bar{k}/N$, in particular for 0, 1/4, 1/3 and 1/2.

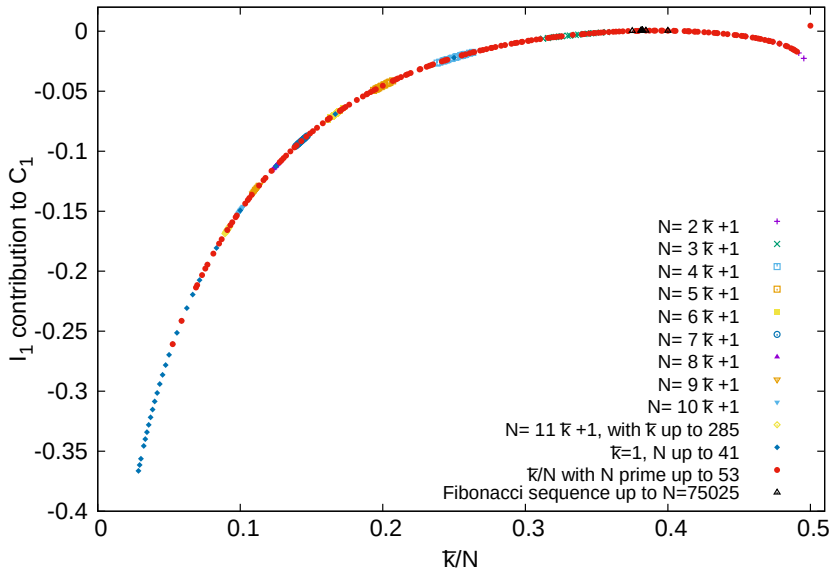

(a) I_1

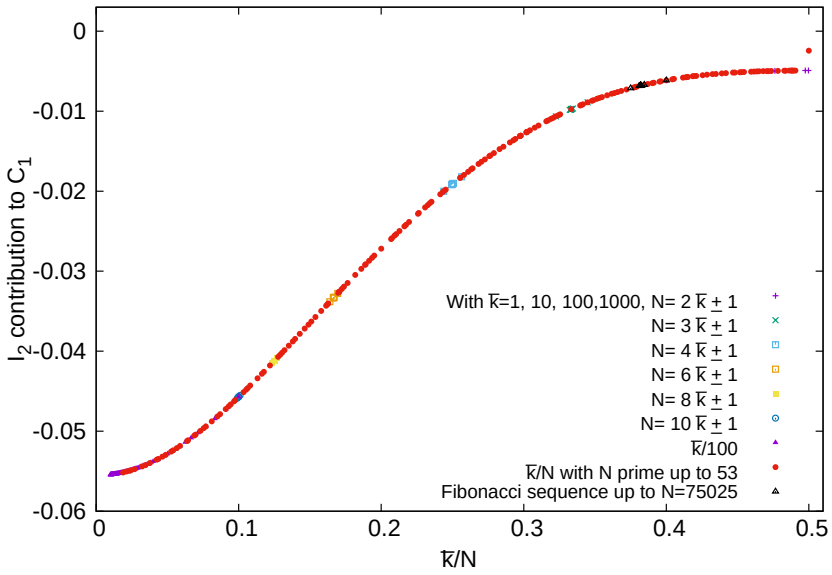

(b) I_2

Figure 2.3: Dependence on $\hat{\theta}$ of the I_1 and I_2 contributions to $\mathcal{C}_1$ at $c = 0.30$.

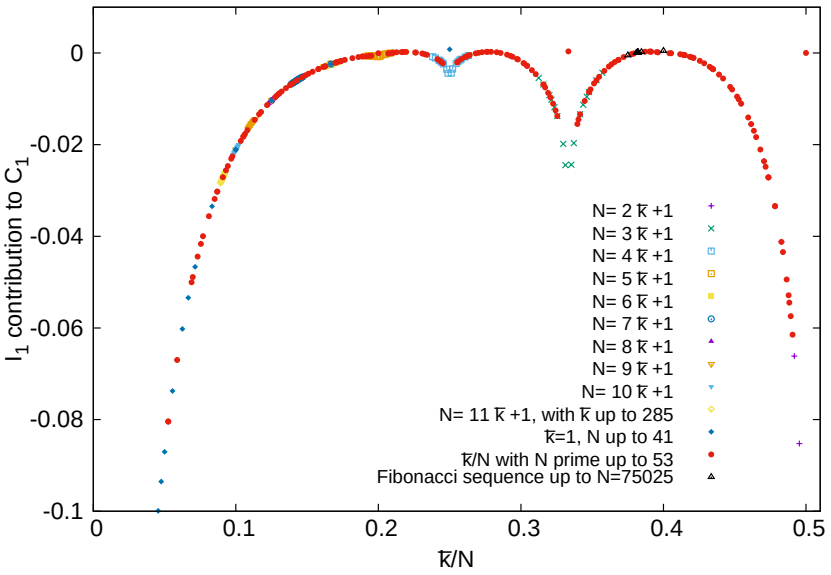

(a) I_1

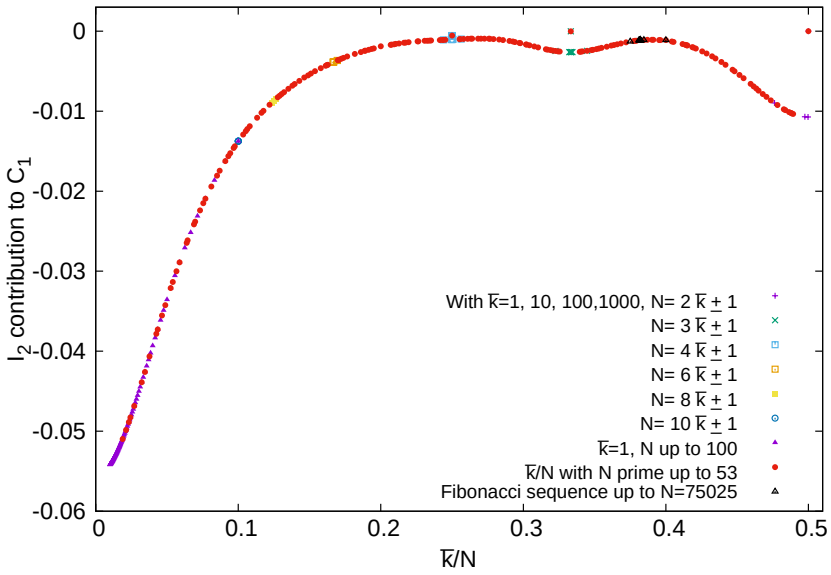

(b) I_2

Figure 2.4: Dependence on $\hat{\theta}$ of the I_1 and I_2 contributions to $\mathcal{C}_1$ at $c = 0.15$.

A similar dependence on $\hat{\theta}$ has been observed in lattice perturbation theory in ref. [44] when considering the contribution at second order of non-planar diagrams to the expectation values of Wilson loops, which can be understood in terms of the parameter $Z_{\min}$ introduced earlier.

Let us take a look at how the dependence in this $Z_{\min}$ quantity enters in the I_1 contribution to $\mathcal{C}_1$. The $\hat{\theta}$-dependent term comes from the function $H(s,u,v,\hat{\theta})$ defined in eq. (2.85). This contribution is finite in the UV and, using Poisson resummation to invert the terms in n, and recovering all factors involved in the definition of $\mathcal{C}_1$, given by:

$$-\frac{\hat{c}^2}{3\mathcal{A}(2\hat{c})}\int_0^1\frac{dx}{x}{\sum_{m\in\mathbb{Z}^4}}'\sum_{n\in\mathbb{Z}^4}\exp\left\{-\frac{\pi\hat{c}}{2}(4-x)m^2-\frac{\pi}{2\hat{c}x}(n-\hat{\theta}\tilde{\epsilon}m)^2+i\pi\, mn\right\}. \tag{2.131}$$

As all terms included in the sum have a non-zero value of $\hat{\theta}\tilde{\epsilon}m$, UV-finiteness is guaranteed. However, in the limit in which this quantity tends to zero, one would retrieve the divergence present in the $\hat{\theta}=0$ term, which as we will show in what follows is approached logarithmically in $Z_{\min}$. We will begin by considering the leading asymptotic behaviour for small x:

$$-\frac{\hat{c}^2}{3\mathcal{A}(2\hat{c})}\theta_3^2\left(0,2i\hat{c}\right){\sum_{m\in\mathbb{Z}^2}}'e^{-2\pi\hat{c}m^2+i\pi\, m\hat{n}}\int_0^1\frac{dx}{x}\exp\left\{-\frac{\pi}{2\hat{c}x}||\hat{\theta}\tilde{\epsilon}m||^2\right\}, \tag{2.132}$$

where $\hat{n}$ denotes the integer closest to $\hat{\theta}\tilde{\epsilon}m$. Integrating over x and defining $Z^2(m)=m^2\,||\hat{\theta}m||^2$, we get an incomplete gamma function:

$$-\frac{\hat{c}^2}{3\mathcal{A}(2\hat{c})}\theta_3^2\left(0,2i\hat{c}\right){\sum_{m\in\mathbb{Z}^2}}'e^{-2\pi\hat{c}m^2+i\pi\, m\hat{n}}\Gamma\left[0,\frac{\pi Z^2(m)}{2\hat{c}m^2}\right], \tag{2.133}$$

which, if the argument of the incomplete Γ function is small, goes as:

$$\frac{\hat{c}^2}{3\mathcal{A}(2\hat{c})}\theta_3^2\left(0,2i\hat{c}\right){\sum_{m\in\mathbb{Z}^2}}'e^{-2\pi\hat{c}m^2+i\pi\, m\hat{n}}\left(\gamma_E+\log\left(\frac{\pi Z^2(m)}{2\hat{c}m^2}\right)\right)+\cdots \tag{2.134}$$

As we can see, the logarithmic dependence in Z is generally tamed by the exponential damping in $\hat{c}m^2$, but this suppression disappears once $\hat{c}$ is small enough, generating the sort of behaviour presented in fig. 2.4a. This is more clearly seen in fig. 2.5, where we show the contribution of I_1 to $\mathcal{C}_1$ as a function of the key

parameter $\log Z_{\min}(N,k)$ in two cases: the upper plot shows the points for which the minimal value is attained at $m = (1,0)$, and the lower one those with the minimum at $m = (2,0)$, with the red vertical line in the plots corresponding to $Z_{\min} = 0.1$. Sequences approaching $\hat{\theta} = 0$ and $\hat{\theta} = 1/2$ in the upper and lower plots respectively are deep in the small $Z_{\min}$ region, and so minuscule changes to the value of $\hat{\theta}$ translate into large changes for the integral.

As a final remark, we will point out that the value of $Z_{\min}$ stays almost constant along the Fibonacci sequence mentioned earlier, meaning that the results of the integrals will depend almost exclusively on the value of c. The singular large N limit can therefore be taken, as expected, safely along such a sequence, making it optimal for the determination of the $SU(\infty)$ running coupling using the reduction techniques employed in ref. [93].

2.5.2 The large volume limit

The previous section discussed the dependence of the matching constant $\mathcal{C}_1$ on the number of colours and the flux-dependent parameter $\hat{\theta}$ for a fixed value of the scheme-defining parameter c. In contrast, in this section we will focus on the limit in which c tends to zero as the effective size is sent to infinity, in such a way as to keep flow time fixed, thus fixing the energy scale of the coupling.

Such a limit can be taken in two different ways: one can either send the smaller torus period l to infinity while keeping the rank of the group N fixed, or send N to infinity at fixed l. If volume independence holds true, the infinite volume expression should be recovered in either case, meaning that $\mathcal{C}_1$ should vanish in both limits.

As we recall, at fixed value of t, $\mathcal{C}_1$ is a function of c, N and the magnetic flux k, the last one containing the dependence on the boundary conditions. This dependence is, for the coupling, fully contained in $\mathcal{C}_1$, and so in the thermodynamic limit it will vanish as long as $\mathcal{C}_1$ does so as well. We will therefore analyse in what follows the behaviour of the matching constant in the approach to the thermodynamic limit, along with the size of the finite volume (or finite N) corrections.

As preparation for such a discussion, let us begin by considering the LO term in the expansion of the energy density from eq. (2.46), while setting $t = (c\tilde{l})^2/8$.

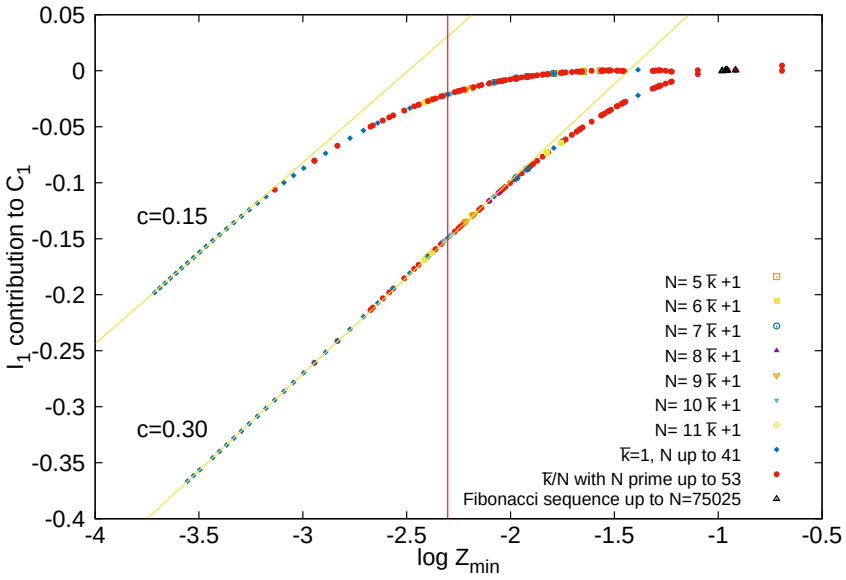

(a) $m_0 = 1$

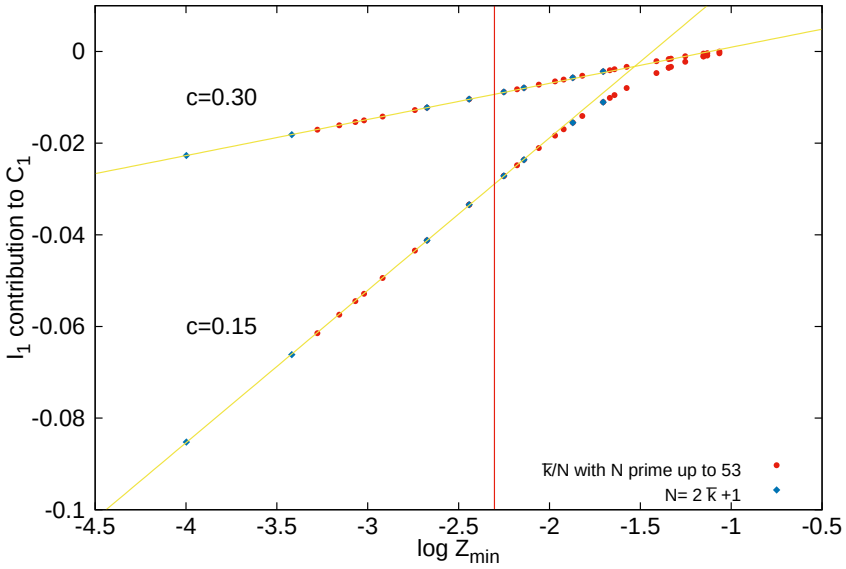

(b) $m_0 = 2$

Figure 2.5: $Z_{\min}$-dependence of the contribution of I_1 to the one-loop matching constant $\mathcal{C}_1$. The red vertical line in the plots corresponds to $Z_{\min} = 0.1$.

As we recall, the dependence on c and N came from:

$$\mathcal{A}(\pi c^2) = F_0(\pi c^2, 4-d_t)\left(F_0(\pi c^2, d_t) - \frac{1}{N^2}F_0(\pi c^2 l_g^2, d_t)\right), \tag{2.135}$$

where for clarity of notation we introduced:

$$F_0(x,d) = \sum_{m\in\mathbb{Z}^d} \exp\left(-\frac{\pi m^2}{x}\right). \tag{2.136}$$

In the infinite volume limit (in the sense of $c \to 0$ at fixed l_g), $F_0(0,d) = 1$, and therefore:

$$\mathcal{A}(\pi c^2) \to 1 - \frac{1}{N^2}, \tag{2.137}$$

leading to a LO term in agreement with the results found in ref. [103]. The leading correction is exponentially suppressed with the square of the volume as:

$$-\frac{2d_t}{N^2}\exp\{-1/(cl_g)^2\} \equiv -\frac{2d_t}{N^2}\exp\{-l^2/(8t)\}. \tag{2.138}$$

If instead one takes the large N limit (i.e. large l_g) at fixed l and constant cl_g, we obtain $\mathcal{A}(\pi c^2) = 1 + \mathcal{O}(1/N^2)$, which is the same result that one observes when looking at the infinite volume large N limit: a powerlike approach with $1/N^2$ corrections.

The discussion of the NLO term, however, is more complicated, requiring some additional considerations before taking the large volume limit. As we recall, the different contributions[7] to $\mathcal{C}_1$ could be written in a compact way as:

$$\bar{I} = \frac{4}{3\mathcal{A}(2\hat{c})}\int (u\alpha)^{-2}\left(\hat{H}(s,u,v,0) - \hat{H}(s,u,v,\hat{\theta}) - \mathcal{A}(2\hat{c})\right), \tag{2.139}$$

where we used the symbol $\int$ to denote the integrals appearing in eqs. (2.69)-(2.80) in a generic manner, including the prefactors multiplying the Φ function and derivatives when required, and where we introduced a quantity $\hat{H}(s,u,v,\hat{\theta})$ related to the function $H(s,u,v,\hat{\theta})$ entering the definition of Φ through:

$$H(s,u,c,\hat{\theta}) = \Phi^{\infty}(s,u,v)\hat{H}(s,u,v,\hat{\theta}). \tag{2.140}$$

[7]The regularised expression for I_9 was done in a slightly different manner, see section 2.3.2 and app. A.6.2 for the details.

This function is given by:

$$\hat{H}(s,u,v,\hat{\theta}) = \mathrm{Re}\Big\{ F_1(\alpha,u,v,0,4-d_t) \times \left(F_1(\alpha,u,v,\hat{\theta},d_t) - \frac{1}{N^2} F_1(\alpha l_g^2, u, v l_g, 0, d_t) \right) \Big\}, \tag{2.141}$$

with:

$$F_1(\alpha,u,v,\hat{\theta},d) = (\hat{c}\alpha)^{d/2} \sum_{m,n\in\mathbb{Z}^d} \exp\left\{ -\pi\hat{c}\alpha m^2 - \frac{\pi}{\hat{c}u}(n-\hat{\theta}\check{\epsilon}m)^2 + 2\pi i \frac{v}{u} mn \right\}. \tag{2.142}$$

It will be convenient, in order to analyse the approach to the infinite volume limit, to look at the expression resulting after Poisson resummation in m. For the sake of simplicity in the analysis, we will henceforth focus on the case of the two-dimensional twist, $d_t = 2$, and move the brunt of the full, detailed computations to appendix A.8.

After a few computations, we managed to split each of the contributions to $\mathcal{C}_1$ into separate $\hat{\theta}-$independent and $\hat{\theta}-$dependent terms, given by:

$$I_{TI} = I_{TI}^{(0)} + \frac{4}{3\mathcal{A}(2\hat{c})} \left\{ \int (u\alpha)^{-2} \hat{H}'(s,u,v,0) + \int \frac{\hat{c}^2}{s^2} \left(1 - \frac{1}{N^2} - \mathcal{A}(\hat{c}s) \right) \right\}, \tag{2.143}$$

$$I_{TD} = I_{TD}^{(0)} - \frac{4}{3\mathcal{A}(2\hat{c})} \left\{ \int (u\alpha)^{-2} \hat{H}'(s,u,v,\hat{\theta}) + \int \frac{\hat{c}^2}{s^2} \left(1 - \frac{1}{N^2} - \mathcal{A}(\hat{c}s) \right) \right\}, \tag{2.144}$$

where the function $\hat{H}'$ is obtained by subtracting the zero modes from $\hat{H}$ after Poisson resummation (see app. A.8), and where:

$$I_{TI}^{(0)} = -\frac{4}{3\mathcal{A}(2\hat{c})} \int (u\alpha)^{-2} \left(\mathcal{A}(2\hat{c}) - \mathcal{A}(\hat{c}\alpha) - \mathcal{A}(\hat{c}\alpha u/s) + 1 - \frac{1}{N^2} \right), \tag{2.145}$$

$$I_{TD}^{(0)} = -\frac{4}{3N^2\mathcal{A}(2\hat{c})} \sum_{n\neq 0} \int (u\alpha)^{-2} e^{-\frac{\pi s n^2}{\hat{c}N^2\alpha u}} \times \mathrm{Re}\left\{ \theta_3^2\left(0, \frac{i}{\hat{c}\alpha}\right) \prod_{\mu} \theta_3\left(z_\mu, \frac{i}{\hat{c}N^2\alpha}\right) - 1 \right\}. \tag{2.146}$$

We defined in that last equation $z_\mu = \epsilon_{\mu\nu} n_\nu k/N + i v n_\mu/(\hat{c}N^2\alpha u)$, and used n to denote a d_t-dimensional vector of integers taking values in the intervals $[-N/2, N/2)$

for even values of N, and $[-(N-1)/2, (N-1)/2]$ for odd ones. The leading correction to the infinite volume limit is in general driven by the contribution of $I_{TI}^{(0)}$ and $I_{TD}^{(0)}$, and is controlled by two quantities: $\hat{c}\alpha$ and $\hat{c}\alpha u/s$.

The simplest case corresponds to integrals $\bar{I}_1$, $\bar{I}_2$ and $\bar{I}_4$, for which both $\hat{c}\alpha$ and $\hat{c}\alpha u/s$ tend to zero in the $\hat{c} \to 0$ limit in all of the integration range. The leading contribution, derived in appendix A.8, is given by:

$$\bar{I}_1 \to \frac{1}{9(N^2-1)} e^{-(cN)^{-2}} \left(1 + 3\gamma_E - 3\log\left(3c^2N^2\right) - 3c^2N^2\right), \tag{2.147}$$

$$\bar{I}_2 \to \frac{2}{9(N^2-1)} e^{-(cN)^{-2}} \left(1 - 6c^2N^2\right), \tag{2.148}$$

$$\bar{I}_4 \to \frac{1}{3(N^2-1)} e^{-(cN)^{-2}} \left(-1 + \gamma_E - \log\left(9c^2N^2\right) + 3.544907702\, cN - c^2N^2\right). \tag{2.149}$$

Integrals for which the infinite volume contribution $I_i(\Phi^\infty, t')$ is UV-divergent in $d = 4$, such as $\bar{I}_1$ and $\bar{I}_4$, have a leading correction that goes as $\sim \log(c^2N^2)\exp(-1/(cN)^2)$, whereas $I_2(\Phi^\infty, t')$ is UV-finite and has a leading correction with a purely exponential decay in the thermodynamic limit, given by $\exp(-1/(cN)^2)$. The dependence of these integrals on cN is shown in fig. 2.6 for several values of $\bar{k}$ and N, displaying their value multiplied by the factor $(N^2-1)\exp(1/(cN)^2)$. The continuous lines shown in the plot correspond to the formulas presented above, which describe very accurately the data for small values of cN. In the $N \to \infty, c \to 0$ limit taken at fixed, small values of cN, all three integrals tend to zero with $\mathcal{O}(1/N^2)$ corrections.

The general dependence of $\mathcal{C}_1$ on cN as $cN \to 0$, on the other hand, follows a formula that is analogous to eq. (2.149), as one can see in the $SU(3)$ case shown as an example in fig. 2.7, where $\mathcal{C}_1$ is displayed as a function of $(cN)^2$ along with a continuous line corresponding to a least squares fit to the functional form $f(cN) = \exp(-1/(cN)^2)(\alpha + \beta\log(cN) + \gamma cN + \delta c^2N^2)$.

It is quite convenient, in order to push the calculation of $\mathcal{C}_1$ to smaller values of c, to split it into two pieces, shown as open blue circles and yellow squares in the plot. The former comes from the contributions of $\bar{I}_3$, $\bar{I}_7$, $\bar{I}_{10}$, $\bar{I}_{11}$ and $\bar{I}_{12}$, and is by far the most relevant piece at small c: we were able to compute it down to $(cN)^2 \sim 0.1$, and it is asymptotically quite well described by the function $f(cN)$, with a leading dependence on c of the form $\log(cN)\exp(-1/(cN)^2)$.

In what is left of this section, now that the the behaviour of $\bar{I}_1$, $\bar{I}_2$, and $\bar{I}_4$

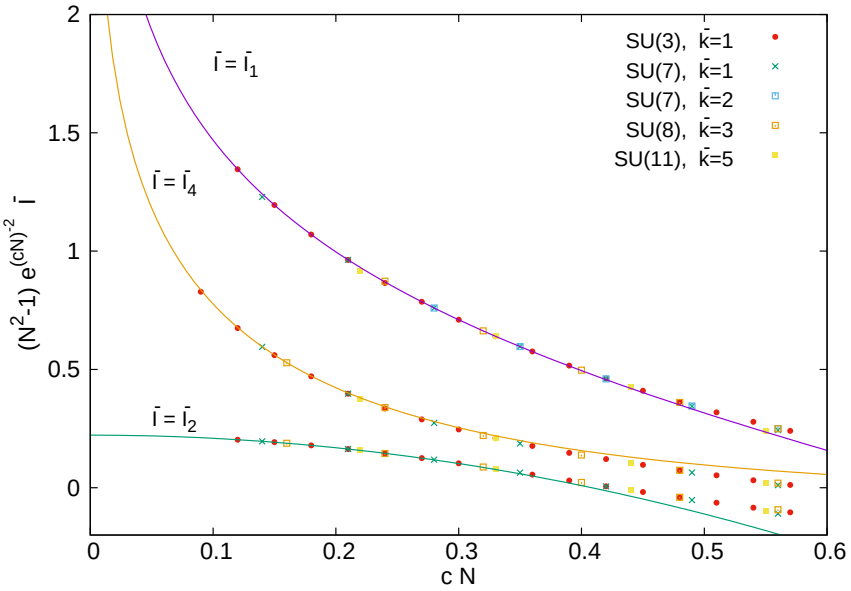

Figure 2.6: The integrals $\bar{I}_1$, $\bar{I}_2$ and $\bar{I}_4$ multiplied by the factor $(N^2-1)e^{(cN)^{-2}}$ as a function of cN. The continuous lines are given by formulas (2.147)- (2.149).

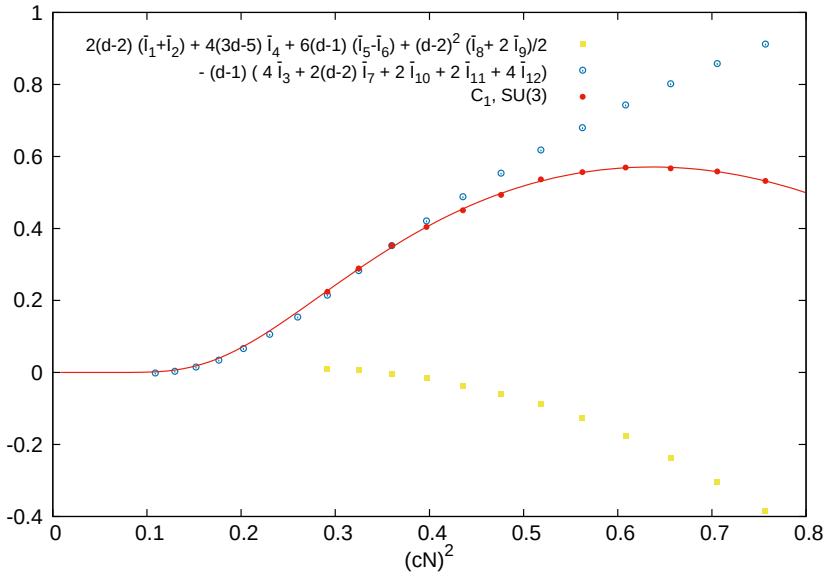

Figure 2.7: Dependence on cN of the SU(3) one-loop matching constant $\mathcal{C}_1$ separated into two pieces, plotted with open circles and squares. The continuous line is a fit to the functional form $f(cN) = e^{-(cN)^{-2}}(\alpha + \beta \log(cN) + \gamma cN + \delta c^2 N^2)$.

has been studied, we will focus on exploring how the infinite volume limit is approached for the remaining integrals. The discussion is a bit more complex than the previous case, as the leading correction will now go as c^2 for each of the integrals, but luckily these corrections will cancel each other out when all contributions to $\mathcal{C}_1$ are considered. We will first analyse the case of $\bar{I}_3$ in detail to see how the cancellation takes place, and then generalise it to the other ones.

For this integral, in the $\hat{c} \to 0$ limit, $\hat{c}\alpha u/s$ goes to zero in the full integration range, and the leading dependence is given by:

$$-\frac{4}{3\mathcal{A}(2\hat{c})}\int_0^\infty dz(3+2z)^{-2}\left\{1-\frac{1}{N^2}-\mathcal{A}(\hat{c}(3+2z)/2)\right\}. \tag{2.150}$$

From this expression one can show (see app. A.8) that the dominant correction in the $cN \to 0$ limit is:

$$I_0 = \frac{\pi(cN)^2}{6N^2\mathcal{A}(2\hat{c})}\left(a_1 - \frac{1}{N^2}a_2(N)\right) + \cdots, \tag{2.151}$$

with, for instance in the case of $SU(3)$:

$$a_1 = -1.76508480122121275; \qquad a_2(N=3) = 3.59085631503990722\,. \tag{2.152}$$

The quantity $a_2(N)/N^2$ grows logarithmically with N^2, as shown in fig. 2.8. All remaining integrals $\bar{I}_i$ converge in the same manner in the infinite volume limit, turning out to be proportional to I_0 (see app. A.8) with a proportionality coefficient of +1 for $i = 5, 6, 7$, of -1 for $i = 10, 11, 12$ and of 4 and -2 in the respective cases of $\bar{I}_8$ and $\bar{I}_9$. Combining eq. (2.52) with these coefficients, it is easy to show that the total contribution of the leading $(cN)^2$ term to $\mathcal{C}_1$ vanishes.

While we did not analyse how the different integrals approach zero after subtracting the quadratic piece in c in detail, based on the results presented in fig. 2.7 we expect other possible power-like correction to $\mathcal{C}_1$ to cancel out as well, with the final result exponentially decaying towards zero with a leading dependence on c of the form $\sim \log(cN)\exp\left(-(cN)^{-2}\right)/(N^2-1)$.

We performed a preliminary analysis for the case of $\bar{I}_3$, shown in fig. 2.9 in which we display the quantity $\bar{I}_3 - I_0$ times the factor $(N^2-1)\exp((cN)^{-2})$ as a function of cN for several values of N. Each point in that plot was obtained from the exact expression for $\bar{I}_3$, and the continuous lines correspond to the approximate expression obtained combining eqs. (2.145) and (2.146). This

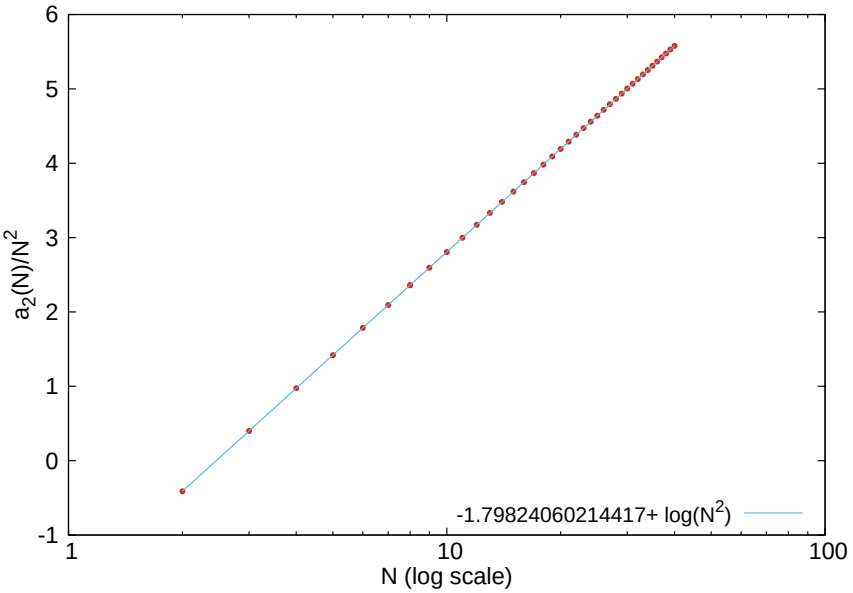

Figure 2.8: Dependence on N of the coefficient $a_2(N)/N^2$ appearing in eq. (2.151).

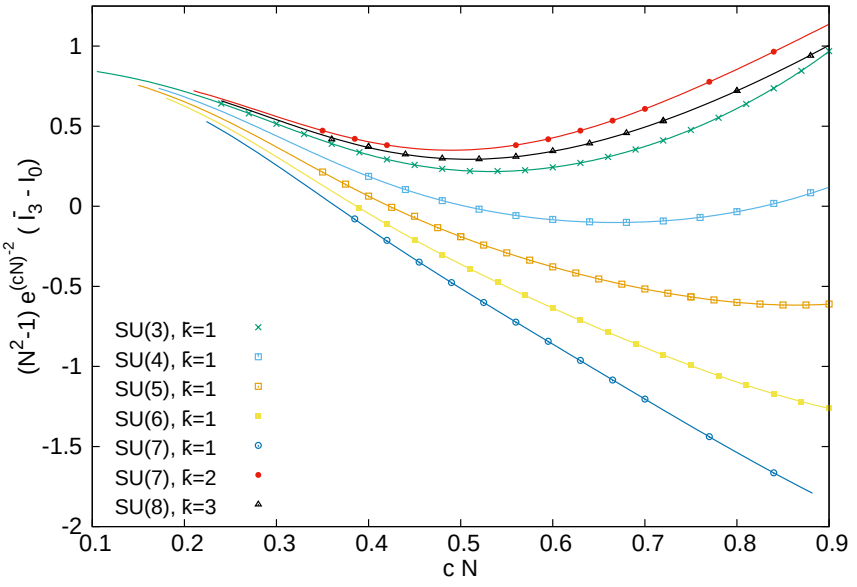

Figure 2.9: The integral $\bar{I}_3 - I_0$ multiplied by the factor $(N^2-1)e^{(cN)^{-2}}$, plotted as a function of cN. The continuous line is obtained from the approximate expression given by the sum of eq. (2.145) and (2.146).

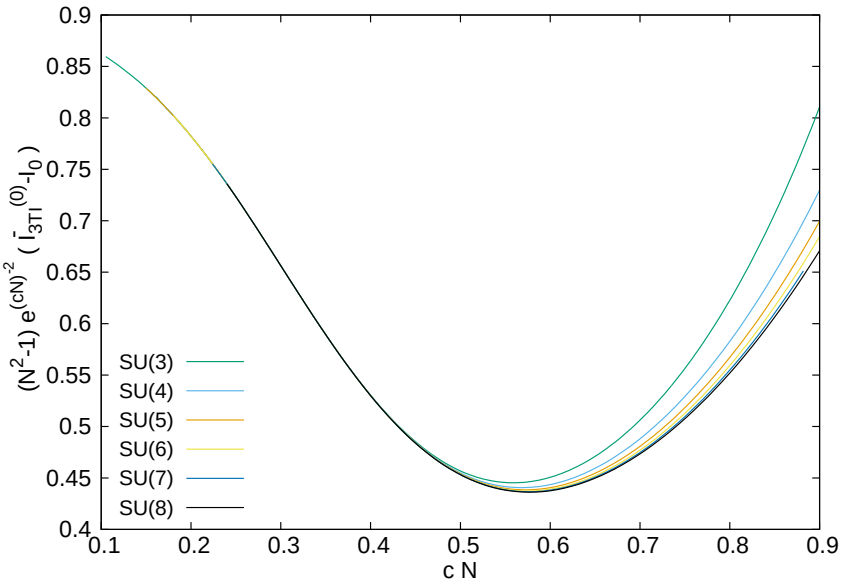

(a) $\bar{I}^{(0)}_{3TI} - I_0$

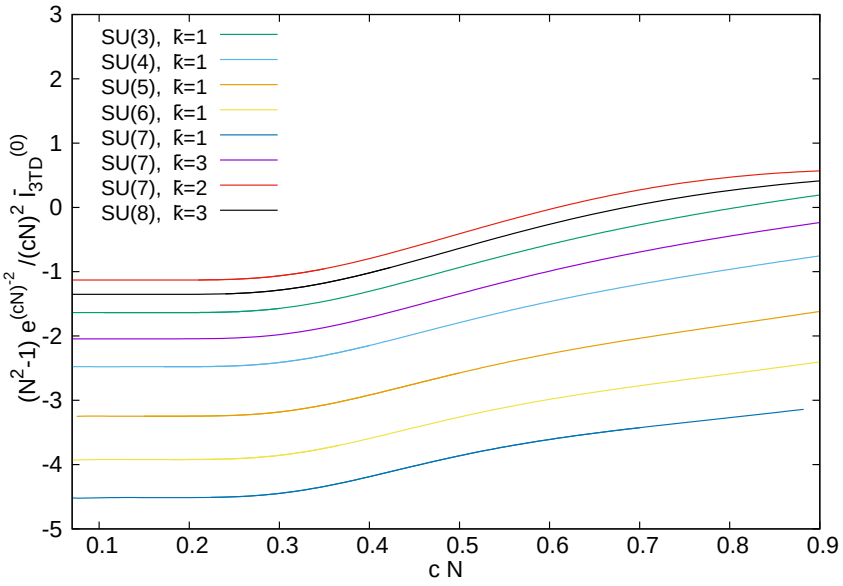

(b) $\bar{I}^{(0)}_{3TD}$

Figure 2.10: The leading contributions to $\bar{I}_3$ from eqs. (2.145) and (2.146), multiplied by factors $(N^2-1)e^{(cN)^{-2}}$ and $(N^2-1)e^{(cN)^{-2}}/(cN)^2$ respectively and displayed as a function of cN for various values of N and the magnetic flux k.

decomposition is actually quite useful for the analysis of the dependence of the integral on N, and so we chose to display each of the two pieces separately as a function of the scaling variable cN in figures. 2.10a and 2.10b.

The $\hat{\theta}$-independent term is presented in fig. 2.10a, multiplied by the factor $(N^2-1)\exp((cN)^{-2})$ scaling away most of its N dependence. For $cN \to 0$, the integral decays exponentially as $\sim \exp(-(cN)^{-2})$, whereas in the large N limit at fixed value of cN it goes to zero with quadratic corrections in $1/N^2$.

The analysis of the $\hat{\theta}$-dependent part is more complicated, as the dependence on the magnetic flux k needs to be taken into account, but the decay of $\bar{I}_3$ towards zero is in this case faster than exponential, going as $\sim (cN)^2 \exp(-(cN)^{-2})$. This is shown in fig. 2.10b, where we plotted $\bar{I}^{(0)}_{3TD}$ divided by said decay factor and by (N^2-1), as a function of cN for several values of N and the magnetic flux. In the large N limit taken at fixed cN, this term also scales to zero as $1/N^2$.

2.6 Conclusions

Let us close this chapter by recapitulating the main results obtained along the way. We have determined the perturbative expansion at one-loop order of the $SU(N)$ twisted gradient flow coupling, including the matching to the $\overline{\text{MS}}$ infinite volume scheme at a renormalisation scale $\mu = 1/(c\tilde{l})$ given by a combination of the size of the torus and the rank of the gauge group. The corresponding one-loop finite piece was computed numerically for the case of a two-dimensional non-trivial twist with $\tilde{l} = lN$, for a range of values of c, the parameter relating the energy scale to the size of the torus, and for several values of the magnetic flux and the rank N of the gauge group. The obtained values of the finite piece allowed us to obtain the ratio at one loop of Λ parameters between the TGF scheme and the $\overline{\text{MS}}$ one for the aforementioned range of parameters.

Moreover, we deemed it interesting to explore the dependence of the coupling λ_{TGF} on the number of colours of the theory and on the magnetic flux in a bit more depth, focusing our analysis in two particularly interesting limits. First, we studied the limit in which N and the physical torus size l are sent to infinity and zero respectively, in such a way as to keep the effective size $\tilde{l}$ fixed (hence keeping the renormalised 't Hooft coupling at scale $\mu = 1/(c\tilde{l})$ constant as well). This is a singular large N limit in the spirit of those introduced in ref. [92], albeit a rather non-standard one since non-planar, $\hat{\theta}$-dependent diagrams survive the

limit provided $\tilde{l}$ is finite.

The connection of this case to non-commutative Yang-Mills theory is straightforward through the use of the Morita duality: the non-commutative dual torus is of length $\tilde{l}$ and has a dimensionless non-commutativity parameter given by $\hat{\theta} = \bar{k}/N$. Our analysis also supports the observation, first presented in refs. [45, 85], that the avoidance of tachyonic instabilities when taking the singular limit is only possible for a zero-measure, though uncountable, set of values of $\hat{\theta}$. Curiously, one of the successful cases found in ref. [85], of limiting parameter $\hat{\theta} = (3 - \sqrt{5})/2$, relies on a sequence of Fibonacci numbers with $k = F_{i-2}$ and $N = F_i$, F_i denoting the i-th element of the Fibonacci series.

The second limit at which we looked was the thermodynamic limit, in which c is sent to zero and $\tilde{l}$ is sent to infinity while keeping the energy scale μ constant. This leads to recovering the one-loop expression of the 't Hooft gradient flow coupling at infinite volume from ref. [104]. Our results thus support the idea of volume reduction, in the sense that the $SU(\infty)$ coupling in the thermodynamic limit can also be recovered at fixed torus size by sending N (and hence $\tilde{l}$) to infinity, in which case the limit is approached with $1/N^2$ corrections.

Chapter 3

The twisted gradient flow coupling on the lattice

3.1 Introduction

The only known way, barring a few exact results, to study quantum field theories in a non-perturbative setting is through a lattice discretisation. As such, many of the finite size renormalisation schemes have been developed over the years for the study of gauge theories, such as the ones in refs. [39, 104, 120, 121], which were presented in a lattice setting from the start. As we have in our case already addressed the perturbative approach to the study of the twisted gradient flow coupling in chapter 2, we will in this chapter focus on performing a lattice study of the running of the twisted gradient flow coupling constant.

Our main concern will be the non-perturbative study of the pure gauge theory, focusing on the specific case of $SU(3)$, as a probe on the feasability of the study and with the aim to extend the analysis to more values of N in the future. Our discrete scheme has strong similarities to the one that we used in the continuum computation, and is inspired on several finite volume schemes introduced in the last years, such as the ones used in refs. [121, 127], though it comes with some peculiarities of its own.

Similar schemes have also been used in recent years in ref. [114] to non-perturbatively determine the $\Lambda_{\overline{\text{MS}}}$ parameter in $SU(3)$ pure gauge theory, in ref. [132] to match with perturbation theory at NNLO and precisely obtain the Λ parameter, or, in ref. [93] and along with ideas of volume reduction from refs. [3–5, 64], in the obtention of the $SU(\infty)$ running coupling on a single-site lattice, through the use of step scaling procedures based on rescaling the rank of the gauge group instead of the size of the lattice.

In particular, we will once more work on top of a four-dimensional torus, now discrete, combining non-trivial twisted boundary conditions (TBC) in a single plane with periodic boundary conditions (PBC) in the rest, and use the gradient flow to define a renormalised 't Hooft coupling in terms of an effective size $\tilde{l}$ combining the physical size of the torus with the rank of the gauge group. This size is once more, in the context of the ideas volume reduction from section 1.1, expected to be the one driving the dynamics of the gauge theory. We will make use of step scaling techniques, which were introduced almost three decades ago in ref. [30] and have since become a staple of finite volume computations, to numerically compute the running of the coupling constant over a wide range of scales. Along the way, we will also study some interesting features pertaining to the topological behaviour of the lattice simulations, as well as take a look at the

magnitude of lattice artifacts in our computation.

We will thus be presenting a lattice step scaling computation of the running 't Hooft coupling constant in the TGF scheme. The chapter will be organised as follows:

In section 3.2 we introduce the theoretical setup used to define and compute the coupling. We begin in section 3.2.1 with a short recapitulation of some of the relevant concepts of the continuum theory mentioned in the previous chapter, followed by a full description of the lattice theory and the non-perturbative definition of the coupling in section 3.2.2. We then close the theoretical part of the chapter by presenting in sec. 3.2.3 the step scaling procedure that will be used to compute the running coupling in detail.

Section 3.3 then describes how the numerical computations were carried out, along with some interesting results regarding the topological behaviour of the generated lattice configurations. Section 3.3.1 describes the algorithm used in the simulations, and reports on the parameters that were used to run them. In section 3.3.2, we present a study on some relevant topological properties of the configuration, in which we will also justify some choices that were made in the definition of the coupling. We will also study how different parameters influence the generation of configurations of different topological charge: we will present some results regarding the effects on the topology of the configurations of the scheme parameter c, of the physical volume of the lattice, and of the lattice spacing, which will give rise to issues related to a critical slowdown of the simulations (i.e. to topological freezing).

We will then present in section 3.4 the results of the step scaling computation of the running coupling. In section 3.4.1 we will show our results and fits of the coupling constant λ_{TGF}, taken as a function of the bare lattice coupling b, while section 3.4.2 will show the numerical results for the discrete step scaling function, including a polynomial fit that will be used to interpolate it for other values of the coupling λ_{TGF}. In section 3.4.3 we will present the results of the continuum extrapolation of the step scaling function, as well as the resulting running of the 't Hooft coupling when $\tilde{l}$ is varied over a wide range of scales. Some considerations regarding the extent of lattice artefacts in our computation and their suppression will be presented in section 3.4.4.

Finally, we will in section 3.5 conclude with a compilation of our main results, along with some brief conclusions. For the sake of clarity, results along the chapter

were mainly displayed in graphical form, moving their precise numerical values to appendices B.1-B.4.

3.2 The running coupling on the twisted lattice

Along this section, we will present a non-perturbative determination of the twisted gradient flow coupling. This can only be achieved using a lattice discretisation, and as such we will need to provide a discrete scheme such that the properties of the coupling presented in section 1.2.5 are recovered in the continuum limit.

We will thus work with an asymmetrical torus with twisted boundary conditions, using, as we did in chapter 2, TBC in a single plane and PBC in the rest, and define a running coupling in terms of the effective size $\tilde{l}$ using the gradient flow. This time, however, we will focus on the particular case of $SU(3)$ gauge theory.

Nevertheless, before fully going into the lattice computation, we will include a short recapitulation of some relevant aspects of the continuum definition of the coupling, particularised to the case of $SU(3)$. We will conclude, after providing the relevant discretisations for the action of the theory, the gradient flow, and the definition of the lattice coupling, with a general description of the step scaling procedure that will be used in the numerical computation.

3.2.1 Recapitulation: the continuum theory

Let us thus begin with the recapitulation of the continuum theory. We defined our $SU(3)$ theory on top of a four-dimensional, asymmetrical $\tilde{l}^2 \times l^2$ torus, endowed with 't Hooft twisted boundary conditions in two dimensions, and periodic boundary conditions in the two remaining ones. We set up a twist in the 01 plane, which translates into the following periodicity conditions for the gauge fields:

$$\begin{aligned} A_\mu(x + l\hat{\nu}) &= \Gamma_\nu A_\mu(x)\Gamma_\nu^\dagger, && \text{for } \nu = 0, 1, \\ A_\mu(x + \tilde{l}\hat{\nu}) &= A_\mu(x), && \text{for } \nu = 1, 2, \end{aligned} \tag{3.1}$$

where Γ_ν denotes the same $SU(N)$ twist-eating matrices defined in eq. (1.5):

$$\Gamma_0\Gamma_1 = Z_{01}\Gamma_1\Gamma_0, \tag{3.2}$$

and where the factor Z_{01} is an orthogonal, irreducible twist tensor that can be rewritten in terms of $n_{\mu\nu}$ as:

$$Z_{01} = \exp\{2\pi i n_{01}/N\}, \qquad n_{01} = kN/l_g. \tag{3.3}$$

The periods of the torus were set to be l in the two twisted directions, and $\tilde{l} = 3l$ in the other two, forcing all momenta to be quantised in units of $2\pi/\tilde{l}$.

We then introduce the flow time parameter t along with a set of flow fields $B_\mu(x,t)$ driven towards the classical solutions of the action by the flow equations from eq. (1.27):

$$\partial_t B_\mu(x,t) = -\partial S/\partial B_\mu(x,t) = D_\nu G_{\nu\mu}(x,t), \tag{3.4}$$

matching the $A_\mu(x)$ field at $t = 0$, and where $G_{\mu\nu}$ and D_μ denote the field strength tensor and covariant derivative of the flow fields.

The 't Hooft running coupling λ_{TGF} is then defined through the expectation value of the energy density observable:

$$\lambda_{TGF}(\tilde{l}) = \frac{1}{N}\mathcal{F}(c)\left\langle t^2 E(t)\right\rangle\Big|_{t=\frac{1}{8}c^2\tilde{l}^2}, \quad E(t) = \frac{1}{2}\mathrm{Tr}(G_{\mu\nu}(x,t)G_{\mu\nu}(x,t)), \tag{3.5}$$

where the normalisation factor $\mathcal{F}(c)$ is introduced to remove the factor multiplying the leading order term in the perturbative expansion. Note that the energy scale μ of the running coupling is related to both the flow time parameter t and to the effective torus size $\tilde{l}$ through $\mu^{-1} = \sqrt{8t} = c\tilde{l}$, where c is a scheme-defining parameter taking values between 0 and 1.

Several of the continuum aspects that we just highlighted will be sought after in the construction of the lattice scheme. For instance, we will also be working on a twisted $SU(3)$ asymmetrical $l^2 \times \tilde{l}^2$ torus, with similar twisted boundary conditions in the 01 plane and periodic ones in the rest. Moreover, we will also use the gradient flow to define the running coupling in terms of the energy density, using the effective size of the torus as the energy scale for the running as well. A similar normalisation factor $\mathcal{F}(c)$ corresponding to the leading order term in perturbation theory will be introduced as well, and will turn out to be extremely useful when attempting to reduce the effects of lattice artefacts in the numerical computation of the running coupling.

3.2.2 Lattice discretisation

Let us now focus on the specific set-up required to build the lattice scheme for the numerical computation. We begin by constructing our lattice: we discretise space-time using a four-dimensional euclidean square lattice of spacing a, and rewrite all positions in lattice units as $x = an$, with $n \in \mathbb{Z}^4$. We will in what follows set a to one for all theoretical computations, expressing everything in terms of $\tilde{L}$ rather than $\tilde{l}$. Dimensional arguments can easily be used to recover the a-dependent expressions.

Then, as we mentioned earlier, we define our $SU(3)$ pure gauge theory on top of an asymmetrical torus with twisted boundary conditions in the 01 plane and periodic ones in the rest, with periods $l = La$ in the $0, 1$ directions and $\tilde{l} = \tilde{L}a$ in the other ones, so that all momenta are quantised in terms of $\tilde{l}$. This choice is related to the idea of volume independence, according to which the entire model should be controlled[1] by the effective length $\tilde{l}$ combining the rank of the gauge group and the physical size of the torus. This quantity will be used as the energy scale for the running coupling.

The procedure to set up the gradient flow on the lattice is then as follows: first, before defining any flow, a lattice gauge action needs to be provided in terms of the standard gauge links. Following that, the flow time parameter t is introduced, along with the flow equations and flow dependent links which replace the original gauge links in the action. Finally, these new flow-dependent links are used to define an observable through which the running coupling is defined.

All in all, this means that there will be three quantities for which a discretisation has to be provided:

- The general, discrete Yang-Mills action, which will be used in the Monte Carlo simulations to generate the gauge configurations from which the lattice coupling will be computed.
- The action whose gradient is taken in the flow equations to smear the flow-dependent gauge links.
- The discrete observable used to define the renormalised gradient flow coupling.

We will go one by one, starting with the general action.

[1] Barring finite N corrections, which in the case of $SU(3)$ can be rather sizeable.

We chose to use the standard Wilson action, without any additional improvement. The lattice action is, as is standard on the lattice, given not in terms of the gauge fields A_μ, but rather using the $SU(N)$ link variables $U_\mu(n)$, whose periodicity conditions are:

$$\begin{aligned} U_\mu(n + L\hat{\nu}) &= \Omega_\nu(n) U_\mu(n) \Omega_\nu^\dagger(n + \hat{\mu}), && \text{for } \nu = 0, 1, \\ U_\mu(n + \tilde{L}\hat{\nu}) &= U_\mu(n), && \text{for } \nu = 2, 3, \end{aligned} \tag{3.6}$$

where Ω_μ is an arbitrary SU(3) gauge transformation that verifies the following consistency condition:

$$\Omega_\nu(n + L\hat{\mu})\Omega_\mu(n) = Z_{\mu\nu}(n)\Omega_\mu(n + L\hat{\nu})\Omega_\nu(n), \qquad \text{for } \{\mu, \nu\} = \{0, 1\}. \tag{3.7}$$

$Z_{\mu\nu}(n)$ denotes the twist tensor, taken with $k = 1$, whose explicit expression will be provided in what follows.

The standard Wilson action can then, in the presence of twisted boundary conditions, be written in the form:

$$S_W(U) = bN \sum_n \sum_{\mu\nu} \text{Tr } [1 - Z_{\mu\nu}(n)\tilde{P}_{\mu\nu}(n)], \tag{3.8}$$

$$\tilde{P}_{\mu\nu}(n) = U_\mu(n) U_\nu(n + \hat{\mu}) U_\mu^\dagger(n + \hat{\nu}) U_\nu^\dagger(n), \tag{3.9}$$

where b denotes the inverse of the bare 't Hooft coupling, $b = 1/\lambda_0$, and $Z_{\mu\nu}(n) = 1$ everywhere except for the plaquette in the corner of the 01 plane, for which $Z_{01}(n) = Z_{10}^*(n) = \exp(2\pi i/3)$.

Naturally, the Wilson action is not the only possible discretisation, as any other choice would also be valid provided they share the same continuum $a \to 0$ limit. Nevertheless, in the scope of this work no improved actions will be considered.

Next, we need to consider the discretisation of the flow equations. We introduce a flow time parameter t, and define a flow-time dependent variable $V_\mu(n, t)$ such that $V_\mu(n, t = 0) = U_\mu(n)$, which replaces the links in the Wilson action:

$$S_W(V, t) = bN \sum_n \sum_{\mu\nu} \text{Tr } [1 - Z_{\mu\nu}(n) P_{\mu\nu}(n, t)], \tag{3.10}$$

$$P_{\mu\nu}(n, t) = V_\mu(n, t) V_\nu(n + \hat{\mu}, t) V_\mu^\dagger(n + \hat{\nu}, t) V_\nu^\dagger(n, t). \tag{3.11}$$

We must then provide a flow equation from which to take the gradient to smear the flowed links, for which we once more chose the simplest option: to use the same Wilson action, in what is known in the literature as the Wilson flow:

$$\partial_t V_\mu(n,t) = -\frac{\lambda_0}{N} T^a \partial^a_{n,\mu} S_W(V,t) V_\mu(n,t), \tag{3.12}$$

where T^a denotes the generators, and $\partial^a_{n,\mu}$ is the Lie-algebra valued derivative:

$$\partial^a_{n,\mu}(f(U_\mu(n)) = \frac{d}{d\epsilon}\left[f(e^\epsilon T^a U_\mu(x))\right]_{\epsilon=0}. \tag{3.13}$$

We will in our simulations integrate this equation numerically, using the third order Runge-Kutta scheme with adaptive step size described in the appendix of ref. [120].

Lastly, we need to provide a lattice definition of the coupling. The definition will formally be identical to the continuum one:

$$\lambda_{TGF}(\tilde{l}) = \frac{1}{N}\mathcal{F}(c)\left\langle t^2 E(t)\right\rangle\Big|_{t=\frac{1}{8}c^2\tilde{l}^2}, \tag{3.14}$$

except for the fact that both the energy density $E(t)$ through which we define the observable and the normalisation factor $\mathcal{F}(c)$ will be discrete, defined on the lattice in terms of the $V_\mu(n,t)$ links.

Two different discretisations for this observable are common in the literature. They are known as the plaquette and clover (or symmetric) definitions of the energy density, and are respectively given by:

$$E_P(t) = \text{Tr}\,[1 - Z_{\mu\nu}(n) P_{\mu\nu}(n,t)], \tag{3.15}$$

$$E_C(t) = \frac{1}{2}\text{Tr}\,[\hat{G}_{\mu\nu}(n,t)\hat{G}_{\mu\nu}(n,t)], \tag{3.16}$$

where we defined, denoting $V_{-\mu}(n,t) = V^\dagger_\mu(n-\hat{\mu},t)$ and abbreviating "complex conjugate" to "c.c.":

$$\begin{aligned}\hat{G}_{\mu\nu}(n,t) = -\frac{i}{8}\{&Z_{\mu\nu}(n)P_{\mu\nu}(n,t) + Z_{\mu\nu}(n-\hat{\nu})P_{-\nu\mu}(n,t)\\ &+ Z_{\mu\nu}(n-\hat{\mu})P_{\nu-\mu}(n,t) + Z_{\mu\nu}(n-\hat{\mu}-\hat{\nu})P_{-\mu-\nu}(n,t) - c.c.\}.\end{aligned} \tag{3.17}$$

It will be quite convenient, in order to obtain an estimation of the magnitude of lattice artefacts, to compute the coupling using both discretisations. The choice

of c in eq. (3.14), as we will show in the next section, will also have significant effects on the relative contribution of the artefacts, with a certain range of values suppressing them rather effectively.

The use of the $\mathcal{F}(c)$ factor in (3.14) also responds to a (rather succesful) attempt to suppress lattice artefacts. As we recall, in the continuum this was simply the factor multiplying the leading order term in the perturbative expansion of the running coupling, and was given in (2.112) by:

$$\mathcal{E}^{(0)}(t) = \frac{(d-1)\mathcal{A}(2\hat{c}t')}{2(8\pi t)^{d/2}}. \tag{3.18}$$

Using the continuum value of $\mathcal{F}(c)$ in the lattice computation, however, is rather inconvenient, as $\mathcal{O}(\lambda_0)$ effects making the effect of artefacts significant are guaranteed to appear[2].

Instead, we will define $\mathcal{F}(c)$ in such a way that $\lambda_{TGF} = \lambda_0 + \mathcal{O}(\lambda_0^2)$ on the lattice, eliminating the coefficient of the leading term of the running coupling expansion in lattice perturbation theory and thereby reducing the artefacts.

We thus need to perform the expansion of the TGF coupling in our scheme up to leading order in perturbation theory. The expansion of the gauge links is given by:

$$V_\mu(n,t) = e^{i\sqrt{\lambda_0/N}B_\mu(n+\frac{\hat{\mu}}{2},t)}, \tag{3.19}$$

everywhere except for the extreme points $n = L_\mu - 1$ in the $\mu = 0, 1$ directions, in which the expansion picks up a twist-eater from the boundary conditions:

$$V_\mu(n,t) = e^{i\sqrt{\lambda_0/N}B_\mu(n+\frac{\hat{\mu}}{2},t)}\Gamma_\mu. \tag{3.20}$$

We then need to solve the lattice flow equations at leading order. Much like in the continuum, adding an extra gauge term to the equation simplifies the computation significantly, without affecting gauge-invariant observables such as the energy density that we use to define the coupling. We will spare the reader the details of the computation, which can be found for instance in refs. [121] and [93], and simply show the resulting gradient flow equation at leading order:

$$\partial_t B_\mu(n,t) = \nabla_\mu^- \nabla_\nu^+ B_\mu(n,t), \tag{3.21}$$

[2]See for instance ref. [93] for a comparison of the artefacts using the continuum and lattice normalisation factors, or refs. [122] and [133].

where $\nabla_\mu^\pm$ denotes the lattice forward and backward derivatives:

$$\nabla_\mu^+ f(n) = f(n+\hat{\mu}) - f(n), \tag{3.22}$$

$$\nabla_\mu^- f(n) = f(n) - f(n-\hat{\mu}). \tag{3.23}$$

The solution to this equation is then obtained expanding the fields in momentum space in a manner akin to what we did in section 2.2, which yields:

$$B_\mu(n,t) = L^{-d/2} \sum_q{}' e^{-\hat{q}^2 t} e^{iq(n+\frac{\hat{\mu}}{2})} A_\mu(q) \hat{\Gamma}(q), \tag{3.24}$$

with lattice momentum $\hat{q}_\mu = 2\sin(q_\mu/2)$, with q_μ quantised in units of $2\pi/\tilde{L}$, and with the prime in the sum denoting the usual exclusion of momenta proportional to l_g in the twisted directions.

Then, one plugs this expansion into the definition of the observable, truncates all terms beyond $\mathcal{O}(\lambda_0)$, sets $t = c^2\tilde{L}^2/8$, and obtains the leading order term of the coupling, from which the normalisation factor can be extracted for both the plaquette and clover definitions. Doing so leads to:

$$1/\mathcal{F}_P(c) = \frac{3c^4}{128} \sum_q{}' e^{-\frac{1}{4}c^2\tilde{L}^2\hat{q}^2}, \tag{3.25}$$

$$1/\mathcal{F}_C(c) = \frac{c^4}{128} \sum_q{}' \sum_{\mu\neq\nu} e^{-\frac{1}{4}c^2\tilde{L}^2\hat{q}^2} \frac{1}{\hat{q}^2} \sin^2(q_\nu)\cos^2(q_\mu/2). \tag{3.26}$$

The use of these lattice normalisation factors removes cutoff effects at leading order, and as such significantly improves scaling when taking the continuum limit, as we will see in our simulations in the next section. Do notice that, while these expressions are formally identical to the ones from ref. [93], the choice to use a twist in a single plane rather than a symmetric one changes which modes are excluded by the prime, as well as the quantisation of momentum.

There is one additional small detail related to the effects of topological charge in the numerical computation, but we will leave the specifics for sec. 3.3, after the numerical results have been presented and can be used to describe the issue and justify the solution.

Thus, with this, the lattice scheme is fully set up, and we can focus in what follows on providing a brief introduction to step scaling techniques, and on de-

scribing how we use them to compute the running coupling.

3.2.3 Step scaling

The running coupling on the lattice was computed using step scaling, a rather popular finite size scaling method introduced in ref. [30]. The main idea behind the method is to compute a "step scaling function" $\sigma(u, s)$ describing the behaviour of the coupling u when one changes the size of the finite box by a factor s, which acts as a discrete version of the beta function. Iterating the procedure n times, one covers a range $L \to s^n L$, which if taken far enough allows one to make contact with physical scales or with perturbation theory.

The idea, thus, is to define the continuum step scaling function $\sigma(u, s)$, along with a corresponding discrete lattice step scaling function $\Sigma(u, s, \tilde{L})$:

$$\sigma(u, s) = \lambda_{TGF}(s\tilde{l})\Big|_{u=\lambda_{TGF}(\tilde{l})}, \tag{3.27}$$

$$\Sigma(u, s, \tilde{L}) = \lambda_{TGF}(s\tilde{l}, b)\Big|_{u=\lambda_{TGF}(\tilde{l},b)}. \tag{3.28}$$

Both quantities are related in the continuum limit through:

$$\sigma(u, s) = \lim_{\tilde{L}\to\infty} \Sigma(u, s, \tilde{L}). \tag{3.29}$$

This technique was used in ref. [93] to compute the $SU(\infty)$ running coupling in a scheme related to ours, using the gradient flow to define a twisted 't Hooft running coupling in terms of a similar effective box size, only defined on a symmetric torus and using the symmetric $d_t = 4$ twist, thus having an effective length $\tilde{l} = l\sqrt{N}$. Moreover, the idea of volume independence was taken to the extreme, using a single-point lattice $l = a$ and having the rank N of the gauge group play the role of the scale for the step scaling procedure, instead of the physical size of the box.

This will not be the case in what follows, as we will proceed in a more standard way, changing $\tilde{l} = a\tilde{L} = aLN$ by rescaling $\tilde{L}$ while keeping N constant. In what follows, only a broad description of the general procedure used to compute the running coupling will be given, leaving the specific details of our simulations, of the obtained results and of their analysis for sections 3.3 and 3.4.

Our aim will thus be to obtain $\Sigma(u, s, \tilde{L})$ from the results of our simulations, and extrapolate $\sigma(u, s)$ from them by taking the continuum limit, which will correspond to the large $\tilde{L}$ limit. The number s, i.e. the scale factor by which

the size of the lattice is multiplied on each step, will in our case be taken to be $s = 2$, meaning that we will be working with pairs of lattices of sizes $[L^2 \times \tilde{L}^2$, $(2L)^2 \times (2\tilde{L})^2]$ for each step.

Thus, we need to run our Monte Carlo simulation many times, with each simulation being characterised by its lattice size $\tilde{L}$ and its bare coupling b. Two methods to obtain the step scaling function are then available to proceed.

The more precise way would be to run simulations for several values of b and $\tilde{L}$, and tune b so that the same value of λ_{TGF} is obtained in all of them. Then, one would run the same simulations for the double lattices at the same value of b, which would yield a set of values of the discrete step scaling function that could be extrapolated to the continuum, as the value of u (which is simply the value of λ_{TGF} in the original lattice) would be tuned to be identical. This approach, however, is rather expensive from a computational standpoint, as the need to tune b every time is quite time-consuming, particularly when one wishes to obtain the running coupling over a large range in scales, iterating the step-scaling procedure many times.

Instead, we opted for the more pragmatical approach used in ref. [93]: rather than tune b every time to obtain the same coupling u in the original lattice, we find it much more convenient to run, for every lattice size $\tilde{L}$, a series of simulations for a range of values in b. We then run the simulations for the corresponding $2\tilde{L}$ double lattices, at the same values of b, and compute the lattice step scaling function, given as a function of u. We thus obtain a series of values of $\Sigma(u, s, \tilde{L})$, from which we can interpolate the value of the lattice step scaling function at any value of u, making the computation of the continuum limit $\tilde{L} \to \infty$ to extract the continuum step scaling function $\sigma(u, s)$, and by extension the running coupling, much easier, and computationally cheaper.

Let us show the full procedure step by step, in order to be as clear as possible. We begin our computation by picking a set of pairs of lattices of effective sizes $[\tilde{L}, 2\tilde{L}]$ and a set of values of the bare coupling b, and then run Monte Carlo simulations to compute the coupling λ_{TGF} as a function of b for each lattice of the pairs, using the same set of values of b for both lattices. As we are also interested in studying the effects of c and of lattice artefacts, the coupling in each simulation is computed using both the plaquette and clover definitions of the observable, and for several values of the scheme constant c.

Then, for each pair of lattices we compute, at the same values of b, the step

scaling function $\Sigma(u, s, \tilde{L})$, which is obtained directly from λ_{TGF} in the double lattices. The resulting functions are, for each pair of lattices, fitted to a fourth order polynomial of the form:

$$\frac{1}{u}\Sigma(u, s, \tilde{L}) = 1 + a_0 u + a_1 u^2 + a_2 u^3 + a_3 u^4. \tag{3.30}$$

Incidentally, and even though it was not used in the step scaling computation, we found that the coupling in each lattice is very nicely fitted to a Padé-like Ansatz, as was the case in ref. [93]:

$$b\lambda_{TGF}(\tilde{L}, b) = \frac{a_0 + a_1 b + b^2}{a_2 + a_3 b + b^2}. \tag{3.31}$$

Going back to the Σ functions, we can then take the continuum limit using the interpolated values of $\Sigma(u, s, \tilde{L})$ for each value of $\tilde{L}$ through a linear fit of the form:

$$\frac{1}{u}\Sigma(u, s, \tilde{L}) = a_0 + a_1/\tilde{L}^2, \tag{3.32}$$

where $\sigma(u, s)$ corresponds directly to the fit parameter a_0.

Last but not least, the continuum step scaling function can be used to recursively compute the running coupling for a very wide range of scales. Indeed, starting from a given value u_0 of the running coupling, we can use our previous fits and interpolations to compute the coupling at the double lattice:

$$u_1 = \frac{\sigma(u, s)}{u}\Big|_{1,0} u_0, \tag{3.33}$$

where $\sigma(u, s)/u\Big|_{1,0}$ denotes the continuum step scaling function extrapolated from the u_0 data. This new coupling u_1 can then be used as input to obtain u_2 in the same manner for the quadruple lattice, then u_2 can be used to obtain u_3, and so on and so forth. Thus, iterating this procedure k times and starting from the coupling in the $\tilde{L}$ lattice, one ends up reaching the coupling in the $2^k\tilde{L}$ lattice, given by:

$$u_k = \frac{\sigma(u, s)}{u}\Big|_{k,k-1} \frac{\sigma(u, s)}{u}\Big|_{k-1,k-2} \dots \frac{\sigma(u, s)}{u}\Big|_{1,0} u_0. \tag{3.34}$$

With this, the full lattice scheme used to compute the coupling has been presented, leaving us ready to take a look at our actual simulations and results in the next section.

3.3 Lattice simulations

Now that the procedure to compute the running coupling has been fully presented, we will in this section describe how the lattice simulations were carried out. As we hinted in the previous section, some issues related to the topological charge of the configurations arise, which motivated us to perform a brief analysis of the behaviour of topological charge depending on the simulation parameters.

3.3.1 Numerical setup

In order to perform the lattice simulations to obtain the running coupling, we used a code built by A. Ramos to simulate the $SU(N)$ TGF lattice coupling in a slightly different scheme, which was easily adapted to implement our definition of the coupling. We will therefore, as the code itself is not an original part of this work, simply give a quick overview of the way the algorithm is set up and report the relevant input parameters and details used in our simulation, leaving the presentation and analysis of the results for sec. 3.4.

The general algorithm used to generate successive gauge configurations from which to compute the observable is based on the hybrid overrelaxation model suggested in ref. [134]. The idea is to generate the configurations by performing succesive Monte Carlo sweeps, each consisting of a combination of a single heat-bath step (HB) and a number of overrelaxation ones (OR), in such a way that autocorrelations between configurations become negligible in the computation of the measured coupling. Several such sweeps are repeated before integrating the flow equations to measure the coupling, as performing the corresponding numerical integration is significantly more time-consuming than the Monte Carlo updates.

In particular, for our simulations we chose to do $\tilde{L}$ overrelaxations per heat-bath in every sweep and to integrate the flow equations up to $t = c^2\tilde{L}^2/8$ every $\tilde{L}$ sweeps, using an integrator that was small enough to ensure that the numerical errors arising from the integration were well below the statistical uncertainty.[3]

In total, we simulated five $L^2 \times \tilde{L}^2$ twisted $SU(3)$ lattices with $k = 1$, for $\tilde{L} = 12, 18, 24, 36, 48$, and for twenty-one values of the bare coupling b ranging

[3] As indicated in ref. [121], the same integrator mentioned in appendix D in ref. [120] was used, with the error tolerance parameters set up in such a way that integration errors are below 10^{-6}. As an additional check, we tried repeating several of the runs with smaller error tolerances and found no significant difference in the coupling results.

from $b = 0.33$ to $b = 0.83$.[4] For every lattice size, a simulation was run with each value of b, in which the coupling was measured for values of c ranging from 0.1 to 0.8 in increments of 0.05.

β	$\tilde{L} = 12$	$\tilde{L} = 18$	$\tilde{L} = 24$	$\tilde{L} = 36$	$\tilde{L} = 48$
6.0	7517(2483)	20248(30694)	3920(13062)	1070(8702)	120(1876)
6.2	9569(431)	36970(15606)	7869(10087)	1120(4159)	220(1713)
6.4	9961(39)	49359(3417)	13050(5356)	3899(6983)	458(1541)
6.6	10000(0)	52807(300)	16713(1287)	6476(4482)	759(1537)
6.8	10000(0)	51840(67)	17807(193)	9593(1616)	1316(989)
7.0	10000(0)	53238(0)	16439(0)	10971(0)	2155(150)
7.2	10000(0)	50544(0)	18000(0)	10974(0)	2307(0)
7.4	10000(0)	53406(0)	16763(0)	10981(0)	2319(0)
7.6	10000(0)	53605(0)	17760(0)	9999(0)	2308(0)
7.8	10000(0)	53560(0)	17501(0)	8979(0)	2319(0)
8.0	10000(0)	53602(0)	18000(0)	9720(0)	2328(0)
8.5	10000(0)	53825(0)	17000(0)	8990(0)	2324(0)
9.0	10000(0)	53654(0)	18000(0)	9000(0)	2333(0)
9.5	10000(0)	54178(0)	16483(0)	7998(0)	1966(0)
10.0	10000(0)	53889(0)	18000(0)	8991(0)	2042(0)
10.5	10000(0)	53415(0)	17000(0)	7990(0)	2043(0)
11.0	10000(0)	53679(0)	8640(0)	7922(0)	1738(0)
12.0	10000(0)	10000(0)	16442(0)	4000(0)	803(0)
13.0	10000(0)	10000(0)	16513(0)	3973(0)	805(0)
14.0	10000(0)	10000(0)	16340(225)	3457(0)	807(0)
15.0	10000(0)	10000(0)	16602(0)	3334(0)	808(0)

Table 3.1: We show the number of generated $Q_t = 0$ configurations in the case of $c = 0.3$. The numbers in the parenthesis denote the number of discarded $Q_t \neq 0$ configurations. The results in terms of the bare coupling b can be easily derived from the fact that $b = \beta/18$.

As we will see in the next section, we confirmed the known result[5] that values of c around $c = 0.3$ constitute a good middle ground that avoids both the large lattice artefacts that appear at low values of c and the large statistical errors that show up at larger values of c, and, as such, chose to use $c = 0.3$ for the step scaling computation of the running coupling. The number of simulated independent configurations for every value of b and $\tilde{L}$ can be found in table 3.1

[4]The full range of simulated values for b can be found in table 3.1, though as we are working with $SU(N = 3)$ we found it more convenient to present the results in terms of β. The corresponding values of b are given by $b = \beta/2N^2$.

[5]See refs. [120] and [121] for more details.

for the case of $c = 0.3$, while the tables for $c = 0.1$ and $c = 0.7$ can be found in appendix B.1.

Moreover, we chose to start the simulations from a zero-action configuration, followed by 2000 thermalisation sweeps without any flow measurements, and then began the aforementioned procedure of alternating $\tilde{L}$ Monte Carlo sweeps (each with the corresponding HB-OR combination) with gradient flow measurements. This choice of this zero-action start is due, as we hinted in the previous section, to the fact that some complications related to topological freezing arise in a portion of our runs, which we will study in more detail in what follows.

3.3.2 Topological effects

The topological issues in our simulations stem from the combination of two well-known effects that depend simultaneously on the physical volume of the lattice and on the value of the bare coupling b, and which are related to both the actual dynamics of the system and to the evolution of the generated configurations in Monte Carlo time.

The first effect is a finite volume one, related to the physical volume of the torus, and has nothing to do with the lattice discretisation. Indeed, when the physical volume of the torus is small enough, topological charge is suppressed, and as such generated configurations will tend to remain, as Monte Carlo time goes by, in the $Q_t = 0$ topological sector. As we venture into intermediate volumes, semiclassical instanton-like configurations may begin to appear, but configurations in the $Q_t = 0$ remain dominant, while for large lattice volumes configurations belonging to larger Q_t sectors become likely.[6].

The second issue is a direct effect of the lattice discretisation of the theory: as the lattice approaches the continuum and the spacing a becomes smaller, topological sectors grow disjoint, and the Monte Carlo algorithm generating the configurations freezes into a single sector, even if the dynamics of the system make configurations of different Q_t very likely. This is the well-known problem of topological freezing, which occurs for larger values of b, famously corresponding, in physical units, to the area around $a = 0.05\text{fm}$[7].

[6]This is an oversimplification, as the dependence of the distribution of topological charge with the lattice volume is complicated. Nevertheless, for very large volumes, the topological susceptibility remains approximately constant, which forces $< Q_t^2 >$ to grow with the volume of the box.

[7]See for instance refs. [125, 135–137].

The combination of both factors leads to three different possible situations, depending on b and $\tilde{L}$:

- A situation where all configurations are stuck in the $Q_t = 0$ sector, remaining there as Monte Carlo time advances.
- A situation where the configurations freely jump between all Q_t sectors, covering all of them in the proportion given by their relative weight in the action.
- An intermediate situation in which configurations tend to stall, staying in a topological sector for a very long time before jumping to a different one. This is a situation in which the Monte Carlo is not completely frozen, yet is cold enough for jumps between sectors to occur rather rarely in Monte Carlo time.

Some of these situations can be quite problematic, particularly in the nearly frozen or fully frozen cases: when the configuration is nearly frozen, the observable remains stuck in a given topological sector for a very long time before jumping to the next one, making the dispersion in the measurement so large as if we effectively had a handful of independent measurements. Or, in the case of being fully frozen in a single sector, giving a different expectation value of the observable than the one that would arise if all topological sectors were covered in the proportion given by their corresponding action.

This can be seen quite clearly in the example shown in fig. 3.1, in which we display the initial evolution of λ_{TGF} and of the topological charge in the case of $\tilde{L} = 24$, $\beta = 7.5$, $c = 0.3$, for several initial values of the action corresponding to $Q_t = -1, 0, 1$: as we can see, each configuration is frozen in the initial topological sector, and each sector yields a very different value of the coupling. This is the case even in non-frozen cases, as shown in the case of $\tilde{L} = 24$, $\beta = 6.8$, $c = 0.3$. The plot also illustrates how the difference in the coupling measured in each topological sector is more dramatic, compared to the fluctuations in each sector, at higher values of β.

While this issue should plague any observable in one way or another, the effects are particularly visible in our computations, as the energy density observable used to compute the coupling is extremely sensitive to the topology of the configuration.

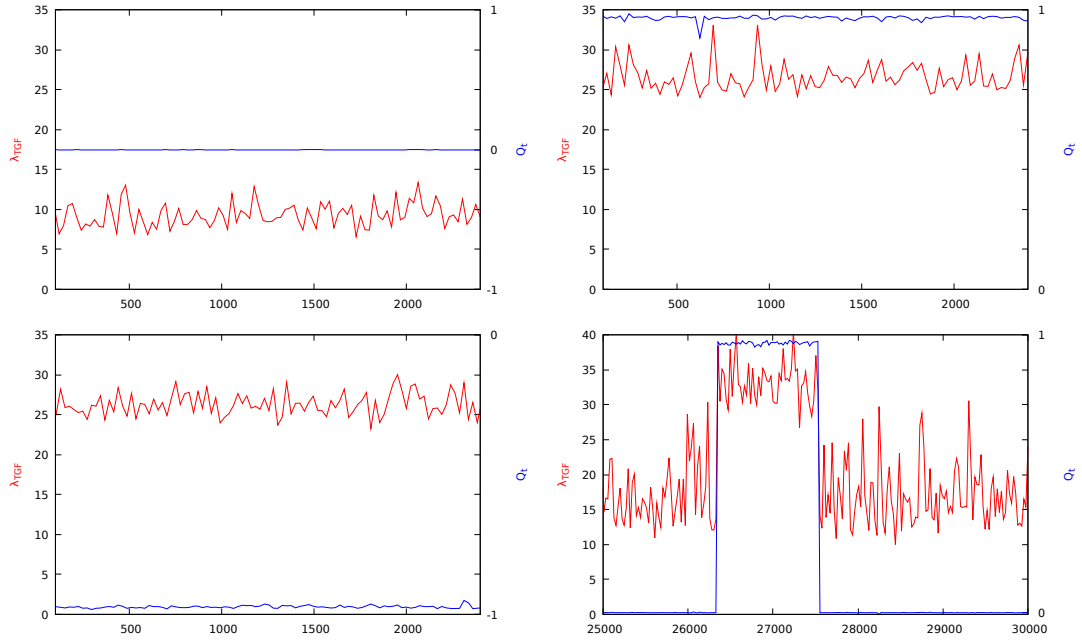

Figure 3.1: We show an example of the effect of topology and freezing in the Monte Carlo evolution of the topological charge (in blue) and the coupling λ_{TGF} (in red), on the $\tilde{L} = 24$ lattice with $c = 0.3$. The first three plots (from left to right and top to bottom) display the coupling and topological charge as a function of the succesive Monte Carlo sweeps, with $\beta = 7.5$ (i.e. $\tilde{l} = a\tilde{L} = 0.34$ fm), for three different configurations of respective initial topological charge $Q_t = 0, -1, 1$. As we can see, the configurations are frozen in the initial topological sector, and yield a very different value of the coupling, though sectors with opposite topological charge still lead to the same coupling. The fourth plot shows what happens in the case of $\beta = 6.8$ (i.e. $\tilde{l} = 0.7$ fm): the configuration is not frozen in a single sector, but the effect on the coupling is still present, with each topological sector leading to a different coupling. Differences in λ_{TGF} between sectors, however, are far less dramatic compared to the fluctuations within a single level.

There are two ways out of such an impasse. The first method is to do as in ref. [114] and use brute force, running the simulations for so long that, despite jumping extremely slowly between sectors, one ends up covering every topological sector in the correct, action-determined proportion, and can work with the results. This amounts to treating each plateau in the Monte Carlo evolution of the topological charge, such as the ones displayed in the last plot of 3.1, as an individual measurement, letting the simulation run for a time long enough to obtain sufficient statistics.

The alternative, on the other hand, is to adopt the approach chosen by the Alpha collaboration, which is the one used in ref. [121] and the one that we

will follow along this work. The idea, introduced in ref. [137], is to change the definition of the scheme, and discard, as a part of the prescription, every single measurement for which the topological charge does not vanish:

$$\lambda_{TGF}(\tilde{l}) = \frac{1}{N}\mathcal{F}(c)\frac{\langle t^2 E(t)\delta_{Q_t,0}\rangle}{\langle \delta_{Q_t,0}\rangle}\bigg|_{t=\frac{1}{8}c^2\tilde{l}^2}, \tag{3.35}$$

where the $\delta_{Q_t,0}$ factor projects over the zero charge sector.

In practice, as the topological charge will never be exactly zero on the lattice, we will define a tolerance threshold ϵ, replacing the delta function with a product of Heaviside functions:

$$\delta_{Q_t,0} \to \theta(Q_t + \epsilon)\theta(Q_t - \epsilon), \tag{3.36}$$

so that every configuration with $|Q_t| > \epsilon$ is rejected. In particular, using $\epsilon = 0.5$ does the job well. Of course, this comes at the price of making the simulations more expensive, since a portion of the generated configurations needs to be thrown away, but the cost still tends to be lower than running the simulation for a long enough time to cover every topological sector.

Interestingly, and as we can see in table 3.1, the simulations are stuck[8] in the $Q_t = 0$ sector for most of our runs: configurations with nonzero topological charge seem to almost only appear for configurations with $\beta \leq 7$, where $b = \beta/18$. Using the formula derived in [114] and denoting b_0, b_1 the universal coefficients of the beta function:

$$a(\beta) = r_0(b_0\beta)^{-b_1/2b_0^2}e^{-1/2b_0\beta}(23977 - 106580\beta + 178094\beta^2 - 132318\beta^3 + 36906\beta^4) \tag{3.37}$$

with $r_0 = 0.5$ fm, we find that $a(\beta = 7) = 0.02$ fm, whereas the critical value $a = 0.05$ fm which tends to characterise critical slowdowns corresponds to $\beta = 6.41$.

As such, what we see in table 3.1 should be the consequence of our choice to use a "cold", zero-action start: as simulations with a large enough b are topologically frozen, starting from a zero action configuration means all following configurations will tend to remain in the $Q_t = 0$ sector. Strictly speaking, however, this is a

[8]Do note that, while the values in table 3.1 can be used to obtain a rough estimation of the topological behaviour of our simulations, they are not enough for a full analysis, as they only analyse the number of configurations with nonzero Q_t, rather than the number and frequency of jumps between topological sectors. The full analysis of such jumps would require further work, and is out of the scope of this thesis.

severe slowdown rather than a complete freezing: if the Monte Carlo simulation is left to run for a long enough time, configurations in other sectors may appear, as is the case, for instance, in the $\tilde{L} = 24$ lattice for $\beta = 14$ displayed in fig. 3.2, in which, after 12000 flow measurements (i.e. 288000 Monte Carlo sweeps), some 200 measurements (4800 configurations) with $Q_t = 1$ appear.

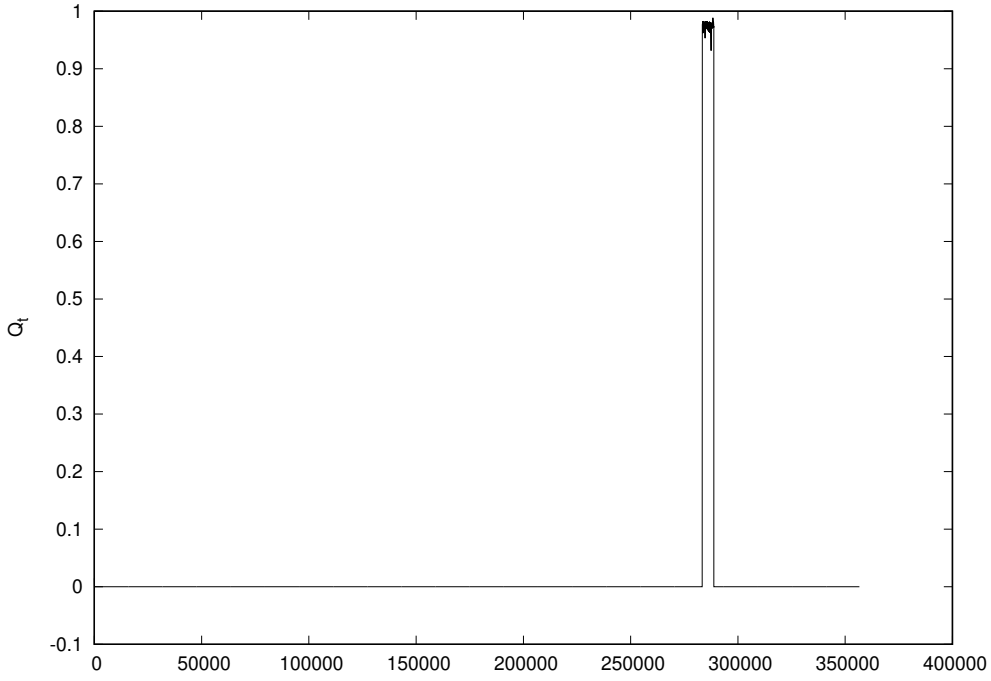

Figure 3.2: We show an example of how the topological charge in a seemingly frozen configuration can jump to a different Q_t sector if the Monte Carlo simulation runs for long enough. The plots display the topological charge on the $\tilde{L} = 24$ lattice with $\beta = 14$ and $c = 0.3$, as a function of the succesive Monte Carlo sweeps, shown in the x-axis. Note that the separation between every plotted point corresponds to $\tilde{L} = 24$ Monte Carlo sweeps.

For $\beta < 7$, on the other hand, we do see that configurations are generated in different topological sectors for some lattices, though the range of sectors reached and the frequency of the jumps depends on b and on $\tilde{L}$. We will be interested in studying the effect of the choice of the parameters b, $\tilde{L}$ and c is in the evolution of the topological charge, particularly to see whether our asymmetrical lattice model behaves in a similar manner to periodic $\tilde{L}^4$ models. The significant effects, as we mentioned earlier, will come in two sorts: physical effects due to changes in the effective volume, controlled by $\tilde{l}$, and freezing effects in the simulation related to the lattice discretisation.

Scheme constant effects

We begin by looking at the simplest dependence of the coupling: the one on the scheme parameter c. As its effect on the configurations is mainly related to the flow time up to which the fluctuations are smeared down, its influence on topological charge is minimal. As we can see in figure 3.3, for most situations its only effect is to reduce fluctuations, bringing the value of the topological charge, as c grows larger, closer to the nearest integer. In some fringe cases, though, c can have a minor efect over a few configurations, notably when the topological charge is halfway between two integer values, but the overall effect in our study of topological sectors is negligible.

Physical volume effects

The next step is to study the physical, finite volume effects, which are characterised by the physical length $\tilde{l} = \tilde{L}a(\beta)$ of the torus. As the physical size is controlled by the number of points of the lattice and the lattice spacing, we will explore these changes in two ways: by changing the number of points on the lattice $\tilde{L}$ at fixed β, and by modifying the lattice spacing a through β at fixed $\tilde{L}$.

Let us thus begin by modifying $\tilde{L}$ while keeping b, and thus the lattice spacing, constant. We display in figure 3.4 the evolution of the topological charge of the generated configurations in Monte Carlo time, at fixed $c = 0.3$ and $\beta = 6.4$, for $\tilde{L} = 12, 18, 24, 36$. As, using (3.37), the lattice spacing corresponds to $a = 0.05$ fm, the figures displayed correspond to physical volumes with $\tilde{l} = 0.6, 0.9, 1.2, 1.8$ fm, and we are therefore looking at a range of physical volumes going from a small volume region that can be described in semiclassical perturbation theory, to the large volume regime.

As we can see, in the smallest $\tilde{l} = 0.6$ fm case, the dynamics of the simulation make configurations with non-zero topological charge very unlikely, and as such all lattice configurations remain in the zero charge sector. However, as the size of the lattice grows, configurations increasingly jump into different topological sectors, with the number of topological sectors that are covered growing as well: the $\tilde{l} = 0.9$, $\tilde{l} = 1.2$ and $\tilde{l} = 1.8$ fm simulations respectively reach up to the $|Q_t| = 1$, $|Q_t| = 2$ and $|Q_t| = 4$ sectors.

Changing β at fixed $\tilde{L}$, on the other hand, has the opposite effect on the physical volume: as β increases, the lattice spacing shrinks, diminishing the physical volume. We display this in figure 3.5, in which we show the evolution of the

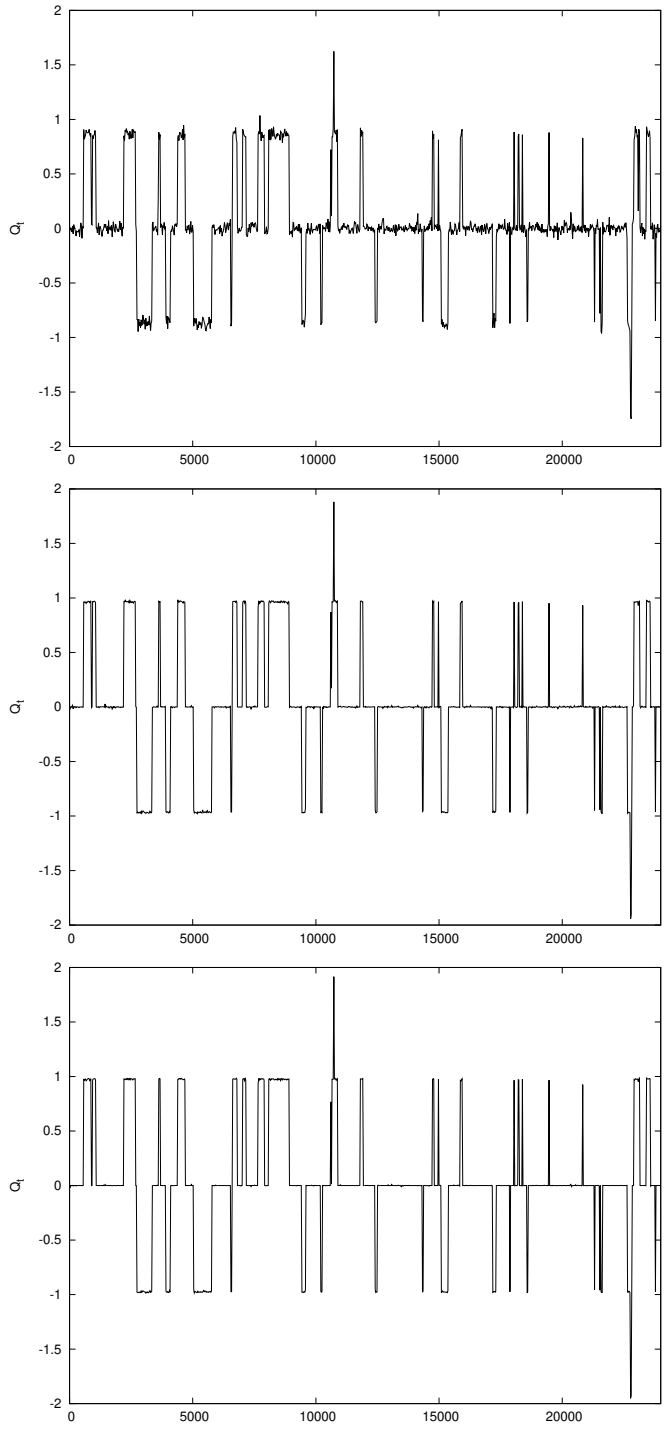

Figure 3.3: We show examples of the evolution of the topological charge as a function of Monte Carlo time, for $\beta = 6.4$ in the $\tilde{L} = 24$ lattice and for a thousand measurements within the simulation. From top to bottom, we display the evolution in the case of $c = 0.1$, $c = 0.3$ and $c = 0.7$. As we can see, the only noticeable effect as c increases is a reduction of the fluctuations around each integer value of the charge.

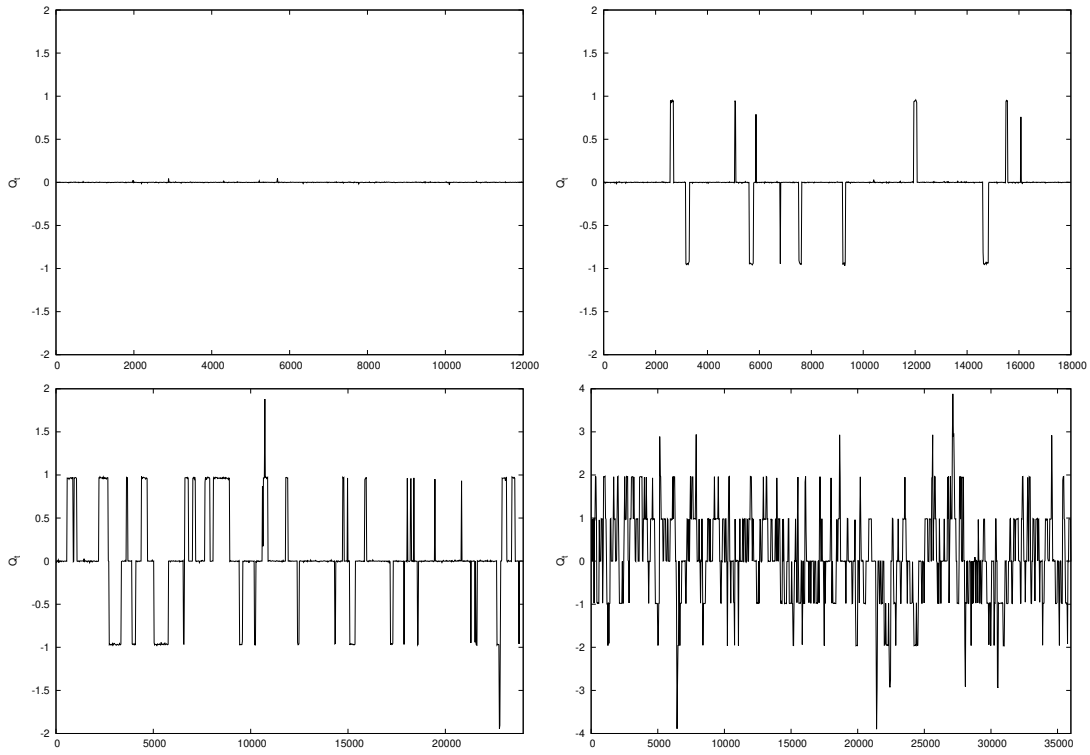

Figure 3.4: We show examples of the evolution of the topological charge in Monte Carlo time for a thousand measurements within the simulation, in the case of $c = 0.3$ and for fixed $\beta = 6.4$. From left to right and from top to bottom, we display the results corresponding to the $\tilde{L} = 12, 18, 24, 36$ lattices, corresponding to physical volumes with $\tilde{l} = 0.6, 0.9, 1.2, 1.8$ fm. The effect of physical volume is evident: for the larger volume, jumps between topological sectors occur often, reaching up to the $Q_t = 4$ sector, but as the volume shrinks jumps become scarcer and fewer topological sectors are reached.

topological charge in Monte Carlo time in the $\tilde{L} = 24$ lattice for $c = 0.3$ and several values of β corresponding to physical volumes with $\tilde{l} = 0.72, 0.96, 1.20, 1.68$ fm. As expected, the results are identical to what was obtained in figure 3.4: at larger volumes, one sees many jumps covering many topological sectors, yet as $\tilde{l}$ decreases the reach in Q_t sectors diminishes and fewer jumps are seen, to the point where at $\tilde{l} = 0.72$ all configurations belong to the $Q_t = 0$ sector.

We have thus found that, as expected, configurations with $Q_t = 0$ dominate the topology of the simulations at small physical volumes, with configurations of increasingly large Q_t becoming more likely as $\tilde{l}$ increases. A further, more detailed study of topological susceptibility would be very interesting, but is beyond the scope of this work.

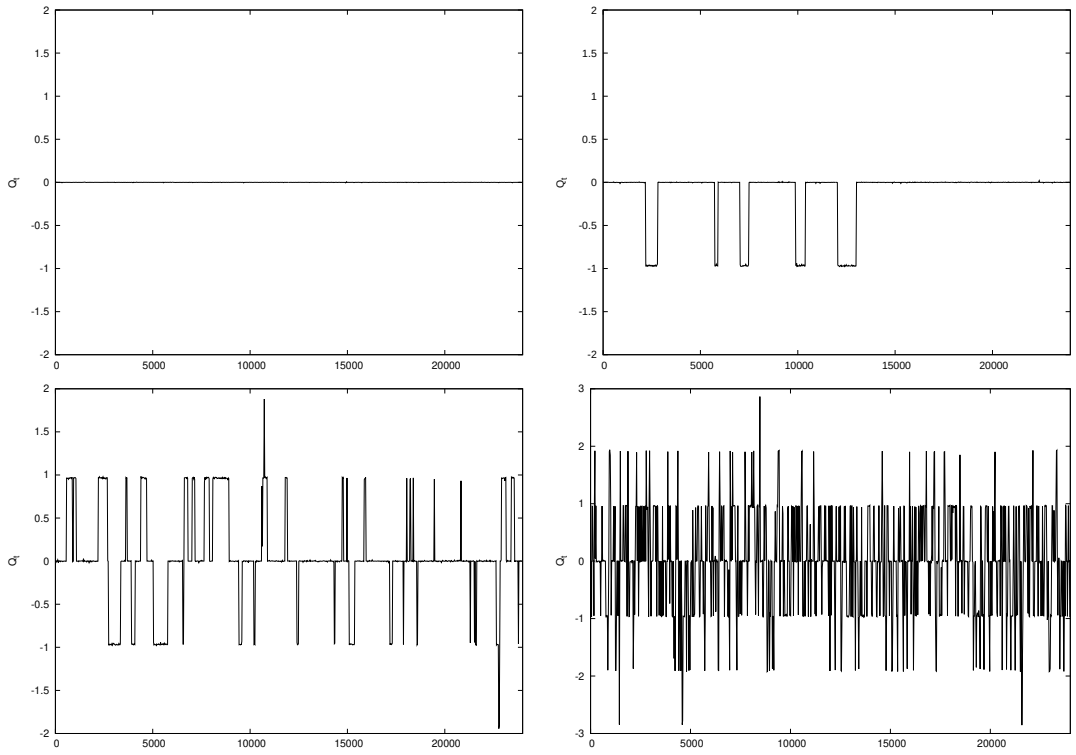

Figure 3.5: We show examples of the evolution of the topological charge in Monte Carlo time for a thousand measurements within the simulation, in the case of $c = 0.3$ and for fixed $\tilde{L} = 24$. From left to right and from top to bottom, we display the results corresponding to $\beta = 6.8, 6.6, 6.4, 6.2$, which respectively correspond to physical volumes with $\tilde{l} = 0.72, 0.96, 1.20, 1.68$ fm. The effect of physical volume is, as expected, identical to the one found in fig 3.4.

Discretisation effects

The next step in our analysis is then to study the effects of the lattice discretisation on our simulations, looking at the evolution of the topology as lattice spacing shrinks. We looked at five simulations of identical physical volume, shown in table 3.2, and which should lead to identical physics in the sense that they should yield a similar value of the λ_{TGF} coupling, which, as we can see in table 3.2, is actually the case[9]. Looking at figure 3.6, in which we display for the five cases shown in the table the evolution of the topological charge in Monte Carlo time for a thousand measurements, we see evidence of the appearance of a critical slowdown: despite all simulations corresponding to the same physical volume, as the lattice spacing decreases, jumps between sectors slow down significantly[10].

[9] See the next section for details of how the coupling is computed.

[10] Note that, looking at table 3.1, even the slower $\beta = 7$ case shown is not completely frozen.

β	$\tilde{L}$	a(fm)	$\tilde{l}$(fm)	λ_{TGF}
6.0	12	0.09	1.11	34.8(1)
6.2	18	0.07	1.22	39.4(1)
6.4	24	0.05	1.23	39.5(1)
6.8	36	0.03	1.10	31.8(1)
7.0	48	0.02	1.14	34.0(2)

Table 3.2: Simulation data for five setups of similar physical volume, using the clover definition for the observable and for $c = 0.3$.

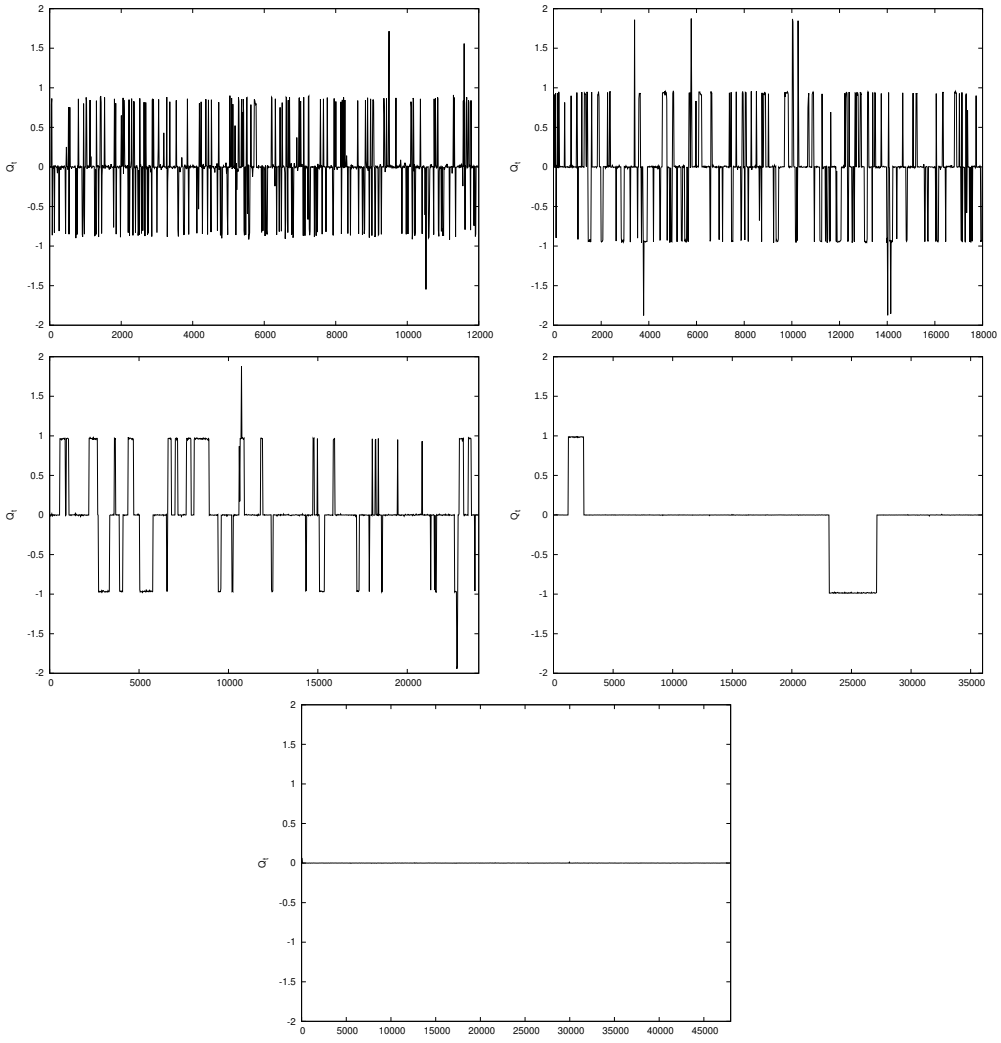

Figure 3.6: We display the evolution of topological charge in Monte Carlo time at $c = 0.3$ along a thousand measurements, for the five lattices of near identical physical volume $\tilde{l} \simeq 1.1 - 1.2$ fm from table 3.2, and shown from left to right and from top to bottom in order of decreasing lattice spacing. As the spacing shrinks, we see that the jumps grow scarcer and reach fewer topological sectors.

3.4 Step scaling results

After the topological considerations of the previous section, we are now finally ready to perform the step scaling procedure mentioned in section 3.2.3. We will in this section present the results that were obtained for the running coupling, along with some considerations regarding the effect of lattice artefacts and some interesting results concerning volume reduction in our model. For the sake of clarity and readability, almost all of the numerical values of the data used to obtain the results and plots of this section will be moved to appendices B.2-B.4.

3.4.1 λ_{TGF} on the lattice

The first step in the step scaling process is the extraction of the 't Hooft coupling λ_{TGF} from the simulated configurations, as a function of the bare coupling b and using both the clover and plaquette discretisations of the observable mentioned in eqs. (3.15) and (3.16), each with its corresponding normalisation factor from eqs. (3.25) and (3.26). This was done for five lattices of effective size $\tilde{L} = 12, 18, 24, 36, 48$, and for each of the values of c mentioned in previous sections, ranging from $c = 0.1$ to $c = 0.8$.

The coupling was found to display a Padé-like behaviour of the form shown in eq. (3.31), with the corresponding fits of the measured points yielding χ^2 per degree of freedom ranging, for $c = 0.3$, between 0.6 and 1.4, where only measures with $b\lambda_{TGF} < 9$ were used for the fits, as in other cases the value of λ_{TGF} was so high that many more simulations at intermediate values of b would have been necessary to properly interpolate the running coupling.

Examples of such fits are displayed in figures 3.7 and 3.8, in which we plot the measured λ_{TGF} coupling as a function of the bare coupling b, for every lattice that was simulated and using both discretisations of the observable.

The results are shown for the cases of $c = 0.1, 0.3, 0.7$, which respectively act as representative examples of the short, intermediate and long flow time behaviour of the coupling. Additionally, we show the next-to-leading-order contribution, given by by $1/\lambda_{TGF}(b) - b$, for the case of $c = 0.3$. The numerical data used to elaborate these plots can be found in appendix B.2.

Two interesting features immediately stand out in the plots. First and foremost, we see that our results present the same general Padé-like behaviour that is found in literature for other schemes, such as the fully twisted one in [93] for

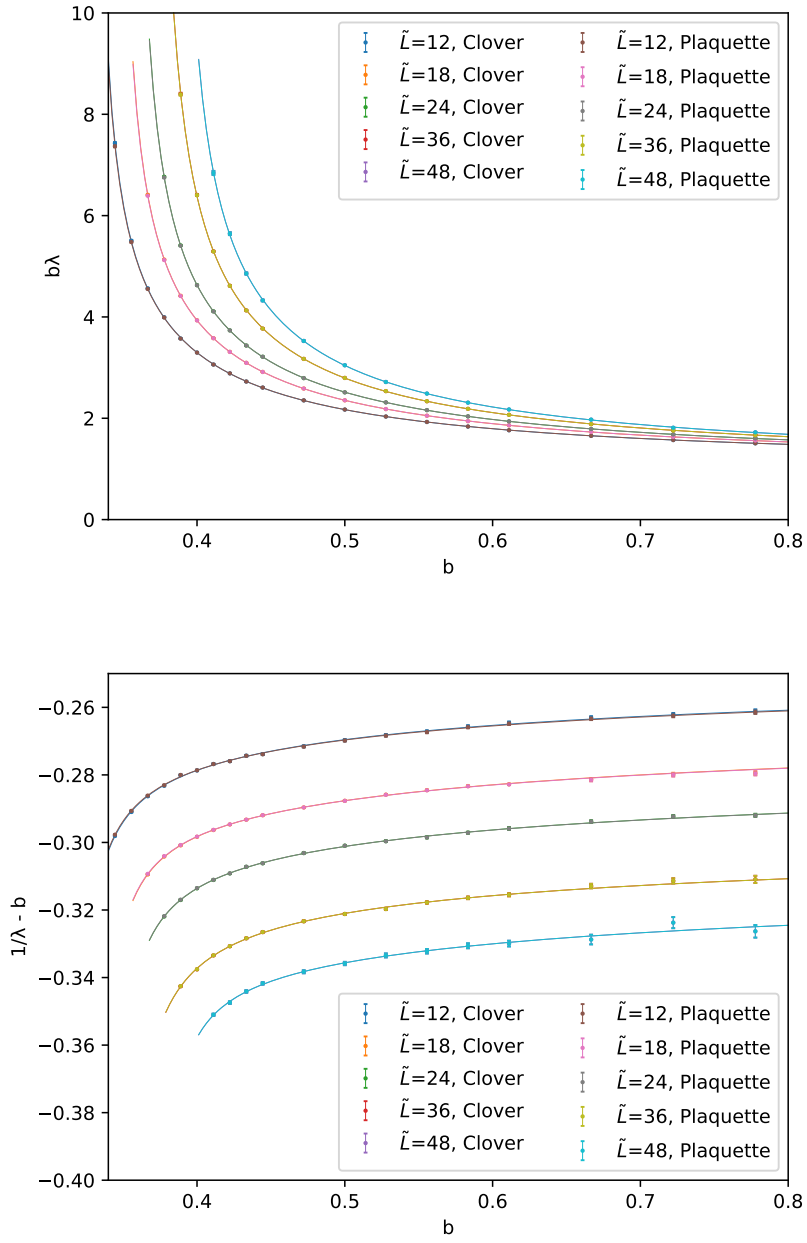

Figure 3.7: We display the 't Hooft coupling at $c = 0.3$ for both the clover and plaquette observables, along with the corresponding Padé fits, for every value of $\tilde{L}$, both for the full coupling (top) and for the NLO contribution (bottom). As we can see, in this region the curves are smooth enough for the interpolating method not bring any significant additional errors, though one must be careful in the steeper regions. Notice that both the clover and plaquette observables are shown, but overlap so much as to appear indistinguishable.

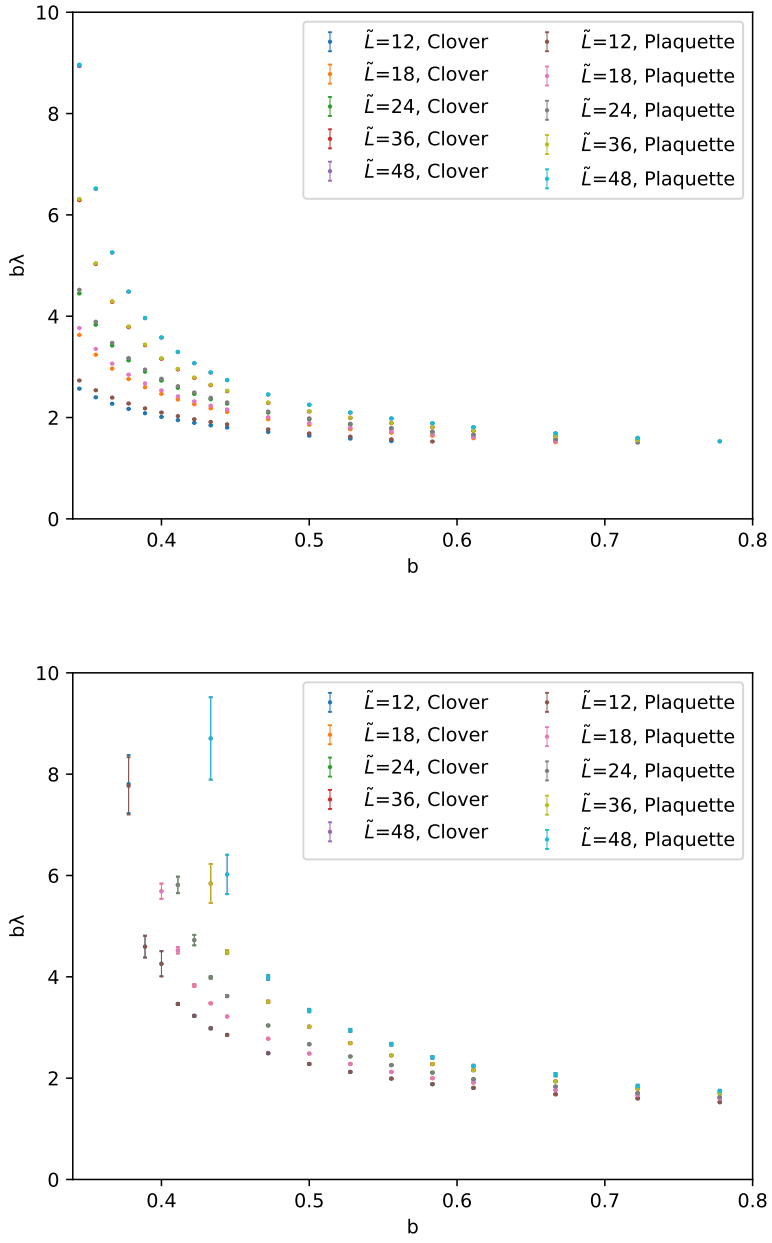

Figure 3.8: We display the 't Hooft coupling for both the clover and plaquette observables, along with the corresponding Padé fits, for every value of $\tilde{L}$, for the cases of $c = 0.1$ (top) and $c = 0.7$ (bottom). The plot illustrates how for short flow times artefacts are large, with the clover and plaquette observables being visibly different, whereas for longer flow times this effect disappears (to the point that they appear indistinguishable) at the price of increased statistical uncertainty.

the $SU(\infty)$ case in the one-point lattice, or the one in [121] for $SU(2)$ on a fully twisted finite lattice. Though these are different schemes, and as such the numerical values obtained are different, the similar behaviour of the coupling hints at $\tilde{l}$ being the parameter controlling the dynamics of the theory.

Second, we see that, while the behaviour of the coupling is quite steep at lower values of b, we can obtain good fits if we start from a point between $b = 0.37$ (for $\tilde{L} = 12$) and $b = 0.4$ (for $\tilde{L} = 48$).

The third feature that pops out is the effect of the flow in the measurement, characterised by c. We immediately notice that the effects of the flow are similar to what was observed in ref. [121]: for shorter flow times, given by smaller values of c, the effect of lattice artefacts is significant, and thus using different definitions of the observable leads to visible differences in λ_{TGF}. The split between the results for either observable, however, quickly shrinks as c grows, to the point where at $c = 0.3$ both definitions yield overlapping results, as seen in fig. 3.7. The price to pay for this, however, is quite apparent when looking the $c = 0.7$ plot in fig. 3.8: as c increases, the statistical uncertainty in the results grows as well[11].

Overall, we find that intermediate values of c are a good compromise, succesfully killing most lattice artefacts without losing control of the statistics. We will thus, in the rest of the step scaling computation, restrict ourselves to the case of $c = 0.3$, with any result in what follows being given for that value of the scheme parameter unless explicitly stated otherwise.

3.4.2 The discrete step scaling function

Let us thus, now that we have measured the value of λ_{TGF} from our configurations, compute the discrete step scaling functions. As the lattice spacing depends on the bare lattice coupling only, the step scaling function Σ can be obtained directly as the quotient of two λ_{TGF} couplings, measured at the same value of b in a lattice of size $\tilde{L}$ and one of size $2\tilde{L}$ respectively:

$$\frac{1}{u}\Sigma(u, s, \tilde{L}) = \frac{\lambda_{TGF}(2\tilde{L})}{\lambda_{TGF}(\tilde{L})}, \tag{3.38}$$

[11] This has a simple intuitive interpretation in terms of the gradient flow: as the flow has an averaging effect over a sphere of radius $\sqrt{8t}$, the number of effectively independent regions within the twisted box is reduced as t grows larger.

where u stands for the value of λ_{TGF} in the smaller lattice, and where we have taken $s = 2$.

Using the five simulated lattices mentioned in the earlier section, of effective sizes $\tilde{L} = 12, 18, 24, 36, 48$, we were able to compute the discrete step scaling functions for three pairs of lattices, labelled $\tilde{L} = 12, 18, 24$. We used the same set of values of b and c as in the previous section, with both the clover and the plaquette definitions of the observable.

The resulting $\Sigma(u)/u$ functions were then fitted, using only points in the $u < 9$ region[12] to polynomials of the form shown in eq. (3.30), yielding values of χ^2 per degree of freedom ranging between 0.75 for the $\tilde{L} = 24$ lattice to 1 for the $\tilde{L} = 12$ one.

Examples of such fits are displayed in figures 3.9 and 3.10, in which we plot the measured $\Sigma(u)/u$ discrete step scaling function as a function of the coupling in the smaller lattice b, for every pair of lattices that was simulated and using both discretisations of the observable.

The results are shown for the cases of $c = 0.1, 0.3, 0.7$, which respectively act as representative examples of the short, intermediate and long flow time behaviour of the function. In particular, in figure 3.9 we show the fits obtained for the three lattices, using both observables and setting $c = 0.3$, for both the full step scaling function and the NLO contribution, whereas in figure 3.10 we show the behaviour of the step scaling function for short and long flow times, corresponding to $c = 0.1$ and $c = 0.7$. Notice that, as all three lattices led to very similar results, for clarity we displaced the $\tilde{L} = 12$ and $\tilde{L} = 18$ curves upwards by 0.2 and 0.1 respectively in the full coupling plots, and by 0.30 and 0.15 respectively in the NLO one.

As the quantities displayed in these two plots are extracted from λ_{TGF}, we naturally see the same features mentioned in the previous section: the step scaling functions are of the same form found in literature in previous computations on symmetrical lattices, the function is smooth enough for the interpolations obtained from the fits not to be problematic, and $c = 0.3$ represents a good balance between reducing artefacts and keeping decent statistical uncertainty.

[12]The reason for this is the same as in the previous section: at larger values of u, λ_{TGF} becomes too steep to properly fit the simulated results. As such, to probe higher values of u additional simulations with more resolution in b would be required.

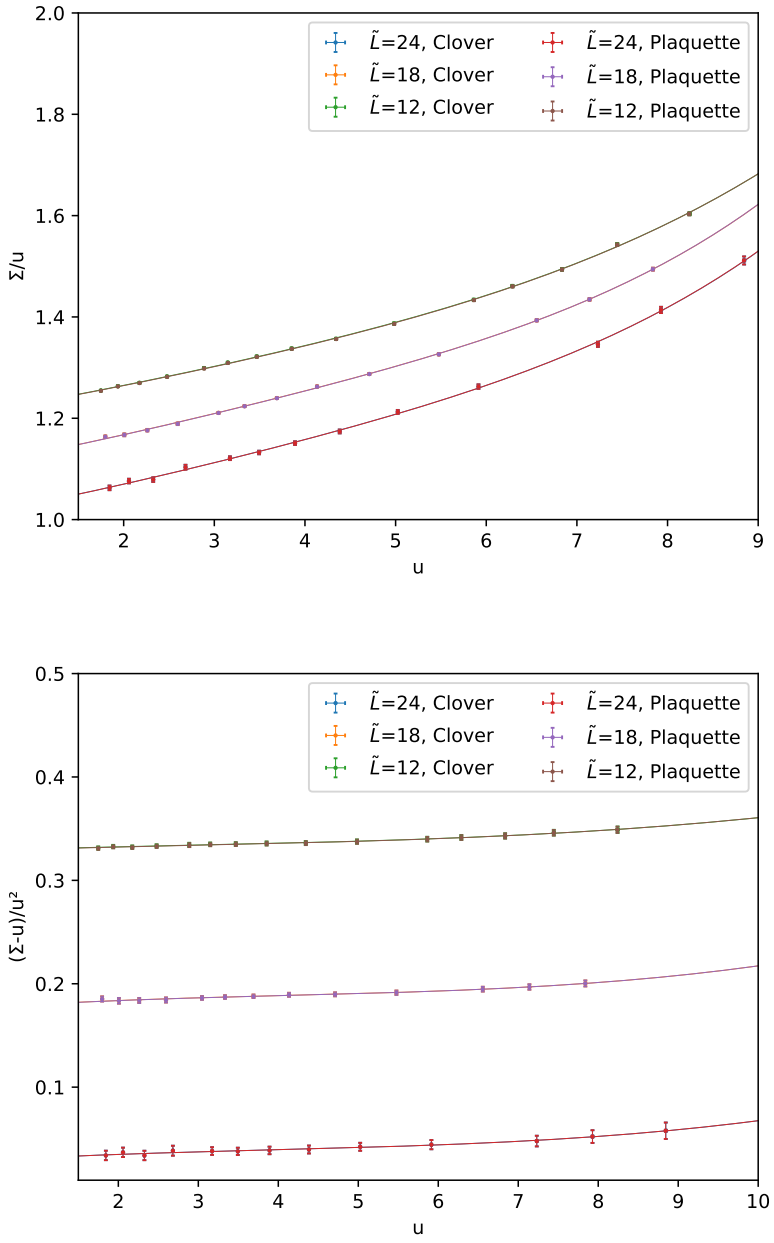

Figure 3.9: We display the lattice step scaling function Σ/u at $c = 0.3$, along with the corresponding polynomial fits, for every value of $\tilde{L}$, both for the full coupling (above) and for the NLO contribution (below). For the sake of visibility, the $\tilde{L} = 12$ and $\tilde{L} = 18$ have been displaced upwards by 0.2 and 0.1 respectively in the upper plot, and by 0.3 and 0.15 in the lower one. Notice that both the clover and plaquette observables are shown, but overlap so much as to appear indistinguishable.

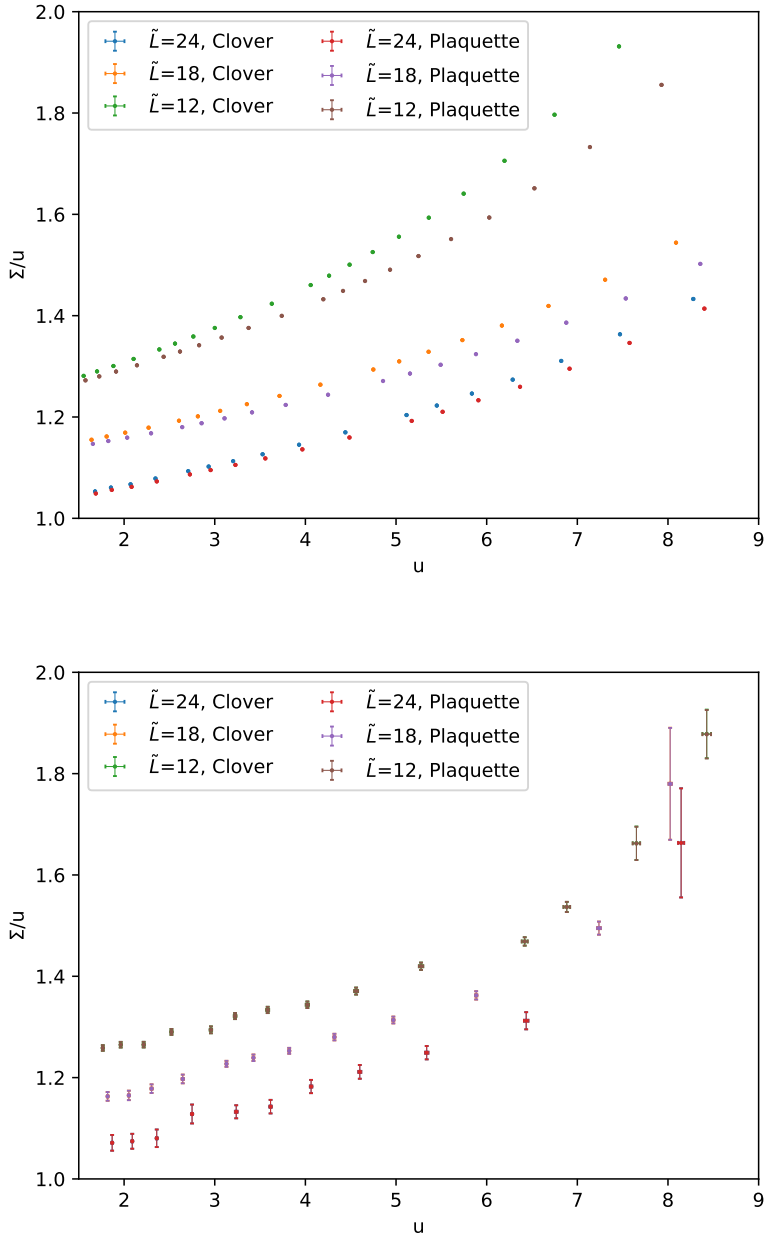

Figure 3.10: We display the discrete step scaling function, along with the corresponding polynomial fits, for every value of $\tilde{L}$, and for $c = 0.1$ (top) and $c = 0.7$ (bottom), and for both the clover and plaquette observables. The $\tilde{L} = 12$ and $\tilde{L} = 18$ cases have been displaced upwards by 0.2 and 0.1 respectively. As we can see, for short flow times, artefacts are large, with the clover and plaquette observables being visibly different, whereas for longer flow times this effect disappears (to the point that they appear indistinguishable), at the price of increased statistical uncertainty.

3.4.3 Continuum extrapolation and running coupling

The next step in the step scaling process is the extrapolation of the fitted discrete step scaling functions from the previous section to the continuum along the line of constant physics. This means that will keep u constant along the way, so that $\tilde{l} = \tilde{L}a$ remains fixed, and as such we will take the continuum limit by simply taking the large $\tilde{L}$ limit at fixed value of u.

The plan is thus to extrapolate the $\sigma(u)$ continuum step scaling functions by taking the $\tilde{L} \to \infty$ limit at constant u in the (fitted) discrete step scaling functions. Note that we will stick to values of u in the same range as the ones obtained directly from simulation data, so that the points derived from the fitted Σ functions correspond only to interpolations and never to extrapolations.

We used the fitted functions from the previous section to obtain, for our three pairs of lattices, the interpolated value of $\Sigma(u)/u$ for a range values of u, using identical values for each of the pairs. This allowed us to plot, at each interpolated value of u, Σ/u as a function of $1/\tilde{L}^2$, which we then fitted linearly in the way shown in eq. (3.32). The extrapolated continuum step scaling function $\sigma(u)/u$ is in this way given simply by the intercept of the fitted line, which we obtained for several interpolated values of u in the $u \in [1.75, 9]$ range.

There was, however, a small issue concerning the propagation of errors that had to be addressed, which concerned the fact that one cannot simply apply standard error propagation to estimate the uncertainty in the $\Sigma(u)/u$ data coming from the fitted curves. Doing so would lead to large correlations and large error overestimations that would spoil the continuum extrapolation.

To avoid this issue, we chose to use resampling methods instead, namely jackknife resampling. We divided the lattice configurations from which the coupling was originally computed into twenty bins of equal size, and constructed twenty new subsets of data, each consisting of the full set of configurations minus a single (different) bin. We repeated, for each of these data subsets, the full process to interpolate Σ/u through the polynomial fit that we described earlier and obtained, for every value of u and for every pair of lattices, twenty values of the discrete step scaling function $\Sigma(u)/u$, each of them derived from a different sample.

Then, for each $\Sigma(u)/u$ point at a given $\tilde{L}$ that was used in the continuum extrapolation, we used the dispersion of the twenty resampled results as the uncertainty. The central value, however, was given by the result obtained earlier using the full set of configurations, rather than by the average of the twenty

subsets.

The same procedure was also used to obtain the error in the intercept of the fitted line, that is the error in the extrapolation of the continuum step scaling function. Indeed, we repeated the same procedure twenty times, but used the values of Σ/u obtained from each of the twenty jackknife subsets to perform the linear fits, leading to twenty different extrapolations of σ/u whose dispersion was used as the uncertainty of the final result (though the central value obtained from using the full set of data was again kept as the central value).

Moreover, and to make sure that the jackknife subdivision into bins did not affect our results, the process was repeated using ten jackknife bins instead of twenty, with no significant differences being found in the results.

We display in figure 3.11 an example of the continuum extrapolation in the $u = 4.0$ case, as well as the plot gathering the continuum extrapolation for all the values of u that we considered. The interception of each curve with the y-axis, which is directly the extrapolated continuum step scaling function $\sigma(u)/u$, is shown with an additional point whose error is obtained through jackknife re-sampling as we just indicated.

The interception is then retrieved from each of the curves, and plotted as a function of u in figure 3.12, along with the corresponding curves that are derived at 1-loop and 2-loops in perturbation theory. These curves are computed by integrating the universal part of the β function up to the corresponding order:

$$\int_u^{\sigma(u,s)} \frac{d\lambda}{\beta(\lambda)} = -2\log s, \tag{3.39}$$

with in our case $s = 2$, as we are doubling the lattice. As we can see, our data are compatible with the 2-loop prediction until $u = 4.5$, after which there is a slight deviation.

To conclude, using the fits of the Σ function that we obtained earlier, and the iterative procedure mentioned at the end of sec. 3.2.3, we computed the full running coupling $\lambda_{TGF}(\tilde{l})$, starting from $\lambda_{TGF}(\tilde{l}_{\min}) = 1.75$ and up to $\lambda_{TGF} = 21.0$, corresponding to an increase of a factor of 2^{15} in the scale. The resulting curve is shown in figure 3.13 as a function of $\log_2(\tilde{l}/\tilde{l}_{\min})$, along with the corresponding one-loop and two-loop predictions from perturbation theory.

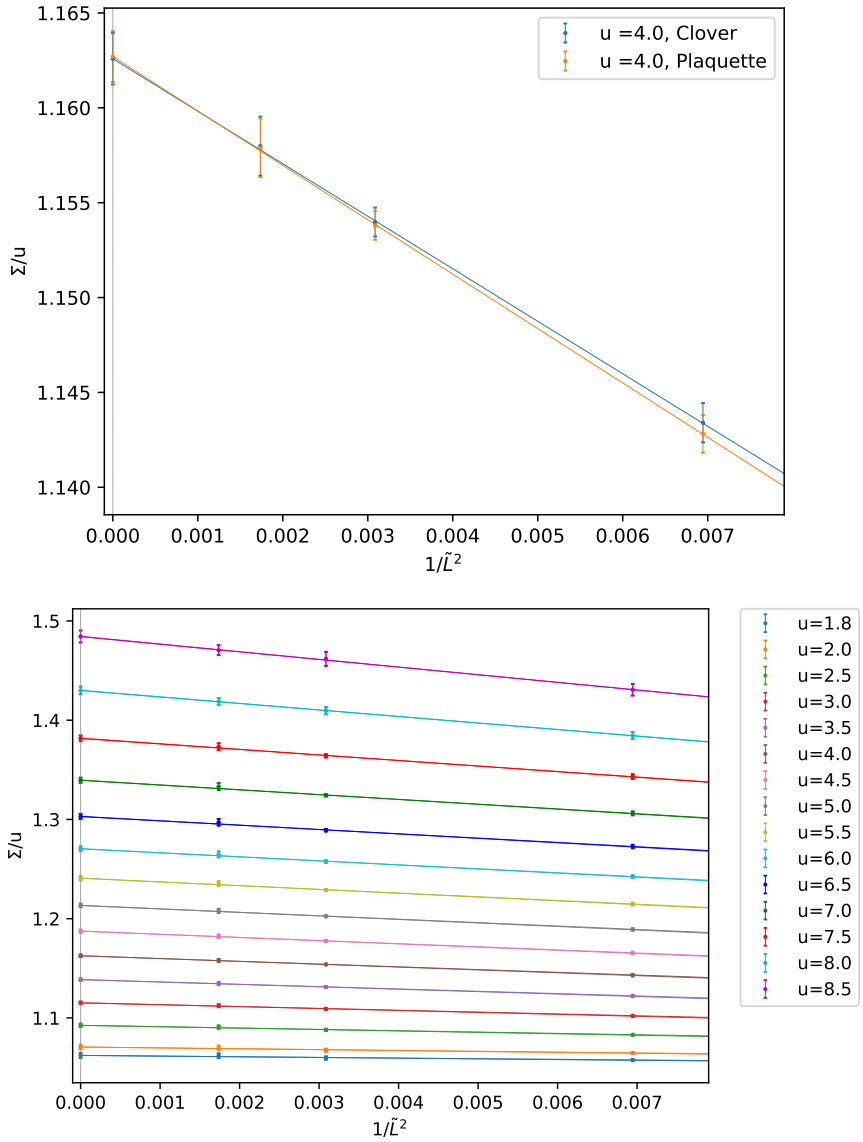

Figure 3.11: We display the continuum extrapolation of the $\Sigma(u)/u$ step scaling function for $c = 0.3$, with the point at $u = 0$ being added manually, and corresponding to the result of the continuum extrapolation. The figure above shows the case $u = 4.0$, while the one below collects the results for several values of u ranging from $u = 1.75$ to $u = 8.5$. The clover and plaquette observables are shown in both plots, though they are often close enough to appear indistinguishable.

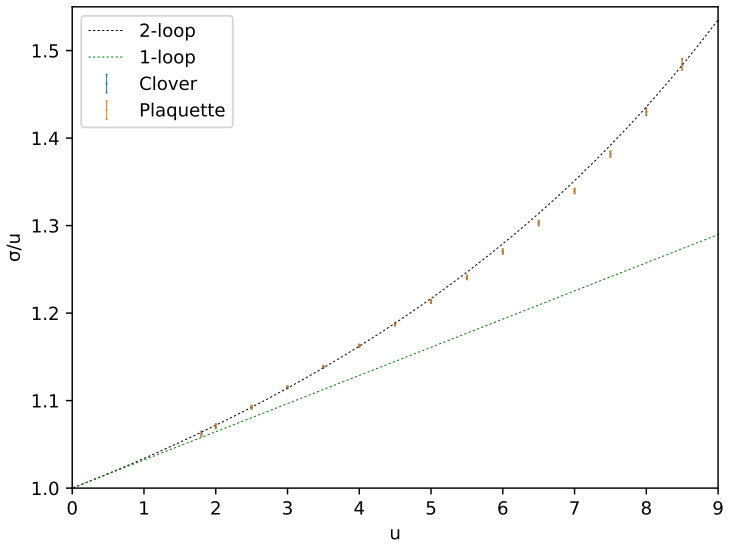

Figure 3.12: We display the continuum extrapolated step scaling function $\sigma(u)/u$ in the $c = 0.3$ scheme, along with the 1-loop and 2-loop perturbative predictions for comparison. Both the plaquette and the clover observables are plotted, but artefacts are small enough for them to be nearly indistinguishable.

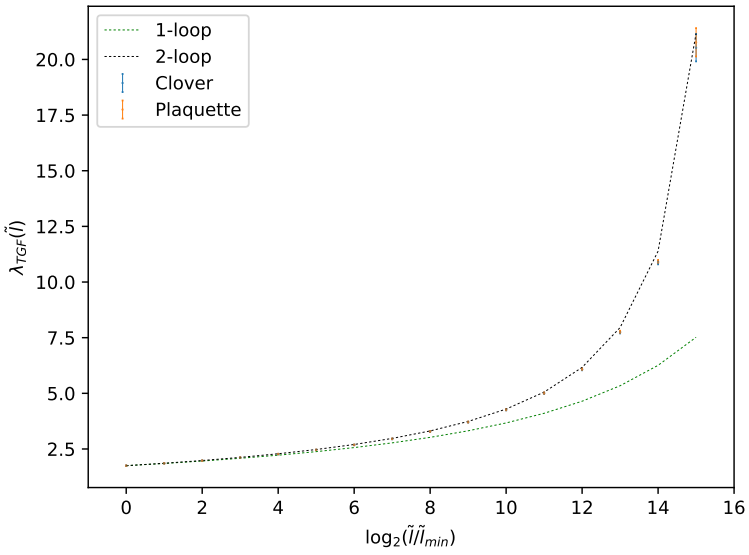

Figure 3.13: We display the continuum determination of the running coupling as a function of $\log_2(\tilde{l}/\tilde{l}_{\text{min}})$ in the $c = 0.3$ scheme, along with the 1-loop and 2-loop perturbative predictions for comparison. The results are obtained starting from $\lambda_{TGF}(\tilde{l}_{\text{min}}) = 1.75$ and up to $\lambda_{TGF} = 21$, corresponding to a 2^{15} increase in scale. Both the plaquette and the clover observables are plotted, but they are so close as to be nearly indistinguishable.

3.4.4 Lattice artefacts

Before closing up, a couple of remarks concerning the magnitude and effects of lattice artefacts are necessary. While the full study of their behaviour is rather complex[13], we have already mentioned a few times along this chapter, looking for instance at our results in figures 3.7, 3.9, and 3.11, that we seem to obtain extremely similar values independently of whether we are using the plaquette or the clover observable to define the coupling, to the point that in some plots they appear to be identical. Even looking at some of the numerical results in appendices B.2 or B.3, the values using the plaquette or clover observables are so similar that one might wonder if there has been a mistake in the computations.

This is actually not the case; instead, what we are seeing is the combination of two of the effects that we mentioned in previous sections: on the one hand, there is a suppression of artefacts at larger values of c, which is already quite strong at $c = 0.3$, and, on the other hand, we are witnessing the fact that leading order effects are suppresed due to the the introduction of the $\mathcal{F}(c)$ factor in the defininition of the coupling in eq. (3.14), which as we recall was the coefficient of the leading order term in perturbation theory. Let us thus take a quick look at the reach that these two effects are having in our simulations.

For the first one, the effects of c on artefacts were already illustrated in figures 3.8 and 3.10. To see it a bit more more clearly, however, one can look at figure 3.14, in which we display $\lambda_{TGF}(b)$ and $\Sigma(u)/u$ at $\tilde{L} = 12$ for several values of c ranging from $c = 0.1$ to $c = 0.3$. As we can see, for $c = 0.1$ the couplings obtained using of the plaquette and clover definitions are visibly different, but, as c increases, these results grow closer to the point that by $c = 0.3$ the difference is smaller than the size of the points in the plot.

As for the normalisation factor $\mathcal{F}(c)$, the easiest way to check its effect on lattice artefacts is to have it replaced, in the definition of the coupling, by the coefficient of the leading term in continuum perturbation theory, found in eq. (3.18), and check how the approach to the continuum in the extrapolation of $\Sigma(u)/u$ is affected. As we are dealing with artefacts, the result of the continuum step scaling function $\sigma(u)$ should remain the same, but we should see significant changes in the slope with which it is approached.

To do so, we display in fig. 3.15 the effect of this replacement in the example

[13] See for instance [126, 133] for a rather comprehensive study on artifacts and on how to improve gradient flow models.

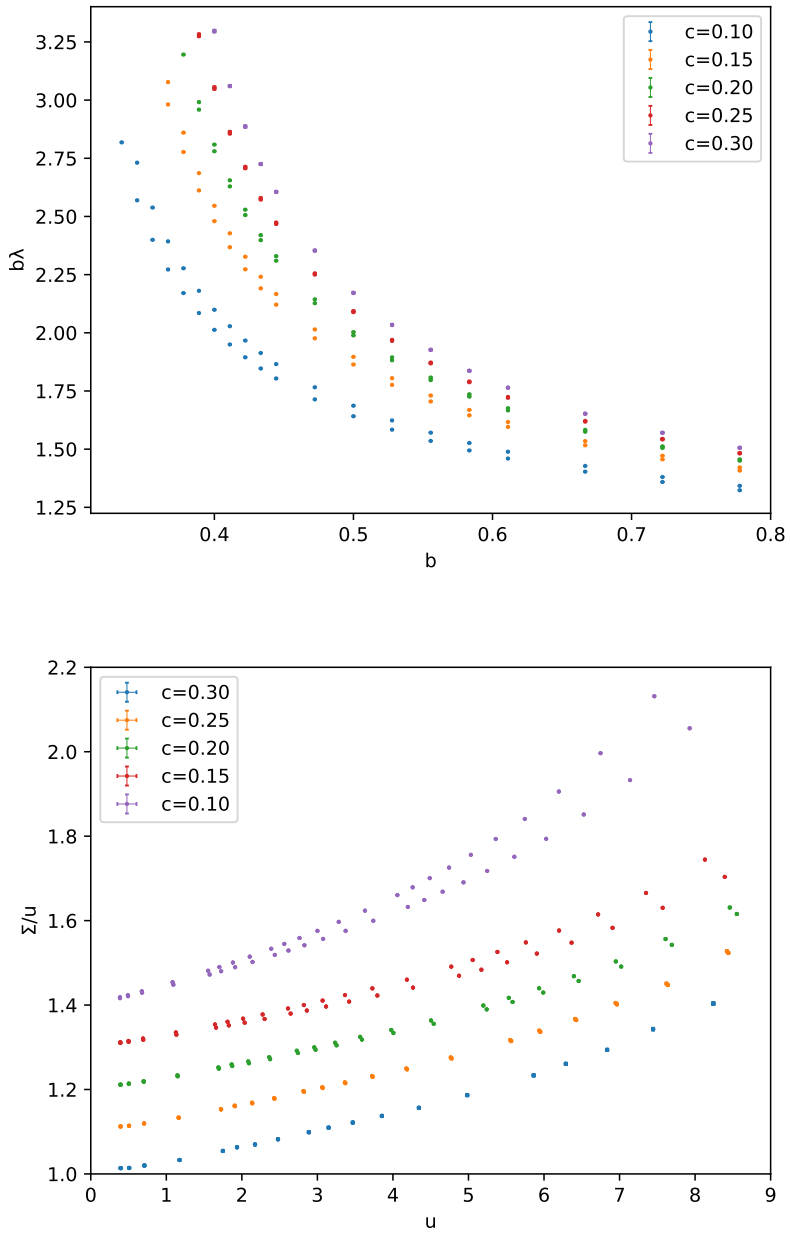

Figure 3.14: We display the results for the coupling $b\lambda_{TGF}(b)$ (top) and $\Sigma(u)/u$ (bottom), for $\tilde{L} = 12$ and several values of c ranging from 0.1 to 0.3, for both the plaquette and clover definitions of the observable (shown in the same colour), to illustrate how lattice artefacts shrink as c grows larger. The results for the step scaling function for $c = 0.10, 0.15, 0.20, 0.25$ have been displaced upwards by $0.4, 0.3, 0.2, 0.1$ respectively for better visibility. As we can see, at $c = 0.1$ the plaquette and points are clearly separate, but as c increases they grow closer to the point of being indistinguishable in the plot for $c = 0.3$.

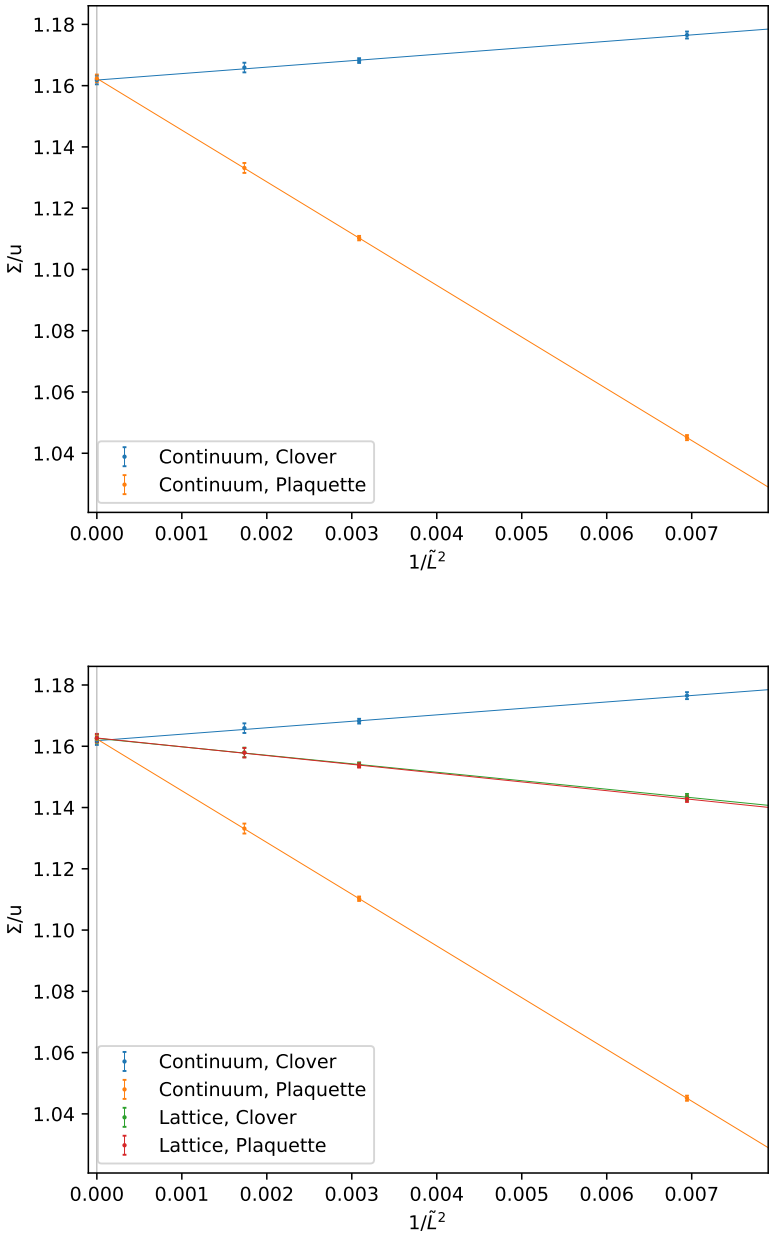

Figure 3.15: We display the continuum extrapolation of $\Sigma(u)/u$ for $c = 0.3$ and $u = 4.0$, for both the plaquette and clover definitions of the observable. The plot above shows the limit when the continuum form of $\mathcal{F}(c)$ is used, whereas the plot below compares it to what happens when the lattice versions of $\mathcal{F}(c)$ are used.

of $c = 0.3$ and $u = 4.0$, for both the plaquette and clover definitions of the observable, comparing it to the result when the lattice normalisation factor is used. As expected, the continuum extrapolation does indeed converge to compatible values of the $\tilde{L} \to \infty$ limit in all four cases, but with significant differences when the continuum normalisation is used.

Two significant differences occur in such a cases: first and most glaringly, we see that the points obtained using the plaquette and clover definitions are no longer anywhere near close to each other, with the clover ones moving upwards and the plaquette ones moving downwards in the plot, more dramatically so for the latter. Second, we notice that the slope with which the continuum is approached becomes steeper, as the points corresponding to smaller $\tilde{L}$ move further away, to the point where it even flips sign for the clover observable.

We are thus seeing, as expected, that the introduction of the $\mathcal{F}(c)$ is suppressing lattice artefacts rather effectively.

3.5 Conclusions

We will close this chapter with a recapitulation of what has been done and of the results that have been obtained. We defined a pure gauge lattice $SU(3)$ theory on top of an asymmetrical torus in four dimensions, with twisted boundary conditions in one plane and periodical ones in the rest, and defined a renormalised 't Hooft coupling using the gradient flow, with the effective size $\tilde{l}$ of the torus acting as the as running scale. Simulations were run using five lattices of characteristic size $\tilde{L} = 12, 18, 24, 36, 48$, for a range of values of the bare lattice coupling b ranging from 0.33 to 0.83, and for values of the scheme constant c between 0.1 and 0.8, with values around $c = 0.3$ being confirmed to represent a good tradeoff between having large lattice artefacts and having too much statistical uncertainty.

We performed an analysis on the behaviour of topological charge along our configurations, and of its evolution in Monte Carlo time, and found indications that topological effects might in our example be controlled by the (physical) effective size $\tilde{l}$ of the torus. Configurations of smaller physical volumes were found to be dominated by the $Q_t = 0$ sector, whereas higher values of Q_t were found to appear more frequently as $\tilde{l}$ increases. In parallel to this, we observed that a critical slowdown of simulations arises as the lattice spacing a becomes smaller: at identical physical volume, we found ourselves going from a regime

in which transitions between different topological sectors are common as Monte Carlo time goes by, to a situation in which all configurations are frozen in the zero charge sector. The slowdown seemeed to occur around a critical lattice spacing of $a \simeq 0.5$ in some examples, but no systematic study of its onset was performed.

We then used step scaling techniques to compute the running of the 't Hooft coupling that we defined. We interpolated the discrete step scaling functions $\Sigma(u)$ from our simulated data, and used the resulting fitted functions for the different lattice sizes to extrapolate the continuum step scaling function $\sigma(u)$, and with it the running of the coupling in wide range of scales, covering an increase of a factor 2^{15} in the scaling. Interestingly, we found that in the scales that we simulated the (continuum) step scaling function is rather close but a bit below the prediction a 2-loops in perturbation theory.

Overall, we found that our preliminary study in $SU(3)$ seems viable, with a behaviour of the running coupling in our model similar, despite using an asymmetrical torus, to the ones found in previous twisted gradient flow computations, such as the one for $SU(2)$ in ref. [121], or the one in a single point lattice in ref. [93]. This hints to the idea that $\tilde{l}$ might indeed be the parameter controlling the running coupling, but further investigation for different $SU(N)$ groups and different twists is required.

Chapter 4

Conclusiones / Conclusions

4.1 Conclusiones y perspectivas de futuro

A lo largo de esta tesis, hemos explorado la conjetura de independencia de volumen a través del estudio del la constante de acoplamiento de 't Hooft en una teoría gauge $SU(N)$ definida en un toro finito con *twisted boundary conditions* (TBC). Definimos la constante de acoplamiento mediante métodos de *gradient flow* en términos de un tamaño efectivo denominado $\tilde{l}$ que combina el rango del grupo y el tamaño físico del toro, y que de cumplirse la conjetura controlaría la dinámica de la teoría Yang-Mills en el toro con TBC.

El estudio realizado se ha dividido en dos partes, con en primer lugar un análisis, en el continuo y hasta segundo orden en teoría de perturbaciones, del comportamiento de la constante de acoplamiento para varios grupos $SU(N)$, seguido del cálculo no perturbativo en el retículo de la constante en el caso particular de $SU(3)$. Esta segunda parte se concibió como una primera exploración de la viabilididad de nuestro estudio, además de como una primera comprobación de la validez de la conjetura de independencia de volumen en un caso simple.

En el capítulo 2, definimos la constante de acoplamiento de 't Hooft usando técnicas de *gradient flow* con TBC en cuatro dimensiones, que a continuación expandimos de manera analítica hasta segundo orden en teoría de perturbaciones, relacionándola con el conocido esquema $\overline{\text{MS}}$ a un valor de la escala de renormalización $\mu = 1/(c\tilde{l})$. Tras realizar de manera general la expansión del observable utilizado para definir la constante de acoplamiento, y tras desarrollar un método para aislar y calcular analíticamente las divergencias ultravioletas que aparecen en dicha expansión, calculamos numéricamente el término finito correspondiente hasta segundo orden. El cálculo numérico se llevó a cabo para el caso particular del twist en dos dimensiones, usando un toro asimétrico de tamaño $l^2 \times \tilde{l}^2$ de forma que la longitud efectiva fuera $\tilde{l} = lN$ en todas las direcciones, y para una serie de valores de tres parámetros: el cociente c entre el tamaño del toro y la escala de energías, el flujo magnético k que caracteriza las condiciones de contorno, y el rango del grupo gauge, N. Los resultados de este cálculo nos permitieron extraer, a segundo orden y para el rango que se escogido para los tres parámetros, el cociente de parámetros Λ entre el esquema TGF que empleamos y el conocido esquema $\overline{\text{MS}}$, un cociente que no había sido calculado anteriormente.

Además, nos interesamos particularmente en la dependencia de la cosntante de acoplamiento con el número de colores N de la teoría y con el flujo magnético k. Estudiamos dicha dependencia haciendo especial enfásis en dos tipos de límites

de gran número de colores: en el límite singular en el que $\tilde{l}$ se mantiene constante a base de mandar el tamaño del toro a cero a la vez que se hace N infinito por un lado, y por el otro en el límite termodinámico en el que la escala de energías $\mu = 1/c\tilde{l}$ se mantiene constante, enviando c a cero a la vez que se toma el límite de gran número de colores.

El primer tipo de límite mencionado reviste una importancia especial, debido a la conexión, a través de la dualidad de Morita, entre las teorías de Yang-Mills definidas sobre un toro finito con TBC y las teorías no conmutativas. En dicho contexto, $\tilde{l}$ corresponde al tamaño físico del toro en la teoría dual, y la variable angular $\hat{\theta} = \bar{l}/N$ pasa a ser el parámetro de no conmutatividad, lo cual ha llevado a sugerir el uso de teorías Yang-Mills con TBC en el retículo como regulador natural de teorías no conmutativas. Para el estudio de valores irracionales de $\hat{\theta}$, se ha propuesto emplear una sucesión de teorías Yang-Mills con valores de $\bar{k}$ y N cuyo cociente tiende en el límite de gran N al valor irracional deseado de $\hat{\theta}$, pero la factibilidad de esta opción se ve limitada por la aparición de inestabilidades taquiónicas. En dicho contexto, nuestros resultados apoyan la observación, hecha en las refs. [45, 85], de que dichas singularidades sólo pueden evitarse para un conjunto incontable pero de medida cero de valores de $\hat{\theta}$. Confirmamos además la validez de la sugerencia hecha en la ref. [85] de emplear una secuencia concreta de elementos de la serie de Fibonacci como valores de $\bar{k}$ y N que tienden al parámetro limitante $\hat{\theta} = (3 - \sqrt{5})/2$, con la cual podemos en nuestro modelo aproximarnos al límite singular sin que aparezcan inestabilidades taquiónicas. Él segundo tipo de límite considerado en nuestro trabajo es un límite de volumen infinito, que nos permite recuperar la expresión de la constante de acoplamiento de 't Hooft en volumen infinito obtenida en la ref. [104]. Ésto apoya la idea de reducción de volumen, visto que la constante de acoplamiento para $SU(\infty)$ puede recuperarse, en el límite $\tilde{l} \to \infty$, haciendo N infinito a tamaño fijo del toro.

En el capítulo 3, llevamos a cabo un estudio de *step scaling* en el caso particular de $SU(3)$ en el retículo y en cuatro dimensiones. De nuevo escogimos usar un toro asimétrico de dimensiones $l^2 \times \tilde{l}^2$, con *twisted boundary conditions* en un plano y condiciones periódicas en los demás, y usamos técnicas de *gradient flow* para definir una constante de acoplamiento en función del tamaño efectivo del toro. Generamos una serie de configuraciones gauge de tamaño característico $\tilde{L} = 12, 18, 24, 36, 48$, a partir de las cuales que medimos la constante de acoplamiento λ para varios valores de la constante de acoplamiento desnuda

b, y para varios valores del parámetro c que relaciona la escala de energías con el tamaño del toro.

En primer lugar, llevamos a cabo un análisis de la carga topológica de nuestras configuraciones conforme avanza el tiempo de Monte Carlo, en el que hallamos indicaciones de que los efectos topológicos están controlados por el tamaño efectivo $\tilde{l}$ del retículo. Vimos que los retículos de menor volumen efectivo están dominados por configuraciones de carga topológica nula, mientras que conforme $\tilde{l}$ crece la proporción de configuraciones con mayores valores de Q_t aumenta. Además, observamos la aparición de un ralentizamiento crítico cuando el espaciado a del retículo es lo bastante pequeño: vimos que simulaciones con volúmenes físicos similares, que para el caso de espaciados grandes daban lugar a configuraciones con diversos valores de la carga topológica, se quedaban para espaciados pequeños atascadas en el sector inicial de carga topológica cero. A continuación, calculamos la variación de la constante de acoplamiento de 't Hooft con la escala de energías mediante técnicas de *step scaling*, utilizando los datos de nuestras simulaciones para interpolar la versión discreta de la función de *step scaling*, y extrapolándola a continuación al continuo. La versión continua de dicha función se usó para determinar la constante de acoplamiento a lo largo de un amplio rango de escalas, cubriendo un incremento de un factor 2^{15} sobre la escala inicialmente considerada. Vimos además que, para el rango de parámetros considerados, la función de *step scaling* en el continuo sigue hasta $u = 4.5$ la predicción de teoría de perturbaciones a dos loops, desviándose a partir de dicho punto ligeramente hacia valores menores.

Los resultados de nuestro estudio preliminar en $SU(3)$, por lo tanto, parecen indicar que la extensión a distintos valores de N es viable. Además, vemos que la constante de acoplamiento parece comportarse, en nuestro toro asimétrico, de manera similar a lo que se encontró en cálculos previos en esquemas TGF con twists simétricos, para el caso de $SU(2)$ en un toro simétrico y para $SU(\infty)$ en un retículo de un punto. Ésto son indicios de que la conjetura de independencia de volumen parece cumplirse.

Llegamos con ésto a las perspectivas de futuro de nuestro trabajo. El cálculo perturbativo está relativamente cerrado, si bien podría resultar interesante repetir los cálculos numéricos para el caso del twist simétrico con $d_t = 4$. La segunda parte de nuestro trabajo, en cambio, pide a gritos ser ampliada. Una primera extensión interesante sería estudiar de manera más profunda y detallada la topología

de las configuraciones generadas, de cara a ver cuál es la estructura de la carga topológica, cómo aparece, y realizar un análisis sistemático de cómo surgen las configuraciones de carga no nula como función del volumen físico del retículo; es decir, su dependencia como función del espaciado de la red, del tamaño del toro y del rango del grupo gauge.

Otro aspecto crítico a expandir es la extensión del análisis a más valores de N y a distintos valores de $\bar{k}$ en el twist, de cara a permitirnos determinar la dependencia de la constante de acoplamiento con N y sus consecuencias respecto a la conjetura de independencia de volumen, así como con el fin de estudiar el límite singular de gran N, en relación con el estudio, conectando con teorías no conmutativas, de la aparición de inestabilidades taquiónicas.

4.2 Conclusions and future prospects

Along this work, we have explored the conjecture of volume independence through the study of the 't Hooft running coupling of a pure gauge $SU(N)$ theory on a finite torus with twisted boundary conditions. The coupling was defined using gradient flow methods and was given in terms of an effective size $\tilde{l}$ combining the rank N of the gauge groups and the physical size of the torus, which is hypothesised to drive the dynamics of twisted Yang-Mills theory.

The study consists of two parts, first with an analysis of the running coupling in continuum perturbation theory up to next-to-leading order for several $SU(N)$ gauge groups, and then with a non-perturbative computation on the lattice of the running coupling for the particular case of $SU(3)$. The second part was envisioned as a probe of the viability of our study, as well as a first check of whether volume independence appears to hold in that simple case.

In chapter 2, we defined a twisted gradient flow 't Hooft running coupling in four dimensions, and analytically expanded it up to one-loop order in perturbation theory, matching it to the well-known $\overline{\text{MS}}$ infinite volume scheme at a renormalisation scale $\mu = 1/(c\tilde{l})$. After performing the expansion of the observable used to define the running coupling in a general way, and after devising a way to isolate and analytically determine the UV divergences appearing in the expansion, we performed a numerical computation of the corresponding one-loop finite piece. This was done for the particular case of a two-dimensional non-trivial twist, using an asymmetrical torus of size $l^2 \times \tilde{l}^2$ such that $\tilde{l} = lN$ in all direc-

tions, and for a range of values of three parameters: the ratio c between the size of the torus and the energy scale, the magnetic flux k characterising the twist, and the rank of the gauge group, N. The results of this computation allowed us to extract, at one-loop and for the range of parameters used in the numerical computation, the ratio of Λ parameters between the TGF scheme that we set up and the well-known $\overline{\text{MS}}$ one, a calculation that had not been done before.

Moreover, we were particularly interested in the dependence of the running coupling on the number of colours N of the theory and on the magnetic flux k. This dependence was studied focusing on two particular types of large N limits: the singular limit in which $\tilde{l}$ is kept constant by sending the physical torus size to zero as N is sent to infinity on one hand, and on the other the thermodynamic limit in which the energy scale $\mu = 1/c\tilde{l}$ is kept constant as $\tilde{l}$ is send to infinity and c to zero.

The first type of limit is particularly relevant due to the connection of twisted Yang-Mills theory with non-commutative theories through the Morita duality, with $\tilde{l}$ being the physical size of the torus in the dual theory and the angular variable $\hat{\theta} = \bar{k}/N$ corresponding to the non-commutativity parameter, which has led to the suggestion to use twisted Yang-Mills theories on the lattice as a natural regulator for non-commutative ones. For irrational values of $\hat{\theta}$, a proposal had been made to try an approach through a succession of theories with values of $\bar{k}$ and N whose quotient approached the target irrational value in the large N limit, but the feasability of this option is limited by the appearance of tachyonic instabilities. In that context, our results supported the observation made in refs. [45, 85] that these singularities can only be avoided for a zero-measure, uncountable set of values of $\hat{\theta}$, and we also found that the suggestion made in ref. [85] to use a particular sequence of elements of the Fibonacci series to build a sequence of $\bar{k}$ and N of limiting parameter $\hat{\theta} = (3-\sqrt{5})/2$ is also a valid sequence to approach the singular limit without tachyonic instabilities in our model.

The second type of limit is a large volume limit, and as such it led us to recover the expression of the 't Hooft gradient flow coupling at infinite volume from ref. [104]. This is evidence in support of the idea of volume reduction, as the $SU(\infty)$ coupling can in the $\tilde{l} \to \infty$ limit be recovered at fixed torus size by sending N to infinity.

In chapter 3, we performed a step scaling study of the running coupling in the case of $SU(3)$, on the lattice and in four dimensions. We once more chose

to use an asymmetrical $l^2 \times \tilde{l}^2$ torus with twisted boundary conditions in one plane and periodical ones in the rest, and used the gradient flow to define the running coupling in terms of the effective size of the torus. We generated a set of gauge configurations for five lattices of characteristic sizes $\tilde{L} = 12, 18, 24, 36, 48$, for a range of values of the lattice bare coupling b and for several values of the parameter c relating the energy scale to the size of the torus, from which we measured the 't Hooft coupling.

We first analysed the behaviour of topological charge in our configurations as Monte Carlo time advances, finding indications that topological effects are controlled by the effective size $\tilde{l}$ of the lattice. We found lattices with smaller effective volumes to be dominated by configurations of vanishing topological charge, with configurations of larger Q_t appearing more frequently as $\tilde{l}$ grows larger. In addition, we found that a critical slowdown can occur in the simulations if the lattice spacing a is small enough: simulations with identical physical volume, which for large lattice spacings gave rise to configurations with a variety of values of the topological charge, were stuck in the initial zero charge sector for simulations at smaller values of a. We then computed the running of the 't Hooft coupling using step scaling techniques, using our simulated data to interpolate the discrete step scaling functions $\Sigma(u)$ and extrapolate the continuum step scaling function. This was then used to compute the running of the coupling over a wide range of scales, covering an increase of a factor 2^{15} in the scaling. We found that, for our range of parameters, the continuum step scaling function follows the 2-loop perturbative prediction up to $u = 4.5$, after which it slightly deviates.

The results of our preliminary $SU(3)$ study thus seem to indicate that its extension to further values of N is viable. Moreover, we find that the running coupling appears in our asymmetrical torus to behave in a similar manner to what was found in previous TGF computations using the symmetric twist for the cases of $SU(2)$ on a symmetric torus and of $SU(\infty)$ on the one-point lattice. This is a hint that volume independence appears to hold.

This brings us to the future prospects of our work. The perturbative computation is pretty much closed, though it might be interesting to repeat the numerical computations in the case of the symmetric $d_t = 4$ twist. The second part of our work, however, practically begs to be expanded. A first point of interest would be a deeper analysis of the topology of the configurations: to see what the structure of the configurations with nonzero topological charge is, how they arise, and to

perform a more systematic study of their appearance as a function of the physical volume of the lattice, i.e. the dependence on lattice spacing, on torus size, and on the rank of the gauge group.

Another crucial aspect to study concerns the extension of the analysis to further values of N and to different values of k in the twist, which should allow us to both determine the dependence of the coupling on N and its consequences regarding volume independence, as well as to study once more the approach to the large N singular limits in relation to non-commutative theories and to the onset of tachyonic instabilities.

Appendix A

Calculations in perturbation theory

A.1 Perturbative expansion of the observable

We will in this appendix expand the energy density observable $E(t)$ in perturbation theory up to order $\mathcal{O}(g_0^4)$, and then Fourier-expand it to obtain its order by order expression in momentum space. As we recall, the observable was given by:

$$E(t) = \frac{1}{2}\mathrm{Tr}\Big(G_{\mu\nu}(x,t)G_{\mu\nu}(x,t)\Big), \tag{A.1}$$

with:

$$D_\mu B_\nu\left(x,t\right) = \partial_\mu B_\nu\left(x,t\right) + i\left[B_\mu\left(x,t\right), B_\nu\left(x,t\right)\right], \tag{A.2}$$

$$G_{\mu\nu}\left(x,t\right) = \partial_\mu B_\nu\left(x,t\right) - \partial_\nu B_\mu\left(x,t\right) + i\left[B_\mu\left(x,t\right), B_\nu\left(x,t\right)\right]. \tag{A.3}$$

Dropping from here on the (x,t) arguments of the fields in position space for the sake of clarity, we expand the field strength tensor and covariant derivatives:

$$E(t) = \frac{1}{2}\mathrm{Tr}(2\partial_\mu B_\nu \partial_\mu B_\nu - 2\partial_\mu B_\nu \partial_\nu B_\mu + 4i\partial_\mu B_\nu [B_\mu, B_\nu] - [B_\mu, B_\nu][B_\mu, B_\nu]), \tag{A.4}$$

and then expand the fields in powers of the bare coupling, $B_\mu = \sum_k g_0^k B_\mu^{(k)}$, and plug them into the expansion of $E(t)$, discarding all terms beyond $\mathcal{O}(g_0^4)$:

$$\begin{aligned}
E(t) = {} & g_0^2\,\mathrm{Tr}\left(\partial_\mu B_\nu^{(1)}\partial_\mu B_\nu^{(1)} - \partial_\mu B_\nu^{(1)}\partial_\nu B_\mu^{(1)}\right) \\
& + 2ig_0^3\,\mathrm{Tr}\left(\partial_\mu B_\nu^{(1)}\left[B_\mu^{(1)}, B_\nu^{(1)}\right]\right) \\
& + 2g_0^3\,\mathrm{Tr}\left(\partial_\mu B_\nu^{(1)}\partial_\mu B_\nu^{(2)} - \partial_\nu B_\mu^{(1)}\partial_\mu B_\nu^{(2)}\right) \\
& + g_0^4\,\mathrm{Tr}\left(\partial_\mu B_\nu^{(2)}\partial_\mu B_\nu^{(2)} - \partial_\mu B_\nu^{(2)}\partial_\nu B_\mu^{(2)}\right) \\
& - \frac{1}{2}g_0^4\,\mathrm{Tr}\left(\left[B_\mu^{(1)}, B_\nu^{(1)}\right]^2\right) \\
& + 2ig_0^4\,\mathrm{Tr}\left(\partial_\mu B_\nu^{(2)}\left[B_\mu^{(1)}, B_\nu^{(1)}\right] + \partial_\mu B_\nu^{(1)}\left[B_\mu^{(1)}, B_\nu^{(2)}\right] + \partial_\mu B_\nu^{(1)}\left[B_\mu^{(2)}, B_\nu^{(1)}\right]\right) \\
& + 2g_0^4\,\mathrm{Tr}\left(\partial_\mu B_\nu^{(3)}\partial_\mu B_\nu^{(1)} - \partial_\mu B_\nu^{(3)}\partial_\nu B_\mu^{(1)}\right) + \mathcal{O}(g_0^5).
\end{aligned} \tag{A.5}$$

Adding for later convenience an additional $1/N$ overall factor, we will assign to each of the lines in the equation above the notation $\mathcal{E}_i(t)$, with i ranging from 0 to 6, and Fourier-expand them in the basis mentioned in eq. (2.12):

$$B_\mu^{(k)}(x,t) = V^{-\frac{1}{2}}{\sum_q}' e^{iqx}\hat{B}_\mu^{(k)}(q,t)\,\hat{\Gamma}(q), \tag{A.6}$$

with the prime denoting, as usual, the exclusion of the terms proportional to l_g in all twisted directions. Taking expectation values, we notice that several terms share similar structures and can be computed together. The simplest four terms are of the form:

$$\begin{aligned}
&\mathrm{Tr}\langle \partial_\mu B_\nu^{(i)} \partial_\mu B_\nu^{(j)} - \partial_\mu B_\nu^{(i)} \partial_\nu B_\mu^{(j)} \rangle = \\
&\quad = V^{-1} {\sum_{p,q}}' (p_\nu q_\mu - p_\alpha q_\alpha \delta_{\mu\nu}) e^{i(p+q)x} \mathrm{Tr}(\hat{\Gamma}(q)\hat{\Gamma}(p)) \langle \hat{B}_\nu^{(i)}(q,t) \hat{B}_\mu^{(j)}(p,t) \rangle \\
&\quad = \frac{1}{2} V^{-1} {\sum_{q}}' (q^2 \delta_{\mu\nu} - q_\mu q_\nu) \langle \hat{B}_\nu^{(i)}(q,t) \hat{B}_\mu^{(j)}(-q,t) \rangle .
\end{aligned} \tag{A.7}$$

There are also four terms of the form:

$$\begin{aligned}
&\mathrm{Tr}\langle \partial_\mu B_\nu^{(i)} [B_\mu^{(j)}, B_\nu^{(k)}] \rangle = \\
&\quad = i V^{-\frac{3}{2}} {\sum_{p_1,p_2,p_3}}' p_{1\mu} e^{i \sum p_i x} \mathrm{Tr}\ (\hat{\Gamma}(p_1)[\hat{\Gamma}(p_2), \hat{\Gamma}(p_3)]) \langle \hat{B}_\nu^{(i)}(p_1,t) \hat{B}_\mu^{(j)}(p_2,t) \hat{B}_\nu^{(k)}(p_3,t) \rangle \\
&\quad = -\frac{1}{2} V^{-\frac{3}{2}} {\sum_{p_1,p_2,p_3}}' p_{1\mu} \delta(\sum p_i) F(p_2,p_3,p_1) \langle \hat{B}_\nu^{(i)}(p_1,t) \hat{B}_\mu^{(j)}(p_2,t) \hat{B}_\nu^{(k)}(p_3,t) \rangle ,
\end{aligned} \tag{A.8}$$

where the shorthand notation $\sum p_i$ denotes the sum over all present momenta, for overall momentum conservation. The last remaining term is then given by:

$$\begin{aligned}
&\mathrm{Tr}\langle [B_\mu^{(1)}, B_\nu^{(1)}][B_\mu^{(1)}, B_\nu^{(1)}] \rangle = \\
&\quad = V^{-2} {\sum_{p_1,p_2,p_3,p_4}}' e^{i \sum p_i x} \mathrm{Tr}([\hat{\Gamma}(p_1), \hat{\Gamma}(p_2)][\hat{\Gamma}(p_3), \hat{\Gamma}(p_4)]) \\
&\qquad\qquad \times \langle \hat{B}_\mu^{(1)}(p_1,t) \hat{B}_\nu^{(1)}(p_2,t) \hat{B}_\mu^{(1)}(p_3,t) \hat{B}_\nu^{(1)}(p_4,t) \rangle \\
&\quad = -\frac{1}{2} V^{-2} {\sum_{p_1,p_2,p_3,p_4}}' \delta(\sum p_i) F(p_1,p_2,-p_1-p_2) F(p_3,p_4,-p_3-p_4) \\
&\qquad\qquad \times \langle \hat{B}_\mu^{(1)}(p_1,t) \hat{B}_\nu^{(1)}(p_2,t) \hat{B}_\mu^{(1)}(p_3,t) \hat{B}_\nu^{(1)}(p_4,t) \rangle .
\end{aligned} \tag{A.9}$$

Plugging all of these terms into the expansion of the observable $\langle E(t) \rangle / N$ above, the resulting expression can be expressed as the sum of seven different terms:

$$\langle E(t) \rangle / N = \mathcal{E}_0(t) + \mathcal{E}_1(t) + \mathcal{E}_2(t) + \mathcal{E}_3(t) + \mathcal{E}_4(t) + \mathcal{E}_5(t) + \mathcal{E}_6(t), \tag{A.10}$$

with:

$$\mathcal{E}_0(t) = \frac{g_0^2}{2NV} \sum_q{}' \left(q^2\delta_{\mu\nu} - q_\mu q_\nu\right) \left\langle \hat{B}^{(1)}_\mu(-q,t)\, \hat{B}^{(1)}_\nu(q,t) \right\rangle , \tag{A.11}$$

$$\mathcal{E}_1(t) = \frac{-g_0^3}{NV^{3/2}} \sum_{p_1,p_2,p_3}{}' \delta\left(\sum p_i\right) F(p_1,p_2,p_3)\, ip_{1\mu} \tag{A.12}$$
$$\times \left\langle \hat{B}^{(1)}_\nu(p_1,t)\, \hat{B}^{(1)}_\mu(p_2,t)\, \hat{B}^{(1)}_\nu(p_3,t) \right\rangle ,$$

$$\mathcal{E}_2(t) = \frac{g_0^3}{NV} \sum_q{}' \left(q^2\delta_{\mu\nu} - q_\mu q_\nu\right) \left\langle \hat{B}^{(1)}_\mu(-q,t)\, \hat{B}^{(2)}_\nu(q,t) \right\rangle , \tag{A.13}$$

$$\mathcal{E}_3(t) = \frac{g_0^4}{2NV} \sum_q{}' \left(q^2\delta_{\mu\nu} - q_\mu q_\nu\right) \left\langle \hat{B}^{(2)}_\mu(-q,t)\, \hat{B}^{(2)}_\nu(q,t) \right\rangle , \tag{A.14}$$

$$\mathcal{E}_4(t) = \frac{g_0^4}{4NV^2} \sum_{p_1,p_2,p_3,p_4}{}' \delta\left(\sum p_i\right)\, F(p_1,p_2,-p_1-p_2)\, F(p_3,p_4,-p_3-p_4)$$
$$\times \left\langle \hat{B}^{(1)}_\mu(p_1,t)\, \hat{B}^{(1)}_\nu(p_2,t)\, \hat{B}^{(1)}_\mu(p_3,t) \hat{B}^{(1)}_\nu(p_4,t) \right\rangle , \tag{A.15}$$

$$\mathcal{E}_5(t) = \frac{-ig_0^4}{NV^{3/2}} \sum_{p_1,p_2,p_3}{}' \delta\left(\sum p_i\right) p_{1\mu}\, F(p_1,p_2,p_3) \Big\{ \left\langle \hat{B}^{(2)}_\nu(p_1,t)\, \hat{B}^{(1)}_\mu(p_2,t)\, \hat{B}^{(1)}_\nu(p_3,t) \right\rangle$$
$$+ \left\langle \hat{B}^{(1)}_\nu(p_1,t) \hat{B}^{(2)}_\mu(p_2,t) \hat{B}^{(1)}_\nu(p_3,t) \right\rangle + \left\langle \hat{B}^{(1)}_\nu(p_1,t)\, \hat{B}^{(1)}_\mu(p_2,t)\, \hat{B}^{(2)}_\nu(p_3,t) \right\rangle \Big\}, \tag{A.16}$$

$$\mathcal{E}_6(t) = \frac{g_0^4}{NV} \sum_q{}' \left(q^2\delta_{\mu\nu} - q_\mu q_\nu\right) \left\langle \hat{B}^{(1)}_\mu(-q,t)\, \hat{B}^{(3)}_\nu(q,t) \right\rangle . \tag{A.17}$$

A.2 The Feynman rules with TBC

The Feynman rules for the set of irreducible twist tensors used in this work have been derived in various contexts, both in the continuum (see for instance ref. [138] and references therein for a review) and in the lattice regularised version of the theory (such as for instance in refs. [4, 27, 41, 44]). In this appendix, we will summarise the ones relevant to our work, derived in the continuum.

The set of allowed gauge transformations in our theory will be restricted to those preserving the form of the boundary conditions in eqs. (2.7) and (2.8), using the irreducible twist given in eq. (1.47), and the remaining gauge degrees of freedom will be fixed using a generalised covariant gauge of parameter ξ consistent with the boundary conditions. After scaling the gauge potential with the bare

coupling g_0, the Lagrangian density, including the gauge fixing terms, reads:

$$\mathcal{L} = \frac{1}{2}\mathrm{Tr}(F_{\mu\nu}^2) + \frac{1}{\xi}\mathrm{Tr}(\partial_\mu A_\mu)^2 - 2\mathrm{Tr}(\bar{c}\,\partial_\mu D_\mu c) \quad , \tag{A.18}$$

where $D_\mu \equiv \partial_\mu + ig_0 A_\mu$ is the covariant derivative and c, $\bar{c}$ denote the ghost fields.

One may then obtain the propagators of the gauge and ghost fields using the Fourier expansion of the gauge potential given in eq. (1.12), along with an analogous one for the ghost fields:

$$P_{\mu\nu}(p,q) = \frac{1}{p^2}\Big(\delta_{\mu\nu} - (1-\xi)\,\frac{p_\mu p_\nu}{p^2}\Big)\,\delta(q+p) \quad , \tag{A.19}$$

$$P_g(p,q) = \frac{1}{p^2}\delta(q+p) \quad , \tag{A.20}$$

where the momenta appearing in these expressions are quantised in units of the effective size $\tilde{l}$.

The Feynman rules for the vertices are then obtained from the commutation relations in eq. (1.13), and are expressed in terms of the momentum-dependent structure constants $F(p,q,-q-r)$. The terms contributing to the (sign-flipped) gauge fixed action are the following:

- 3-gluon term:

$$\frac{1}{3!}\mathcal{V}^{(3)}_{\mu_1\mu_2\mu_3}(p_1,p_2,p_3)\left(\prod_{i=1}^{3} A_{\mu_i}(p_i)\right), \tag{A.21}$$

  with:

$$\mathcal{V}^{(3)}_{\mu_1\mu_2\mu_3}(p_1,p_2,p_3) = ig_0 V^{-\frac{1}{2}} F(p_1,p_2,p_3)\delta\Big(\sum_{i=1}^{3} p_i\Big)\times \tag{A.22}$$
$$\Big((p_3-p_2)_{\mu_1}\delta_{\mu_2\mu_3} + (p_1-p_3)_{\mu_2}\delta_{\mu_1\mu_3} + (p_2-p_1)_{\mu_3}\delta_{\mu_1\mu_2}\Big).$$

- 4-gluon term:

$$\frac{1}{4!}\mathcal{V}^{(4)}_{\mu_1\mu_2\mu_3\mu_4}(p_1,p_2,p_3,p_4)\left(\prod_{i=1}^{4} A_{\mu_i}(p_i)\right), \tag{A.23}$$

with:

$$\mathcal{V}^{(4)}_{\mu_1\mu_2\mu_3\mu_4}(p_1,p_2,p_3,p_4) = -g_0^2 V^{-1}\,\delta\left(\sum_{i=1}^{4} p_i\right)\times \tag{A.24}$$
$$\Big(F(p_1,p_2,-p_1-p_2)F(p_3,p_4,-p_3-p_4)(\delta_{\mu_1\mu_3}\delta_{\mu_2\mu_4}-\delta_{\mu_2\mu_3}\delta_{\mu_1\mu_4})$$
$$+F(p_2,p_3,-p_2-p_3)F(p_4,p_1,-p_4-p_1)(\delta_{\mu_2\mu_4}\delta_{\mu_3\mu_1}-\delta_{\mu_3\mu_4}\delta_{\mu_2\mu_1})$$
$$+F(p_1,p_3,-p_1-p_3)F(p_2,p_4,-p_2-p_4)(\delta_{\mu_1\mu_2}\delta_{\mu_3\mu_4}-\delta_{\mu_3\mu_2}\delta_{\mu_1\mu_4})\Big)\,.$$

- Ghost-gluon term:

$$\mathcal{V}^{(gh)} = ig_0 V^{-\frac{1}{2}} F(p_1,p_2,p_3)\; p_{1\mu}\; \bar{c}(p_1)A_\mu(p_2)c(p_3)\,\delta\left(\sum_{i=1}^{3} p_i\right)\,. \tag{A.25}$$

These rules can be easily used to derive different quantities, such as the one-loop correction to the propagator. At order $\mathcal{O}(g_0^2)$ and in the Feynman gauge $\xi = 1$, the vacuum polarisation tensor can be obtained as shown in ref. [138]:

$$\Pi_{\mu\nu}(p) = \frac{1}{2}g_0^2 V^{-1}\sum_q F^2(p,q,-p-q)\frac{1}{q^2(p+q)^2}\times \tag{A.26}$$
$$\Big\{4\,\left(\delta_{\mu\nu}p^2 - p_\mu p_\nu\right) + (d-2)\,\left((p_\mu+2q_\mu)(p_\nu+2q_\nu) - 2\delta_{\mu\nu}q^2\right)\Big\}\,.$$

A.3 Solution to the flow equations up to third order

In this appendix we will solve the modified flow equations mentioned in eq. (2.21) up to third order in perturbation theory. Setting the gauge parameter χ to unity, we want to solve:

$$\partial_t B_\mu(x,t) = D_\nu G_{\nu\mu}(x,t) + D_\mu\partial_\nu B_\nu(x,t), \quad B_\mu(x,0) = g_0 A_\mu(x). \tag{A.27}$$

While this was already solved in infinite volume in ref. [104], quite a few significant differences arise in finite volume, notably due to the different group structure constants. Note that the arguments of the $B_\mu(x,t)$ fields in position space have been dropped in what follows for clarity, though the ones in the momentum space fields $\hat{B}(p,t)$ will still be shown.

We begin by expanding the fields in the flow equation in perturbation theory in position space. The first order is trivial:

$$\partial_t B_\mu^{(1)} = \partial_\nu(\partial_\nu B_\mu^{(1)} - \partial_\mu B_\nu^{(1)}) + \partial_\mu\partial_\nu B_\nu^{(1)} = \partial_\nu^2 B_\mu^{(1)}, \tag{A.28}$$

whereas the second order expression is a bit longer:

$$\begin{aligned}\partial_t B_\mu^{(2)} &= \partial_\nu^2 B_\mu^{(2)} - \partial_\nu\partial_\mu B_\nu^{(2)} + i\partial_\nu[B_\nu^{(1)}, B_\mu^{(1)}] + i[B_\nu^{(1)}, \partial_\nu B_\mu^{(1)}] \\ &\quad - i[B_\nu^{(1)}, \partial_\mu B_\nu^{(1)}] + i[B_\mu^{(1)}, \partial_\nu B_\nu^{(1)}] + \partial_\mu\partial_\nu B_\nu^{(2)}, \end{aligned} \tag{A.29}$$

$$\partial_t B_\mu^{(2)} = \partial_\nu^2 B_\mu^{(2)} + 2i[B_\nu^{(1)}, \partial_\nu B_\mu^{(1)}] - i[B_\nu^{(1)}, \partial_\mu B_\nu^{(1)}]. \tag{A.30}$$

Renaming the last two terms, we get:

$$\partial_t B_\mu^{(2)} = \partial_\nu^2 B_\mu^{(2)} + R_\mu^{(2)}, \quad R_\mu^{(2)} \equiv 2i[B_\nu^{(1)}, \partial_\nu B_\mu^{(1)}] - i[B_\nu^{(1)}, \partial_\mu B_\nu^{(1)}]. \tag{A.31}$$

The third order expression works in the same manner:

$$\begin{aligned}\partial_t B_\mu^{(3)} &= \partial_\nu^2 B_\mu - [B_\nu, [B_\nu, B_\mu]] + i[B_\nu, \partial_\nu B_\mu] \\ &\quad - i[B_\nu, \partial_\mu B_\nu] + i\partial_\nu[B_\nu, B_\mu] + i[B_\mu, \partial_\nu B_\nu], \end{aligned} \tag{A.32}$$

$$\partial_t B_\mu^{(3)} = \partial_\nu^2 B_\mu - [B_\nu, [B_\nu, B_\mu]] + 2i[B_\nu, \partial_\nu B_\mu] - i[B_\nu, \partial_\mu B_\nu].$$

And thus we have:

$$\partial_t B_\mu^{(3)} = \partial_\nu^2 B_\mu^{(3)} + R_\mu^{(3)}, \tag{A.33}$$

$$\begin{aligned} R_\mu^{(3)} &= -[B_\nu^{(1)}, [B_\nu^{(1)}, B_\mu^{(1)}]] + 2i[B_\nu^{(1)}, \partial_\nu B_\mu^{(2)}] - i[B_\nu^{(1)}, \partial_\mu B_\nu^{(2)}] \\ &\quad + 2i[B_\nu^{(2)}, \partial_\nu B_\mu^{(1)}] - i[B_\nu^{(2)}, \partial_\mu B_\nu^{(1)}]. \end{aligned} \tag{A.34}$$

With this, we are left with three equations to solve, for which we will have to Fourier transform both the flow fields and the R_μ terms:

$$B_\mu^{(k)}(x,t) = V^{-\frac{1}{2}} {\sum_q}' e^{iqx} \hat{B}_\mu^{(k)}(q,t)\hat{\Gamma}(q), \tag{A.35}$$

$$R_\mu^{(k)}(x,t) = V^{-\frac{1}{2}} {\sum_q}' e^{iqx} R_\mu^{(k)}(q,t)\hat{\Gamma}(q). \tag{A.36}$$

The first order in eq. (A.28) is trivial after Fourier transforming:

$$\sum_p{}' \partial_t e^{ipx}\hat{\Gamma}(p)\hat{B}^{(1)}_\mu(p,t) = -\sum_p{}' p^2 e^{ipx}\hat{\Gamma}(p)\hat{B}^{(1)}_\mu(p,t), \tag{A.37}$$

$$\partial_t \hat{B}^{(1)}_\mu(p,t) = -p^2\hat{B}^{(1)}_\mu(p,t), \tag{A.38}$$

and thus:

$$\hat{B}^{(1)}_\mu(p,t) = e^{-p^2 t}\hat{B}^{(1)}_\mu(p,0) = e^{-p^2 t}A_\mu(p). \tag{A.39}$$

The other two are a bit more tedious. After Fourier transforming them, the flow equations become:

$$\partial_t \hat{B}^{(i)}_\mu(p,t) = p^2\hat{B}^{(i)}_\mu(p,t) + R^{(i)}_\mu(p,t), \qquad i = 2,3, \tag{A.40}$$

which is solved by directly integrating $R^{(i)}_\mu(p,t)$:

$$\hat{B}^{(i)}_\mu(p,t) = \int_0^t ds e^{-(t-s)p^2} R^{(i)}_\mu(p,s), \tag{A.41}$$

and so the crux of the matter is to obtain $R^{(i)}_\mu(p,t)$ for the second and third orders. Let us begin with the former, for which we have:

$$R^{(2)}_\mu = 2i[B^{(1)}_\nu, \partial_\nu B^{(1)}_\mu] - i[B^{(1)}_\nu, \partial_\mu B^{(1)}_\nu]. \tag{A.42}$$

We Fourier-expand the flow fields, and get:

$$R^{(2)}_\mu = 2i[B^{(1)}_\nu, \partial_\nu B^{(1)}_\mu] - i[B^{(1)}_\nu, \partial_\mu B^{(1)}_\nu], \tag{A.43}$$

$$\begin{aligned} R^{(2)}_\mu = &-V^{-1}\sum_{p_1 p_2}{}' e^{i(p_1+p_2)x}[\hat{\Gamma}(p_1), \hat{\Gamma}(p_2)] \\ &\times \left(2p_{2\nu}\hat{B}^{(1)}_\nu(p_1,t)\hat{B}^{(1)}_\mu(p_2,t) - p_{2\mu}\hat{B}^{(1)}_\nu(p_1,t)\hat{B}^{(1)}_\nu(p_2,t)\right), \\ R^{(2)}_\mu = &\, iV^{-1}\sum_q{}' e^{iqx}\hat{\Gamma}(q)\sum_p{}' F(p,q,-p-q) \\ &\times \hat{B}^{(1)}_\nu(q-p,t)\left(2p_\nu\hat{B}^{(1)}_\mu(p,t) - p_\mu\hat{B}^{(1)}_\nu(p,t)\right), \end{aligned} \tag{A.44}$$

where we defined $q = p_1 + p_2$ and renamed $p = p_2$, and where we used the fact that $F(q-p,p,-q) = -F(p,q,-p-q)$. Identifying this last expression with the

one in eq. (A.36), we obtain:

$$R_\mu^{(2)}(p,t) = \frac{i}{\sqrt{V}} \sum_q{}' F(q,p,-q-p)\hat{B}_\nu^{(1)}(p-q,t)\Big(2q_\nu \hat{B}_\mu^{(1)}(q,t) - q_\mu \hat{B}_\nu^{(1)}(q,t)\Big), \tag{A.45}$$

which, using the solution we obtained from the previous order, can be integrated to obtain the solution to the flow equation at second order. The third order solution is obtained in the same manner: we once more Fourier expand the fields, and manipulate them to have an expression similar to the one in eq. (A.36), which is then integrated. As we recall, we had:

$$\begin{aligned} R_\mu^{(3)} = &-[B_\nu^{(1)},[B_\nu^{(1)},B_\mu^{(1)}]] + 2i[B_\nu^{(1)},\partial_\nu B_\mu^{(2)}] - i[B_\nu^{(1)},\partial_\mu B_\nu^{(2)}] \\ &+ 2i[B_\nu^{(2)},\partial_\nu B_\mu^{(1)}] - i[B_\nu^{(2)},\partial_\mu B_\nu^{(1)}], \end{aligned} \tag{A.46}$$

which we will separate into three parts, $R_\mu^{(3)} \equiv X + Y + Z$, with:

$$X = \left[[B_\nu^{(1)},B_\mu^{(1)}],B_\nu^{(1)}\right], \tag{A.47}$$

$$Y = 2i[B_\nu^{(1)},\partial_\nu B_\mu^{(2)}] - i[B_\nu^{(1)},\partial_\mu B_\nu^{(2)}], \tag{A.48}$$

$$Z = 2i[B_\nu^{(2)},\partial_\nu B_\mu^{(1)}] - i[B_\nu^{(2)},\partial_\mu B_\nu^{(1)}]. \tag{A.49}$$

Defining p as the sum of all present momenta p_i, and using the fact that $F(p+q,q,-p) = F(p,q,-p-q)$ we have, for all three terms:

$$X = V^{-\frac{3}{2}} \sum_{p_1p_2p_3}{}' e^{ipx}\hat{B}_\nu^{(1)}(p_1)\left[[\hat{\Gamma}(p_1),\hat{\Gamma}(p_2)],\hat{\Gamma}(p_3)\right]\hat{B}_\mu^{(1)}(p_2,t)\hat{B}_\nu^{(1)}(p_3,t) \tag{A.50}$$

$$\begin{aligned} &= -V^{-\frac{3}{2}} \sum_{p_1p_2p_3}{}' e^{ipx}F(p_1,p_2,-p_1-p_2)F(p_1+p_2,p_3,-p)\hat{\Gamma}(p) \\ &\quad\times \hat{B}_\nu^{(1)}(p_1,t)\hat{B}_\mu^{(1)}(p_2,t)\hat{B}_\nu^{(1)}(p_3,t) \\ &= -V^{-\frac{3}{2}} \sum_{pp_2p_3}{}' e^{ipx}F(p-p_3,p_2,-p-p_2+p_3)F(p,p_3,-p-p_3)\hat{\Gamma}(p) \\ &\quad\times \hat{B}_\nu^{(1)}(p-p_2-p_3,t)\hat{B}_\mu^{(1)}(p_2,t)\hat{B}_\nu^{(1)}(p_3,t), \end{aligned} \tag{A.51}$$

$$
\begin{aligned}
Y &= -V^{-1}{\sum_{p_1p_2}}' e^{ipx}[\hat{\Gamma}(p_1),\hat{\Gamma}(p_2)] \qquad (A.52)\\
&\quad\times(2p_{2\nu}\hat{B}^{(1)}_{\nu}(p_1,t)\hat{B}^{(2)}_{\mu}(p_2,t)-p_{2\mu}\hat{B}^{(1)}_{\nu}(p_1,t)\hat{B}^{(2)}_{\nu}(p_2,t))\\
&= -iV^{-1}{\sum_{p_1p_2}}' e^{ipx}\hat{\Gamma}(p)F(p_1,p_2,-p)\\
&\quad\times(2p_{2\nu}\hat{B}^{(1)}_{\nu}(p_1,t)\hat{B}^{(2)}_{\mu}(p_2,t)-p_{2\mu}\hat{B}^{(1)}_{\nu}(p_1,t)\hat{B}^{(2)}_{\nu}(p_2,t))\\
&= -iV^{-1}{\sum_{pq}}' e^{ipx}\hat{\Gamma}(p)F(p,q,-p-q)\\
&\quad\times(2q_{\nu}\hat{B}^{(1)}_{\nu}(p-q,t)\hat{B}^{(2)}_{\mu}(q,t)-q_{\mu}\hat{B}^{(1)}_{\nu}(p-q,t)\hat{B}^{(2)}_{\nu}(q,t)),\\
Z &= -V^{-1}{\sum_{p_1p_2}}' e^{ipx}[\hat{\Gamma}(p_1),\hat{\Gamma}(p_2)] \qquad (A.53)\\
&\quad\times(2p_{2\nu}\hat{B}^{(2)}_{\nu}(p_1,t)\hat{B}^{(1)}_{\mu}(p_2,t)-p_{2\mu}\hat{B}^{(2)}_{\nu}(p_1,t)\hat{B}^{(1)}_{\nu}(p_2,t))\\
&= -iV^{-1}{\sum_{p_1p_2}}' e^{ipx}\hat{\Gamma}(p)F(p_1,p_2,-p)\\
&\quad\times(2p_{2\nu}\hat{B}^{(2)}_{\nu}(p_1,t)\hat{B}^{(1)}_{\mu}(p_2,t)-p_{2\mu}\hat{B}^{(2)}_{\nu}(p_1,t)\hat{B}^{(1)}_{\nu}(p_2,t))\\
&= -iV^{-1}{\sum_{pq}}' e^{ipx}\hat{\Gamma}(p)F(p,q,-p-q)\\
&\quad\times(2q_{\nu}\hat{B}^{(2)}_{\nu}(p-q,t)\hat{B}^{(1)}_{\mu}(q,t)-q_{\mu}\hat{B}^{(2)}_{\nu}(p-q,t)\hat{B}^{(1)}_{\nu}(q,t)).
\end{aligned}
$$

Summing all three contributions, and comparing the resulting expression with eq. (A.33), we can extract:

$$
\begin{aligned}
&R^{(3)}_{\mu}(p,t)= \qquad (A.54)\\
&V^{-1}{\sum_{qr}}' F(p-r,q,r-p-q)F(p,r,-p-r)\hat{B}^{(1)}_{\nu}(p-q-r,t)\hat{B}^{(1)}_{\mu}(q,t)\hat{B}^{(1)}_{\nu}(r,t)\\
&-iV^{-\frac{1}{2}}{\sum_{q}}' F(p,q,-p-q)(2q_{\nu}\hat{B}^{(1)}_{\nu}(p-q,t)\hat{B}^{(2)}_{\mu}(q,t)-q_{\mu}\hat{B}^{(1)}_{\nu}(p-q,t)\hat{B}^{(2)}_{\nu}(q,t))\\
&-iV^{-\frac{1}{2}}{\sum_{q}}' F(p,q,-p-q)(2q_{\nu}\hat{B}^{(2)}_{\nu}(p-q,t)\hat{B}^{(1)}_{\mu}(q,t)-q_{\mu}\hat{B}^{(2)}_{\nu}(p-q,t)\hat{B}^{(1)}_{\nu}(q,t)),
\end{aligned}
$$

which can be easily rewritten in the form given in section 2.2:

$$R_\mu^{(3)}(p,t) = V^{-1} \sum_{q_1,q_2,q_3}{}' \delta\left(p - \sum_i q_i\right) F(q_1,p,-q_1-p)F(q_2,q_3,-q_2-q_3) \tag{A.55}$$
$$\times \hat{B}_\rho^{(1)}(q_1,t)\hat{B}_\rho^{(1)}(q_2,t)\hat{B}_\mu^{(1)}(q_3,t)$$
$$- 2iV^{-\frac{1}{2}} \sum_{q_1,q_2}{}' \delta\left(p - \sum_i q_i\right) F(q_1,q_2,-q_1-q_2)\, \hat{B}_\rho^{(1)}(q_1,t)\hat{B}_\sigma^{(2)}(q_2,t)$$
$$\times \Big(q_{2\rho}\delta_{\sigma\mu} - q_{1\sigma}\delta_{\rho\mu} - \frac{1}{2}(q_2-q_1)_\mu \delta_{\rho\sigma}\Big).$$

The details of replacing all of the lower order $\hat{B}_\mu$ fields into the higher order ones and integrating the resulting expressions to obtain the full solutions are a bit tedious, and will be ommited. We will merely report the final results for all three orders:

$$\hat{B}_\mu^{(1)}(p,t) = e^{-p^2 t} A_\mu(p), \tag{A.56}$$

$$\hat{B}_\mu^{(2)}(p,t) = iV^{-\frac{1}{2}} e^{-p^2 t} \sum_q{}' F(q,p,-p-q) \tag{A.57}$$
$$\times \int_0^t ds e^{2(p-q)qs} A_\alpha(p-q)(2q_\nu A_\mu(q) - q_\mu A_\alpha(q)),$$

$$\hat{B}_\mu^{(3)}(p,t) = V^{-1} \sum_{qr}{}' \int_0^t ds e^{-(t-s)p^2} \Big(\int_0^s dz F(p,q,-p-q)F(r,q,-q-r) \tag{A.58}$$
$$\times e^{-\{q^2+(p-q)^2\}s - 2(r^2-qr)z}(2\alpha - 2\gamma + \delta - \beta) - F(p-r,q,r-p-q)$$
$$\times F(p,r,-p-r) e^{-((p-q-r)^2+q^2+r^2)s} A_\alpha(p-q-r)A_\mu(q)A_\alpha(r)\Big),$$

where we defined:

$$\alpha \equiv 2q_\beta r_\alpha A_\beta(p-q)A_\alpha(q-r)A_\mu(r) - q_\beta r_\mu A_\beta(p-q)A_\alpha(q-r)A_\alpha(r), \tag{A.59}$$

$$\beta \equiv 2q_\mu r_\alpha A_\beta(p-q)A_\alpha(q-r)A_\beta(r) - q_\mu r_\beta A_\beta(p-q)A_\alpha(q-r)A_\alpha(r), \tag{A.60}$$

$$\gamma \equiv 2(p-q)_\beta r_\alpha A_\alpha(q-r)A_\beta(r)A_\mu(p-q)$$
$$- (p-q)_\beta r_\beta A_\alpha(q-r)A_\alpha(r)A_\mu(p-q), \tag{A.61}$$

$$\delta \equiv 2(p-q)_\mu r_\alpha A_\alpha(q-r)A_\beta(r)A_\beta(p-q)$$
$$- (p-q)_\mu r_\beta A_\alpha(q-r)A_\alpha(r)A_\beta(p-q). \tag{A.62}$$

A.4 Contributions to the energy density

In section 2.2.2, we identified seven different terms contributing to the energy density $E(t)/N$, labelled $\mathcal{E}_i(t)$ and given in terms of the flow fields in momentum space, $\hat{B}_\mu(p,t)$. We will in this appendix combine the solutions of the flow equations found in appendix A.3 with the Feynman rules from app. A.2 to determine one by one an expression for each of the aforementioned terms. Let us begin.

Determination of $\mathcal{E}_0(t)$ For the first term, we had:

$$\mathcal{E}_0(t) = \frac{g_0^2}{2NV}\sum_q{}' (q^2\delta_{\mu\nu} - q_\mu q_\nu)\langle \hat{B}^{(1)}_\mu(-q,t)\hat{B}^{(1)}_\nu(q,t)\rangle. \tag{A.63}$$

Inserting the expression of the flow fields obtained in appendix A.3 we obtain, in terms of the vacuum polarisation tensor $\Pi_{\mu\nu}(p)$:

$$\mathcal{E}_0(t) = \frac{g_0^2}{2NV}\sum_q{}' e^{-2q^2t}\left(\delta_{\mu\nu} - q^{-2}q_\mu q_\nu\right)\left(\delta_{\mu\nu} + q^{-2}\Pi_{\mu\nu}(q)\right), \tag{A.64}$$

$$\mathcal{E}_0(t) = \frac{g_0^2}{2NV}\sum_q{}' e^{-2q^2t}\left(d - 1 + q^{-2}\Pi_{\mu\mu}(q)\delta_{\mu\nu} - q^{-4}q_\mu\Pi_{\mu\nu}(q)q_\nu\right), \tag{A.65}$$

$$\begin{aligned}\mathcal{E}_0(t) = {}& \frac{g_0^2}{2NV}(d-1)\sum_q{}' e^{-2q^2t} \\ & + \frac{g_0^2}{2NV}\sum_q{}' e^{-2q^2t}\left(q^{-2}\Pi_{\mu\mu}(q)\delta_{\mu\nu} - q^{-4}q_\mu\Pi_{\mu\nu}(q)q_\nu\right).\end{aligned} \tag{A.66}$$

The rightmost term vanishes on account of the Ward identities, and all that is left is to insert the expression of $\Pi_{\mu\mu}$ from appendix A.2:

$$\begin{aligned}\Pi_{\mu\mu}(q) = {}& \frac{g_0^2}{2V}\sum_p \frac{F^2(p,q,-p-q)}{p^2(p+q)^2} \\ & \times\left(4(d-1)q^2 + (d-2)(-q^2 + 2((p+q)^2 - p^2)) + 2(2-d)p^2)\right).\end{aligned} \tag{A.67}$$

Since $F^2(p,q,-p-q) = F^2(p+q,q,-p-2q)$, one of the terms in the sum vanishes:

$$\sum_p \frac{F^2(p,q,-p-q)}{p^2(p+q)^2}((p+q)^2 - p^2) = \sum_p F^2(p,q,-p-q)\left(\frac{1}{p^2} - \frac{1}{(p+q)^2}\right) = 0, \tag{A.68}$$

and thus:

$$\Pi_{\mu\mu}(q) = \frac{g_0^2}{2V} \sum_p F^2(p,q,-p-q) \left(\frac{(3d-2)q^2}{p^2(p+q)^2} - \frac{2(2-d)^2}{(p+q)^2} \right). \tag{A.69}$$

Therefore:

$$\begin{aligned} \mathcal{E}_0(t) = & \frac{g_0^2}{2NV} \sum_q{}' e^{-2tq^2}(d-1) \\ & + \frac{g_0^4}{4NV^2} \sum_{q,r}{}' e^{-2tq^2} F^2(q,r,-q-r) \frac{(3d-2)q^2 - 2(d-2)^2 r^2}{q^2 r^2 (q+r)^2}. \end{aligned} \tag{A.70}$$

Introducing the bare 't Hooft coupling $\lambda_0 = g_0^2 N$, and, for clarity, the abbreviation:

$$\widehat{\sum_{q,r}} \equiv \tilde{l}^{-2d} \sum_{q,r} N F^2(q,r,-q-r), \tag{A.71}$$

we obtain the expression shown in eq. (2.34):

$$\begin{aligned} \mathcal{E}_0(t) = & \frac{1}{2}\lambda_0 \tilde{l}^{-d} \sum_q{}' e^{-2tq^2}(d-1) \\ & + \frac{1}{4}\lambda_0^2 \widehat{\sum_{q,r}} e^{-2tq^2} \frac{(3d-2)q^2 - 2(d-2)^2 r^2}{q^2 r^2 (q+r)^2}. \end{aligned} \tag{A.72}$$

Derivation of $\mathcal{E}_1(t)$ For the second term, we begin with:

$$\begin{aligned} \mathcal{E}_1(t) = & -\frac{g_0^3}{NV^{\frac{3}{2}}} \sum_{p_1 p_2 p_3}{}' F(p_1,p_2,p_3)\delta(\sum p_i) i p_{1\mu} \\ & \times \left\langle \hat{B}_\nu^{(1)}(p_1,t) \hat{B}_\mu^{(1)}(p_2,t) \hat{B}_\nu^{(1)}(p_3,t) \right\rangle. \end{aligned} \tag{A.73}$$

Inserting the solutions to the flow equations for the first order fields, this becomes:

$$\begin{aligned} \mathcal{E}_1(t) = & -\frac{g_0^3}{NV^{\frac{3}{2}}} \sum_{p_1 p_2 p_3}{}' F(p_1,p_2,p_3)\delta(\sum p_i) e^{-(p_1^2+p_2^2+p_3^2)t} \\ & \times p_{1\mu} \left\langle A_\nu(p_1) A_\mu(p_2) A_\nu(p_3) \right\rangle \end{aligned} \tag{A.74}$$

Pulling the three-point function from the Feynman rules:

$$\Big\langle A_\nu(p_1)A_\mu(p_2)A_\nu(p_3)\Big\rangle = \frac{ig_0}{V^{\frac{1}{2}}}(d-1)F(p_1,p_2,p_3)\frac{(p_3-p_1)_\mu}{p_1^2p_2^2p_3^2}, \tag{A.75}$$

we obtain:

$$\mathcal{E}_1(t) = \frac{g_0^4}{NV^2}\sum_{p_1p_2p_3}{}' F^2(p_1,p_2,p_3)\delta(\sum p_i)(d-1)e^{-(p_1^2+p_2^2+p_3^2)t}\frac{p_1p_3-p_1^2}{p_1^2p_2^2p_3^2}, \tag{A.76}$$

which, respectively renaming p_1, p_2, p_3 to $-p, r, q$ and eliminating p from the sum using the delta function, yields:

$$\mathcal{E}_1(t) = -\frac{g_0^4}{NV^2}\sum_{qr}{}'(d-1)F^2(q,r,-p)e^{-(p^2+q^2+r^2)t}\frac{(q+r)(2q+r)}{p^2q^2r^2}. \tag{A.77}$$

On account of the integrand's $q \leftrightarrow r$ symmetry, the $q^2 - r^2$ terms will cancel out:

$$-(q+r)(2q+r) = -\frac{1}{2}(3(q+r)^2 + q^2 - r^2), \tag{A.78}$$

and therefore:

$$\mathcal{E}_1(t) = \frac{g_0^4}{NV^2}\sum_{qr}{}' F^2(q,r,-p)e^{-(p^2+q^2+r^2)t}\frac{3(1-d)}{2q^2r^2}, \tag{A.79}$$

which, introducing once again the 't Hooft coupling and abbreviated sum yields the expression shown in (2.36):

$$\mathcal{E}_1(t) = \frac{3}{2}\lambda_0^2\widehat{\sum_{q,r}}e^{-t(q^2+r^2+p^2)}\frac{1}{q^2r^2}(1-d). \tag{A.80}$$

Note that, from here onwards, we will keep the convention of denoting the momenta that are summed over q and r, and denote their sum $p = q + r$.

Derivation of $\mathcal{E}_2(t)$ For the next term, we begin with:

$$\mathcal{E}_2(t) = \frac{g_0^3}{NV}\sum_{q}{}'(q^2\delta_{\mu\nu} - q_\mu q_\nu)\Big\langle \hat{B}_\mu^{(1)}(-q,t)\hat{B}_\nu^{(2)}(q,t)\Big\rangle. \tag{A.81}$$

Plugging in the solutions to the flow equation, we get:

$$\mathcal{E}_2(t) = \frac{ig_0^3}{NV^{\frac{3}{2}}}\int_0^t ds \sum_q r' F(r,q,-p) e^{-2(q^2 t+(r^2-qr)s)}(q^2\delta_{\mu\nu}-q_\mu q_\nu) \tag{A.82}$$
$$\times \left(2r_\alpha \Big\langle A_\mu(-q)A_\alpha(q-r)A_\nu(r)\Big\rangle - r_\nu \Big\langle A_\mu(-q)A_\alpha(q-r)A_\alpha(r)\Big\rangle\right).$$

The three-point functions in that function yields, looking at the Feynman rules:

$$\Big\langle A_\mu(-q)A_\alpha(q-r)A_\nu(r)\Big\rangle = \frac{ig_0}{\sqrt{V}}F(q,r,-p)\frac{(2r-q)_\mu\delta_{\alpha\nu}-(q+r)_\alpha\delta_{\mu\nu}-r_\nu\delta_{\mu\alpha}}{q^2r^2(q-r)^2}, \tag{A.83}$$

$$\Big\langle A_\mu(-q)A_\alpha(q-r)A_\alpha(r)\Big\rangle = \frac{ig_0}{\sqrt{V}}F(q,r,-p)\frac{2(d-1)r_\mu-(d+1)q}{q^2r^2(q-r)^2}. \tag{A.84}$$

Contracting these terms with the r and $q^2\delta_{\mu\nu}-q_\mu q_\nu$ terms, one ends up with:

$$\mathcal{E}_2(t) = \frac{2g_0^4}{NV^2}\int_0^t ds \sum_{qr}{}' F^2(q,r,-p)e^{-2(q^2t+(r^2-qr)s)} \tag{A.85}$$
$$\times \frac{(d-1)(q^2r^2+q^2qr)+(d-2)(q^2r^2-(qr)^2)}{q^2r^2(q-r)^2},$$

which under a $q \to q+r$ shift in the sum and after a bit of algebra becomes:

$$\mathcal{E}_2(t) = \frac{g_0^4}{NV^2}\int_0^t ds \sum_{qr}{}' F^2(q,r,-p)e^{-2tp^2+2s(qr)}\frac{1}{p^2q^2r^2} \tag{A.86}$$
$$\times ((d-1)p^2(p^2+q^2+r^2)+2(d-2)(q^2r^2-(qr)^2)).$$

Once more, inserting the expression of the 't Hooft coupling and abbreviated sum, we get the expression given in eq. (2.37):

$$\mathcal{E}_2(t) = \lambda_0^2\int_0^t ds \widehat{\sum_{q,r}} e^{-2tp^2+2s(qr)}\frac{1}{p^2q^2r^2} \tag{A.87}$$
$$\times \left\{(d-1)p^2\left(p^2+q^2+r^2\right)+2(d-2)\left(q^2r^2-(qr)^2\right)\right\}.$$

Derivation of $\mathcal{E}_3(t)$ Next comes:

$$\mathcal{E}_3(t) = \frac{g_0^4}{2NV}\sum_q{}'\left(q^2\delta_{\mu\nu}-q_\mu q_\nu\right)\Big\langle \hat{B}_\mu^{(2)}(-q,t)\hat{B}_\nu^{(2)}(q,t)\Big\rangle. \tag{A.88}$$

Plugging in the solutions to the flow equation we obtain:

$$\mathcal{E}_3(t) = \frac{g_0^4}{2NV^2}\int_0^t ds_1 \int_0^t ds_2 \sum_{qr_1r_2}{}' F(r_1, q, -q-r_1)F(r_2, q, -q-r_2) \\ \times e^{-2(q^2t+(r_1^2+qr_1)s_1+(r_2^2-qr_2)s_2)}(q^2\delta_{\mu\nu} - q_\mu q_\nu)\langle A_{\mu\nu}\rangle, \tag{A.89}$$

where we defined:

$$A_{\mu\nu} = A_\alpha(-q-r_1)(2r_{1\alpha}A_\mu(r_1) - r_{1\mu}A_\alpha(r_1))A_\beta(q-r_2)(2r_{2\beta}A_\nu(r_2) - r_{2\nu}A_\beta(r_2)). \tag{A.90}$$

We will thus need to use the four-gluon vertex of the Feynman rules to compute four terms of the form:

$$\langle A_{\mu\nu}\rangle = 4r_{1\alpha}r_{2\beta}\langle A_1\rangle + r_{1\mu}r_{2\nu}\langle A_2\rangle - 2r_{1\alpha}r_{2\nu}\langle A_3\rangle - 2r_{1\mu}r_{2\beta}\langle A_4\rangle, \tag{A.91}$$

where:

$$\langle A_1\rangle = \langle A_\alpha(-q-r_1)A_\mu(r_1)A_\beta(q-r_2)A_\nu(r_2)\rangle\,, \tag{A.92}$$
$$\langle A_2\rangle = \langle A_\alpha(-q-r_1)A_\alpha(r_1)A_\beta(q-r_2)A_\beta(r_2)\rangle\,, \tag{A.93}$$
$$\langle A_3\rangle = \langle A_\alpha(-q-r_1)A_\mu(r_1)A_\beta(q-r_2)A_\beta(r_2)\rangle\,, \tag{A.94}$$
$$\langle A_4\rangle = \langle A_\alpha(-q-r_1)A_\alpha(r_1)A_\beta(q-r_2)A_\nu(r_2)\rangle\,. \tag{A.95}$$

This yields, ommiting all terms in $\delta(q)$ which will vanish upon summation:

$$\langle A_1\rangle = r_1^{-2}(q+r_1)^{-2}(\delta_{\alpha\beta}\delta_{\mu\nu}\delta(r_1+r_2) + \delta_{\alpha\nu}\delta_{\mu\beta}\delta(r_1+q-r_2)), \tag{A.96}$$
$$\langle A_2\rangle = r_1^{-2}(q+r_1)^{-2}d(\delta(r_1+r_2) + \delta(r_1+q-r_2)), \tag{A.97}$$
$$\langle A_3\rangle = r_1^{-2}(q+r_1)^{-2}(\delta_{\alpha\mu}\delta(r_1+r_2) + \delta_{\alpha\mu}\delta(r_1+q-r_2)), \tag{A.98}$$
$$\langle A_4\rangle = r_1^{-2}(q+r_1)^{-2}(\delta_{\beta\nu}\delta(r_1+r_2) + \delta_{\beta\nu}\delta(r_1+q-r_2)). \tag{A.99}$$

Contracting all of these terms with the corresponding r momenta, renaming r_1 to r and using the deltas to eliminate r_2 from the expression, one obtains:

$$(q^2\delta_{\mu\nu} - q_\mu q_\nu)\langle A_{\mu\nu}\rangle = d(q^2r^2 - (qr)^2)\frac{\delta(r+q-r_2)}{r^2(q+r)^2} \\ - (4(d-1)q^2r^2 + (d-4)(q^2r^2 - (qr)^2))\frac{\delta(r+r_2)}{r^2(q+r)^2}. \tag{A.100}$$

Bringing this into the full expression of $\mathcal{E}_3(t)$, and after a bit of algebra, we get:

$$\mathcal{E}_3(t) = \frac{g_0^4}{NV^2} {\sum_{qr}}' F^2(q,r,-p) \int_0^t ds_1 \int_0^t ds_2 e^{-2p^2t+2qr(s_1+s_2)} \times \frac{1}{q^2r^2}\left(2(d-1)p^2r^2 + (d-2)(q^2r^2-(qr)^2)\right), \tag{A.101}$$

which, defining a new variable $s = s_1 + s_2$, leads to:

$$\mathcal{E}_3(t) = \frac{g_0^4}{NV^2} \int_0^t ds s {\sum_{qr}}' F^2(q,r,-p) e^{-2tp^2}\left(e^{2s(qr)} + e^{2(2t-s)(qr)}\right) \times \frac{1}{q^2r^2}\left(2(d-1)p^2r^2 + (d-2)(q^2r^2-(qr)^2)\right), \tag{A.102}$$

which once more is simply the same expression shown in eq. (2.38):

$$\mathcal{E}_3(t) = \lambda_0^2 \int_0^t ds s \widehat{\sum_{q,r}} e^{-2tp^2}\left(e^{2s(qr)} + e^{2(2t-s)(qr)}\right) \times \frac{1}{q^2r^2}\left(2(d-1)p^2r^2 + (d-2)\left(q^2r^2-(qr)^2\right)\right). \tag{A.103}$$

Derivation of $\mathcal{E}_4(t)$ Next in line is:

$$\mathcal{E}_4(t) = \frac{g_0^4}{4NV^2} {\sum_{p_1p_2p_3p_4}}' F(p_1,p_2,-p_1-p_2)F(p_3,p_4,-p_3-p_4) \times \delta(\sum p_i)\left\langle \hat{B}_\mu^{(1)}(p_1,t)\hat{B}_\nu^{(1)}(p_2,t)\hat{B}_\mu^{(1)}(p_3,t)\hat{B}_\nu^{(1)}(p_4,t)\right\rangle. \tag{A.104}$$

As usual, we plug in the solutions to the flow equation:

$$\mathcal{E}_4(t) = \frac{g_0^4}{4NV^2} {\sum_{p_1p_2p_3p_4}}' F(p_1,p_2,-p_1-p_2)F(p_3,p_4,-p_3-p_4) \times \delta(\sum p_i)e^{-(p_1^2+p_2^2+p_3^2+p_4^2)t}\left\langle A_\mu(p_1)A_\nu(p_2)A_\mu(p_3)A_\nu(p_4)\right\rangle, \tag{A.105}$$

which, using the four-gluon vertex from the Feynman rules, yields:

$$\begin{aligned}\mathcal{E}_4(t) = \frac{g_0^4}{4NV^2} \sum_{p_1p_2p_3p_4}{}' F(p_1,p_2,-p_1-p_2)F(p_3,p_4,-p_3-p_4) \\ \times \delta(\sum p_i) e^{-(p_1^2+p_2^2+p_3^2+p_4^2)t}\Big(\delta(p_1+p_2)\delta(p_3+p_4)\frac{d}{p_1^2p_3^2} \\ + \delta(p_1+p_4)\delta(p_2+p_3)\frac{d}{p_1^2p_3^2} + \delta(p_1+p_3)\delta(p_2+p_4)\frac{d^2}{p_1^2p_2^2}\Big).\end{aligned} \tag{A.106}$$

The deltas can then be used to eliminate two of the sums, namely p_1 and p_4, noting that the $\delta(p_1+p_2)$ term will give rose to a vanishing $F(p_2,p_2,-2p_2)$ term. After a bit of algebra, we get:

$$\begin{aligned}\mathcal{E}_4(t) = \frac{g_0^4}{4NV^2} \sum_{p_2p_3}{}' \frac{d^2}{p_2^2p_3^2} F^2(p_3,p_2,-p_2-p_3)e^{-2(p_2^2+p_3^2)t} \\ - \frac{g_0^4}{4NV^2} \sum_{p_1p_2}{}' \frac{d}{p_1^2p_2^2} F^2(p_1,p_2,-p_1-p_2)e^{-2(p_1^2+p_2^2)t}.\end{aligned} \tag{A.107}$$

Renaming the momenta, both terms can be combined, and we obtain:

$$\mathcal{E}_4(t) = \frac{g_0^4}{4NV^2} \sum_{qr}{}' F^2(q,r,-p)e^{-2(q^2+r^2)t}\frac{d(d-1)}{q^2r^2}, \tag{A.108}$$

which again is the term given in eq. (2.39):

$$\mathcal{E}_4(t) = \frac{1}{4}\lambda_0^2 \widehat{\sum_{q,r}} e^{-2t(q^2+r^2)}\frac{1}{q^2r^2}d(d-1). \tag{A.109}$$

Derivation of $\mathcal{E}_5(t)$ The next term to be computed is:

$$\begin{aligned}\mathcal{E}_5(t) = \frac{-ig_0^4}{NV^{3/2}} \sum_{p_1,p_2,p_3}{}' \delta\left(\sum p_i\right) p_{1\mu}\, F(p_1,p_2,p_3)\Big\{\Big\langle \hat{B}_\nu^{(2)}(p_1,t)\,\hat{B}_\mu^{(1)}(p_2,t)\,\hat{B}_\nu^{(1)}(p_3,t)\Big\rangle \\ + \Big\langle \hat{B}_\nu^{(1)}(p_1,t)\hat{B}_\mu^{(2)}(p_2,t)\hat{B}_\nu^{(1)}(p_3,t)\Big\rangle + \Big\langle \hat{B}_\nu^{(1)}(p_1,t)\,\hat{B}_\mu^{(1)}(p_2,t)\,\hat{B}_\nu^{(2)}(p_3,t)\Big\rangle\Big\}.\end{aligned} \tag{A.110}$$

We first need to use the Feynman rules, after inserting the expressions of the fields, to derive the three contributing terms:

$$\left\langle \hat{B}_\nu^{(2)}(p_1,t)\hat{B}_\mu^{(1)}(p_2,t)\hat{B}_\nu^{(1)}(p_3,t)\right\rangle = \frac{i}{\sqrt{V}}{\sum_{p_4}}' F(p_4-p_1,-p_1-p_4) \times \int_0^t ds e^{-t(p_1^2+p_2^2+p_3^2)-2(p_4^2-p_1p_4)s}(2p_{4\alpha}\langle X_1\rangle - p_{4\nu}\langle Y_1\rangle), \tag{A.111}$$

$$\left\langle \hat{B}_\nu^{(1)}(p_1,t)\hat{B}_\mu^{(2)}(p_2,t)\hat{B}_\nu^{(1)}(p_3,t)\right\rangle = \frac{i}{\sqrt{V}}{\sum_{p_4}}' F(p_4-p_2,-p_2-p_4) \times \int_0^t ds e^{-t(p_1^2+p_2^2+p_3^2)-2(p_4^2-p_2p_4)s}(2p_{4\alpha}\langle X_2\rangle - p_{4\nu}\langle Y_2\rangle), \tag{A.112}$$

$$\left\langle \hat{B}_\nu^{(1)}(p_1,t)\hat{B}_\mu^{(1)}(p_2,t)\hat{B}_\nu^{(2)}(p_3,t)\right\rangle = \frac{i}{\sqrt{V}}{\sum_{p_4}}' F(p_4-p_3,-p_3-p_4) \times \int_0^t ds e^{-t(p_1^2+p_2^2+p_3^2)-2(p_4^2-p_3p_4)s}(2p_{4\alpha}\langle X_3\rangle - p_{4\nu}\langle Y_3\rangle), \tag{A.113}$$

where we defined:

$$\langle X_1\rangle = \langle A_\alpha(p_1-p_4)A_\nu(p_4)A_\mu(p_2)A_\nu(p_3)\rangle, \tag{A.114}$$
$$\langle Y_1\rangle = \langle A_\alpha(p_1-p_4)A_\alpha(p_4)A_\mu(p_2)A_\nu(p_3)\rangle, \tag{A.115}$$
$$\langle X_2\rangle = \langle A_\nu(p_1)A_\alpha(p_2-p_4)A_\mu(p_4)A_\nu(p_3)\rangle, \tag{A.116}$$
$$\langle Y_2\rangle = \langle A_\nu(p_1)A_\alpha(p_2-p_4)A_\alpha(p_4)A_\nu(p_3)\rangle, \tag{A.117}$$
$$\langle X_3\rangle = \langle A_\nu(p_1)A_\mu(p_2)A_\alpha(p_3-p_4)A_\nu(p_4)\rangle, \tag{A.118}$$
$$\langle Y_3\rangle = \langle A_\nu(p_1)A_\mu(p_2)A_\alpha(p_3-p_4)A_\alpha(p_4)\rangle. \tag{A.119}$$

Contracting these terms with their corresponding momenta, and eliminating once again the terms in $\delta(p_i)$ as they will vanish due to the F factors, a global $\delta(\sum p_i)$ factor will appear, and we will have:

$$p_{1\mu}p_{4\alpha}\langle X_1\rangle = \frac{p_1p_4}{p_2^2p_3^2}(\delta(p_4+p_3)d+\delta(p_4+p_2)), \tag{A.120}$$
$$p_{1\mu}p_{4\nu}\langle Y_1\rangle = \frac{p_1p_4}{p_2^2p_3^2}(\delta(p_4+p_3)+\delta(p_4+p_2)), \tag{A.121}$$
$$p_{1\mu}p_{4\alpha}\langle X_2\rangle = \frac{p_1p_4}{p_1^2p_3^2}(\delta(p_4+p_3)+\delta(p_1+p_4)), \tag{A.122}$$
$$p_{1\mu}p_{4\nu}\langle Y_2\rangle = \frac{p_1p_4}{p_1^2p_3^2}(\delta(p_4+p_3)d+\delta(p_1+p_4)d), \tag{A.123}$$

$$p_{1\mu}p_{4\alpha}\langle X_3\rangle = \frac{p_1p_4}{p_1^2p_2^2}(\delta(p_1+p_4)d+\delta(p_2+p_4)), \tag{A.124}$$

$$p_{1\mu}p_{4\nu}\langle Y_3\rangle = \frac{p_1p_4}{p_1^2p_2^2}(\delta(p_2+p_4)+\delta(p_1+p_4)), \tag{A.125}$$

which in turn will yield three contributions:

$$p_{1\mu}(2p_{4\alpha}\langle X_1\rangle - p_{4\nu}\langle Y_1\rangle) = \frac{p_1p_4}{p_2^2p_3^2}((2d-1)\delta(p_3+p_4)+\delta(p_2+p_4)), \tag{A.126}$$

$$p_{1\mu}(2p_{4\alpha}\langle X_2\rangle - p_{4\mu}\langle Y_2\rangle) = \frac{p_1p_4}{p_1^2p_3^2}((2-d)\delta(p_3+p_4)+(2-d)\delta(p_1+p_4)), \tag{A.127}$$

$$p_{1\mu}(2p_{4\alpha}\langle X_3\rangle - p_{4\nu}\langle Y_3\rangle) = \frac{p_1p_4}{p_1^2p_2^2}((2d-1)\delta(p_1+p_4)+\delta(p_2+p_4)). \tag{A.128}$$

After inserting this into the expression of $\mathcal{E}_4$, we use the delta functions to eliminate the sum over p_4, and rename the variables so as to pull out a common exponent and group similar terms. After a bit of algebra, we obtain:

$$\begin{aligned}\mathcal{E}_5(t) = \frac{g_0^4}{NV^2}\int_0^t ds \sum_{p_1p_2p_3}{}' \delta(\sum p_i)e^{-t(p_1^2+p_2^2+p_3^2)-2(p_3^2+p_2p_3)s}(d-1) \\ \times\Big(\frac{2p_2p_3}{p_1^2p_3^2}F(p_1,p_3,-p_1-p_3)F(p_3,p_2,-p_2-p_3) \\ +\frac{3}{p_1^2}F(p_1,p_2,-p_1-p_2)F(p_3,p_2,-p_2-p_3)+\frac{p_1p_3}{p_1^2p_3^2}F^2(p_3,p_2,-p_2-p_3)\Big),\end{aligned} \tag{A.129}$$

from which we eliminate the sum over p_1 using the delta function, rename the remaining momenta to p and q and shift one of the variables to obtain our final result:

$$\mathcal{E}_5(t) = \frac{g_0^4}{NV^2}\int_0^t ds \sum_{qr}{}' F^2(q,r,-p)e^{-(t+s)(q^2+r^2)-(t-s)p^2}\frac{1}{q^2r^2}(1-d)\left(5r^2+(qr)\right), \tag{A.130}$$

which once again is the term shown in eq. (2.40):

$$\mathcal{E}_5(t) = \lambda_0^2\int_0^t ds \widehat{\sum_{q,r}} e^{-(t+s)(q^2+r^2)-(t-s)p^2}\frac{1}{q^2r^2}(1-d)\left(5r^2+(qr)\right). \tag{A.131}$$

Derivation of $\mathcal{E}_6(t)$ Finally, for the last term:

$$\mathcal{E}_6(t) = \frac{g_0^4}{NV}\sum_q{}'\left(q^2\delta_{\mu\nu}-q_\mu q_\nu\right)\left\langle \hat{B}_\mu^{(1)}(-q,t)\,\hat{B}_\nu^{(3)}(q,t)\right\rangle, \tag{A.132}$$

the procedure is the same as for the previous five, starting with the solutions to the flow equation. This is a bit long, so to make it more readable we begin by defining nine auxiliary functions:

$$\beta_0 = (q^2\delta_{\mu\nu} - q_\mu q_\nu)\langle A_\alpha(q-p-r)A_\mu(p)A_\alpha(r)A_\nu(-q)\rangle, \tag{A.133}$$
$$\beta_1 = (q^2\delta_{\mu\nu} - q_\mu q_\nu)\langle 4p_\beta r_\alpha A_\beta(q-p)A_\alpha(p-r)A_\mu(r)A_\nu(-q)\rangle, \tag{A.134}$$
$$\beta_2 = -(q^2\delta_{\mu\nu} - q_\mu q_\nu)\langle 4(q-p)_\beta r_\alpha A_\alpha(p-r)A_\beta(r)A_\mu(q-p)A_\nu(-q)\rangle, \tag{A.135}$$
$$\beta_3 = -(q^2\delta_{\mu\nu} - q_\mu q_\nu)\langle 2p_\mu r_\alpha A_\beta(q-p)A_\alpha(p-r)A_\beta(r)A_\nu(-q)\rangle, \tag{A.136}$$
$$\beta_4 = (q^2\delta_{\mu\nu} - q_\mu q_\nu)\langle 2(q-p)_\beta r_\beta A_\alpha(p-r)A_\alpha(r)A_\mu(q-p)A_\nu(-q)\rangle, \tag{A.137}$$
$$\beta_5 = -(q^2\delta_{\mu\nu} - q_\mu q_\nu)\langle 2p_\beta R_\mu A_\beta(q-p)A_\alpha(p-r)A_\alpha(r)A_\nu(-q)\rangle, \tag{A.138}$$
$$\beta_6 = (q^2\delta_{\mu\nu} - q_\mu q_\nu)\langle 2(q-p)_\mu r_\alpha A_\alpha(p-r)A_\beta(r)A_\beta(q-p)A_\nu(-q)\rangle, \tag{A.139}$$
$$\beta_7 = (q^2\delta_{\mu\nu} - q_\mu q_\nu)\langle p_\mu r_\beta A_\beta(q-p)A_\alpha(p-r)A_\alpha(r)A_\nu(-q)\rangle, \tag{A.140}$$
$$\beta_8 = -(q^2\delta_{\mu\nu} - q_\mu q_\nu)\langle (q-p)_\mu r_\beta A_\alpha(p-r)A_\alpha(r)A_\beta(q-p)A_\nu(-q)\rangle. \tag{A.141}$$

With this, we can rewrite:

$$\begin{aligned}\mathcal{E}_6(t) = -\frac{g_0^4}{NV^2}\Big(\int_0^t ds \sum_{pqr}{}' F(q-r,p,r-p-q)F(q,r,-q-r) \\ \times e^{-2tq^2-2s(p^2+r^2+pr-pq-qr}\beta_0\Big) + \frac{g_0^4}{NV^2}\Big(\int_0^t ds_1\int_0^{s_1} ds_2 \\ \times \sum_{pqr}{}' F(q,p,-p-q)F(r,p,-p-r)e^{-2tq^2-2s_1(p^2-pq)-2s_2(r^2-pr)}\sum_{i=1}^{8}\beta_i\Big).\end{aligned} \tag{A.142}$$

For the first term, we can simply plug in the Feynman rules for the four-point vertex and get:

$$\beta_0 = (d-1)\left(\frac{1}{p^2}\delta(q-r) + \frac{d}{r^2}\delta(p-q) + \frac{1}{r^2}\delta(p+r)\right). \tag{A.143}$$

The contribution of this term will be, using the fact that $F(q,q,0) = 0$:

$$-\frac{g_0^4}{NV^2}(d-1)^2\int_0^t ds\sum_{qr}{}' F^2(q,r,-p)\frac{1}{r}e^{-2tq^2-2sr^2}. \tag{A.144}$$

The other eight terms are a bit longer, but the idea is the same. We use the Feynman rules, keeping in mind that all terms in $\delta(p_i)$ will vanish on account of

the F functions, and get:

$$\beta_1 = 4(d-1)\frac{pq}{(p-q)^2}\delta(q-r) + 4\frac{q^2r^2-(qr)^2}{q^2r^2}\delta(p-q-r), \tag{A.145}$$

$$\beta_2 = 4\frac{q^2r^2-(qr)^2}{q^2r^2}\delta(p-q-r), \tag{A.146}$$

$$\beta_3 = \beta_6 = -2d\frac{q^2r^2-(qr)^2}{q^2r^2}\delta(p-q-r), \tag{A.147}$$

$$\beta_4 = 2(d-1)\frac{q^2-pq}{(p-q)^2}\delta(q-r) - 2(d-1)\delta(p-q-r), \tag{A.148}$$

$$\beta_5 = -2\frac{q^2r^2-(qr)^2}{q^2r^2}\delta(p-q-r), \tag{A.149}$$

$$\beta_7 = \beta_8 = \frac{q^2r^2-(qr)^2}{q^2r^2}\delta(p-q-r), \tag{A.150}$$

whose sum will be:

$$\begin{aligned}\sum_{i=1}^{8}\beta_i = &\Big[2(d-1)\frac{q^2+pq}{(p-q)^2}\Big]\delta(q-r) \\ &+ \Big[4(2-d)\frac{q^2r^2-(qr)^2}{q^2r^2} - 2(d-1)\Big]\delta(p-q-r).\end{aligned} \tag{A.151}$$

The contribution of these two terms to $\mathcal{E}_6$ will then be:

$$\sum_{pqr}{}' F(q,p,-p-q)F(r,p,-p-r)e^{-2tq^2-2s_1(p^2-pq)-2s_2(r^2-pr)}\delta(q-r) \tag{A.152}$$

$$= \quad -\sum_{qr}{}' F^2(q,r,-p)e^{-2tq^2-s_1(2r^2-2qr)-s_2(2qr)},$$

$$\sum_{pqr}{}' F(q,p,q-p)F(r,p,-p-r)e^{-2tq^2-2s_1(p^2-pq)-2s_2(r^2-pr)}\delta(p-q-r) \tag{A.153}$$

$$= \quad -\sum_{qr}{}' F^2(q,r,-q-r)e^{-2tq^2-s_1(2r^2-2qr)-s_2(2qr)}. \tag{A.154}$$

And thus, combining them with the contribution of the β_0 term and shifting $q \to q+r$ we end up with:

$$\mathcal{E}_6(t) = \frac{g_0^4}{NV^2}\int_0^t ds \sum_{qr}{}' F^2(q,r,-p)e^{-2tq^2-2sr^2}\frac{1}{r^2}(d-1)^2 \tag{A.155}$$
$$+ 2\frac{g_0^4}{NV^2}\int_0^t ds_1\int_0^{s_1} ds_2 \sum_{qr}{}' F^2(q,r,-p)e^{-2tp^2+2s_1(qr)-2s_2(pq)}\frac{1}{p^2q^2}$$
$$\times\left\{2(d-2)\left(p^2q^2-(pq)^2\right)+(d-1)p^2\left(2p^2-(qr)\right)\right\}.$$

This is, one last time, the same expression as in eq. (2.41):

$$\mathcal{E}_6(t) = -\lambda_0^2\int_0^t ds\widehat{\sum_{q,r}} e^{-2tq^2-2sr^2}\frac{1}{r^2}(d-1)^2 \tag{A.156}$$
$$+ 2\lambda_0^2\int_0^t ds_1\int_0^{s_1} ds_2\widehat{\sum_{q,r}} e^{-2tp^2+2s_1(qr)-2s_2(pq)}\frac{1}{p^2q^2}$$
$$\times\left\{2(d-2)\left(p^2q^2-(pq)^2\right)+(d-1)p^2\left(2p^2-(qr)\right)\right\}.$$

Summary We have therefore used the perturbative expansion that we derived earlier, and combined it with the solutions to the flow equations up to third order and the Feynman rules of the theory to obtain the seven $\mathcal{E}_i(t)$ contributions to the energy density observable at NLO, given in terms of the 't Hooft coupling by:

$$\mathcal{E}_0(t) = \frac{1}{2}\lambda_0\,\tilde{l}^{-d}\sum_q{}' e^{-2tq^2}(d-1) \tag{A.157}$$
$$+\frac{1}{4}\lambda_0^2\widehat{\sum_{q,r}} e^{-2tq^2}\frac{1}{q^2r^2(q+r)^2}\left((3d-2)q^2-2(d-2)^2r^2\right), \tag{A.158}$$
$$\mathcal{E}_1(t) = \frac{3}{2}\lambda_0^2\widehat{\sum_{q,r}} e^{-t(q^2+r^2+p^2)}\frac{1}{q^2r^2}(1-d), \tag{A.159}$$
$$\mathcal{E}_2(t) = \lambda_0^2\int_0^t ds\widehat{\sum_{q,r}} e^{-2tp^2+2s(qr)}\frac{1}{p^2q^2r^2} \tag{A.160}$$
$$\times\left\{(d-1)p^2\left(p^2+q^2+r^2\right)+2(d-2)\left(q^2r^2-(qr)^2\right)\right\},$$
$$\mathcal{E}_3(t) = \lambda_0^2\int_0^t ds s\widehat{\sum_{q,r}} e^{-2tp^2}\left(e^{2s(qr)}+e^{2(2t-s)(qr)}\right)\frac{1}{q^2r^2} \tag{A.161}$$
$$\times\left\{2(d-1)p^2r^2+(d-2)\left(q^2r^2-(qr)^2\right)\right\},$$

$$\mathcal{E}_4(t) = \frac{1}{4}\lambda_0^2 \widehat{\sum_{q,r}} e^{-2t(q^2+r^2)} \frac{1}{q^2 r^2} d(d-1), \tag{A.162}$$

$$\mathcal{E}_5(t) = \lambda_0^2 \int_0^t ds \widehat{\sum_{q,r}} e^{-(t+s)(q^2+r^2)-(t-s)p^2} \frac{1}{q^2 r^2} (1-d)\left(5r^2 + (qr)\right), \tag{A.163}$$

$$\begin{aligned}\mathcal{E}_6(t) = &-\lambda_0^2 \int_0^t ds \widehat{\sum_{q,r}} e^{-2tq^2-2sr^2} \frac{1}{r^2}(d-1)^2 \\ &+ 2\lambda_0^2 \int_0^t ds_1 \int_0^{s_1} ds_2 \widehat{\sum_{q,r}} e^{-2tp^2+2s_1(qr)-2s_2(pq)} \frac{1}{p^2 q^2} \\ &\times \left\{2(d-2)\left(p^2q^2 - (pq)^2\right) + (d-1)p^2\left(2p^2 - (qr)\right)\right\},\end{aligned} \tag{A.164}$$

and where we defined:

$$\widehat{\sum_{q,r}} \equiv \tilde{l}^{-2d} \sum_{q,r} NF^2(q, r, -q-r). \tag{A.165}$$

A.5 Integral form of the energy density

As shown in section 2.2.5, the energy density at NLO in the twisted gradient flow scheme can be expressed in terms of twelve integrals whose derivation we chose, for both clarity and concision, to show for a single example, leaving the integral expression of the full seven $\mathcal{O}(\lambda_0^2)$ contributions to the observable $\langle E/N \rangle$ for this appendix. We will thus see how one passes from the sums over momenta to this integral formulation, for each of the seven contributions, right after mentioning a couple of steps that will be repeated quite often in the procedure to avoid going over them constantly along the appendix.

First, we will mention that we will constantly rewrite the momentum quotients from which we start in two ways: we will use Schwinger's representation to rewrite the denominators as integrals, and replace the numerators with derivatives of the exponentials:

$$\frac{1}{p} = \int_0^\infty dz e^{-zp^2}, \qquad p^2 e^{-sp^2} = -\partial_s e^{-sp^2}. \tag{A.166}$$

Moreover, there are some divergences within the terms to be computed, which will arise at the points in which the (s, u, v) variables in eq. (2.58) are such that $su - v^2 = 0$. In our integrals, this will occur in two situations: either when $(s, u, v) = (2, 0, 0)$, or when $(s, u, v) = (2, 2, 2)$. We will show how to deal with the

former in section 2.3, but for the latter we will simply perform a shift $m \to m-n$ in the momentum sums in eq. (2.58), which amounts to changing u and v to:

$$u' = s + u - 2v \qquad v' = v - s, \tag{A.167}$$

effectively transforming the divergences of the second kind into the ones of the first kind.

Last but not least, we will quite often run into equations of the general form:

$$\int_0^\infty dz \int_0^t dx e^{-sq^2 - ur^2 - 2v(qr)}. \tag{A.168}$$

In order to transform these sorts of expressions into integrals of the auxiliary $\Phi(s,u,v,\hat{\theta})$ functions from eq. (2.66), we will often have to rescale some or all of the integration variables by a factor $\hat{c}\tilde{l}^2/4\pi$, replace t by its expression in terms of t' from eq. (2.44), and use the quantisation of momenta in the twisted box to express q, r in terms of integers:

$$\begin{aligned} &(x,z) \to \frac{\hat{c}\tilde{l}^2}{4\pi}(x,z), \qquad t = \frac{\hat{c}\tilde{l}^2}{4\pi}t', \\ &(q,r) = \frac{2\pi}{\tilde{l}}(m,n) \text{ with } m,n \in \mathbb{Z}. \end{aligned} \tag{A.169}$$

With that said, we may now begin the computation. Some of the appearing integrals will cancel out when resumming all of the terms and will not need to be rewritten in terms of $\Phi(s,u,v,\hat{\theta})$ functions, and so we will advance the expression of the contributing $\mathcal{E}_i$ to avoid manipulating them later:

$$\mathcal{E}_0' = \frac{1}{2}\lambda_0^2\Big\{(3d-2)\mathbb{I}_1 + 2(d-2)^2 I_9\Big\}, \tag{A.170}$$

$$\mathcal{E}_1 = -3\lambda_0^2(d-1)\mathbb{I}_2, \tag{A.171}$$

$$\mathcal{E}_2 = \lambda_0^2\Big\{8(d-1)I_5 + d(\mathbb{I}_2 - \mathbb{I}_1) + 4(d-2)\mathbb{I}_3\Big\}, \tag{A.172}$$

$$\begin{aligned} \mathcal{E}_3 = \frac{1}{2}\lambda_0^2\Big\{&(d-2)(4I_1 + 4I_2 + 2\mathbb{I}_2 - \mathbb{I}_1 - I_8) \\ &- 4(d-1)(I_{10} + I_{11} + 2I_3 - 2I_6)\Big\}, \end{aligned} \tag{A.173}$$

$$\mathcal{E}_4 = \frac{1}{2}\lambda_0^2\, d(d-1)I_8, \tag{A.174}$$

$$\mathcal{E}_5 = -\lambda_0^2(d-1)(10I_6 + I_8 - \mathbb{I}_2), \tag{A.175}$$

$$\mathcal{E}_6 = -2\lambda_0^2\Big\{(d-1)(I_5 + 2I_{12}) + 2(d-2)\mathbb{I}_3 + (d-2)(d-1)I_7 - 2(3d-5)I_4\Big\}, \tag{A.176}$$

where $\mathcal{E}_0'$ denotes the $\mathcal{O}(\lambda_0^2)$ part of $\mathcal{E}_0$, and I_i are the integrals given in eqs. (2.69)-(2.80). When summing all of the terms contributing to $\mathcal{E}^{(1)}(t)$, the $\mathbb{I}_i$ terms cancel out, and we are left with:

$$\mathcal{E}^{(1)}(t) = 2(d-2)\,(I_1 + I_2) - 4(d-1)I_3 + 4(3d-5)I_4 + 6(d-1)\,(I_5 - I_6) - 2(d-2)(d-1)I_7 + \frac{1}{2}(d-2)^2(I_8 + 2I_9) - 2(d-1)\,(I_{10} + I_{11}) - 4(d-1)I_{12}, \tag{A.177}$$

which is the NLO result given in eq. (2.52). We will in what follows go term by term, defining each intervening integral as they show up, and rewriting them in terms of the $\Phi(s,u,v,\hat{\theta})$ functions.

Integral form of $\mathcal{E}_0$ We will begin with the NLO part of $\mathcal{E}_0$ from eq. (2.35), which we denoted $\mathcal{E}_0'$:

$$\mathcal{E}_0' = \frac{1}{4}\lambda_0^2\widehat{\sum_{q,r}} e^{-2tq^2}\frac{1}{q^2r^2(q+r)^2}\left((3d-2)q^2 - 2(d-2)^2r^2\right). \tag{A.178}$$

Defining two integrals:

$$\mathbb{I}_1 = \frac{1}{2}\widehat{\sum_{q,r}}\int_0^\infty dx_1\int_0^\infty dx_2 e^{-(2t+x_1)q^2-(2t+x_2)r^2-2t(2qr)}, \tag{A.179}$$

$$I_9 = -\frac{1}{2}\widehat{\sum_{q,r}}\frac{r^2}{q^2}\int_0^\infty dx_1\int_0^\infty dx_2 e^{-(2t+x_2)q^2-(x_1+x_2)r^2-x_2(2qr)}, \tag{A.180}$$

we can, using Schwinger's representation, rewrite $\mathcal{E}_0'$ as:

$$\mathcal{E}_0' = \lambda_0^2\left[\frac{1}{2}(3d-2)\mathbb{I}_1 + (d-2)^2 I_9\right]. \tag{A.181}$$

As mentioned earlier, $\mathbb{I}_1$ will cancel out after summing all contributions and as such will be left as is, but we will reformulate I_9 as integrals of Φ functions. Defining $z = x_1 + x_2$ and $x = x_2/x_1$ to change variables in the double integral,

and defining an auxiliary variable $\tilde{z}$ in the r^2 term in the exponent to rewrite the numerator as a derivative, we get:

$$I_9 = \frac{1}{2}\int_0^\infty dzz\int_0^1 dx\int_0^\infty dy\partial_{\tilde{z}}\widehat{\sum_{q,r}} e^{-(2t+xz+y)q^2-\tilde{z}r^2-xz(2qr)}\Big|_{\tilde{z}=z}. \tag{A.182}$$

We can then perform the rescaling and rewriting from eq. (A.169) to the $y, z, \tilde{z}$ and t variables to recast the sum and exponential as a $\Phi(s,u,v,\hat{\theta})$ function from eq. (2.65), and obtain:

$$I_9(\Phi,t') = \int_0^\infty zdz\int_0^\infty dy\int_0^1 dx\,\partial_{z'}\Phi(2t'+xz+y,z',xz,\hat{\theta})\Big|_{z'=z}, \tag{A.183}$$

which is the integral shown in eq. (2.77).

Integral form of $\mathcal{E}_1$ The contribution from $\mathcal{E}_1$ will turn out to be quite simple. Indeed, we have:

$$\mathcal{E}_1 = \frac{3}{2}\lambda_0^2(1-d)\widehat{\sum_{q,r}} e^{-(p^2+q^2+r^2)t}\frac{1}{q^2r^2}, \tag{A.184}$$

which, expanding $p^2=(q+r)^2$ and turning the denominators into Schwinger integrals, allows us to define the integral:

$$\mathbb{I}_2 = \frac{1}{2}\widehat{\sum_{q,r}}\int_0^\infty dx_1\int_0^\infty dx_2 e^{-(2t+x_1)q^2-(2t+x_2)r^2-t(2qr)}, \tag{A.185}$$

to rewrite:

$$\mathcal{E}_1 = -3\lambda_0^2\,(d-1)\,\mathbb{I}_2, \tag{A.186}$$

which is one of the vanishing integrals mentioned earlier.

Integral form of $\mathcal{E}_2$ The $\mathcal{E}_2$ contribution is a bit longer to derive, as we start from:

$$\begin{aligned}\mathcal{E}_2 =&\lambda_0^2\int_0^t ds\widehat{\sum_{q,r}} e^{-2tp^2+2s(qr)}\frac{1}{p^2q^2r^2}\\ &\times\left\{(d-1)p^2\left(p^2+q^2+r^2\right)+2(d-2)\left(q^2r^2-(qr)^2\right)\right\}.\end{aligned} \tag{A.187}$$

Playing with the $p=q+r$ expansion in the exponent and numerator, using the $q\leftrightarrow r$ symmetry in the sum over momenta to group the q^2 and r^2 terms together,

and rewriting the qr terms as ∂_s derivatives we get, after a bit of algebra:

$$\begin{aligned}\mathcal{E}_2 = 4(d-1)\lambda_0^2 \int_0^t ds \widehat{\sum_{q,r}} \frac{1}{r^2} e^{-2tq^2-2tr^2-(2t-s)(2qr)} \\ + 2(d-2)\lambda_0^2 \int_0^t ds \widehat{\sum_{q,r}} \left[\frac{1}{p^2} + \frac{1}{2p^2r^2}\partial_s\right] e^{-2tq^2-2tr^2-(2t-s)(2qr)} \\ + \frac{d}{2}\lambda_0^2 \int_0^t ds \widehat{\sum_{q,r}} \frac{1}{q^2r^2}\partial_s e^{-2tq^2-2tr^2-(2t-s)(2qr)},\end{aligned} \tag{A.188}$$

which, integrating over s in the last term, becomes:

$$\begin{aligned}\mathcal{E}_2 = \lambda_0^2 \int_0^t ds \widehat{\sum_{q,r}} \left(\frac{4(d-1)}{r^2} + \frac{2(d-2)}{p^2}(1 + \frac{\partial_s}{2r^2})\right) e^{-2tq^2-2tr^2-(2t-s)(2qr)} \\ + \lambda_0^2 \widehat{\sum_{q,r}} \frac{d}{2q^2r^2}\left(e^{-2tq^2-2tr^2-t(2qr)} - e^{-2tq^2-2tr^2-2t(2qr)}\right).\end{aligned} \tag{A.189}$$

Lifting all denominators as Schwinger integrals, we notice that the last two terms correspond directly to $\mathbb{I}_2 - \mathbb{I}_1$, and thus we only need to define two integrals:

$$\mathbb{I}_3 = \frac{1}{4}\widehat{\sum_{q,r}} \int_0^\infty dx_1 \int_0^\infty dx_2 \int_0^t ds(\partial_s - 2\partial_{x_2}) e^{-(2t+x_1)q^2-(2t+x_1+x_2)r^2-(2t-s+x_1)(2qr)}, \tag{A.190}$$

$$I_5 = \frac{1}{2}\widehat{\sum_{q,r}} \int_0^\infty dz \int_0^t dx e^{-2tq^2-(2t+z)r^2-(2t-x)(2qr)}, \tag{A.191}$$

which allow us to write:

$$\mathcal{E}_2 = \lambda_0^2 \left\{8\,(d-1)\,I_5 + d\,(\mathbb{I}_2 - \mathbb{I}_1) + 4\,(d-2)\,\mathbb{I}_3\right\}. \tag{A.192}$$

As we did in the previous case, we leave all $\mathbb{I}_i$ terms as they are, and rewrite I_5 in terms of the Φ functions. Rewriting x, z, t as in eq. (A.169), we obtain:

$$I_5 = \int_0^\infty dz \int_0^{t'} dx \Phi(2t', 2t' + z, 2t' - x, \hat{\theta}). \tag{A.193}$$

This, however, passes through the previously mentioned $(s, u, v) = (2, 2, 2)$ point. Performing the shift from eq. (A.167), flipping the sign of v for convenience, and

changing $z \to zx$ within the integral, we end up with:

$$I_5(\Phi, t') = \int_0^\infty dz \int_0^{t'} dx x \, \Phi(2t', (z+2)x, x, \hat{\theta}). \tag{A.194}$$

Integral form of $\mathcal{E}_3$ The $\mathcal{E}_3$ contribution came from:

$$\begin{aligned}\mathcal{E}_3 = \lambda_0^2 \int_0^t ds s \widehat{\sum_{q,r}} e^{-2tp^2} \left(e^{2s(qr)} + e^{2(2t-s)(qr)}\right) \frac{1}{q^2 r^2} \\ \times \left\{2(d-1)p^2 r^2 + (d-2)\left(q^2 r^2 - (qr)^2\right)\right\}.\end{aligned} \tag{A.195}$$

Combining the exponentials, we obtain:

$$\begin{aligned}\mathcal{E}_3 = \frac{1}{2}\lambda_0^2 \int_0^t ds s \widehat{\sum_{q,r}} \left(e^{-sq^2 - sr^2 - (2t-s)p^2} + e^{-(2t-s)q^2 - (2t-s)r^2 - sp^2}\right) \\ \times \left(4(d-1)\frac{p^2}{q^2} + 2(d-2)(1 - \frac{(qr)^2}{q^2 r^2})\right),\end{aligned} \tag{A.196}$$

in which we will replace the momenta in the numerator with flow time derivatives. In particular, in the $(d-1)$ terms p^2 can be replaced by:

$$-\frac{1}{2}\partial_t e^{-sq^2 - sr^2 - (2t-s)p^2} = p^2 e^{-sq^2 - sr^2 - (2t-s)p^2}, \tag{A.197}$$

$$-\frac{1}{2}\left(\partial_t + 2\partial_s\right) e^{-(2t-s)q^2 - (2t-s)r^2 - sp^2} = p^2 e^{-(2t-s)q^2 - (2t-s)r^2 - sp^2}, \tag{A.198}$$

whereas in the $(d-2)$ term we expand $p = q + r$ in the numerator and replace one of the qr terms by derivatives:

$$\begin{aligned}&\frac{qr}{q^2 r^2} \int_0^t ds s \left((qr)\, e^{-2tq^2 - 2tr^2 - (2t-s)(2qr)} + (qr)\, e^{-2tq^2 - 2tr^2 - s(2qr)}\right) \\ &= \frac{1}{2}\frac{qr}{q^2 r^2} \int_0^t ds s \left(\partial_s e^{-2tq^2 - 2tr^2 - (2t-s)(2qr)} - \partial_s e^{-2tq^2 - 2tr^2 - s(2qr)}\right),\end{aligned} \tag{A.199}$$

and then integrate over s in both terms:

$$\int_0^t ds s \partial_s e^{-2tq^2 - 2tr^2 - (2t-s)(2qr)} = t e^{-2tq^2 - 2tr^2 - t(2qr)} - \int_0^t ds e^{-2tq^2 - 2tr^2 - (2t-s)(2qr)}, \tag{A.200}$$

$$\int_0^t ds s \partial_s e^{-2tq^2 - 2tr^2 - s(2qr)} = t e^{-2tq^2 - 2tr^2 - t(2qr)} - \int_0^t ds e^{-2tq^2 - 2tr^2 - s(2qr)}. \tag{A.201}$$

This allows us to rewrite, replacing the remaining qr term in the numerator with yet another ∂_s derivative:

$$\begin{aligned}
&\frac{(qr)^2}{q^2r^2}\int_0^t sds\left(e^{-2tq^2-2tr^2-(2t-s)(2qr)}+e^{-2tq^2-2tr^2-s(2qr)}\right) \\
&=\frac{1}{2}\frac{qr}{q^2r^2}\left(\int_0^t dse^{-2tq^2-2tr^2-s(2qr)}-\int_0^t dse^{-2tq^2-2tr^2-(2t-s)(2qr)}\right) \\
&=\frac{-1}{4q^2r^2}\left(\int_0^t ds\partial_s e^{-2tq^2-2tr^2-s(2qr)}+\int_0^t ds\partial_s e^{-2tq^2-2tr^2-(2t-s)(2qr)}\right) \\
&=\frac{-1}{4q^2r^2}\left(2e^{-2tq^2-2tr^2-t(2qr)}-e^{-2tq^2-2tr^2-2t(2qr)}-e^{-2tq^2-2tr^2}\right).
\end{aligned} \tag{A.202}$$

Putting all of this back together and raising the denominators via Schwinger parametrisation, we end up with an expression for $\mathcal{E}_3$ in terms of several integrals:

$$\begin{aligned}
\mathcal{E}_3 &= 2(1-d)\frac{1}{2}\lambda_0^2\widehat{\sum_{q,r}}\int_0^\infty dx_1\int_0^t sds\partial_t e^{-(2t+x_1)q^2-2tr^2-(2t-s)(2qr)} \\
&+2(1-d)\frac{1}{2}\lambda_0^2\widehat{\sum_{q,r}}\int_0^\infty dx_1\int_0^t sds\partial_t+2\partial_s)e^{-(2t+x_1)q^2-2tr^2-s(2qr)}, \\
&+2(d-2)\frac{1}{2}\lambda_0^2\widehat{\sum_{q,r}}\int_0^t sds\left[e^{-2tq^2-2tr^2-(2t-s)(2qr)}+e^{-2tq^2-2tr^2-s(2qr)}\right] \\
&+\frac{1}{4}(d-2)\lambda_0^2\widehat{\sum_{q,r}}\int_0^\infty dx_1\int_0^\infty dx_2\Big[2e^{-(2t+x_1)q^2-(2t+x_2)r^2-t(2qr)} \\
&\qquad -e^{-(2t+x_1)q^2-(2t+x_2)r^2-2t(2qr)}-e^{-(2t+x_1)q^2-(2t+x_2)r^2}\Big].
\end{aligned} \tag{A.203}$$

We immediately recognise $\mathbb{I}_1$ and $\mathbb{I}_2$ in the last term, and define brand new integrals for four of the other terms:

$$I_1=\frac{1}{2}\widehat{\sum_{q,r}}\int_0^t xdxe^{-2tq^2-2tr^2-(2t-x)(2qr)}, \tag{A.204}$$

$$I_2=\frac{1}{2}\widehat{\sum_{q,r}}\int_0^t xdxe^{-2tq^2-2tr^2-x(2qr)}, \tag{A.205}$$

$$I_8=\frac{1}{2}\widehat{\sum_{q,r}}\int_0^\infty dz\int_0^\infty dye^{-(2t+z)q^2-(2t+y)r^2}, \tag{A.206}$$

$$I_{11}=\frac{1}{2}\widehat{\sum_{q,r}}\int_0^\infty dz\int_0^t xdx\partial_t e^{-(2t+z)q^2-2tr^2-(2t-x)(2qr)}. \tag{A.207}$$

With this, we can write:

$$\mathcal{E}_3 = \frac{1}{2}\lambda_0^2 \left[(d-2)(4I_1 + 4I_2 + 2\mathbb{I}_2 - \mathbb{I}_1 - I_8) - 4(d-1)(I_{11} + \mathcal{I})\right], \tag{A.208}$$

where we dubbed $\mathcal{I}$ the remaining integral:

$$\mathcal{I} = \frac{1}{2}\widehat{\sum_{q,r}} \int_0^\infty dx_1 \int_0^t s ds (\partial_t + 2\partial_s) e^{-(2t+x_1)q^2 - 2tr^2 - s(2qr)}, \tag{A.209}$$

which will be further split into three more integrals shortly. Before, however, we will rewrite the four integrals that we just defined in terms of Φ functions. The usual change from eq. (A.169) will be applied for x, t in I_1 and I_2, for y, z, t in I_8, and for x, z, t in I_{11}, and the shift from eq. (A.167) will be necessary for I_1, and for I_{11}, leading to:

$$I_1(\Phi, t') = \int_0^{t'} dx x \Phi(2t', 2x, x, \hat{\theta}), \tag{A.210}$$

$$I_2(\Phi, t') = \int_0^{t'} dx x \Phi(2t', 2t', x, \hat{\theta}), \tag{A.211}$$

$$I_8(\Phi, t') = \int_0^\infty dz \int_0^\infty dy \Phi(2t' + z, 2t' + y, 0, \hat{\theta}), \tag{A.212}$$

$$I_{11}(\Phi, t') = \int_0^\infty dz \int_0^{t'} dx x^2 \partial_{t'} \Phi(2t, (z+2)x, x, \hat{\theta}), \tag{A.213}$$

where for I_{11} we swapped q and r in the arguments before the momentum shift, rescaled $z \to xz$, and where in both I_1 and I_{11} we flipped the sign of v in the end.

We then look at $\mathcal{I}$, separately considering each of the two derivative terms:

$$\mathcal{I}^{(1)} = \frac{1}{2}\widehat{\sum_{q,r}} \int_0^\infty dz \int_0^t x dx \partial_t e^{-(2t+z)q^2 - 2tr^2 - x(2qr)}, \tag{A.214}$$

$$\mathcal{I}^{(2)} = \widehat{\sum_{q,r}} \int_0^\infty dz \int_0^t x dx \partial_x e^{-(2t+z)q^2 - 2tr^2 - x(2qr)}, \tag{A.215}$$

and integrate the second one, leading to:

$$\mathcal{I}^{(2)} = \widehat{\sum_{q,r}} \int_0^\infty dz \Big[t e^{-(2t+z)q^2 - 2tr^2 - t(2qr)} - \int_0^t dx e^{-(2t+z)q^2 - 2tr^2 - x(2qr)} \Big]. \tag{A.216}$$

Thus, defining three integrals:

$$I_3 = \widehat{\sum_{q,r}} \int_0^\infty t dz e^{-(2t+z)q^2-2tr^2-t(2qr)}, \tag{A.217}$$

$$I_6 = \widehat{\sum_{q,r}} \int_0^\infty dz \int_0^t dx e^{-(2t+z)q^2-2tr^2-x(2qr)}, \tag{A.218}$$

$$I_{10} = \frac{1}{2}\widehat{\sum_{q,r}} \int_0^\infty dz \int_0^t x dx \partial_t e^{-(2t+z)q^2-2tr^2-x(2qr)}, \tag{A.219}$$

we have:

$$\mathcal{I} = I_{10} + 2(I_3 - I_6). \tag{A.220}$$

We then apply eq. (A.169) as usual to the x, z, t variables in order to rewrite all three integrals in terms of Φ functions:

$$I_3(\Phi, t') = \int_0^\infty dz t' \Phi(2t' + z, 2t', t', \hat{\theta}), \tag{A.221}$$

$$I_6(\Phi, t') = \int_0^\infty dz \int_0^{t'} dx\, \Phi(2t' + z, 2t', x, \hat{\theta})\,, \tag{A.222}$$

$$I_{10}(\Phi, t') = \int_0^\infty dz \int_0^{t'} dx x\, \partial_{t'} \Phi(2t' + z, 2t', x, \hat{\theta})\,, \tag{A.223}$$

which leaves us with:

$$\begin{aligned}\mathcal{E}_3 = \frac{1}{2}\lambda_0^2 \Big[&(d-2)(4I_1 + 4I_2 + 2\mathbb{I}_2 - \mathbb{I}_1 - I_8) \\ &- 4(d-1)(I_{10} + I_{11} + 2I_3 - 2I_6)\Big].\end{aligned} \tag{A.224}$$

Integral form of $\mathcal{E}_4$ The $\mathcal{E}_4$ contribution was the one shown as a simple example in section 2.2.5. We had:

$$\mathcal{E}_4 = \frac{1}{4}\lambda_0^2 \widehat{\sum_{q,r}} e^{-2t(q^2+r^2)} \frac{1}{q^2 r^2} d(d-1), \tag{A.225}$$

Which, writing the denominators as Schwinger integrals, is immediately the term I_8 defined in $\mathcal{E}_3$, and thus:

$$\mathcal{E}_4 = \frac{1}{2}\lambda_0^2\, d\,(d-1)\, I_8. \tag{A.226}$$

Integral form of $\mathcal{E}_5$ For the $\mathcal{E}_5$ contribution we had:

$$\mathcal{E}_5 = (1-d)\lambda_0^2 \int_0^t ds \widehat{\sum_{q,r}} e^{-(t+s)(q^2+r^2)-(t-s)p^2} \frac{1}{q^2r^2}\left(5r^2+qr\right), \tag{A.227}$$

$$\mathcal{E}_5 = (1-d)\lambda_0^2 \int_0^t ds \widehat{\sum_{q,r}} e^{-2tq^2-2tr^2-(t-s)(2qr)} \left(\frac{5}{r^2}+\frac{qr}{q^2r^2}\right), \tag{A.228}$$

where we expanded p in the exponent and used the $q \leftrightarrow r$ symmetry in the sum. We replace qr with a ∂_s derivative, and integrate over s in that term, leading to:

$$\mathcal{E}_5 = 10(1-d)\frac{1}{2}\lambda_0^2 \widehat{\sum_{q,r}} \int_0^t ds \frac{1}{r^2} e^{-2tq^2-2tr^2-(t-s)(2qr)} \tag{A.229}$$

$$+ (1-d)\frac{1}{2}\lambda_0^2 \widehat{\sum_{q,r}} int_0^t ds \frac{1}{q^2r^2}\left(e^{-2tq^2-2tr^2} - e^{-2tq^2-2tr^2-t(2qr)}\right), \tag{A.230}$$

which, replacing the denominators with Schwinger integrals, becomes:

$$\mathcal{E}_5 = 10(1-d)\frac{1}{2}\lambda_0^2 \widehat{\sum_{q,r}} \int_0^\infty dx_1 \int_0^t ds e^{-2tq^2-(2t+x_1)r^2-(t-s)(2qr)} \tag{A.231}$$

$$- (1-d)\frac{1}{2}\lambda_0^2 \widehat{\sum_{q,r}} \int_0^\infty dx_1 \int_0^\infty dx_2 e^{-(2t+x_1)q^2-(2t+x_2)r^2-t(2qr)}$$

$$+ (1-d)\frac{1}{2}\lambda_0^2 \widehat{\sum_{q,r}} \int_0^\infty dx_1 \int_0^\infty dx_2 e^{-(2t+x_1)q^2-(2t+x_2)r^2}.$$

The last two terms in this sum are I_8 and $\mathbb{I}_2$ respectively, and so we only need to define:

$$I_6 = \frac{1}{2}\widehat{\sum_{q,r}} \int_0^\infty dz \int_0^t dx e^{-2tq^2-(2t+z)r^2-(t-x)(2qr)}, \tag{A.232}$$

with which we rewrite:

$$\mathcal{E}_5 = -\lambda_0^2 (d-1)\left(10I_6 + I_8 - \mathbb{I}_2\right). \tag{A.233}$$

The procedure to relate I_6 to the Φ functions is then the usual: we rescale x, z, t as in eq. (A.169), and after a $x \to 1-x$ change of variable get:

$$I_6(\Phi, t') = \int_0^\infty dz \int_0^{t'} dx\, \Phi(2t'+z, 2t', x, \hat{\theta}). \tag{A.234}$$

Integral form of $\mathcal{E}_6$ Finally, for the $\mathcal{E}_6$ contribution we have:

$$\begin{aligned}\mathcal{E}_6 =& -\lambda_0^2 \int_0^t ds \widehat{\sum_{q,r}} e^{-2tq^2-2sr^2} \frac{1}{r^2}(d-1)^2 \\ &+ 2\lambda_0^2 \int_0^t ds_1 \int_0^{s_1} ds_2 \widehat{\sum_{q,r}} e^{-2tp^2+2s_1(qr)-2s_2(pq)} \frac{1}{p^2q^2} \\ &\times \left\{2(d-2)\left(p^2q^2-(pq)^2\right)+(d-1)p^2\left(2p^2-(qr)\right)\right\}.\end{aligned} \tag{A.235}$$

The first term can after a $q \to q+r$ shift be rewritten as:

$$\begin{aligned}&\int_0^t ds \widehat{\sum_{q,r}} \frac{1}{r^2} e^{-2tq^2-2sr^2} = \int_0^t ds \widehat{\sum_{q,r}} \frac{1}{q^2} e^{-2tp^2+s(2qr)} \Big(1+\int_0^s ds_2 \partial_{s_2} e^{-s_2(2pq)}\Big) \\ &= \widehat{\sum_{q,r}} \frac{1}{q^2} \Big[\int_0^t ds e^{-2tp^2+s(2qr)} - \int_0^t ds \int_0^s ds_2 (2pq) e^{-2tp^2+s(2qr)-s_2(2pq)}\Big],\end{aligned} \tag{A.236}$$

where we swapped the q and r variables in the first step. Rewriting qr in the numerator of the other two terms we obtain:

$$\begin{aligned}\mathcal{E}_6 =& \lambda_0^2 \widehat{\sum_{q,r}} \int_0^t ds_1 \int_0^{s_1} ds_2 e^{-2tp^2+s_1(2qr)-s_2(2pq)} \Big[4(d-1)\frac{1}{q^2}(p^2+\frac{1}{2}q^2-\frac{1}{2}pq) \\ &+ (d-1)^2 q^{-2}(2pq) + 4(d-2)\frac{1}{p^2q^2}(p^2q^2-(pq)^2)\Big] \\ &- \lambda_0^2 \widehat{\sum_{q,r}} (d-1)^2 \int_0^t ds \frac{1}{r^2} e^{-2tp^2+s(2qr)},\end{aligned} \tag{A.237}$$

at which point we change variables in the double integrals, taking $s = s_1$ and $x = \frac{s_2}{s_1}$, and replace the following momenta in the numerators with derivatives:

$$\frac{1}{2}pq - p^2 \to \frac{1}{2}\partial_t - \frac{1}{4s}\partial_x, \qquad (pq)^2 \to -\frac{1}{2}(pq)\partial_{s_2}.$$

The second replacement allows us, before the change of variable, to integrate one of the $(d-2)$ terms directly:

$$\int_0^t ds_1 \int_0^{s_1} ds_2 \frac{(pq)^2}{p^2q^2} e^{-2tp^2+s_1(2qr)-s_2(2pq)} = \frac{1}{2}\int_0^t ds \frac{q^2+qr}{p^2q^2} e^{-2tp^2+s(2qr)}, \tag{A.238}$$

where one of the resulting terms was eliminated, as being odd in q it vanishes upon integration. We then replace the remaining momenta in the numerator by

derivatives:

$$\int_0^t ds_1 \int_0^{s_1} ds_2 \frac{(pq)^2}{p^2q^2} e^{-2tp^2+s_1(2qr)-s_2(2pq)} = \frac{1}{2}\int_0^t ds(\frac{1}{p^2}+\frac{\partial_s}{2p^2q^2})e^{-2tp^2+s(2qr)}, \tag{A.239}$$

allowing us to rewrite the full expression as:

$$\begin{aligned}\mathcal{E}_6 = \lambda_0^2 \widehat{\sum_{q,r}}\Big[&\int_0^t sds \int_0^1 dx e^{-2tp^2+s(x-1)(2pq)-2sq^2} \\ &\times \left(-\frac{2(d-1)}{q^2}\partial_t - \frac{(d-1)(d-2)}{sq^2}\partial_x + 2(3d-5)\right) \\ &- \int_0^t ds e^{-2tp^2+s(2qr)}\left(2(d-2)\frac{1}{p^2}+(d-1)^2\frac{1}{r^2}+(d-2)\frac{\partial_s}{p^2q^2}\right)\Big].\end{aligned} \tag{A.240}$$

Finally, replacing the denominators with Schwinger integrals, and expanding $p = q + r$, we can express $\mathcal{E}_6$ as:

$$\begin{aligned}\mathcal{E}_6 = \lambda_0^2 \widehat{\sum_{q,r}}\Big[&-(d-1)^2 \int_0^t ds \int_0^\infty dx_1 e^{-2tq^2-(2t+x_1)r^2-(2t-s)(2qr)} \\ &-2(d-1)\int_0^t sds\int_0^1 dx\int_0^1 dx_1 \partial_t e^{-(2t+2sx+x_1)q^2-2tr^2-(2t-s(1-x))(2qr)} \\ &-(d-1)(d-2)\int_0^t ds\int_0^1 dx\int_0^1 dx_1 \partial_x e^{-(2t+2sx+x_1)q^2-2tr^2-(2t-s(1-x))(2qr)} \\ &+2(3d-5)\int_0^t sds\int_0^1 dx e^{-(2t+2sx)q^2-2tr^2-(2t-s(1-x))(2qr)} \\ &-2(d-2)\int_0^t ds\int_0^\infty dx_1 e^{-(2t+x_1)q^2-(2t+x_1)r^2-(2t-s+x_1)(2qr)} \\ &-(d-2)\int_0^t ds\int_0^\infty dx_1\int_0^\infty dx_2 \partial_s e^{-(2t+x_1+x_2)q^2-(2t+x_1)r^2-(2t-s+x_1)(2qr)}\Big].\end{aligned} \tag{A.241}$$

The terms in $(d-1)^2$ and $(d-2)$ directly correspond to I_5 and $\mathbb{I}_3$ from earlier, and we will define new integrals for the remaining terms. We begin with two of them:

$$I_4 = \frac{1}{2}\widehat{\sum_{q,r}}\int_0^1 dx\int_0^t sdse^{-(2t+2sx)q^2-2tr^2-(2t+s(x-1))(2qr)}, \tag{A.242}$$

$$I_{12} = \frac{1}{2}\widehat{\sum_{q,r}}\int_0^\infty dz\int_0^1 dy\int_0^t xdx\partial_t e^{-(2t+2xy+z)q^2-2tr^2-(2t+x(y-1))(2qr)}, \tag{A.243}$$

which we want to rewrite as integrals of Φ functions. The procedure is the standard one: we simply perform the usual changes from eq. (A.169), swap the s and u terms, and change variables to $y \to 1-y$, which leaves us with:

$$I_4 = \int_0^{t'} dxx \int_0^1 dy \Phi(2t', 2t' + 2xy, 2t' + x(y-1), \hat{\theta}), \tag{A.244}$$

$$I_{12} = \int_0^{\infty} dz \int_0^1 dy \int_0^{t'} dx x^2 \, \partial_{t'} \Phi(2t', (z+2)x, xy, \hat{\theta}), \tag{A.245}$$

where the usual momentum shift from eq. (A.167) was performed for I_4, and where we rescaled $z \to xz$ for I_{12}.

As for the remaining term:

$$\mathcal{I} = \frac{1}{2}\widehat{\sum_{q,r}} \int_0^{\infty} dz \int_0^t dx \int_0^1 dy \partial_y e^{-(2t+2xy+z)q^2 - 2tr^2 - (2t+x(y-1))(2qr)}, \tag{A.246}$$

it turns out to be expressable as a difference of two integrals. Integrating over y and swapping s and u as in the previous integrals we get:

$$\mathcal{I} = \frac{1}{2}\widehat{\sum_{q,r}} \int_0^{\infty} dz \int_0^t dx \left[e^{-2tq^2 - (2t+2x+z)r^2 - 2t(2qr)} - e^{-2tq^2 - (2t+z)r^2 - (2t-x)(2qr)} \right]. \tag{A.247}$$

The second term corresponds once more to I_5, and we define a new integral for the first one, which after the usual changes from eq. (A.169) and momentum shift from eq. (A.167), and after yet another $z \to xz$ shift, becomes:

$$I_7 = \int_0^{\infty} dz \int_0^{t'} dxx \, \Phi(2t', (z+2)x, 0, \hat{\theta}). \tag{A.248}$$

This way:

$$\mathcal{I} = I_7 - I_5, \tag{A.249}$$

and, regrouping all contributions, we end up with:

$$\begin{aligned} \mathcal{E}_6 = -2\lambda_0^2 \Big\{ & (d-1)(I_5 + 2I_{12}) + 2(d-2)\mathbb{I}_3 \\ & + (d-2)(d-1)I_7 - 2(3d-5)I_4 \Big\}. \end{aligned} \tag{A.250}$$

Summary We have expressed all contributions to the NLO term $\mathcal{E}^{(1)}(t)$ as a sum of twelve integral terms:

$$\mathcal{E}^{(1)}(t) = 2(d-2)\,(I_1+I_2) - 4(d-1)I_3 + 4(3d-5)I_4 + 6(d-1)\,(I_5-I_6) \tag{A.251}$$
$$-\,2(d-2)(d-1)I_7 + \frac{1}{2}(d-2)^2(I_8+2I_9) - 2(d-1)\,(I_{10}+I_{11}) - 4(d-1)I_{12},$$

where we defined:

$$I_1(\Phi,t') = \int_0^{t'} dx x\,\Phi(2t',2x,x,\hat{\theta})\,, \tag{A.252}$$
$$I_2(\Phi,t') = \int_0^{t'} dx x\,\Phi(2t',2t',x,\hat{\theta})\,, \tag{A.253}$$
$$I_3(\Phi,t') = \int_0^{\infty} dz t'\Phi(2t'+z,2t',t',\hat{\theta}), \tag{A.254}$$
$$I_4(\Phi,t') = \int_0^{t'} dx x \int_0^1 dy\,\Phi(2t',2x,xy,\hat{\theta})\,, \tag{A.255}$$
$$I_5(\Phi,t') = \int_0^{\infty} dz \int_0^{t'} dx x\,\Phi(2t',(z+2)x,x,\hat{\theta})\,, \tag{A.256}$$
$$I_6(\Phi,t') = \int_0^{\infty} dz \int_0^{t'} dx\,\Phi(2t'+z,2t',x,\hat{\theta})\,, \tag{A.257}$$
$$I_7(\Phi,t') = \int_0^{\infty} dz \int_0^{t'} dx x\,\Phi(2t',(z+2)x,0,\hat{\theta})\,, \tag{A.258}$$
$$I_8(\Phi,t') = \int_0^{\infty} dz \int_0^{\infty} dy\,\Phi(2t'+z,2t'+y,0,\hat{\theta})\,, \tag{A.259}$$
$$I_9(\Phi,t') = \int_0^{\infty} z dz \int_0^{\infty} dy \int_0^1 dx\,\partial_{z'}\Phi(2t'+xz+y,z',xz,\hat{\theta})\Big|_{z'=z}\,, \tag{A.260}$$
$$I_{10}(\Phi,t') = \int_0^{\infty} dz \int_0^{t'} dx x\,\partial_{t'}\Phi(2t'+z,2t',x,\hat{\theta})\,, \tag{A.261}$$
$$I_{11}(\Phi,t') = \int_0^{\infty} dz \int_0^{t'} dx x^2\,\partial_{t'}\Phi(2t',(z+2)x,x,\hat{\theta})\,, \tag{A.262}$$
$$I_{12}(\Phi,t') = \int_0^{\infty} dz \int_0^1 dy \int_0^{t'} dx x^2\,\partial_{t'}\Phi(2t',(z+2)x,xy,\hat{\theta})\,. \tag{A.263}$$

A.6 Regularisation of the integrals

In this appendix, we will present the details of the regularisation procedure for the integrals introduced in eqs. (2.69)-(2.80). We will first address the integrals that were regularised using the general treatment described in section 2.3.2, and then consider the special case of I_9, which is a bit more complicated.

A.6.1 General regularisation of the integrals

We begin, setting aside I_9, by looking at the integrals one by one. The general procedure will be the same that we showed in detail in section 2.3.2 for the case of I_1: we will replace Φ in the integrals with $\Phi^{(0)}$, expand the function $\mathcal{A}(2\hat{c}t')$ around $u = 0$ to obtain its asymptotic behaviour, and, retaining the leading term, use it to define a set of integrals $I_i(\Phi^\infty, t')$ to be treated in dimensional regularisation.

The case of I_1 was already treated in section 2.3.2, so we will merely perform the dimensional regularisation. As we recall, we had:

$$I_1(\Phi^\infty, t') = \mathcal{N}\hat{c}^{-d}\int_0^{t'} dx x^{1-d/2}(4t'-x)^{-d/2}, \tag{A.264}$$

which is divergent in four dimensions. Integration yields an incomplete beta function:

$$I_1(\Phi^\infty, t') = \mathcal{N}\hat{c}^{-d}(4t')^{2-d}\beta_{\frac{1}{4}}(2-\frac{d}{2}, 1-\frac{d}{2}) = \frac{\eta}{2^{d-1}}\beta_{\frac{1}{4}}(\epsilon, \epsilon-1), \tag{A.265}$$

where we defined $\eta = (4\pi)^{-d}(2t)^{2-d} = 2\mathcal{N}\hat{c}^{-d}(2t')^{2-d}$, and expressed $d = 4-2\epsilon$. The β function can be expanded in powers of ϵ:

$$\beta_z(\epsilon, \epsilon-1) = z^\epsilon\left(\frac{1}{\epsilon} + \frac{z}{1-z} - \log(1-z) + \mathcal{O}(\epsilon)\right), \tag{A.266}$$

which taking $z = 1/4$ leads to:

$$I_1(\Phi^\infty, t') = \frac{\eta}{8}(\frac{1}{\epsilon} + \frac{1}{3} + \log\frac{4}{3}). \tag{A.267}$$

We may then look at I_2, which reads:

$$I_2(\Phi^{(0)}, t') = \int_0^{t'} dx x \Phi^{(0)}(2t', 2t', x). \tag{A.268}$$

Expanding $\Phi^{(0)}$, we get:

$$I_2(\Phi^{(0)}, t') = \mathcal{N}\hat{c}^{-d} \int_0^{t'} dx x (4t'^2 - x^2)^{-\frac{d}{2}} \mathcal{A}(\hat{c}(2t' - x^2/2t')), \tag{A.269}$$

which, expanding the $\mathcal{A}$ function around $x = 0$, allows us to rewrite:

$$I_2(\Phi^{(0)}, t') = \mathcal{A}(2\hat{c}t') I_2(\Phi^{\infty}, t'), \tag{A.270}$$

$$I_2(\Phi^{\infty}, t') = \mathcal{N}\hat{c}^{-d} \int_0^{t'} dx x (4t'^2 - x^2)^{-\frac{d}{2}}. \tag{A.271}$$

The integral is convergent in four dimensions, so we can integrate it directly taking $d = 4$:

$$I_2(\Phi^{\infty}, t') = \mathcal{N}\hat{c}^{-d}(t')^{2-d}/24 = \eta/12. \tag{A.272}$$

As for I_3, we had:

$$I_3(\Phi^{(0)}, t') = \int_0^{\infty} dz t' \Phi^{(0)}(2t' + z, 2t', t'). \tag{A.273}$$

It is in this case convenient to introduce a trivial integral:

$$I_3(\Phi^{(0)}, t') = \int_0^{\infty} dz \int_0^{t'} dx \partial_x [x \Phi^{(0)}(2t' + z, 2t', x)], \tag{A.274}$$

which replacing the expression of $\Phi^{(0)}$ yields:

$$I_3(\Phi^{(0)}, t') = \mathcal{N}\hat{c}^{-d} \int_0^{\infty} dz \int_0^{t'} dx \partial_x [x(4t'^2 + 2t'z - x^2)^{-\frac{d}{2}} \mathcal{A}(\hat{c}(2t' + z - x^2/2t'))], \tag{A.275}$$

and in turn, expanding the $\mathcal{A}$ function and keeping the leading term, we can rewrite:

$$I_3(\Phi^{(0)}, t') = \mathcal{A}(2\hat{c}t') I_3(\Phi^{\infty}, t'), \tag{A.276}$$

$$I_3(\Phi^{\infty}, t') = \mathcal{N}\hat{c}^{-d} \int_0^{\infty} dz \int_0^{t'} dx \partial_x [x(4t'^2 + 2t'z - x^2)^{-\frac{d}{2}}], \tag{A.277}$$

after which we redo the integral over x, leading to:

$$I_3(\Phi^\infty, t') = \mathcal{N}\hat{c}^{-d}\int_0^\infty dz t'^{1-d/2}(3t'+2z)^{-d/2}. \tag{A.278}$$

Integrating over z, we get:

$$I_3(\Phi^\infty, t') = \frac{\mathcal{N}\hat{c}^{-d}}{d-2}(3t'^2)^{1-d/2} = \frac{\eta}{3}. \tag{A.279}$$

Next comes I_4, given by:

$$I_4(\Phi^{(0)}, t') = \int_0^{t'} dx x \int_0^1 dy\, \Phi^{(0)}(2t', 2x, xy), \tag{A.280}$$

which replacing the expression of $\Phi^{(0)}$ reads:

$$I_4(\Phi^{(0)}, t') = \mathcal{N}\hat{c}^{-d}\int_0^{t'} dx x^{1-d/2}\int_0^1 dy(4t'-xy^2)^{-d/2}\mathcal{A}(\hat{c}(2t'-xy^2/2)), \tag{A.281}$$

and in turn, expanding the $\mathcal{A}$ function around $x=0$, we can rewrite:

$$I_4(\Phi^{(0)}, t') = \mathcal{A}(2\hat{c}t')I_4(\Phi^\infty, t'), \tag{A.282}$$

$$I_4(\Phi^\infty, t') = \mathcal{N}\hat{c}^{-d}\int_0^{t'} dx x^{1-d/2}\int_0^1 dy(4t'-xy^2)^{-d/2}). \tag{A.283}$$

This integral diverges, so we take $d = 4-2\epsilon$, rewrite the prefactor in terms of η, and integrate over both x and y to get:

$$I_4(\Phi^\infty, t') = \frac{\eta}{8(2\epsilon-1)}\left(2\,{}_2F_1(\frac{1}{2}, 2-\epsilon, \frac{3}{2}, \frac{1}{4}) - 4^\epsilon\beta_{\frac{1}{4}(\epsilon,\epsilon-1)}\right), \tag{A.284}$$

where ${}_2F_1$ denotes the hypergeometric function. The expansion of the special functions in powers of ϵ then yields:

$$4^\epsilon\beta_{\frac{1}{4}(\epsilon,\epsilon-1)} = \frac{1}{\epsilon} + \frac{1}{3} - \log\frac{3}{4} + \mathcal{O}(\epsilon), \tag{A.285}$$

$$2\,{}_2F_1(\frac{1}{2}, 2-\epsilon, \frac{3}{2}, \frac{1}{4}) = \frac{4}{3} + \log 3 + \mathcal{O}(\epsilon), \tag{A.286}$$

$$(2\epsilon-1)^{-1} = -(1+2\epsilon) + \mathcal{O}(\epsilon^2). \tag{A.287}$$

which leaves us with:

$$I_4(\Phi^\infty, t') = \frac{\eta}{8}\left(\frac{1}{\epsilon} + 1 + \log\frac{4}{9}\right). \tag{A.288}$$

As for I_5, we had:

$$I_5(\Phi^{(0)}, t') = \int_0^\infty dz \int_0^{t'} dx x\, \Phi^{(0)}(2t', (z+2)x, x). \tag{A.289}$$

Replacing the expression of $\Phi^{(0)}$:

$$I_5(\Phi^{(0)}, t') = \mathcal{N}\hat{c}^{-d} \int_0^\infty dz \int_0^{t'} dx x^{1-d/2}(2t'(2+z) - x)^{-d/2}\mathcal{A}(\hat{c}(2t' - x/(z+2))), \tag{A.290}$$

which, expanding $\mathcal{A}$ once more, becomes:

$$I_5(\Phi^{(0)}, t') = \mathcal{A}(2\hat{c}t')I_5(\Phi^\infty, t'), \tag{A.291}$$

$$I_5(\Phi^\infty, t') = \mathcal{N}\hat{c}^{-d} \int_0^\infty dz \int_0^{t'} dx x^{1-d/2}(2t'(2+z) - x)^{-d/2}. \tag{A.292}$$

Integrating over z, we get:

$$I_5(\Phi^\infty, t') = \frac{\mathcal{N}\hat{c}^{-d}}{t'(d-2)} \int_0^{t'} dx x^{1-d/2}(4t' - x)^{1-d/2}, \tag{A.293}$$

which diverges in four dimensions. We may, taking $d = 4 - 2\epsilon$, rewrite this in terms of an incomplete beta function:

$$I_5(\Phi^\infty, t') = \frac{\eta}{2(d-2)} 4^\epsilon \beta_{\frac{1}{4}}(\epsilon, \epsilon), \tag{A.294}$$

and thus, using the fact that:

$$\beta_{\frac{1}{4}}(\epsilon, \epsilon) = 4^{-\epsilon}(\frac{1}{\epsilon} + \log\frac{4}{3}) + \mathcal{O}(\epsilon), \tag{A.295}$$

we end up with:

$$I_5(\Phi^\infty, t') = \frac{\eta}{2(d-2)}(\frac{1}{\epsilon} + \log\frac{4}{3}). \tag{A.296}$$

The next integral to address is I_6:

$$I_6(\Phi^{(0)}, t') = \int_0^\infty dz \int_0^{t'} dx\, \Phi^{(0)}(2t' + z, 2t', x), \tag{A.297}$$

where we replace as always the expression of $\Phi^{(0)}$:

$$I_6(\Phi^{(0)}, t') = \mathcal{N}\hat{c}^{-d} \int_0^\infty dz \int_0^{t'} dx (4t'^2 + 2zt' - x^2)^{-d/2} \mathcal{A}(\hat{c}(2t' + z - x^2/2t')), \tag{A.298}$$

and expand $\mathcal{A}$, leading to:

$$I_6(\Phi^{(0)}, t') = \mathcal{A}(2\hat{c}t') I_6(\Phi^\infty, t'), \tag{A.299}$$

$$I_6(\Phi^\infty, t') = \mathcal{N}\hat{c}^{-d} \int_0^\infty dz \int_0^{t'} dx (4t'^2 + 2zt' - x^2)^{-d/2}. \tag{A.300}$$

Integrating over z, we get:

$$I_6(\Phi^\infty, t') = \frac{\mathcal{N}\hat{c}^{-d}}{t'(d-2)} \int_0^\infty dz \int_0^{t'} dx (4t'^2 - x^2)^{1-d/2}, \tag{A.301}$$

which is a finite integral in four dimensions, and thus:

$$I_6(\Phi^\infty, t') = \frac{\mathcal{N}\hat{c}^{-d}}{4(d-2)t'^2} \log 3 = \frac{\eta}{4} \log 3. \tag{A.302}$$

We then recall the expression of I_7:

$$I_7(\Phi^{(0)}, t') = \int_0^\infty dz \int_0^{t'} dx x\, \Phi^{(0)}(2t', (z+2)x, 0), \tag{A.303}$$

and repeat the procedure. We replace $\Phi^{(0)}$:

$$I_7(\Phi^{(0)}, t') = \mathcal{N}\hat{c}^{-d} \int_0^\infty dz \int_0^{t'} dx x^{1-d/2} (2t'(z+2))^{-d/2} \mathcal{A}(\hat{c}(2t')), \tag{A.304}$$

leading directly to:

$$I_7(\Phi^{(0)}, t') = \mathcal{A}(2\hat{c}t') I_7(\Phi^\infty, t'), \tag{A.305}$$

$$I_7(\Phi^\infty, t') = \mathcal{N}\hat{c}^{-d} \int_0^\infty dz \int_0^{t'} dx x^{1-d/2} (2t'(z+2))^{-d/2}. \tag{A.306}$$

Integrating over z, we get:

$$I_7(\Phi^\infty, t') = \frac{2^{2-d}\mathcal{N}\hat{c}^{-d}}{(d-2)t^{d/2}} \int_0^{t'} x^{1-d/2} dx, \tag{A.307}$$

which integrating over x with $d = 4 - 2\epsilon$ yields:

$$I_7(\Phi^\infty, t') = \frac{2\mathcal{N}\hat{c}^{-d}}{(d-2)(4-d)}(2t')^{2-d} = \frac{\eta}{2(d-2)}\frac{1}{\epsilon}. \tag{A.308}$$

Then comes I_8:

$$I_8(\Phi^{(0)}, t') = \int_0^\infty dz \int_0^\infty dy\, \Phi^{(0)}(2t'+z, 2t'+y, 0), \tag{A.309}$$

which inserting the expression of $\Phi^{(0)}$ becomes:

$$I_8(\Phi^{(0)}, t') = \mathcal{N}\hat{c}^{-d} \int_0^\infty dz \int_0^\infty dy (2t'+z)^{-d/2}(2t+y)^{-d/2}\mathcal{A}(\hat{c}(2t'+z)), \tag{A.310}$$

and expanding the $\mathcal{A}$ function once more, we rewrite:

$$I_8(\Phi^{(0)}, t') = \mathcal{A}(2\hat{c}t')I_8(\Phi^\infty, t'), \tag{A.311}$$

$$I_8(\Phi^\infty, t') = \mathcal{N}\hat{c}^{-d}\left(\int_0^\infty dz (2t'+z)^{-d/2}\right)^2. \tag{A.312}$$

This integral is finite in four dimensions, and as such can be integrated directly after setting $d = 4$:

$$I_8(\Phi^\infty, t') = \mathcal{N}\hat{c}^{-d}(2t')^{-2} = \frac{\eta}{2}. \tag{A.313}$$

As we mentioned, we will leave the case of I_9 for the next section, and jump directly to I_{10}:

$$I_{10}(\Phi^{(0)}, t') = \int_0^\infty dz \int_0^{t'} dx x\, \partial_{t'}\Phi^{(0)}(2t'+z, 2t', x), \tag{A.314}$$

which inserting the expression of $\Phi^{(0)}$ becomes:

$$I_{10}(\Phi^{(0)}, t') = \mathcal{N}\hat{c}^{-d} \int_0^\infty dz \int_0^{t'} dx x \partial_{t'}(4t'^2 + 2t'z - x^2)^{-d/2}\mathcal{A}(\hat{c}(2t'+z-x^2/2t')), \tag{A.315}$$

and expanding the $\mathcal{A}$ function:

$$I_{10}(\Phi^{(0)}, t') = \mathcal{A}(2\hat{c}t')I_{10}(\Phi^{\infty}, t'), \tag{A.316}$$

$$I_{10}(\Phi^{\infty}, t') = \mathcal{N}\hat{c}^{-d}\int_0^{\infty} dz \int_0^{t'} dx x \partial_{t'}(2t'(z+2) - x)^{-d/2}. \tag{A.317}$$

Integrating over z then yields:

$$I_{10}(\Phi^{\infty}, t') = \frac{\mathcal{N}\hat{c}^{-d}}{d-2}\int_0^{t'} dx x \partial_{t'}(4t'^2 - x^2)^{1-d/2}(t)'^{-1}), \tag{A.318}$$

which is finite in four dimensions and can be integrated directly. Thus we have:

$$I_{10}(\Phi^{\infty}, t') = \frac{\mathcal{N}\hat{c}^{-d}}{2}\int_0^{t'} dx \frac{x(x^2 - 12t'^2)}{t'(4t'^2 - x^2)}, \tag{A.319}$$

and thus:

$$I_{10}(\Phi^{\infty}, t') = \frac{\mathcal{N}\hat{c}^{-d}}{4t^2}(\log\frac{3}{4} - \frac{2}{3}) = \frac{\eta}{2}(\log\frac{3}{4} - \frac{2}{3}). \tag{A.320}$$

We then look at integral I_{11}, which was given by:

$$I_{11}(\Phi^{(0)}, t') = \int_0^{\infty} dz \int_0^{t'} dx x^2 \partial_{t'}\Phi^{(0)}(2t', (z+2)x, x). \tag{A.321}$$

Inserting the expression of $\Phi^{(0)}$:

$$I_{11}(\Phi^{(0)}, t') = \mathcal{N}\hat{c}^{-d}\int_0^{\infty} dz \int_0^{t'} dx x^{2-d/2}\partial_{t'}(2t'(z+2) - x)^{-d/2}\mathcal{A}(\hat{c}(2t' - x/(z+2))), \tag{A.322}$$

which expanding the $\mathcal{A}$ function leads us to:

$$I_{11}(\Phi^{(0)}, t') = \mathcal{A}(2\hat{c}t')I_{11}(\Phi^{\infty}, t'), \tag{A.323}$$

$$I_{11}(\Phi^{\infty}, t') = \mathcal{N}\hat{c}^{-d}\int_0^{\infty} dz \int_0^{t'} dx x^{2-d/2}\partial_{t'}(2t'(z+2) - x)^{-d/2}. \tag{A.324}$$

Integrating over z then leaves us with:

$$I_{11}(\Phi^{\infty}, t') = \frac{\mathcal{N}\hat{c}^{-d}}{d-2}\int_0^{t'} dx x^{2-d/2}\partial_{t'}(4t' - x)^{1-d/2}t'^{-1}), \tag{A.325}$$

which is once more finite in two dimensions, so substituting $d = 4$ we can take

the derivative:

$$I_{11}(\Phi^\infty, t') = -\frac{\mathcal{N}\hat{c}^{-d}}{2}\int_0^{t'} dx \frac{8t' - x}{(4t'^2 - t'x)^2}, \tag{A.326}$$

and thus, integrating over x:

$$I_{11}(\Phi^\infty, t') = -\frac{\mathcal{N}\hat{c}^{-d}}{2t^2}(\log\frac{4}{3} + \frac{1}{3}) = -\eta(\log\frac{4}{3} + \frac{1}{3}). \tag{A.327}$$

Finally, for I_{12} we had:

$$I_{12}(\Phi^{(0)}, t') = \int_0^\infty dz \int_0^1 dy \int_0^{t'} dx x^2\, \partial_{t'}\Phi^{(0)}(2t', (z+2)x, xy), \tag{A.328}$$

which inserting the expression of $\Phi^{(0)}$ becomes:

$$I_{12}(\Phi^{(0)}, t') = \tag{A.329}$$
$$\mathcal{N}\hat{c}^{-d}\int_0^\infty dz \int_0^1 dy \int_0^{t'} dx x^{2-d/2}\partial_{t'}(2t'(z+2) - xy^2)^{-d/2}\mathcal{A}(\hat{c}(2t' - \frac{xy^2}{z+2})).$$

We expand the $\mathcal{A}$ function for the last time, and get:

$$I_{12}(\Phi^{(0)}, t') = \mathcal{A}(2\hat{c}t')I_{12}(\Phi^\infty, t'), \tag{A.330}$$
$$I_{12}(\Phi^\infty, t') = \mathcal{N}\hat{c}^{-d}\int_0^\infty dz \int_0^1 dy \int_0^{t'} dx x^{2-d/2}\partial_{t'}(2t'(z+2) - xy^2)^{-d/2}. \tag{A.331}$$

Integrating over z then yields:

$$I_{12}(\Phi^\infty, t') = \frac{\mathcal{N}\hat{c}^{-d}}{d-2}\int_0^1 dy \int_0^{t'} dx x^{2-d/2}\partial_{t'}(4t' - xy^2)^{1-d/2}t'^{-1}), \tag{A.332}$$

Which is once more finite in four dimensions, so taking $d = 4$ and derivating we get:

$$I_{12}(\Phi^\infty, t') = -\frac{\mathcal{N}\hat{c}^{-d}}{2}\int_0^1 dy \int_0^{t'} dx \frac{8t' - xy^2}{(4t'^2 - t'xy^2)^2}, \tag{A.333}$$

which can be integrated directly and yields:

$$I_{12}(\Phi^\infty, t') = -\frac{\mathcal{N}\hat{c}^{-d}}{2t^2}(-\frac{7}{4}\log 3 + \log 4) = \frac{\eta}{2}(-\frac{7}{2}\log 3 + 2\log 4). \tag{A.334}$$

To summarise, the infinite volume expressions are thus, putting everything to-

gether:

$$I_1(\Phi^\infty,t') = \mathcal{N}\hat{c}^{-d}\int_0^{t'} dx x^{1-d/2}(4t'-x)^{-d/2} = \frac{\eta}{8}(\frac{1}{\epsilon}+\frac{1}{3}+\log\frac{4}{3}), \tag{A.335}$$

$$I_2(\Phi^\infty,t') = \mathcal{N}\hat{c}^{-d}\int_0^{t'} dx x(4t'^2-x^2)^{-d/2} = \eta/12, \tag{A.336}$$

$$I_3(\Phi^\infty,t') = \frac{\mathcal{N}\hat{c}^{-d}}{(d-2)}(3t'^2)^{1-\frac{d}{2}} = \eta/3, \tag{A.337}$$

$$I_4(\Phi^\infty,t') = \mathcal{N}\hat{c}^{-d}\int_0^1 dy\int_0^{t'} dx x^{1-\frac{d}{2}}(4t'-y^2x)^{-\frac{d}{2}} = \frac{\eta}{8}(\frac{1}{\epsilon}+1+\log\frac{4}{9}), \tag{A.338}$$

$$I_5(\Phi^\infty,t') = \frac{\mathcal{N}\hat{c}^{-d}}{t'(d-2)}\int_0^{t'} dx x^{1-\frac{d}{2}}(4t'-x)^{1-\frac{d}{2}} = \frac{\eta}{2(d-2)}(\frac{1}{\epsilon}+\log\frac{4}{3}), \tag{A.339}$$

$$I_6(\Phi^\infty,t') = \frac{\mathcal{N}\hat{c}^{-d}}{t'(d-2)}\int_0^{t'} dx(4t'^2-x^2)^{1-\frac{d}{2}} = \frac{\eta}{4}\log 3, \tag{A.340}$$

$$I_7(\Phi^\infty,t') = \frac{2\mathcal{N}\hat{c}^{-d}}{(d-2)(4-d)}(2t')^{2-d} = \frac{\eta}{2(d-2)}\frac{1}{\epsilon}, \tag{A.341}$$

$$I_8(\Phi^\infty,t') = \mathcal{N}\hat{c}^{-d}(\int_0^\infty dz(2t'+z)^{-\frac{d}{2}})^2 = \eta/2, \tag{A.342}$$

$$I_{10}(\Phi^\infty,t') = \frac{\mathcal{N}\hat{c}^{-d}}{(d-2)}\int_0^{t'} dx x\partial_{t'}\{(4t'^2-x^2)^{1-\frac{d}{2}}(t')^{-1}\} = \frac{\eta}{2}(\log\frac{3}{4}-\frac{2}{3}), \tag{A.343}$$

$$I_{11}(\Phi^\infty,t') = \frac{\mathcal{N}\hat{c}^{-d}}{(d-2)}\int_0^{t'} dx x^{2-\frac{d}{2}}\partial_{t'}\{(4t'-x)^{1-\frac{d}{2}}(t')^{-1}\} = -\eta(\log\frac{4}{3}+\frac{1}{3}), \tag{A.344}$$

$$\begin{aligned} I_{12}(\Phi^\infty,t') &= \frac{\mathcal{N}\hat{c}^{-d}}{(d-2)}\int_0^1 dy\int_0^{t'} dx x^{2-\frac{d}{2}}\partial_{t'}\{(4t'-xy^2)^{1-\frac{d}{2}}(t')^{-1}\} \\ &= \frac{\eta}{2}(-\frac{7}{2}\log 3+2\log 4). \end{aligned} \tag{A.345}$$

where we set $d=4-2\epsilon$, and we used the definition of $\mathcal{N}$, $\hat{c}$ and t' to define:

$$\eta = (4\pi)^{-d}(2t)^{2-d}, \qquad \mathcal{N}\hat{c}^{-d}(t')^{2-d} = 1/2(4\pi)^d t^{d-2} = 2^{d-3}\eta. \tag{A.346}$$

The term $I_9(\Phi^\infty,t')$ will be treated in the next subsection, but will turn out to be vanishing.

A.6.2 Regularisation of I_9

We may now look at the procedure used to regularise the integral I_9, defined in eq. (2.77), which differs slightly from the general treatment used above. As we recall, the initial integral is split into three terms:

$$I_9(t') = I_9(\Phi - \theta(1-z)\Phi^{(0)}, t') - I_9(\theta(z-1)\Phi^{(0)}, t') + I_9(\Phi^{(0)}, t')\,, \qquad \text{(A.347)}$$

with the Heaviside function θ restricting the integration intervals in z. The first term on the r.h.s. of this expression is by construction finite in four dimensions, whereas the other two will be shown to be so as well after analytical continuation to $d = 4$.

Both $I_9(\Phi^{(0)}, t')$ and $I_9(\theta(z-1)\Phi^{(0)}, t')$ can be rewritten as the the $a = 0$ and $a = 1$ cases of a generic integral:

$$\bar{I}_9 = \frac{1}{2}\int_a^\infty dz \int_0^\infty dy \int_0^1 dx (x^2 z\partial_{t'} - d)\Phi^{(0)}\left(2t' + xz + y, z, xz\right), \qquad \text{(A.348)}$$

which, expanding the $\Phi^{(0)}$ function, becomes:

$$\bar{I}_9 = \frac{1}{2}\mathcal{N}\hat{c}^{-\frac{d}{2}}\int_a^\infty dz \int_0^1 dx (x^2 z\partial_{t'} - d) z^{-\frac{d}{2}} {\sum_m}' e^{-\pi\hat{c}m^2(2t' + zx(1-x))} \int_0^\infty dy e^{-\pi\hat{c}m^2 y}. \qquad \text{(A.349)}$$

Integrating over y and taking the derivative:

$$\bar{I}_9 = -\frac{1}{2}\mathcal{N}\hat{c}^{-\frac{d}{2}}\int_a^\infty dz \int_0^1 dx (2x^2 z + \frac{d}{\pi\hat{c}m^2}) z^{-\frac{d}{2}} {\sum_m}' e^{-\pi\hat{c}m^2(2t' + zx(1-x))}, \qquad \text{(A.350)}$$

and then we can define $\omega = \pi\hat{c}m^2 x(1-x)$:

$$\bar{I}_9 = -\frac{1}{2}\mathcal{N}\hat{c}^{-\frac{d}{2}}\int_0^1 dx {\sum_m}' e^{-2\pi\hat{c}m^2 t'} \int_a^\infty dz (2x^2 z + \frac{d}{\pi\hat{c}m^2}) z^{-\frac{d}{2}} e^{-\omega z}, \qquad \text{(A.351)}$$

allowing us to split the integral into two different terms:

$$\bar{I}_9 = -\frac{1}{2}\mathcal{N}\hat{c}^{-\frac{d}{2}}\int_0^1 dx {\sum_m}' e^{-2\pi\hat{c}m^2 t'} (2x^2 A + \frac{d}{\pi\hat{c}m^2} B). \qquad \text{(A.352)}$$

The two integrals A and B, after a $z' = \omega z$ change of variable, can be expressed

in terms of incomplete Γ functions:

$$A = \int_a^\infty dz z^{1-\frac{d}{2}} e^{-\omega z} = \omega^{\frac{d}{2}-2}\Gamma(2-\frac{d}{2},\omega a), \tag{A.353}$$

$$B = \int_a^\infty dz z^{-\frac{d}{2}} e^{-\omega z} = \omega^{\frac{d}{2}-1}\Gamma(1-\frac{d}{2},\omega a), \tag{A.354}$$

leading to:

$$\begin{aligned}\bar{I}_9 = &-\frac{1}{2}\mathcal{N}\hat{c}^{-\frac{d}{2}}\int_0^1 dx {\sum_m}' e^{-2\pi\hat{c}m^2t'}\omega^{\frac{d}{2}-2} \\ &\times\left(2x^2\Gamma(2-\frac{d}{2},\omega a)+x(1-x)d\Gamma(1-\frac{d}{2},\omega a)\right),\end{aligned} \tag{A.355}$$

where we used the definition of ω to eliminate $\pi\hat{c}m^2$ from the denominator in B.

At this point, we need to start looking at $I_9(\Phi^{(0)},t')$ and $I_9(\theta(z-1)\Phi^{(0)},t')$ separately. We begin with the former, obtained by taking $a=0$. The incomplete Γ functions then become complete ones, and so we use the standard recurrence relation to write everything in terms of $\Gamma(2-d/2)$:

$$I_9(\Phi^{(0)},t') = \mathcal{N}\hat{c}^{-\frac{d}{2}}\int_0^1 dx {\sum_m}' e^{-2\pi\hat{c}m^2t'}\frac{x^2(2-d)+x(1-x)d}{d-2}\omega^{\frac{d}{2}-2}\Gamma(2-\frac{d}{2}). \tag{A.356}$$

The Γ function on the right can then be eliminated if one uses Schwinger parametrisation to rewrite ω:

$$\omega^{\frac{d}{2}-2} = \frac{[x(1-x)]^{\frac{d}{2}-2}}{(\pi\hat{c}m^2)^{2-\frac{d}{2}}} = \frac{[x(1-x)]^{\frac{d}{2}-2}}{\Gamma(2-\frac{d}{2})}\int_0^\infty dz z^{1-\frac{d}{2}}e^{-\pi\hat{c}m^2z}, \tag{A.357}$$

and therefore:

$$\begin{aligned}I_9(\Phi^{(0)},t') &= \frac{\mathcal{N}\hat{c}^{-\frac{d}{2}}}{d-2}\mathcal{I}\int_0^\infty dz z^{1-\frac{d}{2}}{\sum_m}' e^{-\pi\hat{c}m^2(2t'+z)} \\ &= \frac{\mathcal{N}\hat{c}^{-d}}{d-2}\mathcal{I}\int_0^\infty dz z^{1-\frac{d}{2}}(2t'+z)^{-\frac{d}{2}}\mathcal{A}(\hat{c}(2t'+z)),\end{aligned} \tag{A.358}$$

where we defined:

$$\mathcal{I} = \int_0^1 dx[x(1-x)]^{\frac{d}{2}-2}\left(x(1-x)d-x^2(d-2)\right). \tag{A.359}$$

The asymptotic behaviour at $z = 0$ can then be obtained by expanding $\mathcal{A}(\hat{c}(2t' + z))$ around $z = 0$, leading to:

$$I_9^{\text{div}}(\Phi^{(0)}, t') = \mathcal{A}(2\hat{c}t')I_9(\Phi^{\infty}, t')\,, \tag{A.360}$$

where:

$$I_9(\Phi^{\infty}, t') = \frac{\mathcal{N}\hat{c}^{-d}}{d-2}\mathcal{I}\int_0^{\infty} dz\, z^{1-d/2}(2t'+z)^{-d/2}. \tag{A.361}$$

The integral over z presents a pole in $1/\epsilon$, but it is multiplied by the integral $\mathcal{I}$, which in $d = 4-2\epsilon$ dimensions is identically zero. As such, the integral will make the pole vanish, and the final result will be exactly zero in $d = 4$ dimensions. This $I_9(\Phi^{\infty}, t')$ is precisely the integral appearing in the infinite volume calculation, and vanishes, as we have just seen, for $d = 4$ in dimensional regularisation.

The remaining $I_9(\theta(z-1)\Phi^{(0)}, t')$ term, obtained taking $a = 1$ in eq. (A.355), can then be treated in a similar way, though the recurrence relation for the incomplete Γ functions is a bit different:

$$\Gamma(1-\frac{d}{2}, \omega a) = \frac{2}{2-d}\left(\Gamma(2-\frac{d}{2}, \omega a) - (\omega a)^{1-\frac{d}{2}}e^{-\omega a}\right), \tag{A.362}$$

which means that we can separate eq. (A.355) into the sum $\bar{I}_9^a + \bar{I}_9^b$ of two contributions:

$$\bar{I}_9^a = \frac{\mathcal{N}\hat{c}^{-\frac{d}{2}}}{d-2}\int_0^1 dx[x(1-x)d - x^2(d-2)]\sum_m{}' \omega^{\frac{d}{2}-2}e^{-2\pi\hat{c}m^2t'}\Gamma(2-\frac{d}{2}, \omega), \tag{A.363}$$

$$\bar{I}_9^b = \mathcal{N}\hat{c}^{-\frac{d}{2}}\frac{d}{2-d}\int_0^1 dx \sum_m{}' \frac{1}{(\pi\hat{c}m^2)}e^{-\pi\hat{c}m^2(2t'+x(1-x))}. \tag{A.364}$$

The second term is quite simple, as by simpling using Schwinger parametrisation to lift up the m^2 term we get:

$$\bar{I}_9^b = \mathcal{N}\hat{c}^{-\frac{d}{2}}\frac{d}{2-d}\int_0^1 dx \int_0^{\infty} dz \sum_m{}' e^{-\pi\hat{c}m^2(2t'+x(1-x)+z)}, \tag{A.365}$$

which can then be rewritten in terms of the $\mathcal{A}$ function:

$$\bar{I}_9^b = \frac{\mathcal{N}\hat{c}^{-d}d}{2-d}\int_0^1 dx \int_0^{\infty} dz(2t'+x(1-x)+z)^{-\frac{d}{2}}\mathcal{A}(\hat{c}(2t'+x(1-x)+z)). \tag{A.366}$$

The $\bar{I}_9^a$ term, however, is a bit more complicated. Defining $\sigma = \pi\hat{c}m^2 = \omega/x(1-x)$, we can rewrite:

$$\bar{I}_9^a = \frac{\mathcal{N}\hat{c}^{-\frac{d}{2}}}{d-2}\sum_m{}' e^{-2\sigma t'}\mathcal{I}', \tag{A.367}$$

where we defined an integral:

$$\mathcal{I}' = \sigma^{\frac{d}{2}-2}\int_0^1 dx[x(1-x)d - x^2(d-2)][x(1-x)]^{\frac{d}{2}-2}\Gamma(2-\frac{d}{2}, x(1-x)\sigma). \tag{A.368}$$

After a bit of algebra, this can be rewritten as:

$$\bar{I}_9^a = \frac{2\mathcal{N}\hat{c}^{-\frac{d}{2}}}{d-2}\sum_m{}'\frac{1}{\sigma}e^{-2\sigma t'}(\int_0^1 dx e^{-\sigma x(1-x)} - 1), \tag{A.369}$$

which, using Schwinger parametrisation to eliminate σ from the denominator and rewriting σ in terms of x becomes:

$$\bar{I}_9^a = \frac{2\mathcal{N}\hat{c}^{-\frac{d}{2}}}{d-2}\int_0^\infty dz\sum_m{}'(\int_0^1 dx e^{-\pi\hat{c}m^2(2t'+x(1-x)+z)} - e^{-\pi\hat{c}m^2(2t'+z)}). \tag{A.370}$$

In terms of the $\mathcal{A}$ functions, this yields two different contributions :

$$\begin{aligned}\bar{I}_9^a =& \frac{2\mathcal{N}\hat{c}^{-d}}{d-2}\int_0^\infty dz\int_0^1 dx(2t'+x(1-x)+z)^{-\frac{d}{2}}\mathcal{A}(\hat{c}(2t'+x(1-x)+z)) \\ &- \frac{2\mathcal{N}\hat{c}^{-d}}{d-2}\int_0^\infty dz(2t'+z)^{-\frac{d}{2}}\mathcal{A}(\hat{c}(2t'+z))),\end{aligned} \tag{A.371}$$

And so, combining all contributions to $I_9(\theta(z-1)\Phi^{(0)}, t')$, the regularised result becomes:

$$\begin{aligned}I_9^{\text{reg}}(\theta(z-1)\Phi^{(0)}, t') = -\frac{\mathcal{N}\hat{c}^{-d}}{d-2}\int_0^\infty dz\ \Big\{&2(2t'+z)^{-d/2}\mathcal{A}\left(\hat{c}(2t'+z)\right) \\ &+(d-2)\int_0^1 dx\ (2t'+x(1-x)+z)^{-d/2}\,\mathcal{A}\left(\hat{c}(2t'+x(1-x)+z)\right)\Big\},\end{aligned} \tag{A.372}$$

which is finite in $d=4$ dimensions, and which we were able to evaluate numerically.

A.7 Implementation of the integration algorithm

To perform the numerical computation presented in section 2.4.2, a numerical code was used to determine the values of the Φ functions and their derivatives at any point, and to integrate them along the corresponding ranges using the trapezoidal rule up to a target precision. We will in this section explain how the computation in the C++ code of each Φ is performed at each point of the integration range, along with the inner workings of the integration algorithm.

A.7.1 Computation of the momentum sums

Let us begin by explaining how the sums over infinite momenta were computed. As we recall, we had to compute the following quantity:

$$\Phi^{\text{fin}}(s,u,v) = H\left(s,u,v,0\right) - H\left(s,u,v,\hat{\theta}\right) - \Phi^{(0)}(s,u,v)\,, \tag{A.373}$$

which was made finite through the procedure explained in section 2.3.2, in which one can also find the definitions of H and $\Phi^{(0)}$. Taking $d = 4$ and $d_t = 2$, the right hand side of the equation can be rewritten in terms of momentum sums of the general form:

$$\sum_{M\in\mathbb{Z}^s} \exp\left(-\pi M^t X M\right) = (\det X)^{-\frac{s}{2}} \sum_{M\in\mathbb{Z}^s} \exp\left(-\pi M^t X^{-1} M\right), \text{ with } s\in\mathbb{Z}, \tag{A.374}$$

where we introduced a generic matrix X to denote either A_0 or B from eqs. (2.124) and (2.125). We used Poisson resummation from eq. (2.47) to write the sums in terms of both X and its inverse, allowing us to simultaneously compute several equivalent versions of the three terms of Φ^{fin} so as to exploit, to optimise the program, the fact that the convergence speed of the sums depends on which (s,u,v) point is being considered. We then defined eight quantities to be computed:

$$E_0 = \sum_{m\neq 0 \bmod N} e^{-\pi M^t B_\theta M}, \qquad E_1 = \sum_{m,n} e^{-\pi M^t B_0 M}, \tag{A.375}$$

$$E_2 = (\det B_\theta)^{-\frac{1}{2}} \sum_{m,n} e^{-\pi M^t B_\theta^{-1} M}, \qquad E_3 = (\det B_0)^{-\frac{1}{2}} \sum_{n\neq 0} e^{-\pi M^t B_0^{-1} M}, \tag{A.376}$$

$$E_4 = \sum_{m=0 \bmod N} e^{-\pi M^t B_\theta M}, \qquad E_5 = (\det B_0)^{-\frac{1}{2}} \sum_{n=0} e^{-\pi M^t B_0^{-1} M}, \tag{A.377}$$

$$E_6 = (\det \tilde{B})^{-\frac{1}{2}} \sum_{n=0} e^{-\pi M^t \tilde{B}^{-1} M}, \qquad E_7 = \sum_{n=0} e^{-\pi M^t \tilde{B} M}, \tag{A.378}$$

where we used the shorthands $B_\theta \equiv B(\hat{c}s, \hat{c}u, \hat{c}v, \hat{\theta})$, $B_0 \equiv B(\hat{c}s, \hat{c}u, \hat{c}v, 0)$, and $\tilde{B} \equiv B(\hat{c}sN^2, \hat{c}u, \hat{c}vN, 0)$ for clarity. Several of these expressions are redundant:

$$E_1 = E_3 + E_5, \qquad E_2 = E_0 + E_4, \qquad E_6 = E_7, \tag{A.379}$$

allowing us to rewrite the observable $\Phi^{\text{fin}}(s, u, v)$ in four equivalent forms:

$$\Phi^{\text{fin}}(s, u, v) = \mathcal{N}\left[E_1(E_1 - E_0 - E_4) + E_5(E_6 - E_5)\right], \tag{A.380}$$

$$\Phi^{\text{fin}}(s, u, v) = \mathcal{N}\left[E_1(E_1 - E_0 - E_4) + E_5(E_7 - E_5)\right], \tag{A.381}$$

$$\Phi^{\text{fin}}(s, u, v) = \mathcal{N}\left[E_5(E_6 - E_2) + (E_3 + E_5)(E_3 + E_5 - E_2)\right], \tag{A.382}$$

$$\Phi^{\text{fin}}(s, u, v) = \mathcal{N}\left[E_5(E_7 - E_2) + (E_3 + E_5)(E_3 + E_5 - E_2)\right]. \tag{A.383}$$

In the integrals with derivatives, we simply computed the derivatives of each E_i function (analitically; no finite differences were used in this code) and used the chain rule as needed.

The algorithm used to generate the momenta in the sums works by defining a four-dimensional integer vector $M^t = (m_1, n_1, m_2, n_2)$, and generating the corresponding combinations of integers m_i, n_i, using the $M \to -M$ symmetry in the integrand for optimisation. The momentum tetrads were generated in an orderly manner, starting with all contributions of the tetrads with $|m_i|, |n_i| = 0, 1$, then adding the ones with some $|m_i|, |n_i| = 2$, then $|m_i|, |n_i| = 3$ and so forth, adding terms with momenta of increasing order until the sum converges (in the sense that we will detail below).

Thus, the code simply runs through momentum tetrads of increasing order, and passes them through a filter that checks whether or not m is proportional to N and whether or not n vanishes, computing the relevant exponential terms and adding them to each of the eight corresponding E_i terms when needed. Once every tetrad of a particular order has been processed, the program computes the value of Φ^{fin} up to that order in the four equivalent ways shown earlier, and checks whether the variation of each term between the previous order and the new one is smaller than a set quantity ϵ times the value of the function. If that

turns out to be the case for any of the four expressions, the sum is considered to have converged and that particular Φ^{fin} is returned as the result. We set a minimum order of four for the sum to avoid early spurious convergences, and chose to use the same relative error ϵ as the one used as the convergence criterion for the integration algorithm (which we will explain in the next section). The chosen values of ϵ ranged between 10^{-3} and 10^{-8} depending on the integral, due to differences in runtime.

A.7.2 Computation of the integrals

Once we know how to compute the integrand at each point, the next step is to look at the integration algorithm, for which we used a rather standard trapezoidal rule for multiple integrals in which the integral along each coordinate is approximated using an increasing number of trapezoids until a target precision is reached. We will begin by quickly illustrating how a generic single-dimensional integral works in our code, generalise it to the multiple ones, and then mention a few specific choices and particularities of our strategy.

Consider thus a single integral over a finite interval, say for instance the interval $z \in [0, 1]$. The code begins by computing the value of the integrand, which in this case would be the Φ function (or its derivative), at the beginning and end of the interval, and approximates the integral as the area of the corresponding trapezoid. The integrand is then computed at the middle point $z = 0.5$, and the integral is approximated with the two $z \in [0, 0.5], [0.5, 1]$ trapezoids. Then, at third order, the integrand is obtained in the midpoints of the previous trapezoids, and the integral is approximated with the four trapezoids $[0, 0.25], [0.25, 0.5], [0.5, 0.75], [0.75, 1]$. This subdivision generated by computing the integrand at the midpoints goes on, until the variation in the approximated integral between one order and the next is smaller than a set target ϵ (the same that we used for the Φ functions in the momentum sums) times the value of the integral at that order, at which point we consider that convergence has been reached and the integral is finished. As we mentioned earlier, in our runs ϵ ranged between 10^{-3} and 10^{-8}.

Multiple integrals are trivial in such a setting: one simply starts with the integral over the outermost coordinate, z, but at every point in which the integrand needs to be determined instead of computing the Φ function, one recursively calls the integration routine to obtain the integral over the next coordinate.

To allow for easier parallelisation, and since the integrand tends to have more structure near $z = 0$, we chose to split the integral in z into a set of pre-chosen subintervals, with a shorter step size at smaller values of z, and treated the integration along each of these subintervals separately. To avoid spurious convergences, we imposed a minimum of eight points in each integration subinterval. Moreover, in the cases in which the integrals went up to infinity in the z coordinate, we ran the integration code up to $z_{max} = 10^4$ and extrapolated the result by fitting the results of the last ten subintervals to a simple shifted exponential of the form $I_{fit} = a_0 - a_1 e^{-a_2(z-z_{max})}$, using the fitted a_0 as the final result of the integral. A simple least squares method algorithm was used to perform the fits.

There were a couple of peculiarities worth mentioning regarding integrals I_8 and I_9. For the former, and after performing a change of variables so that the second integral runs up to $x = 1$, we noticed that the contribution to the integral is concentrated around $z = 0$, with the profiles of the integrand over x peaking at small values of z and vanishing after a range around $\sim z^{-1}$. This means that the strategy to keep dividing the integration interval into halves in the x coordinate is quite inefficient, as the contribution is concentrated in a small region and one is throwing many points into areas that are effectively zero. To avoid this issue, we chose to subdivide the inner integral into 1,5,50,500 and 1000 equal subintervals as z runs up to 1,10,1000 and 10000 respectively. As soon as the integral over two consecutive subintervals in the x axis vanishes for $z > 1$, the subintervals that follow are ignored entirely, greatly speeding up the computation without affecting the result.

The case of I_9 is a bit special in that the regularisation was different from the other integrals, with a Heaviside $\theta(1 - z)$ function being introduced in the integrand (see the end of section 2.3.2 and appendix A.6.2 for the specifics) and separating the bits before and after $z = 1$. For the numerical computation, we performed the same change of integral as in I_8 to make the second integral run up to $y' = 1$, but then the Heaviside function became a $\theta(1 - y'z')$ function, with the integrands being different before and after this point. As convergence turned out to be painfully slow when both integrands were considered jointly, we simply forced the integrals in y' to be split from $z' = 1$ onwards into two subintervals $[0, 1/z']$ and $[1/z', 1]$, with the convergence of each side being considered separately.

Due to the procedure we used to determine the convergence of the integrals,

for a given integral $\mathcal{I}$, and given n_i integrals to perform (as in single, double or triple inegrals), the final error of the integral is:

$$\Delta\mathcal{I} = (1 + n_i)\epsilon\mathcal{I}. \tag{A.384}$$

This comes from the fact that both the error of the Φ functions and the convergence criterion for the integrals is given by the same ϵ, so for a single integral:

$$\mathcal{I} + \Delta\mathcal{I} = (1 + \epsilon) \sum (\Phi + \Delta\Phi) \simeq (1 + 2\epsilon)\, \mathcal{I}. \tag{A.385}$$

Additional integrals simply add extra $1 + \epsilon$ factors, which end up generating the $(1 + n_i)$ term. In the cases where the integrals ran up to infinity in z and had to be fitted, we presented as the final error either $\Delta\mathcal{I}$ or the error from the fit itself, whichever was larger.

Moreover, some issues were caused by some computed quantities hitting machine precision, slowing down the computation while leaving the results effectively unaffected. To deal with them, we introduced several hard cuts in the integrals, integrands and determinants. In particular, we made it so that any Φ function returning a value under 10^{-12}, any inner integral returning any value under 5×10^{-12} (or 10^{-10} in the cases of a few intervals in which using 5×10^{-12} led to severe slowdowns), and any exponential returning a result over 10^{-13} is automatically set to be exactly zero. The cut in the integrals is also used in the convergence checks we mentioned earlier: whenever the value of the integral times ϵ becomes smaller than the precision cut, the precision cut is used as the convergence criterion instead.

Lastly, we need to mention that, despite the integrals computed being finite, convergence near the point $(s, u, v) = (2, 0, 0)$ can become quite slow, as the integrand approaches machine precision. To address this issue, a cut in u was introduced, setting the integrand to zero when $u < 0.01$ in the integrals in which such point is part of the integration region (namely, in I_i for $i = 1, 4, 5, 7, 9, 11, 12$). This cut does not appreciably change the results, as the contribution of the excluded area is well below the uncertainty of the total result. To illustrate this, we show in fig. A.1 some examples of the profile of the integrand near the aforementioned $(s, u, v) = (2, 0, 0)$ point, in which one can both see that the integrand is indeed finite and that the area excluded by the cut is negligible compared to the rest of the integrand.

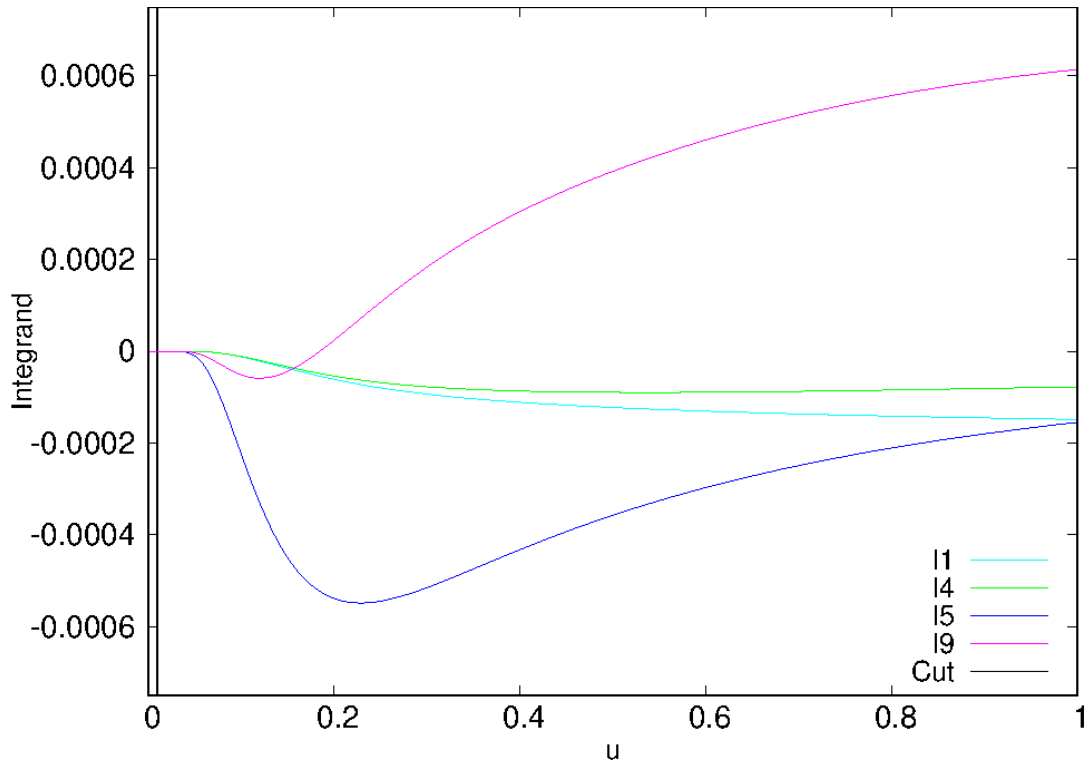

Figure A.1: We display several examples of the profile of the integrand as a function of u near $(s,u,v)=(2,0,0)$ for several integrals for $c=0.7$, to illustrate that the cut introduced in u (displayed as a vertical line near the origin) has no effect on the results.

A.8 The infinite volume and large N limits

This appendix will be dedicated to the derivation of the formulas mentioned in sec. 2.5, which were used to analyse the dependence of $\mathcal{C}_1$ on N and $\hat{\theta}$ at NLO for the case of a two-dimensional twist ($d_t=2$). As we recall from section 2.5, all contributions to $\mathcal{C}_1$ (except the one coming from I_9, see app. A.6.2) could be written in the form:

$$\bar{I}=\frac{4}{3\mathcal{A}(2\hat{c})}\int(u\alpha)^{-2}\left(\hat{H}(s,u,v,0)-\hat{H}(s,u,v,\hat{\theta})-\mathcal{A}(2\hat{c})\right), \tag{A.386}$$

where the generic notation $\int$ denotes the integrals from eqs.(2.69)-(2.80), including the prefactors multiplying the Φ functions and sometimes derivatives. The function $\hat{H}(s,u,v,\hat{\theta})$ is defined through the relation:

$$H(s,u,v,\hat{\theta})=\Phi^{\infty}(s,u,v)\hat{H}(s,u,v,\hat{\theta}), \tag{A.387}$$

with H and Φ^∞ denoting the functions defined in eqs. (2.85) and (2.89) respectively. The former, as we recall, was used to rewrite the Φ functions entering the integrals:

$$\Phi(s,u,v,\hat{\theta}) = H(s,u,v,0) - H(s,u,v,\hat{\theta}). \tag{A.388}$$

The function $\hat{H}$ can then be expressed in terms of a new function:

$$\begin{aligned}\hat{H}(s,u,v,\hat{\theta}) = \mathrm{Re}\Big\{ & F_1(\alpha,u,v,0,4-d_t) \\ & \times \left(F_1(\alpha,u,v,\hat{\theta},d_t) - \frac{1}{N^2} F_1(\alpha l_g^2, u, v l_g, 0, d_t) \right) \Big\},\end{aligned} \tag{A.389}$$

where we defined:

$$F_1(\alpha,u,v,\hat{\theta},d) = (\hat{c}\alpha)^{d/2} \sum_{m,n\in\mathbb{Z}^d} \exp\left\{ -\pi\hat{c}\alpha m^2 - \frac{\pi}{\hat{c}u}(n-\hat{\theta}\tilde{\epsilon}m)^2 + 2\pi i \frac{v}{u} mn \right\}. \tag{A.390}$$

It is convenient, in order to analyse the infinite volume limit, to look at the expressions resulting after Poisson resummation in m for both the $\hat{\theta}$-dependent and $\hat{\theta}$-independent parts. For the latter, Poisson resummation yields:

$$F_1(\alpha,u,v,\hat{\theta}=0,d) = \sum_{m,n\in\mathbb{Z}^d} \exp\left\{ -\frac{\pi}{\hat{c}\alpha} m^2 - \frac{\pi s}{\hat{c}\alpha u} n^2 + \frac{2\pi v}{\hat{c}\alpha u}\, mn \right\} \tag{A.391}$$

whereas in the $\hat{\theta}$-dependent case we begin by splitting m into $m = \hat{m} l_g + m^c$, with the components of m^c_μ taking values in the intervals $[-l_g/2, l_g/2)$ and $[-(l_g-1)/2, (l_g-1)/2]$ for even and odd values of l_g respectively. Poisson resummation is then performed with respect to $\hat{m}$ only, leading to:

$$\begin{aligned}F_1(\alpha,u,v,\hat{\theta},d_t) = \frac{1}{N^2} \sum_{m,n\in\mathbb{Z}^{d_t}} \sum_{m^c} \exp\Big\{ & -\frac{\pi}{\hat{c}\alpha l_g^2} m^2 - \frac{\pi s}{\hat{c}\alpha u}(n-\chi)^2 \\ & + \frac{2\pi v}{\hat{c}\alpha u l_g} m(n-\chi) + i\,\frac{2\pi}{l_g} m m^c \Big\},\end{aligned} \tag{A.392}$$

where we introduced a d_t-dimensional vector χ whose components are given by $\chi_\mu = ||\hat{\theta}\tilde{\epsilon} m^c_\mu||$, the symbol $||x||$ denoting the distance from x to the nearest integer.

Introducing $\chi_\mu = n^c_\mu / l_g$ and inverting the relation between m^c and n^c to write

$m^c = k\epsilon n^c \,(\mathrm{mod}\; l_g)$, we obtain:

$$F_1(\alpha,u,v,\hat{\theta},d_t) = \frac{1}{N^2}\sum_{m,n\in\mathbb{Z}^{d_t}}\sum_{n^c}\exp\Big\{-\frac{\pi}{\hat{c}\alpha u l_g^2}\Big(um^2+s(nl_g-n^c)^2 - 2vm(nl_g-n^c)\Big)+i\frac{2\pi k}{l_g}m\epsilon n^c\Big\}. \tag{A.393}$$

The two terms entering $\hat{H}(s,u,v,\hat{\theta})$ and $\hat{H}(s,u,v,0)$ can then be rewritten in matrix form. Recalling the expressions of A_0 and B from eqs.(2.124) and(2.125) we have, in terms of Siegel theta functions, and particularising to the case of $d_t = 2$:

$$\begin{aligned}\hat{H}(s,u,v,0) =&\Theta^2\left(0\Big|iA_0\left(\frac{1}{\hat{c}\alpha},\frac{s}{\hat{c}\alpha u},\frac{v}{\hat{c}\alpha u}\right)\right)\Big\{\Theta^2\left(0\Big|iA_0\left(\frac{1}{\hat{c}\alpha},\frac{s}{\hat{c}\alpha u},\frac{v}{\hat{c}\alpha u}\right)\right)\\ &-\frac{1}{N^2}\Theta^2\left(0\Big|iA_0\left(\frac{1}{\hat{c}N^2\alpha},\frac{s}{\hat{c}\alpha u},\frac{v}{\hat{c}N\alpha u}\right)\right)\Big\},\end{aligned} \tag{A.394}$$

and:

$$\begin{aligned}\hat{H}(s,u,v,\hat{\theta}) =&\frac{1}{N^2}\Theta^2\left(0\Big|iA_0\left(\frac{1}{\hat{c}\alpha},\frac{s}{\hat{c}\alpha u},\frac{v}{\hat{c}\alpha u}\right)\right)\\ &\times\Big\{\mathrm{Re}\Theta\left(0\Big|iB\left(\frac{1}{\hat{c}N^2\alpha},\frac{s}{\hat{c}N^2\alpha u},\frac{v}{\hat{c}N^2\alpha u},\frac{k}{N}\right)\right)\\ &-\Theta^2\left(0\Big|iA_0\left(\frac{1}{\hat{c}N^2\alpha},\frac{s}{\hat{c}\alpha u},\frac{v}{\hat{c}N\alpha u}\right)\right)\Big\}.\end{aligned} \tag{A.395}$$

It will be convenient to split the original integral into two separate pieces, one containing all of the $\hat{\theta}$ dependence, and another with $\hat{\theta}=0$. As we want both of them to be well behaved both in the IR and in the UV, it will be useful to first isolate the terms corresponding to zero-modes at each step of the calculation, both before and after Poisson resummation.

For zero-modes before resummation, we simply need to look at the original definition of H given in eq. (2.85), in which the terms with $m=0$ were already subtracted, and set $n=0$. Subtracting this quantity to both the $\hat{\theta}$-dependent

and independent pieces leads to:

$$\bar{I} = \frac{4}{3\mathcal{A}(2\hat{c})}\int\left\{(u\alpha)^{-2}\left(\hat{H}(s,u,v,0)-\mathcal{A}(2\hat{c})\right)-\frac{\hat{c}^2}{s^2}\mathcal{A}(\hat{c}s)\right\} \\ -\frac{4}{3\mathcal{A}(2\hat{c})}\int\left\{(u\alpha)^{-2}\hat{H}(s,u,v,\hat{\theta})-\frac{\hat{c}^2}{s^2}\mathcal{A}(\hat{c}s)\right\}. \tag{A.396}$$

The analogous procedure after Poisson resummation is achieved, for the $\hat{\theta}$-independent term, setting $m = 0$ and $n = 0$ (separately) in eq. (A.394) and in the $\mathcal{A}(\hat{c}s)$ terms and subtracting the resulting expressions. Notice that the $m = n = 0$ term is then subtracted twice, and needs to be added back. Setting $m = 0$, we have:

$$\hat{H}(s,u,v,0) \underset{m=0}{=} (1-\frac{1}{N^2})\sum_{n\in\mathbb{Z}^4} e^{-\frac{\pi s}{\hat{c}\alpha u}n^2} = \frac{N^2-1}{N^2}\theta_3^4\left(0,\frac{is}{\hat{c}\alpha u}\right), \tag{A.397}$$

whereas setting $n = 0$ directly yields an expression of the form shown in eq. (2.49):

$$\hat{H}(s,u,v,0) \underset{n=0}{=} \mathcal{A}(\hat{c}\alpha), \tag{A.398}$$

and then setting both m and n to zero simply yields $1-1/N^2$. Putting everything together, we have:

$$\hat{H}(s,u,v,0) = \hat{H}'(s,u,v,0) + \mathcal{A}(\hat{c}\alpha) + \frac{N^2-1}{N^2}\left\{\theta_3^4\left(0,\frac{is}{\hat{c}\alpha u}\right)-1\right\}, \tag{A.399}$$

where $\hat{H}'$ denotes the resulting function after subtracting the aforementioned zero modes.

For the term in $\mathcal{A}(\hat{c}s)$, the determination of the zero mode is direct, as simply rewriting it in the form of eq. (2.49) and setting $m = 0$ gives a contribution:

$$-\frac{\hat{c}^2}{s^2}\mathcal{A}(\hat{c}s) \underset{m=0}{=} -\frac{\hat{c}^2}{s^2}\frac{N^2-1}{N^2}. \tag{A.400}$$

The last remaining term $\hat{H}(s,u,v,\hat{\theta})$, which contains the full $\hat{\theta}$ dependence, is a bit more complicated. The idea is nevertheless the same: we subtract the $m = 0$ terms and $n = 0$ terms, and add back the doubly subtracted $m = n = 0$ one. However, in this case insted of actually subtracting all $n = 0$ terms, we rewrite the components of the 4-vector n along the twisted directions as $n_\mu = \tilde{n}_\mu N + n_c$,

where n_c denotes a 2-dimensional vector of integers taking values in the intervals $[-N/2, N/2)$ and $[-(N-1)/2, (N-1)/2]$ for N even and odd respectively, and subtract the terms corresponding to $n_\mu = 0$ along periodic directions and $\tilde{n}_\mu = 0$ along the twisted ones.

The $m = 0$ term is immediate, as setting $m = 0$ in the expressions of $F_1(\alpha, u, v, \hat{\theta}, d_t)$ directly gives Jacobi theta functions:

$$\hat{H}(s,u,v,\hat{\theta}) \underset{m=0}{=} (1-\frac{1}{N^2}) \sum_{n\in\mathbb{Z}^4} e^{-\frac{\pi s}{\hat{c}\alpha u} n^2} = (1-\frac{1}{N^2})\theta_3^4\left(0, \frac{is}{\hat{c}\alpha u}\right). \tag{A.401}$$

Substracting both this term and the aforementioned $n = 0$ terms, and adding back the doubly substracted ones, we end up with:

$$\begin{aligned}\hat{H}(s,u,v,\hat{\theta}) = \hat{H}'(s,u,v,\hat{\theta}) - \mathcal{A}\left(\frac{\hat{c}\alpha u}{s}\right) + \frac{N^2-1}{N^2}\theta_3^4\left(0,\frac{is}{\hat{c}\alpha u}\right) \\ + \frac{1}{N^2}\sum_{n_c\neq 0} \exp\left\{-\frac{\pi s n_c^2}{\hat{c}N^2\alpha u}\right\} \mathrm{Re}\left(\theta_3^2\left(0,\frac{i}{\hat{c}\alpha}\right)\prod_{\mu=0,1}\theta_3\left(z_\mu, \frac{i}{\hat{c}N^2\alpha}\right) - 1\right),\end{aligned} \tag{A.402}$$

where $z_\mu = \epsilon_{\mu\nu} n_{c\nu} k/N + i n_{c\mu} v/(\hat{c}N^2\alpha u)$.

We may then rewrite each of the integrals contributing to $\mathcal{C}_1$ as the the sum of two components $I = I_{TI} + I_{TD}$, the latter containing all of the $\hat{\theta}$ dependence:

$$I_{TI} \quad = I_{TI}^{(0)} + \frac{4}{3\mathcal{A}(2\hat{c})}\left\{\int (u\alpha)^{-2}\hat{H}'(s,u,v,0) + \int \frac{\hat{c}^2}{s^2}\left(1-\frac{1}{N^2}-\mathcal{A}(\hat{c}s)\right)\right\}, \tag{A.403}$$

$$I_{TD} \quad = I_{TD}^{(0)} - \frac{4}{3\mathcal{A}(2\hat{c})}\left\{\int (u\alpha)^{-2}\hat{H}'(s,u,v,\hat{\theta}) + \int \frac{\hat{c}^2}{s^2}\left(1-\frac{1}{N^2}-\mathcal{A}(\hat{c}s)\right)\right\}, \tag{A.404}$$

where:

$$I_{TI}^{(0)} = \frac{-4}{3\mathcal{A}(2\hat{c})}\int (u\alpha)^{-2}\left(\mathcal{A}(2\hat{c}) - \mathcal{A}(\hat{c}\alpha) - \mathcal{A}(\hat{c}\alpha u/s) + 1 - \frac{1}{N^2}\right), \tag{A.405}$$

$$I_{TD}^{(0)} = \frac{-4}{3N^2\mathcal{A}(2\hat{c})}\sum_{n_c\neq 0}\int (u\alpha)^{-2} e^{-\frac{\pi s n_c^2}{\hat{c}N^2\alpha u}}\mathrm{Re}\left\{\theta_3^2\left(0,\frac{i}{\hat{c}\alpha}\right)\prod_\mu \theta_3\left(z_\mu,\frac{i}{\hat{c}N^2\alpha}\right) - 1\right\}, \tag{A.406}$$

and with n_c and z_μ as defined above.

From this expression, we may begin the analysis of the the $\hat{c} \to 0$ limit, whose approach is driven by two variables: $\hat{c}\alpha$ and $\hat{c}\alpha u/s$. In all contributing integrals but I_8 and I_9, one of the two variables vanishes for all of the integration range when taking such a limit.

The first thing worth noting is the fact that zero modes have already been subtracted from all terms not included in $I_{TI}^{(0)}$ and $I_{TD}^{(0)}$, and hence the leading order in the $\hat{c} \to 0$ limit for them will be proportional to:

$$-\frac{4}{3N^2\mathcal{A}(2\hat{c})}\int (u\alpha)^{-2}\exp\left\{-\frac{\pi}{\hat{c}N^2\alpha}-\frac{\pi s}{\hat{c}N^2\alpha u}+\cdots\right\}, \tag{A.407}$$

which approaches zero at least exponentially in the $\hat{c}N^2 \to 0$ limit, and goes, in the large N limit taken keeping $\hat{c}N^2$ constant, as $1/N^2$. The leading contribution in the $\hat{c} \to 0$ limit is thus given by $I_{TI}^{(0)}$ and $I_{TD}^{(0)}$ in most cases.

The simplest cases are those of $\bar{I}_1$, $\bar{I}_2$ and $\bar{I}_4$, for which both $\hat{c}\alpha$ and $\hat{c}\alpha u/s$ tend to zero in the whole integral range. Starting from the expressions of I_{TI} and I_{TD}, it is easy to derive the leading correction to the large volume limit, given in all three cases by:

$$\frac{16}{3(N^2-1)}\int (u\alpha)^{-2}\left\{e^{-\frac{\pi}{2\hat{c}N^2}}-e^{-\frac{\pi}{\hat{c}\alpha N^2}}-e^{-\frac{\pi s}{\hat{c}\alpha u N^2}}\right\}. \tag{A.408}$$

All three integrals can be analytically approximated with this, leading to:

$$\bar{I}_1 \to \frac{1}{9(N^2-1)}e^{-(cN)^{-2}}\left(1+3\gamma_E-3\log\left(3c^2N^2\right)-3c^2N^2\right), \tag{A.409}$$

$$\bar{I}_2 \to \frac{2}{9(N^2-1)}e^{-(cN)^{-2}}\left(1-6c^2N^2\right), \tag{A.410}$$

$$\bar{I}_4 \to -\frac{1}{3(N^2-1)}e^{-(cN)^{-2}}\left(1-\gamma_E+\log\left(9c^2N^2\right)-3.544907702\,cN+c^2N^2\right), \tag{A.411}$$

Which is the result presented in section 2.5.

As for the remaining integrals, we will begin by first looking at the $\hat{c}$ dependence of $I_{TI}^{(0)}$ and $I_{TD}^{(0)}$. For $\bar{I}_3$, $\bar{I}_6$ and $\bar{I}_{10}$, the variable going to zero in the $\hat{c} \to 0$ limit is $\hat{c}\alpha u/s$, and the leading dependence is given by:

$$\frac{4}{3\mathcal{A}(2\hat{c})}\int (u\alpha)^{-2}\left\{\mathcal{A}(\hat{c}\alpha)-1+\frac{1}{N^2}\right\}, \tag{A.412}$$

whereas for $\bar{I}_5$, $\bar{I}_7$, $\bar{I}_{11}$, and $\bar{I}_{12}$, the variable going to zero is $\hat{c}\alpha$, and we have instead:

$$\frac{4}{3\mathcal{A}(2\hat{c})}\int (u\alpha)^{-2}\left\{\mathcal{A}\left(\frac{\hat{c}\alpha u}{s}\right)-1+\frac{1}{N^2}\right\}. \tag{A.413}$$

To leading order all these integrals go to zero as $\sim c^2$, with a coefficient depending on N that is identical in absolute value for all of them.

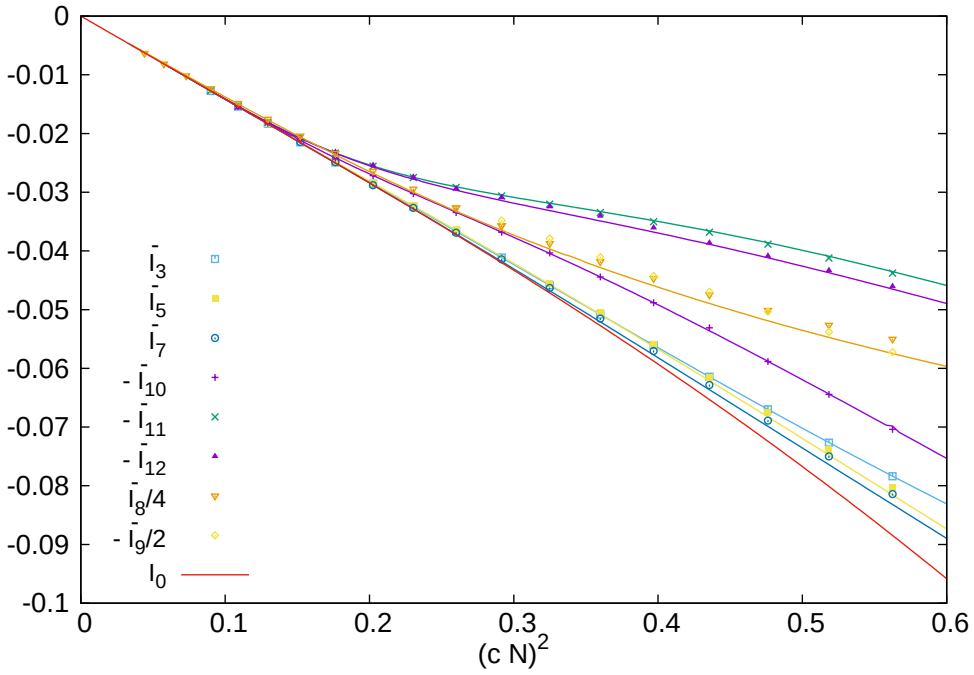

Figure A.2: The contribution to $\mathcal{C}_1$ from the integrals $\bar{I}_i$ with $i = 5-10$, shown as a function of $(cN)^2$. The continuous lines are obtained from the approximate expression given by the sum of eq. (A.405) and (A.406), and the red line represents I_0 as defined in eq. (A.419).

It is interesting to take a look at $\bar{I}_3$ as an illustrative example of how these integrals will work. The leading contribution in the $\hat{c} \to 0$ limit for this integral is given by:

$$-\frac{4}{3\mathcal{A}(2\hat{c})}\int_0^\infty dz(3+2z)^{-2}\left\{1-\frac{1}{N^2}-\mathcal{A}(\hat{c}(3+2z)/2)\right\}, \tag{A.414}$$

which allows us to separate $\mathcal{A}$ into two N-dependent and N-independent parts:

$$\mathcal{A}^{(1)}(x) = x^2(\theta_3^4(0,ix) - 1)\,, \tag{A.415}$$

$$\mathcal{A}^{(2)}(x) = x^2(\theta_3^2(0,ix)\theta_3^2(0,ixN^2) - 1)\,. \tag{A.416}$$

Rescaling z to $z' = \hat{c}z$ in the first expression and to $z' = \hat{c}N^2 z$ in the second, we can decompose the integral into the difference of two pieces $\bar{I}_3^{(1)} - \bar{I}_3^{(2)}$, which in the $cN \to 0$ limit become:

$$\bar{I}_3^{(1)} = \frac{\hat{c}}{3\mathcal{A}(2\hat{c})}\int_0^\infty dz \left\{\theta_3^4\,(0,iz) - 1 - \frac{1}{z^2}\right\}, \tag{A.417}$$

$$\bar{I}_3^{(2)} = \frac{\hat{c}}{3N^2\mathcal{A}(2\hat{c})}\int_0^\infty dz \left\{\theta_3^2\,(0,iz)\,\theta_3^2\left(0,iz/N^2\right) - 1 - \frac{N^2}{z^2}\right\}. \tag{A.418}$$

The leading order result in the $cN \to 0$ limit is thus given by:

$$I_0 = \frac{\pi(cN)^2}{6N^2\mathcal{A}(2\hat{c})}\left(a_1 - \frac{1}{N^2}a_2(N)\right) + \cdots\,, \tag{A.419}$$

with $a_1 = -1.76508480122121275$ and for instance $a_2(3) = 3.59085631503990722$. One can show that all the other integrals are also proportional to I_0, with the proportionality coefficient being +1 for $i = 5, 6, 7$ and -1 for $i = 10, 11, 12$ respectively. The results for the case of the SU(3) gauge group are displayed on fig. A.2, with the red line in the plot showing I_0 and the remaining continuous lines representing the contribution of $I_{TI}^{(0)} + I_{TD}^{(0)}$. The cases of $\bar{I}_8$ and $\bar{I}_9$ are shown in the plot as well, which also turn out to be proportional to I_0 with respective coefficients 4 and -2.

Appendix B

Calculations on the lattice

B.1 Generated configurations

We display here the number of generated $Q_t = 0$ configurations for different values of c. The numbers within parenthesis denote the number of discarded $Q_t \neq 0$ configurations. The results in terms of the bare coupling b can be easily derived from the fact that $b = \beta/18$. The table for $c = 0.3$ was aready displayed in table 3.1, and will thus not be shown here.

β	$\tilde{L} = 12$	$\tilde{L} = 18$	$\tilde{L} = 24$	$\tilde{L} = 36$	$\tilde{L} = 48$
6.0	9343(657)	24732(26210)	4533(12449)	1139(8633)	133(1863)
6.2	9823(177)	37260(15316)	7888(10068)	1119(4160)	232(1701)
6.4	10000(28)	49367(3409)	13051(5355)	3892(6990)	455(1544)
6.6	10000(0)	52806(301)	16712(1288)	6474(4484)	758(1538)
6.8	10000(0)	51840(67)	17807(193)	9592(1617)	1316(989)
7.0	10000(0)	53238(0)	16439(0)	10971(0)	2155(150)
7.2	10000(0)	50544(0)	18000(0)	10974(0)	2307(0)
7.4	10000(0)	53406(0)	16763(0)	10981(0)	2319(0)
7.6	10000(0)	53605(0)	17760(0)	9999(0)	2308(0)
7.8	10000(0)	53560(0)	17501(0)	8979(0)	2319(0)
8.0	10000(0)	53602(0)	18000(0)	9720(0)	2328(0)
8.5	10000(0)	53825(0)	17000(0)	8990(0)	2324(0)
9.0	10000(0)	53654(0)	18000(0)	9000(0)	2333(0)
9.5	10000(0)	54178(0)	16483(0)	7998(0)	1966(0)
10.0	10000(0)	53889(0)	18000(0)	8991(0)	2042(0)
10.5	10000(0)	53415(0)	17000(0)	7990(0)	2043(0)
11.0	10000(0)	53679(0)	8640(0)	7922(0)	1738(0)
12.0	10000(0)	10000(0)	16442(0)	4000(0)	803(0)
13.0	10000(0)	10000(0)	16513(0)	3973(0)	805(0)
14.0	10000(0)	10000(0)	16340(225)	3457(0)	807(0)
15.0	10000(0)	10000(0)	16602(0)	3334(0)	808(0)

Table B.1: Number of generated $Q_t = 0$ configurations in the case of $c = 0.1$.

β	$\tilde{L}=12$	$\tilde{L}=18$	$\tilde{L}=24$	$\tilde{L}=36$	$\tilde{L}=48$
6.0	7577(2423)	20571(30371)	4023(12959)	1077(8695)	138(1858)
6.2	9570(430)	37057(15519)	7898(10058)	1140(4139)	219(1714)
6.4	9961(39)	49370(3406)	13059(5347)	3899(6983)	454(1545)
6.6	10000(0)	52809(298)	16714(1286)	6477(4481)	758(1538)
6.8	10000(0)	51840(67)	17807(193)	9593(1616)	1316(989)
7.0	10000(0)	53238(0)	16439(0)	10971(0)	2155(150)
7.2	10000(0)	50544(0)	18000(0)	10974(0)	2307(0)
7.4	10000(0)	53406(0)	16763(0)	10981(0)	2319(0)
7.6	10000(0)	53605(0)	17760(0)	9999(0)	2308(0)
7.8	10000(0)	53560(0)	17501(0)	8979(0)	2319(0)
8.0	10000(0)	53602(0)	18000(0)	9720(0)	2328(0)
8.5	10000(0)	53825(0)	17000(0)	8990(0)	2324(0)
9.0	10000(0)	53654(0)	18000(0)	9000(0)	2333(0)
9.5	10000(0)	54178(0)	16483(0)	7998(0)	1966(0)
10.0	10000(0)	53889(0)	18000(0)	8991(0)	2042(0)
10.5	10000(0)	53415(0)	17000(0)	7990(0)	2043(0)
11.0	10000(0)	53679(0)	8640(0)	7922(0)	1738(0)
12.0	10000(0)	10000(0)	16442(0)	4000(0)	803(0)
13.0	10000(0)	10000(0)	16513(0)	3973(0)	805(0)
14.0	10000(0)	10000(0)	16340(225)	3457(0)	807(0)
15.0	10000(0)	10000(0)	16602(0)	3334(0)	808(0)

Table B.2: Number of generated $Q_t = 0$ configurations in the case of $c = 0.7$.

B.2 Running coupling

We will in this section show the numerical data for $b\lambda_{TGF}$ obtained from the simulations that was used to elaborate the plots in section 3.4.1. The coupling λ_{TGF} can be retrieved dividing by $b = \beta/18$, though the relevant values of the coupling used in the continuum extrapolation of the step scaling function will be explicitly presented in the next section.

β	$\tilde{L} = 12$	$\tilde{L} = 18$	$\tilde{L} = 24$	$\tilde{L} = 36$	$\tilde{L} = 48$
6.0	2.8184(8)	4.2653(7)	5.5564(21)	8.9876(66)	8.9370(136)
6.2	2.5695(6)	3.6308(4)	4.4492(11)	6.2903(46)	6.5129(74)
6.4	2.3994(5)	3.2396(3)	3.8310(7)	5.0307(18)	5.2546(42)
6.6	2.2721(5)	2.9658(3)	3.4211(5)	4.2827(11)	4.4818(27)
6.8	2.1707(5)	2.7603(2)	3.1276(4)	3.7840(8)	3.9608(18)
7.0	2.0850(4)	2.5985(2)	2.9052(4)	3.4279(7)	3.5767(15)
7.2	2.0128(4)	2.4670(2)	2.7288(4)	3.1589(6)	3.2920(13)
7.4	1.9499(4)	2.3563(2)	2.5846(3)	2.9495(5)	3.0712(11)
7.6	1.8948(4)	2.2627(2)	2.4644(3)	2.7803(5)	2.8872(10)
7.8	1.8466(3)	2.1817(2)	2.3616(3)	2.6394(5)	2.7371(10)
8.0	1.8039(3)	2.1108(1)	2.2737(3)	2.5197(4)	2.4530(8)
8.5	1.7139(3)	1.9670(1)	2.0971(3)	2.2891(4)	2.2503(7)
9.0	1.6415(3)	1.8572(1)	1.9650(2)	2.1202(3)	2.0975(7)
9.5	1.5837(3)	1.7704(1)	1.8620(2)	1.9923(3)	1.9802(7)
10.0	1.5354(3)	1.6998(1)	1.7793(2)	1.8903(3)	1.8856(6)
10.5		1.6413(1)	1.7109(2)	1.8077(3)	1.8085(6)
11.0		1.5921(1)	1.6543(3)	1.7395(3)	1.6869(9)
12.0		1.5135(2)	1.5640(2)	1.6329(4)	1.5964(8)
13.0				1.5535(3)	1.5302(8)

Table B.3: Numerical values of $b\lambda_{TGF}$ used to elaborate the plots from section 3.4.1, for the case of $c = 0.1$ and for the clover observable.

β	$\tilde{L}=12$	$\tilde{L}=18$	$\tilde{L}=24$	$\tilde{L}=36$	$\tilde{L}=48$
6.0	3.0118(7)	4.4424(6)	5.6662(21)	6.3127(45)	8.9646(137)
6.2	2.7310(6)	3.7666(4)	4.5213(10)	5.0456(17)	6.5214(74)
6.4	2.5383(5)	3.3533(3)	3.8906(6)	4.2963(11)	5.2605(41)
6.6	2.3930(4)	3.0639(2)	3.4732(5)	3.7969(8)	4.4875(26)
6.8	2.2774(4)	2.8463(2)	3.1739(4)	3.4400(6)	3.9664(17)
7.0	2.1805(3)	2.6747(2)	2.9463(4)	3.1702(5)	3.5824(14)
7.2	2.0990(3)	2.5352(2)	2.7657(3)	2.9599(5)	3.2974(13)
7.4	2.0284(3)	2.4180(1)	2.6179(3)	2.7897(5)	3.0761(12)
7.6	1.9667(3)	2.3189(1)	2.4947(3)	2.6480(4)	2.8918(10)
7.8	1.9132(3)	2.2333(1)	2.3894(3)	2.5277(4)	2.7413(9)
8.0	1.8656(3)	2.1584(1)	2.2992(2)	2.2957(4)	2.4564(8)
8.5	1.7659(2)	2.0070(1)	2.1184(2)	2.1258(3)	2.2532(7)
9.0	1.6867(2)	1.8916(1)	1.9833(2)	1.9971(3)	2.1000(7)
9.5	1.6235(2)	1.8005(1)	1.8779(2)	1.8946(3)	1.9824(7)
10.0	1.5708(2)	1.7266(1)	1.7933(2)	1.8115(3)	1.8876(6)
10.5	1.5264(2)	1.6654(1)	1.7235(2)	1.7430(3)	1.8102(6)
11.0		1.6139(1)	1.6657(2)	1.6358(4)	1.6883(8)
12.0		1.5318(2)	1.5736(2)	1.5559(3)	1.5976(8)
13.0			1.5042(1)		1.5312(8)

Table B.4: Numerical values of $b\lambda_{TGF}$ used to elaborate the plots from section 3.4.1, for the case of $c = 0.1$ and for the plaquette observable.

β	$\tilde{L}=12$	$\tilde{L}=18$	$\tilde{L}=24$	$\tilde{L}=36$	$\tilde{L}=48$
6.2	7.429(23)				
6.4	5.505(15)				
6.6	4.564(10)	6.411(8)			
6.8	3.995(8)	5.132(5)	6.765(15)		
7.0	3.574(6)	4.418(4)	5.412(10)	8.401(25)	
7.2	3.297(5)	3.935(3)	4.628(7)	6.409(17)	
7.4	3.060(5)	3.582(3)	4.111(6)	5.294(11)	6.844(39)
7.6	2.886(4)	3.310(2)	3.735(5)	4.615(9)	5.645(29)
7.8	2.725(4)	3.094(2)	3.436(4)	4.129(8)	4.858(20)
8.0	2.605(4)	2.914(2)	3.214(4)	3.770(6)	4.326(16)
8.5	2.353(3)	2.586(2)	2.793(3)	3.172(5)	3.526(12)
9.0	2.171(3)	2.355(1)	2.512(3)	2.796(4)	3.046(9)
9.5	2.033(3)	2.182(1)	2.313(2)	2.536(4)	2.716(8)
10.0	1.926(2)	2.050(1)	2.161(2)	2.336(3)	2.487(7)
10.5	1.836(2)	1.944(1)	2.038(2)	2.185(3)	2.308(7)
11.0	1.764(2)	1.861(1)	1.938(3)	2.067(3)	2.173(7)
12.0	1.652(2)	1.730(2)	1.788(2)	1.885(4)	1.973(8)
13.0	1.570(2)	1.633(2)	1.680(2)	1.758(3)	1.812(7)
14.0	1.506(2)	1.561(2)	1.601(1)	1.666(4)	1.723(7)
15.0			1.537(1)	1.593(3)	1.633(7)

Table B.5: Numerical values of $b\lambda_{TGF}$ used to elaborate the plots from section 3.4.1, for the case of $c = 0.3$ and for the clover observable.

β	$\tilde{L}=12$	$\tilde{L}=18$	$\tilde{L}=24$	$\tilde{L}=36$	$\tilde{L}=48$
6.2	7.370(22)				
6.4	5.480(14)				
6.6	4.552(10)	6.392(8)			
6.8	3.989(7)	5.124(5)	6.753(15)		
7.0	3.572(6)	4.413(4)	5.407(10)	8.393(25)	
7.2	3.296(5)	3.932(3)	4.626(7)	6.405(17)	
7.4	3.061(5)	3.580(3)	4.109(6)	5.292(11)	6.842(39)
7.6	2.886(4)	3.309(2)	3.734(5)	4.614(9)	5.644(29)
7.8	2.725(4)	3.094(2)	3.435(4)	4.129(8)	4.857(20)
8.0	2.606(4)	2.914(2)	3.214(4)	3.769(6)	4.326(16)
8.5	2.354(3)	2.586(2)	2.793(3)	3.172(5)	3.526(12)
9.0	2.172(3)	2.355(1)	2.512(3)	2.796(4)	3.046(9)
9.5	2.034(3)	2.182(1)	2.313(2)	2.536(4)	2.716(8)
10.0	1.927(2)	2.050(1)	2.161(2)	2.336(3)	2.487(7)
10.5	1.837(2)	1.945(1)	2.038(2)	2.185(3)	2.308(7)
11.0	1.765(2)	1.862(1)	1.939(3)	2.067(3)	2.173(7)
12.0	1.653(2)	1.731(2)	1.788(2)	1.885(4)	1.973(8)
13.0	1.571(2)	1.633(2)	1.680(2)	1.758(3)	1.812(7)
14.0	1.506(2)	1.561(2)	1.601(1)	1.666(4)	1.723(7)
15.0			1.537(1)	1.593(3)	1.633(7)

Table B.6: Numerical values of $b\lambda_{TGF}$ used to elaborate the plots from section 3.4.1, for the case of $c = 0.3$ and for the plaquette observable.

β	$\tilde{L}=12$	$\tilde{L}=18$	$\tilde{L}=24$	$\tilde{L}=36$	$\tilde{L}=48$
6.8	7.80(0.57)				
7.0	4.60(0.22)				
7.2	4.26(0.25)	5.69(0.15)			
7.4	3.46(0.02)	4.52(0.06)	5.82(0.16)		
7.6	3.23(0.02)	3.83(0.02)	4.73(0.10)		
7.8	2.98(0.02)	3.48(0.01)	3.99(0.02)	5.84(0.38)	8.71(0.81)
8.0	2.85(0.01)	3.22(0.01)	3.62(0.01)	4.49(0.04)	6.02(0.39)
8.5	2.49(0.01)	2.78(0.01)	3.04(0.01)	3.51(0.02)	3.99(0.05)
9.0	2.28(0.01)	2.49(0.00)	2.67(0.01)	3.02(0.02)	3.33(0.03)
9.5	2.12(0.01)	2.28(0.00)	2.43(0.01)	2.69(0.01)	2.94(0.03)
10.0	1.99(0.01)	2.12(0.00)	2.26(0.01)	2.45(0.01)	2.67(0.03)
10.5	1.88(0.01)	2.00(0.00)	2.11(0.01)	2.28(0.01)	2.41(0.03)
11.0	1.81(0.01)	1.91(0.00)	1.98(0.01)	2.16(0.01)	2.24(0.02)
12.0	1.68(0.01)	1.76(0.01)	1.83(0.01)	1.94(0.01)	2.07(0.03)
13.0	1.60(0.01)	1.66(0.01)	1.70(0.01)	1.79(0.01)	1.84(0.03)
14.0	1.53(0.01)	1.60(0.01)	1.63(0.01)	1.70(0.01)	1.75(0.02)
15.0		1.52(0.01)	1.56(0.00)	1.61(0.01)	1.67(0.02)

Table B.7: Numerical values of $b\lambda_{TGF}$ used to elaborate the plots from section 3.4.1, for the case of $c = 0.7$ and for the clover observable.

β	$\tilde{L}=12$	$\tilde{L}=18$	$\tilde{L}=24$	$\tilde{L}=36$	$\tilde{L}=48$
6.8	7.77(0.57)				
7.0	4.59(0.21)				
7.2	4.26(0.25)	5.69(0.15)			
7.4	3.46(0.02)	4.52(0.06)	5.81(0.16)		
7.6	3.23(0.02)	3.83(0.02)	4.72(0.10)		
7.8	2.98(0.02)	3.48(0.01)	3.99(0.02)	5.84(0.38)	8.70(0.81)
8.0	2.85(0.01)	3.22(0.01)	3.62(0.01)	4.49(0.04)	6.02(0.39)
8.5	2.49(0.01)	2.78(0.01)	3.04(0.01)	3.51(0.02)	3.99(0.05)
9.0	2.28(0.01)	2.49(0.01)	2.67(0.01)	3.02(0.02)	3.33(0.03)
9.5	2.12(0.01)	2.28(0.01)	2.43(0.01)	2.69(0.01)	2.94(0.03)
10.0	1.99(0.01)	2.12(0.01)	2.26(0.01)	2.45(0.01)	2.67(0.03)
10.5	1.88(0.01)	2.00(0.01)	2.11(0.01)	2.28(0.01)	2.41(0.03)
11.0	1.81(0.01)	1.91(0.01)	1.98(0.01)	2.16(0.01)	2.24(0.02)
12.0	1.68(0.01)	1.76(0.01)	1.83(0.01)	1.94(0.01)	2.07(0.03)
13.0	1.60(0.01)	1.66(0.01)	1.70(0.01)	1.79(0.01)	1.84(0.03)
14.0	1.53(0.01)	1.60(0.01)	1.63(0.01)	1.70(0.01)	1.75(0.02)
15.0		1.52(0.01)	1.56(0.01)	1.61(0.01)	1.67(0.02)

Table B.8: Numerical values of $b\lambda_{TGF}$ used to elaborate the plots from section 3.4.1, for the case of $c = 0.7$ and for the plaquette observable.

B.3 Discrete step scaling function

We display in this appendix the values of the twisted gradient flow coupling (denoted u) and the corresponding discrete step scaling function Σ/u used in the plots and fits from section 3.4.2.

u	Σ/u (C)	u	Σ/u (P)
1.5538(3)	1.0812(2)	1.5738(2)	1.0724(2)
1.7016(3)	1.0901(2)	1.7258(2)	1.0801(2)
1.8818(3)	1.1007(2)	1.9113(2)	1.0897(2)
2.1048(4)	1.1146(2)	2.1417(2)	1.1021(2)
2.3886(4)	1.1333(3)	2.4362(3)	1.1188(2)
2.5617(4)	1.1449(2)	2.6167(3)	1.1291(2)
2.7637(5)	1.1589(2)	2.8274(3)	1.1417(2)
3.0006(5)	1.1758(3)	3.0760(4)	1.1567(2)
3.2830(6)	1.1971(3)	3.3735(4)	1.1758(2)
3.6295(7)	1.2235(3)	3.7396(5)	1.1996(2)
4.0587(8)	1.2604(3)	4.1976(6)	1.2324(2)
4.2614(8)	1.2789(3)	4.4151(6)	1.2489(2)
4.4876(9)	1.3006(3)	4.6581(6)	1.2684(2)
4.7429(10)	1.3255(3)	4.9339(8)	1.2906(2)
5.0319(10)	1.3558(3)	5.2474(8)	1.3176(2)
5.3615(11)	1.3934(3)	5.6071(9)	1.3512(3)
5.7461(12)	1.4408(4)	6.0283(10)	1.3937(3)
6.1966(13)	1.5057(4)	6.5264(11)	1.4514(3)
6.7484(15)	1.5966(5)	7.1389(13)	1.5328(4)
7.4599(19)	1.7315(6)	7.9286(16)	1.6556(5)
8.4551(24)	1.9715(9)		

Table B.9: Numerical value of the discrete step scaling function Σ from the simulations, in the case of $c = 0.1$ and for the pair of lattices going from $\tilde{L} = 12$ to $\tilde{L} = 24$ for both the clover (C) and plaquette (P) definitions of the observable. The errors are shown within parenthesis.

u	Σ/u (C)	u	Σ/u (P)
1.6407(2)	1.0551(3)	1.6556(2)	1.0469(3)
1.8074(3)	1.0615(3)	1.8253(2)	1.0526(3)
2.0120(3)	1.0690(3)	2.0339(2)	1.0592(3)
2.2702(3)	1.0789(3)	2.2977(3)	1.0679(3)
2.6053(2)	1.0926(2)	2.6409(1)	1.0800(2)
2.8137(2)	1.1013(2)	2.8550(1)	1.0877(2)
3.0597(2)	1.1121(2)	3.1078(2)	1.0973(2)
3.3544(2)	1.1254(2)	3.4115(2)	1.1092(2)
3.7144(3)	1.1416(2)	3.7832(2)	1.1238(2)
4.1653(3)	1.1638(2)	4.2500(2)	1.1439(2)
4.7493(3)	1.1937(2)	4.8565(3)	1.1711(2)
5.0347(4)	1.2098(2)	5.1538(3)	1.1857(2)
5.3591(4)	1.2287(2)	5.4921(3)	1.2030(2)
5.7316(4)	1.2517(2)	5.8817(3)	1.2241(2)
6.1676(5)	1.2805(2)	6.3380(4)	1.2505(2)
6.6818(5)	1.3192(3)	6.8777(4)	1.2862(2)
7.3067(6)	1.3709(3)	7.5343(5)	1.3340(3)
8.0886(7)	1.4440(4)	8.3562(6)	1.4022(4)

Table B.10: Numerical value of the discrete step scaling function Σ from the simulations, in the case of $c = 0.1$ and for the pair of lattices going from $\tilde{L} = 18$ to $\tilde{L} = 36$ for both the clover (C) and plaquette (P) definitions of the observable. The errors are shown within parenthesis.

u	Σ/u (C)	u	Σ/u (P)
1.6800(2)	1.0531(5)	1.6877(2)	1.0490(5)
1.8548(2)	1.0607(6)	1.8641(2)	1.0561(6)
2.0712(2)	1.0672(6)	2.0827(2)	1.0622(6)
2.3461(3)	1.0785(6)	2.3604(2)	1.0729(5)
2.7071(4)	1.0932(4)	2.7257(4)	1.0867(4)
2.9329(3)	1.1022(4)	2.9546(3)	1.0952(4)
3.2027(4)	1.1129(4)	3.2280(3)	1.1054(4)
3.5281(4)	1.1264(4)	3.5581(4)	1.1183(4)
3.9300(4)	1.1452(4)	3.9665(4)	1.1361(4)
4.4408(5)	1.1697(4)	4.4861(5)	1.1596(4)
5.1157(6)	1.2038(4)	5.1732(5)	1.1923(4)
5.4498(7)	1.2226(5)	5.5139(6)	1.2103(5)
5.8367(7)	1.2462(5)	5.9085(6)	1.2330(5)
6.2870(8)	1.2737(5)	6.3678(7)	1.2596(5)
6.8221(9)	1.3107(6)	6.9142(8)	1.2953(5)
7.4705(10)	1.3633(6)	7.5762(9)	1.3462(6)
8.2790(12)	1.4330(9)	8.4015(11)	1.4139(8)

Table B.11: Numerical value of the discrete step scaling function Σ from the simulations, in the case of $c = 0.1$ and for the pair of lattices going from $\tilde{L} = 24$ to $\tilde{L} = 48$ for both the clover (C) and plaquette (P) definitions of the observable. The errors are shown within parenthesis.

u	Σ/u (C)	u	Σ/u (P)
1.748(2)	1.055(2)	1.749(2)	1.054(2)
1.936(2)	1.063(2)	1.936(2)	1.063(2)
2.174(3)	1.070(2)	2.175(2)	1.070(2)
2.478(3)	1.082(2)	2.479(3)	1.082(2)
2.886(4)	1.099(2)	2.888(3)	1.099(2)
3.148(4)	1.110(2)	3.150(4)	1.109(2)
3.468(4)	1.122(2)	3.469(4)	1.121(2)
3.853(5)	1.138(2)	3.855(5)	1.137(2)
4.343(6)	1.157(2)	4.344(6)	1.156(2)
4.983(7)	1.187(2)	4.985(7)	1.186(2)
5.862(8)	1.234(2)	5.863(8)	1.233(2)
6.288(9)	1.261(2)	6.289(9)	1.260(2)
6.836(11)	1.294(3)	6.836(10)	1.294(2)
7.444(11)	1.343(3)	7.445(11)	1.343(3)
8.243(13)	1.404(3)	8.240(13)	1.403(3)

Table B.12: Numerical value of the discrete step scaling function Σ from the simulations, in the case of $c = 0.3$ and for the pair of lattices going from $\tilde{L} = 12$ to $\tilde{L} = 24$ for both the clover (C) and plaquette (P) definitions of the observable. The errors are shown within parenthesis.

u	Σ/u (C)	u	Σ/u (P)
1.797(2)	1.064(2)	1.797(2)	1.063(2)
2.007(2)	1.067(3)	2.007(2)	1.067(3)
2.261(3)	1.077(2)	2.261(3)	1.076(2)
2.596(3)	1.089(2)	2.596(3)	1.089(2)
3.046(2)	1.111(2)	3.046(2)	1.111(2)
3.333(2)	1.124(2)	3.334(2)	1.124(2)
3.689(2)	1.140(2)	3.690(2)	1.140(2)
4.133(2)	1.163(2)	4.134(2)	1.163(2)
4.710(3)	1.187(2)	4.710(3)	1.187(2)
5.477(3)	1.226(2)	5.477(3)	1.226(2)
6.557(4)	1.294(2)	6.557(4)	1.293(2)
7.140(5)	1.335(3)	7.139(5)	1.335(3)
7.840(5)	1.394(3)	7.838(5)	1.394(3)

Table B.13: Numerical value of the discrete step scaling function Σ from the simulations, in the case of $c = 0.3$ and for the pair of lattices going from $\tilde{L} = 18$ to $\tilde{L} = 36$ for both the clover (C) and plaquette (P) definitions of the observable. The errors are shown within parenthesis.

u	Σ/u (C)	u	Σ/u (P)
1.844(2)	1.063(5)	1.844(2)	1.063(5)
2.058(2)	1.076(5)	2.059(2)	1.076(5)
2.326(2)	1.079(5)	2.326(2)	1.079(5)
2.682(3)	1.103(5)	2.682(3)	1.103(5)
3.172(4)	1.121(4)	3.172(4)	1.121(4)
3.494(3)	1.132(4)	3.494(3)	1.132(3)
3.890(4)	1.151(4)	3.890(4)	1.151(4)
4.383(5)	1.174(4)	4.383(5)	1.174(4)
5.024(5)	1.213(4)	5.024(5)	1.213(4)
5.914(7)	1.263(4)	5.914(7)	1.262(4)
7.232(8)	1.346(5)	7.232(8)	1.346(5)
7.929(10)	1.414(6)	7.928(9)	1.414(6)
8.846(11)	1.511(8)	8.844(11)	1.511(8)

Table B.14: Numerical value of the discrete step scaling function Σ from the simulations, in the case of $c = 0.3$ and for the pair of lattices going from $\tilde{L} = 24$ to $\tilde{L} = 48$ for both the clover (C) and plaquette (P) definitions of the observable. The errors are shown within parenthesis.

u	Σ/u (C)	u	Σ/u (P)
1.7650(73)	1.0585(55)	1.7650(73)	1.0585(55)
1.9624(81)	1.0650(56)	1.9624(81)	1.0649(56)
2.2159(91)	1.0651(56)	2.2160(91)	1.0651(56)
2.5223(105)	1.0902(58)	2.5224(105)	1.0902(58)
2.9579(127)	1.0943(68)	2.9579(127)	1.0943(68)
3.2241(136)	1.1215(60)	3.2242(136)	1.1215(60)
3.5841(157)	1.1336(62)	3.5842(156)	1.1335(62)
4.0219(176)	1.1438(64)	4.0220(176)	1.1438(64)
4.5596(216)	1.1708(69)	4.5596(215)	1.1708(69)
5.2759(240)	1.2198(72)	5.2760(240)	1.2198(72)
6.4195(326)	1.2688(83)	6.4195(325)	1.2688(83)
6.8840(365)	1.3369(100)	6.8839(365)	1.3369(100)
7.6519(409)	1.4626(330)	7.6517(408)	1.4623(328)
8.4277(475)	1.6784(480)	8.4275(475)	1.6778(478)

Table B.15: Numerical value of the discrete step scaling function Σ from the simulations, in the case of $c = 0.7$ and for the pair of lattices going from $\tilde{L} = 12$ to $\tilde{L} = 24$ for both the clover (C) and plaquette (P) definitions of the observable. The errors are shown within parenthesis.

u	Σ/u (C)	u	Σ/u (P)
1.8183(74)	1.0629(86)	1.8183(74)	1.0629(86)
2.0524(85)	1.0649(93)	2.0524(85)	1.0649(93)
2.3032(97)	1.0782(85)	2.3032(97)	1.0782(85)
2.6470(112)	1.0973(86)	2.6471(112)	1.0973(86)
3.1293(58)	1.1272(59)	3.1293(58)	1.1272(59)
3.4269(64)	1.1392(64)	3.4270(64)	1.1392(64)
3.8214(72)	1.1529(58)	3.8215(72)	1.1529(58)
4.3203(83)	1.1800(65)	4.3203(83)	1.1800(65)
4.9702(99)	1.2137(67)	4.9702(99)	1.2137(67)
5.8840(122)	1.2623(82)	5.8841(122)	1.2623(82)
7.2384(211)	1.3950(129)	7.2384(211)	1.3950(129)
8.0241(189)	1.6801(1105)	8.0241(189)	1.6798(1104)

Table B.16: Numerical value of the discrete step scaling function Σ from the simulations, in the case of $c = 0.7$ and for the pair of lattices going from $\tilde{L} = 18$ to $\tilde{L} = 36$ for both the clover (C) and plaquette (P) definitions of the observable. The errors are shown within parenthesis.

u	Σ/u (C)	u	Σ/u (P)
1.8682(60)	1.0713(155)	1.8682(60)	1.0713(155)
2.0899(67)	1.0743(147)	2.0899(67)	1.0743(147)
2.3601(76)	1.0802(173)	2.3601(76)	1.0802(173)
2.7498(90)	1.1282(186)	2.7498(90)	1.1282(186)
3.2368(145)	1.1325(129)	3.2369(145)	1.1325(129)
3.6159(120)	1.1427(134)	3.6159(120)	1.1426(134)
4.0628(133)	1.1824(131)	4.0629(133)	1.1824(131)
4.6003(163)	1.2113(136)	4.6003(163)	1.2113(135)
5.3384(188)	1.2492(132)	5.3384(188)	1.2492(132)
6.4358(245)	1.3122(169)	6.4358(245)	1.3122(169)
8.1449(336)	1.6634(1077)	8.1449(336)	1.6633(1076)

Table B.17: Numerical value of the discrete step scaling function Σ from the simulations, in the case of $c = 0.7$ and for the pair of lattices going from $\tilde{L} = 24$ to $\tilde{L} = 48$ for both the clover (C) and plaquette (P) definitions of the observable. The errors are shown within parenthesis.

B.4 Continuum extrapolation and running coupling

We display in this appendix the relevant numerical data used for the interpolations, continuum extrapolations and plots of the continuum step scaling function $\sigma(u)$ and the running coupling from section 3.4.3.

u	$\tilde{L} = 12$(C)	$\tilde{L} = 18$(C)	$\tilde{L} = 24$(C)	$\tilde{L} = 12$(P)	$\tilde{L} = 18$(P)	$\tilde{L} = 24$(P)
1.8	1.058(1)	1.060(2)	1.062(2)	1.057(1)	1.060(2)	1.062(2)
2.0	1.065(1)	1.068(2)	1.070(2)	1.064(1)	1.067(2)	1.070(2)
2.5	1.083(1)	1.088(1)	1.091(2)	1.083(1)	1.088(1)	1.091(2)
3.0	1.102(1)	1.109(1)	1.112(1)	1.102(1)	1.109(1)	1.112(1)
3.5	1.122(1)	1.131(1)	1.135(1)	1.122(1)	1.131(1)	1.135(1)
4.0	1.143(1)	1.154(1)	1.158(2)	1.143(1)	1.154(1)	1.158(2)
4.5	1.166(1)	1.178(1)	1.182(2)	1.165(1)	1.177(1)	1.182(2)
5.0	1.189(1)	1.202(1)	1.208(2)	1.189(1)	1.202(1)	1.208(2)
5.5	1.215(1)	1.229(1)	1.235(3)	1.214(1)	1.229(1)	1.235(2)
6.0	1.243(1)	1.258(1)	1.265(3)	1.242(1)	1.258(1)	1.265(3)
6.5	1.273(2)	1.289(1)	1.297(3)	1.272(2)	1.289(1)	1.297(3)
7.0	1.306(2)	1.324(1)	1.333(4)	1.306(2)	1.324(1)	1.333(4)
7.5	1.343(2)	1.364(2)	1.373(3)	1.343(2)	1.364(2)	1.373(3)
8.0	1.385(4)	1.409(4)	1.419(3)	1.384(4)	1.410(4)	1.419(3)
8.5	1.431(6)	1.462(7)	1.470(5)	1.431(6)	1.462(7)	1.471(5)

Table B.18: Interpolated $\Sigma(u)/u$ points used to extrapolate the continuum step scaling function $\sigma(u)/u$ for $c = 0.3$, for both the clover (C) and the plaquette (P) definitions of the observable. The error in the last decimal is shown within parenthesis.

u	σ/u (C)	σ/u (P)
1.8	1.0622(25)	1.0623(24)
2.0	1.0706(23)	1.0707(23)
2.5	1.0925(17)	1.0926(17)
3.0	1.1152(13)	1.1153(13)
3.5	1.1386(12)	1.1387(12)
4.0	1.1626(14)	1.1627(13)
4.5	1.1874(16)	1.1875(16)
5.0	1.2133(18)	1.2134(18)
5.5	1.2407(21)	1.2409(21)
6.0	1.2703(24)	1.2706(24)
6.5	1.3029(26)	1.3031(26)
7.0	1.3394(26)	1.3397(26)
7.5	1.3816(29)	1.3819(28)
8.0	1.4299(39)	1.4302(38)
8.5	1.4842(61)	1.4845(60)

Table B.19: Results for the extrapolated continuum step scaling function $\sigma(u)/u$ for $c = 0.3$ for both the clover (C) and the plaquette (P) definitions of the observable. The error in the last decimal is shown within parenthesis.

$\log_2(\tilde{L}/\tilde{L}_{\min})$	$\lambda_{TGF}(\tilde{L})$ (C)	$\lambda_{TGF}(\tilde{L})$ (P)
0	1.7500(0)	1.7500(0)
1	1.8552(44)	1.8553(44)
2	1.9749(65)	1.9752(64)
3	2.1123(83)	2.1128(82)
4	2.272(10)	2.272(10)
5	2.459(12)	2.460(12)
6	2.682(14)	2.683(13)
7	2.952(15)	2.954(15)
8	3.285(18)	3.288(18)
9	3.707(20)	3.711(20)
10	4.257(24)	4.263(24)
11	5.004(29)	5.012(28)
12	6.072(36)	6.085(36)
13	7.740(48)	7.763(48)
14	10.87(7)	10.92(7)
15	20.53(61)	20.77(64)

Table B.20: Results for the running coupling $\lambda_{TGF}(\tilde{L})$ as a function of the scale increase factor for both the clover (C) and the plaquette (P) definitions of the observable. The error in the last decimal is shown within parenthesis.

Bibliography

[1] Gerard 't Hooft. A Property of Electric and Magnetic Flux in Nonabelian Gauge Theories. *Nucl. Phys.*, B153:141–160, 1979.

[2] Antonio Gonzalez-Arroyo, J. Jurkiewicz, and C. P. Korthals-Altes. Ground state metamorphosis for Yang-Mills fields on a finite periodic lattice. In *Freiburg ASI 1981:0339*, page 0339, 1981.

[3] Tohru Eguchi and Hikaru Kawai. Reduction of Dynamical Degrees of Freedom in the Large N Gauge Theory. *Phys. Rev. Lett.*, 48:1063, 1982.

[4] Antonio González-Arroyo and M. Okawa. The Twisted Eguchi-Kawai Model: A Reduced Model for Large N Lattice Gauge Theory. *Phys.Rev.*, D27:2397, 1983.

[5] Antonio González-Arroyo and M. Okawa. A Twisted Model for Large N Lattice Gauge Theory. *Phys.Lett.*, B120:174, 1983.

[6] Antonio González-Arroyo and C.P. Korthals Altes. Reduced Model for Large N Continuum Field Theories. *Phys.Lett.*, B131:396, 1983.

[7] Pierre van Baal. Some Results for SU(N) Gauge Fields on the Hypertorus. *Commun. Math. Phys.*, 85:529, 1982.

[8] M. Luscher. Some Analytic Results Concerning the Mass Spectrum of Yang-Mills Gauge Theories on a Torus. *Nucl. Phys.*, B219:233–261, 1983.

[9] M. Luscher and G. Munster. Weak Coupling Expansion of the Low Lying Energy Values in the SU(2) Gauge Theory on a Torus. *Nucl. Phys.*, B232:445, 1984.

[10] M. Luscher and P. Weisz. On-Shell Improved Lattice Gauge Theories. *Commun. Math. Phys.*, 97:59, 1985. [Erratum: Commun. Math. Phys.98,433(1985)].

[11] M. Lüscher and P. Weisz. Computation of the Action for On-Shell Improved Lattice Gauge Theories at Weak Coupling. *Phys. Lett.*, 158B:250–254, 1985.

[12] Jeffrey Koller and Pierre van Baal. A Rigorous Nonperturbative Result for the Glueball Mass and Electric Flux Energy in a Finite Volume. *Nucl. Phys.*, B273:387–412, 1986.

[13] Pierre van Baal and Jeffrey Koller. QCD on a Torus and Electric Flux Energies From Tunneling. *Annals Phys.*, 174:299, 1987.

[14] P. Weisz and V. Ziemann. Weak Coupling Expansions of the Low Lying Energy Values in SU(3) Gauge Theory on a Torus. *Nucl. Phys.*, B284:157, 1987.

[15] T. H. Hansson, Pierre van Baal, and I. Zahed. Chromomagnetic Energy of SU(2) Gauge Fields on a Torus. *Nucl. Phys.*, B289:628–644, 1987.

[16] A. Coste, Antonio González-Arroyo, C. P. Korthals Altes, B. Soderberg, and A. Tarancón. Finite Size Effects and Twisted Boundary Conditions. *Nucl. Phys.*, B287:569–588, 1987.

[17] Jeffrey Koller and Pierre van Baal. A Nonperturbative Analysis in Finite Volume Gauge Theory. *Nucl. Phys.*, B302:1–64, 1988.

[18] Antonio González-Arroyo and C. P. Korthals Altes. The Spectrum of Yang-Mills Theory in a Small Twisted Box. *Nucl. Phys.*, B311:433–449, 1988.

[19] D. Daniel, Antonio González-Arroyo, C. P. Korthals Altes, and B. Soderberg. Energy Spectrum of SU(2) Yang-Mills Fields With Space - Like Symmetric Twist. *Phys. Lett.*, B221:136–142, 1989.

[20] David Daniel, Antonio González-Arroyo, and Chris P. Korthals Altes. The Energy levels of lattice gauge theory in a small twisted box. *Phys. Lett.*, B251:559–566, 1990.

[21] P. W. Stephenson and M. Teper. Glueball Masses and the String Tension in SU(2) Lattice Gauge Theory With Twisted Boundary Conditions. *Nucl. Phys.*, B327:307–322, 1989.

[22] M. Garcia Perez et al. Instanton like contributions to the dynamics of Yang-Mills fields on the twisted torus. *Phys. Lett.*, B305:366–374, 1993.

[23] M. Garcia Perez, Antonio Gonzalez-Arroyo, and P. Martinez. From perturbation theory to confinement: How the string tension is built up. *Nucl. Phys. Proc. Suppl.*, 34:228–230, 1994.

[24] Antonio Gonzalez-Arroyo and P. Martinez. Investigating Yang-Mills theory and confinement as a function of the spatial volume. *Nucl. Phys.*, B459:337–354, 1996.

[25] Antonio Gonzalez-Arroyo, P. Martinez, and A. Montero. Gauge invariant structures and confinement. *Phys. Lett.*, B359:159–165, 1995.

[26] Jeroen R. Snippe. Square Symanzik action to one loop order. *Phys. Lett.*, B389:119–120, 1996.

[27] Jeroen R. Snippe. Computation of the one loop Symanzik coefficients for the square action. *Nucl. Phys.*, B498:347–396, 1997.

[28] A. González-Arroyo. Yang-Mills fields on the 4-dimensional Torus. Part I: Classical Theory. *World Scientific. Proceedings of the Peñiscola 1997 advanced school on non-perturbative quantum field physics*, page Singapore, 1998.

[29] Pierre van Baal. QCD in a finite volume. 2000.

[30] Martin Lüscher, Peter Weisz, and Ulli Wolff. A Numerical method to compute the running coupling in asymptotically free theories. *Nucl.Phys.*, B359:221–243, 1991.

[31] Martin Lüscher, Rainer Sommer, Ulli Wolff, and Peter Weisz. Computation of the running coupling in the SU(2) Yang-Mills theory. *Nucl.Phys.*, B389:247–264, 1993.

[32] Martin Luscher, Rajamani Narayanan, Peter Weisz, and Ulli Wolff. The Schrodinger functional: A Renormalizable probe for nonAbelian gauge theories. *Nucl. Phys.*, B384:168–228, 1992.

[33] Martin Lüscher, Rainer Sommer, Peter Weisz, and Ulli Wolff. A precise determination of the running coupling in the SU(3) Yang-Mills theory. *Nucl.Phys.*, B413:481–502, 1994.

[34] Stefan Sint and Rainer Sommer. The Running coupling from the QCD Schrodinger functional: A One loop analysis. *Nucl. Phys.*, B465:71–98, 1996.

[35] Jochen Heitger and Rainer Sommer. Nonperturbative heavy quark effective theory. *JHEP*, 02:022, 2004.

[36] Stefano Capitani, Martin Luscher, Rainer Sommer, and Hartmut Wittig. Non-perturbative quark mass renormalization in quenched lattice QCD. *Nucl. Phys.*, B544:669–698, 1999. [Erratum: Nucl. Phys.B582,762(2000)].

[37] Thomas Appelquist, George T. Fleming, and Ethan T. Neil. Lattice Study of Conformal Behavior in SU(3) Yang-Mills Theories. *Phys. Rev.*, D79:076010, 2009.

[38] Szabolcs Borsanyi, Gergely Endrodi, Zoltan Fodor, Antal Jakovac, Sandor D. Katz, Stefan Krieg, Claudia Ratti, and Kalman K. Szabo. The QCD equation of state with dynamical quarks. *JHEP*, 11:077, 2010.

[39] Zoltan Fodor, Kieran Holland, Julius Kuti, Daniel Nogradi, and Chik Him Wong. The Yang-Mills gradient flow in finite volume. *JHEP*, 1211:007, 2012.

[40] K. Fabricius and C. P. Korthals Altes. Reduction of fermion-gluon systems on extended lattices. *Nucl. Phys.*, B269:97–108, 1986.

[41] M. Lüscher and P. Weisz. Efficient Numerical Techniques for Perturbative Lattice Gauge Theory Computations. *Nucl.Phys.*, B266:309, 1986.

[42] Margarita García Pérez, Antonio González-Arroyo, and Masanori Okawa. Spatial volume dependence for 2+1 dimensional SU(N) Yang-Mills theory. *JHEP*, 1309:003, 2013.

[43] Antonio González-Arroyo and Masanori Okawa. Testing volume independence of SU(N) pure gauge theories at large N. *JHEP*, 1412:106, 2014.

[44] Margarita García Pérez, Antonio González-Arroyo, and Masanori Okawa. Perturbative contributions to Wilson loops in twisted lattice boxes and reduced models. *JHEP*, 10:150, 2017.

[45] Margarita García Pérez, Antonio González-Arroyo, Mateusz Koren, and Masanori Okawa. The spectrum of 2+1 dimensional Yang-Mills theory on a twisted spatial torus. *JHEP*, 07:169, 2018.

[46] Antonio González-Arroyo, Issaku Kanamori, Ken-Ichi Ishikawa, Kanata Miyahana, Masanori Okawa, and Ryoichiro Ueno. Numerical stochastic perturbation theory applied to the twisted Eguchi-Kawai model. *JHEP*, 06:127, 2019.

[47] J. Kiskis, R. Narayanan, and H. Neuberger. Proposal for the numerical solution of planar QCD. *Phys. Rev.*, D66:025019, 2002.

[48] R. Narayanan and H. Neuberger. Large N reduction in continuum. *Phys. Rev. Lett.*, 91:081601, 2003.

[49] R. Narayanan, H. Neuberger, and F. Reynoso. Phases of three dimensional large N QCD on a continuum torus. *Phys. Lett.*, B651:246–252, 2007.

[50] R. Narayanan and H. Neuberger. Universality of large N phase transitions in Wilson loop operators in two and three dimensions. *JHEP*, 12:066, 2007.

[51] Joe Kiskis and Rajamani Narayanan. Computation of the string tension in three dimensional Yang-Mills theory using large N reduction. *JHEP*, 09:080, 2008.

[52] Mithat Unsal and Laurence G. Yaffe. Center-stabilized Yang-Mills theory: Confinement and large N volume independence. *Phys. Rev.*, D78:065035, 2008.

[53] Dusan Simic and Mithat Unsal. Deconfinement in Yang-Mills theory through toroidal compactification with deformation. *Phys. Rev.*, D85:105027, 2012.

[54] Pavel Kovtun, Mithat Unsal, and Laurence G. Yaffe. Volume independence in large N(c) QCD-like gauge theories. *JHEP*, 06:019, 2007.

[55] Tatsuo Azeyanagi, Masanori Hanada, Mithat Unsal, and Ran Yacoby. Large-N reduction in QCD-like theories with massive adjoint fermions. *Phys. Rev.*, D82:125013, 2010.

[56] Piotr Korcyl and Mateusz Koren. Preliminary study of two-dimensional SU(N) Yang-Mills theory with adjoint matter by Hybrid Monte Carlo approach. *PoS*, LATTICE2011:071, 2011.

[57] Barak Bringoltz, Mateusz Koren, and Stephen R. Sharpe. Large-N reduction with two adjoint Dirac fermions. *PoS*, LATTICE2011:072, 2011.

[58] Barak Bringoltz, Mateusz Koren, and Stephen R. Sharpe. Large-N reduction in QCD with two adjoint Dirac fermions. *Phys. Rev.*, D85:094504, 2012.

[59] Barak Bringoltz, Mateusz Koren, and Stephen R. Sharpe. Large-N reduction with adjoint Wilson fermions. *PoS*, LATTICE2012:045, 2012.

[60] Liam Keegan. Mass Anomalous Dimension at Large N. *PoS*, LATTICE2012:044, 2012.

[61] A. Hietanen and R. Narayanan. Numerical evidence for non-analytic behavior in the beta function of large N SU(N) gauge theory coupled to an adjoint Dirac fermion. *Phys. Rev.*, D86:085002, 2012.

[62] Gokce Basar, Aleksey Cherman, Daniele Dorigoni, and Mithat Unsal. Volume Independence in the Large N Limit and an Emergent Fermionic Symmetry. *Phys. Rev. Lett.*, 111(12):121601, 2013.

[63] Robert Lohmayer and Rajamani Narayanan. Weak-coupling analysis of the single-site large-N gauge theory coupled to adjoint fermions. *Phys. Rev.*, D87(12):125024, 2013.

[64] Antonio González-Arroyo and Masanori Okawa. Large N reduction with the Twisted Eguchi-Kawai model. *JHEP*, 1007:043, 2010.

[65] Antonio Gonzalez-Arroyo and Masanori Okawa. The string tension for Large N gauge theory from smeared Wilson loops. *PoS*, LATTICE2012:221, 2012.

[66] Antonio González-Arroyo and Masanori Okawa. The string tension from smeared Wilson loops at large N. *Phys. Lett.*, B718:1524–1528, 2013.

[67] Antonio Gonzalez-Arroyo and Masanori Okawa. Twisted reduction in large N QCD with two adjoint Wilson fermions. *PoS*, LATTICE2012:046, 2012.

[68] Antonio Gonzalez-Arroyo and Masanori Okawa. Confinement in large N gauge theories. 2013. [PoSConfinementX,277(2012)].

[69] Antonio Gonzalez-Arroyo and Masanori Okawa. Twisted reduction in large N QCD with adjoint Wilson fermions. *PoS*, LATTICE2013:099, 2014.

[70] Margarita Garcia Perez, Antonio Gonzalez-Arroyo, Liam Keegan, and Masanori Okawa. Mass anomalous dimension from large N twisted volume reduction. *PoS*, LATTICE2013:098, 2014.

[71] Antonio González-Arroyo and Masanori Okawa. Twisted space-time reduced model of large N QCD with two adjoint Wilson fermions. *Phys. Rev.*, D88:014514, 2013.

[72] Margarita García Pérez, Antonio González-Arroyo, Liam Keegan, and Masanori Okawa. Mass anomalous dimension of Adjoint QCD at large N from twisted volume reduction. *JHEP*, 08:034, 2015.

[73] Gyan Bhanot, Urs M. Heller, and Herbert Neuberger. The Quenched Eguchi-Kawai Model. *Phys. Lett.*, 113B:47–50, 1982.

[74] Alain Connes, Michael R. Douglas, and Albert S. Schwarz. Noncommutative geometry and matrix theory: Compactification on tori. *JHEP*, 02:003, 1998.

[75] Jan Ambjorn, Y. M. Makeenko, J. Nishimura, and R. J. Szabo. Finite N matrix models of noncommutative gauge theory. *JHEP*, 11:029, 1999.

[76] Jan Ambjorn, Y. M. Makeenko, J. Nishimura, and R. J. Szabo. Lattice gauge fields and discrete noncommutative Yang-Mills theory. *JHEP*, 05:023, 2000.

[77] Jan Ambjorn, Y. M. Makeenko, J. Nishimura, and R. J. Szabo. Nonperturbative dynamics of noncommutative gauge theory. *Phys. Lett.*, B480:399–408, 2000.

[78] Zachary Guralnik and Jan Troost. Aspects of gauge theory on commutative and noncommutative tori. *JHEP*, 05:022, 2001.

[79] Mithat Unsal and Laurence G. Yaffe. Large-N volume independence in conformal and confining gauge theories. *JHEP*, 08:030, 2010.

[80] Margarita Garcia Perez, Antonio Gonzalez-Arroyo, and Masanori Okawa. Volume dependence in 2+1 Yang-Mills theory. *PoS*, LATTICE2012:219, 2012.

[81] Mohamed M. Anber and Mithat Unsal. QCD in magnetic field, Landau levels and double-life of unbroken center-symmetry. *JHEP*, 12:107, 2014.

[82] Margarita Garcia Perez, Antonio Gonzalez-Arroyo, and Masanori Okawa. Perturbative analysis of twisted volume reduced theories. *PoS*, LATTICE2013:342, 2014.

[83] Gerard 't Hooft. Some Twisted Selfdual Solutions for the Yang-Mills Equations on a Hypertorus. *Commun. Math. Phys.*, 81:267–275, 1981.

[84] Pierre van Baal. Surviving Extrema for the Action on the Twisted SU(infinity) One Point Lattice. *Commun. Math. Phys.*, 92:1, 1983.

[85] Fernando Chamizo and Antonio González-Arroyo. Tachyonic instabilities in 2+1 dimensional Yang-Mills theory and its connection to number theory. *J. Phys.*, A50(26):265401, 2017.

[86] T. Ishikawa and M. Okawa. Z_N^D symmetry breaking on the numerical simulation of twisted N Eguchi-Kawai model. *Talk given at the Annual Meeting of the Physical Society of Japan, Sendai, Japan*, 2003.

[87] Wolfgang Bietenholz, Jun Nishimura, Yoshiaki Susaki, and Jan Volkholz. A Non-perturbative study of 4-D U(1) non-commutative gauge theory: The Fate of one-loop instability. *JHEP*, 10:042, 2006.

[88] Michael Teper and Helvio Vairinhos. Symmetry breaking in twisted Eguchi-Kawai models. *Phys. Lett.*, B652:359–369, 2007.

[89] Tatsuo Azeyanagi, Masanori Hanada, Tomoyoshi Hirata, and Tomomi Ishikawa. Phase structure of twisted Eguchi-Kawai model. *JHEP*, 01:025, 2008.

[90] Antonio Gonzalez-Arroyo and Masanori Okawa. Large N meson propagators from twisted space-time reduced model. *PoS*, LATTICE2015:291, 2016.

[91] Antonio González-Arroyo and Masanori Okawa. Large N meson masses from a matrix model. *Phys. Lett.*, B755:132–137, 2016.

[92] L. Álvarez-Gaumé and J. L. F. Barbón. Morita duality and large N limits. *Nucl. Phys.*, B623:165–200, 2002.

[93] Margarita García Pérez, Antonio González-Arroyo, Liam Keegan, and Masanori Okawa. The $SU(\infty)$ twisted gradient flow running coupling. *JHEP*, 1501:038, 2015.

[94] Kyle Aitken, Aleksey Cherman, and Mithat Ünsal. Vacuum structure of yang-mills theory as a function of θ. *JHEP*, 2018(9):30, 2018.

[95] M. Hayakawa. Perturbative analysis on infrared aspects of noncommutative QED on R**4. *Phys. Lett.*, B478:394–400, 2000.

[96] Zachary Guralnik, Robert C. Helling, Karl Landsteiner, and Esperanza Lopez. Perturbative instabilities on the noncommutative torus, Morita duality and twisted boundary conditions. *JHEP*, 05:025, 2002.

[97] M. F. Atiyah and R. Bott. The Yang-Mills equations over Riemann surfaces. *Phil. Trans. Roy. Soc. Lond.*, A308:523–615, 1982. [,265(1982)].

[98] S. K. Donaldson. Anti self-dual Yang-Mills connections over complex algebraic surfaces and stable vector bundles. *Proc. Lond. Math. Soc.*, 50:1–26, 1985.

[99] M. Albanese et al. Glueball Masses and String Tension in Lattice QCD. *Phys. Lett.*, B192:163–169, 1987.

[100] Claude W. Bernard and Thomas A. DeGrand. Perturbation theory for fat link fermion actions. *Nucl. Phys. Proc. Suppl.*, 83:845–847, 2000.

[101] R. Narayanan and H. Neuberger. Infinite N phase transitions in continuum Wilson loop operators. *JHEP*, 03:064, 2006.

[102] Robert Lohmayer and Herbert Neuberger. Continuous smearing of Wilson Loops. *PoS*, LATTICE2011:249, 2011.

[103] Martin Lüscher. Trivializing maps, the Wilson flow and the HMC algorithm. *Commun.Math.Phys.*, 293:899–919, 2010.

[104] Martin Lüscher. Properties and uses of the Wilson flow in lattice QCD. *JHEP*, 1008:071, 2010.

[105] Martin Lüscher and Peter Weisz. Perturbative analysis of the gradient flow in non-abelian gauge theories. *JHEP*, 1102:051, 2011.

[106] Martin Lüscher. Chiral symmetry and the Yang–Mills gradient flow. *JHEP*, 1304:123, 2013.

[107] Martin Lüscher. Future applications of the Yang-Mills gradient flow in lattice QCD. *PoS*, LATTICE2013:016, 2014.

[108] Martin Lüscher. Step scaling and the Yang-Mills gradient flow. *JHEP*, 1406:105, 2014.

[109] Mattia Dalla Brida and Martin Lüscher. The gradient flow coupling from numerical stochastic perturbation theory. *PoS*, LATTICE2016:332, 2016.

[110] M. Dalla Brida, P. Fritzsch, T. Korzec, A. Ramos, S. Sint, et al. Towards a new determination of the QCD Lambda parameter from running couplings in the three-flavour theory. *PoS*, LATTICE2014:291, 2014.

[111] Mattia Dalla Brida, Patrick Fritzsch, Tomasz Korzec, Alberto Ramos, Stefan Sint, and Rainer Sommer. Slow running of the Gradient Flow coupling from 200 MeV to 4 GeV in $N_{\rm f} = 3$ QCD. *Phys. Rev.*, D95(1):014507, 2017.

[112] Mattia Bruno, Mattia Dalla Brida, Patrick Fritzsch, Tomasz Korzec, Alberto Ramos, Stefan Schaefer, Hubert Simma, Stefan Sint, and Rainer Sommer. QCD Coupling from a Nonperturbative Determination of the Three-Flavor Λ Parameter. *Phys. Rev. Lett.*, 119(10):102001, 2017.

[113] Tomasz Korzec. Determination of the Strong Coupling Constant by the ALPHA Collaboration. *EPJ Web Conf.*, 175:01018, 2018.

[114] Ken-Ichi Ishikawa, Issaku Kanamori, Yuko Murakami, Ayaka Nakamura, Masanori Okawa, and Ryoichiro Ueno. Non-perturbative determination of the Λ-parameter in the pure SU(3) gauge theory from the twisted gradient flow coupling. *JHEP*, 12:067, 2017.

[115] C. J. David Lin, Kenji Ogawa, and Alberto Ramos. The Yang-Mills gradient flow and SU(3) gauge theory with 12 massless fundamental fermions in a colour-twisted box. *JHEP*, 12:103, 2015.

[116] Zoltan Fodor, Kieran Holland, Julius Kuti, Santanu Mondal, Daniel Nogradi, and Chik Him Wong. Fate of the conformal fixed point with twelve massless fermions and SU(3) gauge group. *Phys. Rev.*, D94(9):091501, 2016.

[117] Anna Hasenfratz and David Schaich. Nonperturbative β function of twelve-flavor SU(3) gauge theory. *JHEP*, 02:132, 2018.

[118] Zoltan Fodor, Kieran Holland, Julius Kuti, Daniel Nogradi, and Chik Him Wong. The gradient flow running coupling scheme. 2012.

[119] Szabolcs Borsanyi, Stephan Dürr, Zoltan Fodor, Christian Hoelbling, Sandor D. Katz, et al. High-precision scale setting in lattice QCD. *JHEP*, 1209:010, 2012.

[120] Patrick Fritzsch and Alberto Ramos. The gradient flow coupling in the Schrödinger Functional. *JHEP*, 1310:008, 2013.

[121] Alberto Ramos. The gradient flow running coupling with twisted boundary conditions. *JHEP*, 1411:101, 2014.

[122] Zoltan Fodor, Kieran Holland, Julius Kuti, Santanu Mondal, Daniel Nogradi, et al. The lattice gradient flow at tree-level and its improvement. *JHEP*, 1409:018, 2014.

[123] Rainer Sommer. Scale setting in lattice QCD. *PoS*, LATTICE2013:015, 2014.

[124] R. Sommer. A New way to set the energy scale in lattice gauge theories and its applications to the static force and alpha-s in SU(2) Yang-Mills theory. *Nucl. Phys.*, B411:839–854, 1994.

[125] Martin Lüscher and Stefan Schaefer. Lattice QCD without topology barriers. *JHEP*, 1107:036, 2011.

[126] A. Ramos and S. Sint. Symanzik improvement of the gradient flow in lattice gauge theories. *Eur. Phys. J.*, C76(1):15, 2016.

[127] Alberto Ramos and Liam Keegan. (Dimensional) twisted reduction in large N gauge theories. *PoS*, LATTICE2015:290, 2016.

[128] Alberto Ramos. The Yang-Mills gradient flow and renormalization. *PoS*, LATTICE2014:017, 2015.

[129] Robert V. Harlander and Tobias Neumann. The perturbative QCD gradient flow to three loops. *JHEP*, 06:161, 2016.

[130] Mattia Dalla Brida and Martin Lüscher. SMD-based numerical stochastic perturbation theory. *Eur. Phys. J.*, C77(5):308, 2017.

[131] E. Brezin and Jean Zinn-Justin. Finite Size Effects in Phase Transitions. *Nucl. Phys.*, B257:867–893, 1985.

[132] Mattia Dalla Brida and Alberto Ramos. The gradient flow coupling at high-energy and the scale of SU(3) Yang Mills theory. *Eur. Phys. J.*, C79(8):720, 2019.

[133] Alberto Ramos and Stefan Sint. On $\mathcal{O}(a^2)$ effects in gradient flow observables. 2014.

[134] Ulli Wolff. Dynamics of hybrid overrelaxation in the Gaussian model. *Phys. Lett.*, B288:166–170, 1992.

[135] Stefan Schaefer, Rainer Sommer, and Francesco Virotta. Investigating the critical slowing down of QCD simulations. *PoS*, LAT2009:032, 2009.

[136] Stefan Schaefer, Rainer Sommer, and Francesco Virotta. Critical slowing down and error analysis in lattice QCD simulations. *Nucl. Phys.*, B845:93–119, 2011.

[137] Patrick Fritzsch, Alberto Ramos, and Felix Stollenwerk. Critical slowing down and the gradient flow coupling in the Schrödinger functional. *PoS*, Lattice2013:461, 2013.

[138] Margarita García Pérez, Antonio González-Arroyo, and Masanori Okawa. Volume independence for Yang-Mills fields on the twisted torus. *Int. J. Mod. Phys.*, A29(25):1445001, 2014.